THESIS FOR THE DEGREE OF DOCTOR OF PHILOSOPHY

Wind Turbine Characterization by Voltage Source Converter Based Test Equipment

NICOLÁS ESPINOZA

Department of Energy and Environment
CHALMERS UNIVERSITY OF TECHNOLOGY
Gothenburg, Sweden, 2016

Wind Turbine Characterization by Voltage Source Converter Based Test Equipment
NICOLÁS ESPINOZA
ISBN 978-91-7597-514-6

Doktorsavhandlingar vid Chalmers Tekniska Högskola
Ny serie nr. 4195
ISSN 0346-718X

Division of Electric Power Engineering
Department of Energy and Environment
Chalmers University of Technology
SE–412 96 Gothenburg
Sweden
Telephone +46 (0) 31–772 1000

Printed by Chalmers Reproservice
Gothenburg, Sweden, 2016

To my family and friends...

Wind Turbine Characterization by Voltage Source Converter Based Test Equipment
NICOLÁS ESPINOZA
Department of Energy and Environment
Chalmers University of Technology

Abstract

In countries where wind power has become a relevant part of the total generated electrical power, transmission system operators (TSOs) have included in their Grid Codes specific technical requirements for interconnection of wind power plants. Some Grid Codes demand specific testing procedures in order to verify the fulfilment for their requirements. These tests are today carried out using an impedance-based test equipment, which is limited to voltage dips and swells. For this reason, many of the requirements remain untested by field experiment. The use of a fully controllable converter system operated as test equipment allows for a wide variety of tests that can be carried out, in order to assess for successful grid integration of the generating unit. In this regard, a different approach for testing of multi-megawatt wind turbines by fully-rated converter system is presented in this thesis.

The investigated testing setup consists of a 4 MW full power converter (FPC) based wind turbine and an 8 MW testing equipment constituted by a set of two voltage source converters (VSCs) in back-to-back configuration. In particular, this thesis focuses on the use of the testing equipment in order to obtain a full characterization of the behavior of the wind turbine system in both steady-state and dynamic condition of the grid. A detailed description of the technical requirements for grid interconnection of wind power plants included in the selected Grid Codes is given. The control algorithms that govern both the testing equipment and the wind turbine are derived in detail, with special focus on the control scheme of each VSC. The risk for poorly damped resonances and possible interactions between the testing equipment and the tested object are investigated through small signal stability analysis. In this regard, the characteristic impedance of the wind turbine unit is derived and verified by frequency scan using the testing device. The testing methodology is verified through time-domain simulations. Moreover, the ability of the testing equipment in reproducing a low voltage ride through (LVRT) profile that is typically included in Grid Codes is analysed in detail, including other features such as the emulation of the short-circuit impedance of the grid at the connection point. In addition, wind turbine testing of active power curtailment during grid-frequency deviation is also investigated in this thesis. Laboratory experiments comprising of a low-voltage prototype of the testing equipment and a reduced model of the FPC wind turbine equipped with the derived control features are carried out to verify the investigated methodology. Finally, field tests carried out on a full-size testing facility in Gothenburg, Sweden, are included in this thesis. The obtained results demonstrate the flexibility of the investigated testing equipment in controlling the voltage at the wind turbine terminals, which allows for a full characterization of the generating unit.

Index Terms: Grid Code, Wind Power, Low Voltage Ride Through (LVRT), Voltage Source Converter (VSC), Discrete Control, Grid Emulation, Grid Integration, Frequency Scan.

Acknowledgements

This project is financed through the Swedish Wind Power Technology Centre (SWPTC). SWPTC is a research Centre for design of wind turbines. The purpose of the Centre is to support Swedish industry with knowledge of design techniques as well as maintenance in the field of wind power. The Centre is funded by the Swedish Energy Agency, Chalmers University of Technology as well as academic and industrial partners. The support from SWTPC is gratefully acknowledged.

Additionally, I would like to acknowledge the support from the Swedish Energy Agency, Göteborg Energi, Västra Götalandsregionen, PROTROL and General Electric that allowed the unique opportunity of carrying out the field test presented in this thesis. Thank you for the trust given to me and to my research group within the SWPTC.

I would like to express my deepest and sincere gratitude to my supervisor Professor Massimo Bongiorno and my examiner Professor Ola Carlson for their professional guidance, encouragement and invaluable help throughout the research work. I am also grateful to Sara Fogelström for her administrative support within the SWPTC. Special thanks to Massimo for his help in supervising and correcting this manuscript and for his patience, insightful comments, and hard questions.

My acknowledgements to the members of ABB Corporate Research Centre, especially Luca Peretti and former member Ville Sarkimaki, and to GE Global Research members Emad Ahmed and Christof Sihler for sharing their experience with me and for providing valuable data used in this work. I would like to thank Michael Lindgren and Pehr Hjalmarsson (PROTOL) and Christer Pettersson (Göteborg Energi) for their support in providing experimental data used in this thesis. Without them, the test carried out on Big Glenn wind turbine by the 8 MW VSC-HVDC would not have been possible.

I take this opportunity to express my gratitude to all my colleagues at the Division of Electric Power Engineering at Chalmers University of Technology, especially to Georgios Stamatiou, Joachim Härsjö, Pramod Bangalore, Pavan Balram, Daniel Pehrman, Pinar Tokat, Gustavo Pinares and Ehsan Behrouzian for their company, their friendship and their support during this project. Special thanks to Ehsan, Daniel, Georgios Mademlis, Robert Karlsson, Torbjörn Thiringer, Magnus Ellsen and Massimo for their help when building the laboratory setup. I would like to thank my friends Tomás Baeza and Giuseppe Leanza for their good friendship and support, as well as my dear friends who are in Chile, Diego Molina and Carlos Chaparro for their support and for their long and true friendship.

Finally, my warm gratitude to my family for their love and encouragement and to my beautiful and beloved fiancée Paola. Thank you *Amore* with all my heart.

Nicolás,
Gothenburg, November 18th, 2016

Preface

The Swedish Wind Power Technology Centre (SWPTC), placed at Chalmers University of Technology in Gothenburg, Sweden, focuses on developing knowledge of the design of wind turbines and optimizing maintenance and production costs.

One of the objectives of the Centre is to supply the industry with in-depth know-how within the field of wind power. Specific projects are being carried out within the Centre regarding the following topics: power and control system, turbine and wind load, mechanical power transmission and system operation, structure and foundation, maintenance and reliability, and operation in cold climate. Other research projects at Chalmers University of Technology are related to semiconductors, converter topologies and control for renewable energy sources.

At the SWPTC, the wind turbine is seen as a complete system, and for this reason, there is a strong cooperation between the mechanical, electrical and control departments within the University and the Centre. By integrating education, research and innovation, the SWPTC hope to contribute with competence, knowledge and experience that today's industry needs.

This project is part of Theme Group 1: Power and Control Systems.

SWPTC's work is funded by the Swedish Energy Agency, by three academic and thirteen industrial partners, including Göteborg Energi, amog others. Västra Götalandsregionen also contributes to the Centre through several collaboration projects.

List of Acronyms

IG	Inductor Generator
VSC	Voltage Source Converter
FPC	Full-Power Converter
DFIG	Doubly-Fed Induction Generator
WT	Wind Turbine (in plots only)
back-EMF	Back Electromotive Force
TE	Testing Equipment
TSO	Transmission System Operator
PCC	Point of Common Coupling
LVRT	Low Voltage Ride Through
EWEA	European Wind Energy Association
SWPTC	Swedish Wind Power Technology Centre
FACTS	Flexible AC Transmission System
STATCOM	Static Compensator
HVDC	High Voltage Direct Current
HV	High Voltage
MV	Medium Voltage
LV	Low Voltage
LC	Inductive Capacitive
IGBT	Insulated Gate Bipolar Transistors
LPF	Low-Pass Filter
PWM	Pulse Width Modulation
OL	Open-Loop
CL	Close-Loop
PI	Proportional-Integral
P	Proportional
PD	Proportional-Derivative
PLL	Phase-Locked Loop
PMU	Phasor Measurement Unit
IMC	Internal Model Control

Contents

Chapter 1

Introduction

1.1 Background and motivation

Wind energy is a renewable source of energy that plays a key role towards a sustainable future. For this reason, wind turbines with larger and larger power ratings are being installed every year [1]. Among other factors, the reliability of the electrical grid depends on how well the generating units are prepared to support the grid in case of abnormal condition. In the specific case of integration of renewable energy sources, Transmission System Operators (TSOs) have included in their Grid Codes specific technical requirements for interconnection of wind power plants with the electricity grid.

In general words, a Grid Code specifies how a generating plant should behave during normal and abnormal condition of the grid. The continuous increase of electrical energy from wind power injected into the power system has lead TSOs to impose more and more stringent requirements for this kind of plants. For instance, voltage and frequency range in which the wind turbine has to operate in steady-state are given in a detailed manner. In addition, typical system disturbances such as voltage dips are specified in terms of level of retained voltage, including the duration in which the generating plant should withstand without disconnecting from the grid. Disconnection is possible in extreme cases and only when it is permitted by the TSO. In this regard, a wind turbine manufacturer has to ensure a safe operation of the generating unit by fulfilling the technical requirements relevant for the interconnection of the plant. Moreover, these requirements are always a design criteria for wind turbine manufacturers. For this reason, it is crucial to develop testing methodologies for this type of technology in order to ensure a correct integration of wind energy into the electricity grids.

Furthermore, in the future, wind turbines will be required to participate more actively in the regulation of the grid [2]. It is a common believe that international standards and local Grid Codes will contemplate a wide variety of new requirements addressing a reliable operation of the wind power plant. Smart control algorithms will allow them to behave as any conventional energy source in terms of inertia, power oscillation damping and voltage and frequency support of the grid, contributing to the overall stability enhancement of the power system.

To evaluate the capability of the wind turbine to withstand grid disturbances, today tests are

performed on the generating unit by using an impedance-based voltage dip generator. By developing further new testing methodologies, it will be possible to test for grid scenarios other than voltage dips, ensuring a reliable and fault-tolerant operation of the wind turbine system.

In this regard, it is well known that voltage source converters (VSC) can provide the necessary flexibility in order to control the terminal voltage as desired. On the other hand, power electronic devices have become cheaper and more accessible over the years [1]. It is, therefore, natural that future testing devices will be fully, or if not, partially driven by VSC devices. Recently, this trend has been followed in testing facilities such as the ones described in [3], [4], [5] and [6]. In small scale, other works such as the ones presented [7] and in [8] have shown some of the advantages provided by the use of VSC-based testing equipment.

However, previous works lack of a comprehensive analysis on the integration of the renewable energy source and the investigated testing device. In the literature, the focus has been mainly on the capability of the testing equipment in reproducing a typical voltage dip. For this reason, other equally important aspects such as: the impact of the control settings and system parameters of both wind turbine and testing equipment on the overall stability of the system; analysis of the transient dynamics of the system during the testing; or the development of advanced control features for the testing device in order to perform a specific test, as covered in this thesis, have not been fully investigated.

For example, reference [9] presents a control algorithm for a VSC-based test system capable of varying the magnitude and phase angle of the applied voltage. Its focus is on the controllability aspects of the testing equipment in order to test low voltage electrical devices and not renewable energy sources. While aspects such as the necessary control algorithm to accurately reproduce an unbalanced voltage dip are discussed in the paper, analysis on the dynamics of the complete system when interconnecting a wind turbine unit is not within the scope of the investigation. Other works such as the one presented in [10] have successfully modelled a doubly-fed induction generator (DFIG) based wind turbine interconnected to a VSC-based testing equipment. However, their focus has been on the analysis of the behavior of the wind turbine model during a typical voltage dip, while other abnormal grid scenarios, such as frequency deviation or phase-angle variation, which can be included in future Grid Code requirements [2], have not been investigated.

For these reasons, a comprehensive system-level analysis on the use of a VSC-based testing device, in particular on the capability of emulating a variety of abnormal grid scenarios, is investigated in this thesis. Other features of the testing equipment such as the ability in emulating the interconnecting grid-impedance for the wind turbine and the ability of evaluating the wind turbine input admittance has also been addressed in this work.

1.2 Purpose of the thesis and main contribution

The objective of this work is to develop a method to characterize a wind turbine system by means of a fully-rated VSC-based testing equipment. In particular, this work addresses the specific control features to be implemented on the testing equipment which allow for testing and characterizing a full power converter (FPC) based wind turbine system.

To the best knowledge of the author, the main contribution of this work can be summarized in the following points:

- A better understanding on the use of specific VSC-based test equipment for testing wind energy systems. In particular, on the necessary control algorithms that allow for a complete electrical characterization of the generating unit. This includes the development of a grid-emulation algorithm used for evaluating possible grid contingencies on the tested object.
- The variety of Grid Codes and the increasing strictness on their regulation for the integration of wind farms calls for the development of a flexible testing device. This thesis addresses the controllability and the stability of such device when testing wind turbine systems.
- The flexibility of the investigated testing device is here shown and demonstrated with core examples. Considering that the testing device is used to impose the voltage for the tested wind turbine unit, specific voltage controllers has been developed and evaluated by high-order simulation models and small-scale laboratory experiment.
- The overall performance of the testing setup is validated through full-scale field test, providing unique experience on the use of VSC-based testing equipment for performance evaluation and characterization of wind turbine systems. The results from this work have been used to evaluate the proposed methodology.

1.3 Structure of the thesis

This thesis is organized in 9 chapters. After the first introductory chapter, a brief review of the development of wind power installation, including the interconnection of wind power plants with the electricity grid and the description of the most common wind turbine topologies is given in Chapter 2.

In Chapter 3, technical requirements for interconnection of wind parks with the electricity grid have been identified within the selected Grid Codes. Moreover, a detailed description of the requirements for normal and fault conditions of the grid including the methodology for testing wind turbine systems are also introduced in this chapter.

The derivation of the necessary control features for both the testing equipment and the wind turbine system are discussed in Chapter 4. This includes the modelling and implementation of the VSC-based testing equipment and its control strategies, including PCC voltage control and short-circuit grid impedance emulation algorithm. The modelling of the FPC wind turbine, including crow-bar protection and current control strategy during fault, is also described here.

In Chapter 5, the stability of the system is investigated through the use of high-order linearized models. Root-locus has been used to assess the risk for interaction between the modelled wind turbine and the testing equipment against the variation of system parameters, such as filter size, interfacing impedance and control settings of both interconnected subsystems. The transfer

function of the characteristic impedance of the modelled wind turbine is also identified and evaluated in this chapter.

In Chapter 6, the investigated testing methodology is verified through time-domain simulations. The case studies treated and discussed in this chapter include, for example, reproducing the effect of a balanced and unbalanced voltage dip at the terminals of the wind turbine, including the ability of the testing equipment in emulating the short-circuit impedance of an interconnecting grid. Phase-angle jumps on the applied voltage are here used for testing grid-synchronization methods implemented in the wind turbine controller. Similarly, the input admittance of the modelled wind turbine is verified via on-line frequency scan. In this regard, frequency characterization of the wind turbine is here performed by introducing asynchronous frequency content into the applied voltage while observing the equivalent admittance at the connection point of the tested generating unit.

In Chapter 7, laboratory test are carried out in order to further verify the investigated methodology. Starting with the verification of its relevant sub-systems and control features, all grid contingencies studied in the previous chapter are carried out. The performance of the back-to-back VSC-based testing equipment in characterizing the small-scale wind turbine model is here shown and discussed.

The investigated methodology is validated in Chapter 8, where the obtained results from fully-rated field tests are presented. Here, a 4 MW FPC wind turbine is tested by the use of an actual testing equipment consisting of an 8 MW VSC-HVDC in back-to-back.

Finally, in Chapter 9 the conclusions of the overall work are drawn, together with interesting ideas that, if investigated, can open new doors in the path for successful integration of renewable energy sources in the electricity grid.

1.4 List of publications

Part of the results presented in this work has been published in three scientific papers listed as follows:

1. N. Espinoza, M. Bongiorno and O. Carlson, “Grid Code Testing of Full Power Converter Based Wind Turbine Using Back-to-Back Voltage Source Converter System,” European Wind Energy Conference and Exhibition, EWEC 2013, Vienna, Austria; 4-7 February, 2013.

2. N. Espinoza, M. Bongiorno and O. Carlson, “Novel LVRT Testing Method for Wind Turbines Using Flexible VSC Technology,” in *IEEE Transactions on Sustainable Energy*, vol.6, no.3, pp.1140-1149, July 2015

3. N. Espinoza, M. Bongiorno and O. Carlson, “Frequency Characterization of Type-IV Wind Turbine Systems,” in 2016 IEEE Energy Conversion Congress and Exposition (ECCE), Milwaukee, WI, USA, 2016.

Chapter 2

Wind energy systems

2.1 Introduction

Wind parks are today being installed in large scale in many countries. Moreover, wind turbines with greater power are being produced every year, making possible to extract more energy from wind [1].

From a global perspective, the total installed wind power in the world in 2015 is 433 GW, growing with an average rate of 47 GW per year in the last 5 years. The main players are China, USA and western Europe. China has the biggest wind power installation in the world with 145 GW, behind USA and Germany with 75 GW and 45 GW installed, respectively. India posses 25 GW of wind capacity, followed by Spain with 23 GW and UK with 13 GW of wind power capacity [11].

Statistics data from the European Wind Energy Association (EWEA) [12], [13], shows that from year 2000 to 2015, the installed wind power capacity in Europe has increased from 12.9 GW to 141.6 GW, with a sustainable growth of approximately 10 GW per year [12].

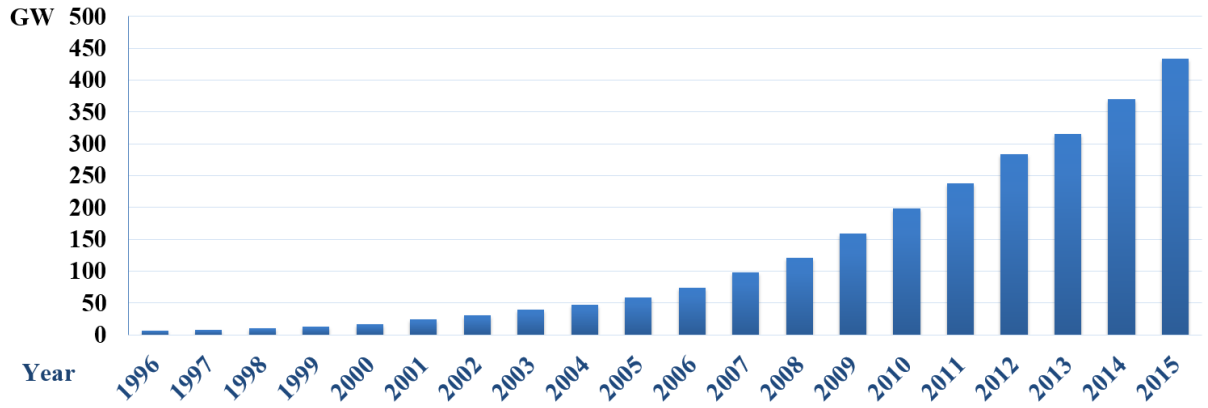

Fig. 2.1 Cumulative world installed wind capacity (values in GW per year) [12].

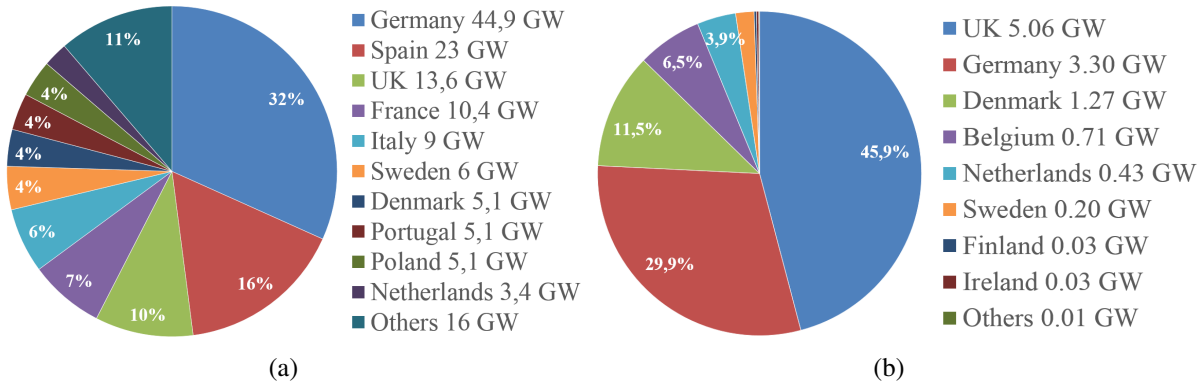

(a) (b)

Fig. 2.2 Share of the (a) total [12], and (b) off-shore [13] installed wind power capacity in EU in 2013.

In Fig. 2.2(a) is shown the total shared capacity among the European countries. Observe that nearly 50% of the total installed capacity is placed in Germany and Spain. Moreover, UK posses 10% of the total share. The remaining 42% is shared among the rest of the EU countries.

In particular for off-shore wind energy, with reference to Fig. 2.2(b), there is a total off-shore installed capacity of 11 GW in EU by the end of 2015. The largest capacity is placed in UK with 46%, followed by Germany with 30%, Denmark with 12% of the share, Belgium with 6% and The Netherlands with 5%.

Finally, a total power of 63.5 GW were installed worldwide during 2015. China, which represents the largest overall wind power market in the world, installed 30.8 GW. USA installed 8.6 GW, followed by Germany with 6 GW, corresponding to 47% of the total new installation in Europe. Brazil and India installed 2.7 GW and 2.6 GW, respectively, of wind capacity during 2015.

2.2 Wind turbine systems

The increasing use of wind energy pushes the development of wind turbine systems in size and technology [1]. Wind turbines are mainly classified in fixed-speed and variable-speed operation. In the following, a brief description of wind turbine topologies is presented.

2.2.1 Fixed-speed wind turbine

A typical diagram of a fixed-speed wind turbine is given in Fig. 2.3. The induction generator (IG) is connected to the grid by a coupling transformer. The rotor of the IG can be either squirrel-cage or wounded type. Depending on the number of poles in the stator, the rotor shaft can rotate at a nominal speed of 1000 rpm or 1500 rpm. For this reason, the wind turbine blades and hub are connected to the generator shaft by a step-up gearbox [14].

The fixed-speed wind turbine is a simple system in which the mechanical power is transformed into electrical power by means of a grid-connected IG. The applied stator voltage can be regulated by a series soft-starter, depicted in Fig. 2.3, when starting-up the IG. This is done by controlling

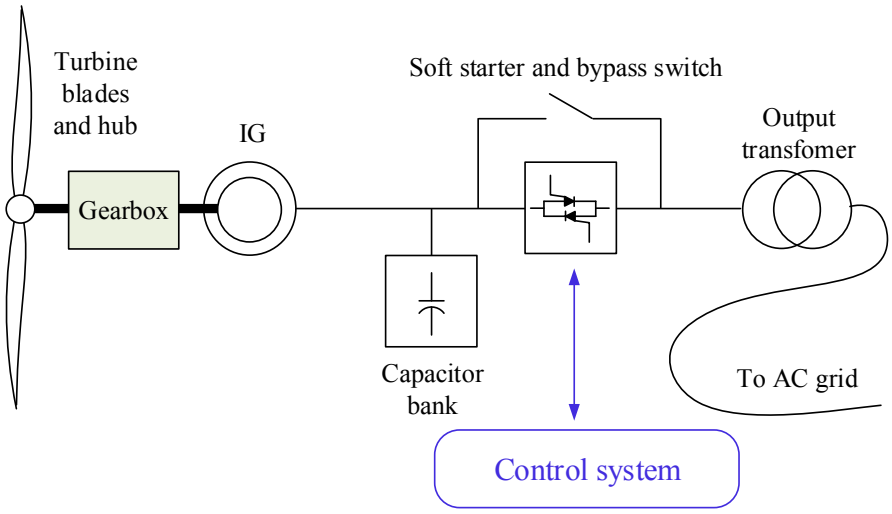

Fig. 2.3 Schematic representation of a fixed-speed wind turbine given in [15].

a set of thyristors, and thereby limiting the inrush current. During normal operation of the wind turbine, the soft-starter is bypassed [14].

Given the inductive nature of electrical machines, the IG consumes a significant amount reactive power during normal operation. This is not only related to the magnetization of the iron core, but also with the machine's speed and thus with the active power output. For this reason, a capacitor bank can be use to provide reactive power compensation, improving the power factor when interconnecting the wind turbine with the grid [16].

The direct coupling of the IG with the grid presents a number of disadvantages, especially during grid disturbances. For instance, when a sever grid fault occurs resulting in a low retained voltage at the terminals of the wind turbine, large inrush current can be experienced due to the sudden demagnetization of the core. This event can activate the protection system, disconnecting the wind turbine from the grid. For this reason, Grid Code fulfilment is a challenge for this kind of generating units; especially when disconnection of the wind farm, depending of the magnitude and duration of the voltage dip, might not be allowed by the TSO [2], [17], [18]. Finally, the narrow speed window where wind energy extraction is optimal is strictly related on the reduced slip range of the IG. Thus, mechanical stress across the turbine structure can be experienced when coping with wind speed fluctuations. For these reasons, the fixed-speed wind turbine is less efficient in producing electrical power, as compared with variable-speed wind turbines [14].

2.2.2 Doubly-fed induction generator wind turbine

A typical scheme representation of the Doubly-Fed Induction Generator (DFIG) wind turbine is given in Fig. 2.4. The stator of the IG can be, for example, a four-pole system [16], where the terminals of the stator are connected with the grid through a three-winding transformer. The rotor windings are accessible via slip rings and brushes, where a partially-rated back-to-back VSC is connected, enabling a circuit between the rotor and the grid. The grid-side VSC is connected to the low voltage (LV) side of the coupling transformer. The medium voltage (MV) side of the

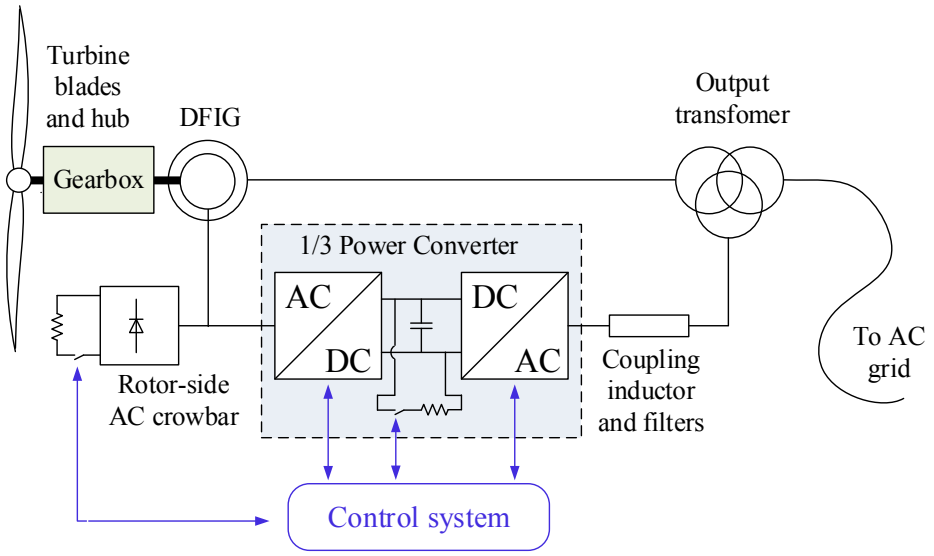

Fig. 2.4 Schematic representation of a DFIG wind turbine given in [15].

transformer can be either connected to the grid, or to a dedicated AC collector bus.

The use of the bi-directional VSC enables the absorption or injection of rotor currents. The VSC is typically rated 20% to 30% of the wind turbine power [19], meaning that one third of the power can circulate through the rotor circuit. This feature opens up the operational speed range of the wind turbine, as compared with the fixed-speed wind turbine described in the previous section. With the introduction of variable-speed operation of the IG, the turbine can extract energy from the wind more efficiently for a wider range of wind speeds. In addition, it allows for a more precise control of the torque across the drive train, avoiding high mechanical stress [14].

Depending of the operation mode of the DFIG wind turbine, i.e.: sub-synchronous mode or super-synchronous mode, the power flow throughout the back-to-back VSC can be either toward the rotor or toward the grid [19]. Moreover, the speed of the turbine is controlled by the rotor-side converter by means of controlling the active current that flows in the rotor windings. The rotor-side converter also provides the reactive power needed for magnetizing the DFIG. Similarly, the reactive power output of the wind turbine is controlled by the reactive current that is exchanged in the rotor windings.

The control structure of the rotor-side converter is usually constituted by a speed or torque controller and a reactive power controller in cascade with an inner current control [20]. The valves of the VSC can be operated either by using Pulse Width Modulation (PWM) or by hysteresis control [19]. Similarly, the grid-side converter controls the DC-link voltage by exchanging active power with the grid. The control structure of the grid-side VSC is constituted by a DC voltage control in cascade with a current control [20]. The valves of the converter are usually operated with PWM [19].

When a grid fault occurs resulting in a low voltage at the terminals of the wind turbine, the grid-side converter cannot inject the produced power into the grid without exceeding nominal current. Observe that power electronic devices are very sensitive to damage when an over-current is experienced [19]. In this scenario, the excess of energy produced by the turbine that cannot be

delivered is accumulated in the DC-link capacitor. When the instantaneous voltage exceeds a certain threshold, an over-voltage protection activates the DC crowbar, redirecting the generated power into a resistor. Through this protective action, the DC voltage is controlled within a safe margin. In a more severe event in which a DC-crowbar protection is not enough to burn the excess of energy produced, an extra degree of protection can be achieved by the use of a diode-rectifier based AC-crowbar at the terminals of the rotor circuit [19], as shown in Fig. 2.4. Similarly, an over-current protection activates the power electronic switch, when the rotor current exceeds the nominal current of the converter. In this scenario, the rotor windings are short-circuited and the additional rotor energy is dissipated in a resistor placed at the DC side of the diode rectifier [14], [20]. Finally, voltage support capabilities of a DFIG wind turbine can be enhanced by two set of actions: the grid-side VSC can be able to inject small amount of reactive power, if it is dimensioned accordingly; the rotor-side VSC can over-excite the rotor circuit increasing the magnitude of the back electromotive force (back-EMF) of the DFIG, thus, injecting reactive power into the grid through the stator circuit [19]. These protection and control measures enhances the LVRT capability of the DFIG wind turbine, allowing it to comply with actual Grid Codes (described later in Chapter 3).

2.2.3 Full-power converter wind turbine

In an FPC wind turbine, or so called type-IV wind turbine system [21], the generator is connected to the grid through a full-power rated back-to-back VSC, as depicted in Fig. 2.5. This configuration allows for an improved fault-tolerant capability of the wind turbine as compared with the DFIG, avoiding severe transients in the generator when a grid fault occurs. Moreover, the grid-side converter of an FPC wind turbine can be designed and controlled in order to provide additional reactive power support, without having the need of over-magnetizing the generator core. However, the use of a fully-rated power electronic interface increases the cost and the system losses as compared a DFIG wind turbine [16] [22].

As depicted in Fig. 2.5, a gearbox is typically used to step-up the rotational speed when coupling the wind turbine hub with the generator shaft. For a direct-drive configuration i.e.: absence of the gearbox in the drive train, a dedicated low-speed multi-pole generator must be used in order

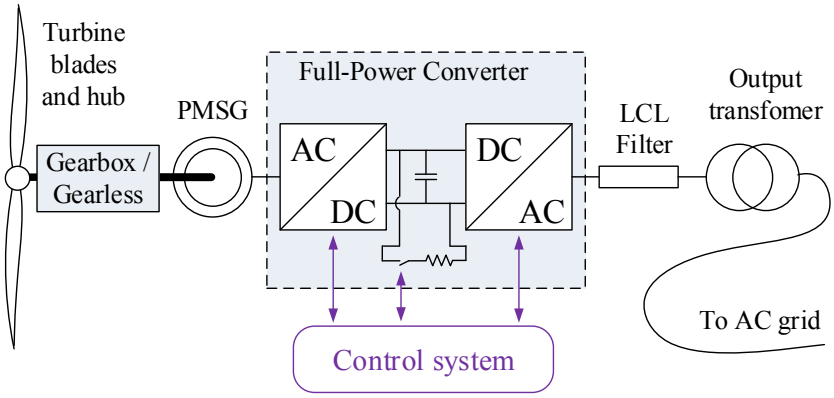

Fig. 2.5 Schematic representation of an FPC wind turbine given in [15].

to achieve the desired nominal frequency in the stator terminals. A filtering stage between the generator and the VSC can be used to reduce high-order transients as well as harmonics in the generator current [16].

During normal operation of the wind turbine, the generator is decoupled from the grid as both VSCs are connected in back-to-back configuration. The generator-side VSC is usually operated in torque control mode or speed control mode allowing the generated power to be injected into the DC-link [16]. The grid-side VSC controls the DC-link voltage by injecting active power into the grid. In addition, if reactive power exchange is allowed by the TSO, the grid-side converter can be operated either in voltage control mode or reactive power control mode. Finally, the wind turbine is grid-interfaced by using a step-up coupling transformer, which increases the voltage from generator-level to distribution-level.

The use of fully-rated back-to-back VSC for grid interconnection of wind turbine generators allows for a fast response during abnormal condition of the grid [16], [23]. For instance, during a voltage dip, the generated power cannot be delivered into the grid due to the absence of sufficient grid voltage. In this scenario, the grid-side-converter can quickly control the current output, avoiding feeding fault currents of large magnitude into the grid. The DC-link capacitor is protected by a DC-crowbar, which allows for the redirection of the produced power into a resistor providing a fast protection during DC overvoltages. If the voltage dip has a relatively longer duration, the wind turbine system can vary the pitch angle extracting less power from the incoming wind [24]. Further explanation of operation and control of the FPC wind turbine is given in Chapter 4.

2.3 Wind power plants

A wind power plant (also called wind park or wind farm) is an arrangement of several individual wind turbines connected to the AC grid through a collector bus. The interconnected generating units are controlled by a main wind farm controller that sets the reference for the active and reactive power set-point of the whole generating plant. The wind park can be placed either on-shore or off-shore. The point of common coupling (PCC) is defined by the TSO as the first mesh connection point of the wind power plant with the electricity grid [25].

On-shore wind farms are grid-interfaced by using a common collector system in which all the terminals of the wind turbines are interconnected. As depicted in Fig. 2.6(a), the collector bus is interfaced with the grid by using a high-power step-up transformer. The HV-side of the transformer is connected, for example, to the transmission system. Finally, the grid connection point of the wind plant is where the PCC is denoted.

Off-shore wind farms can be interconnected via AC submarine transmission lines, or by High Voltage Direct Current (HVDC) interconnection systems, enabling bulk energy transfer across long distances, as depicted in Fig. 2.6(b). In this case, the wind turbines are connected to an AC collector bus in MV level. Similarly, a high-power step-up transformer is used to interface the collector bus with the HVDC-VSC terminals. The grid-side VSC of the HVDC is interfaced with the AC transmission system by means of a high-power coupling transformer. The PCC is

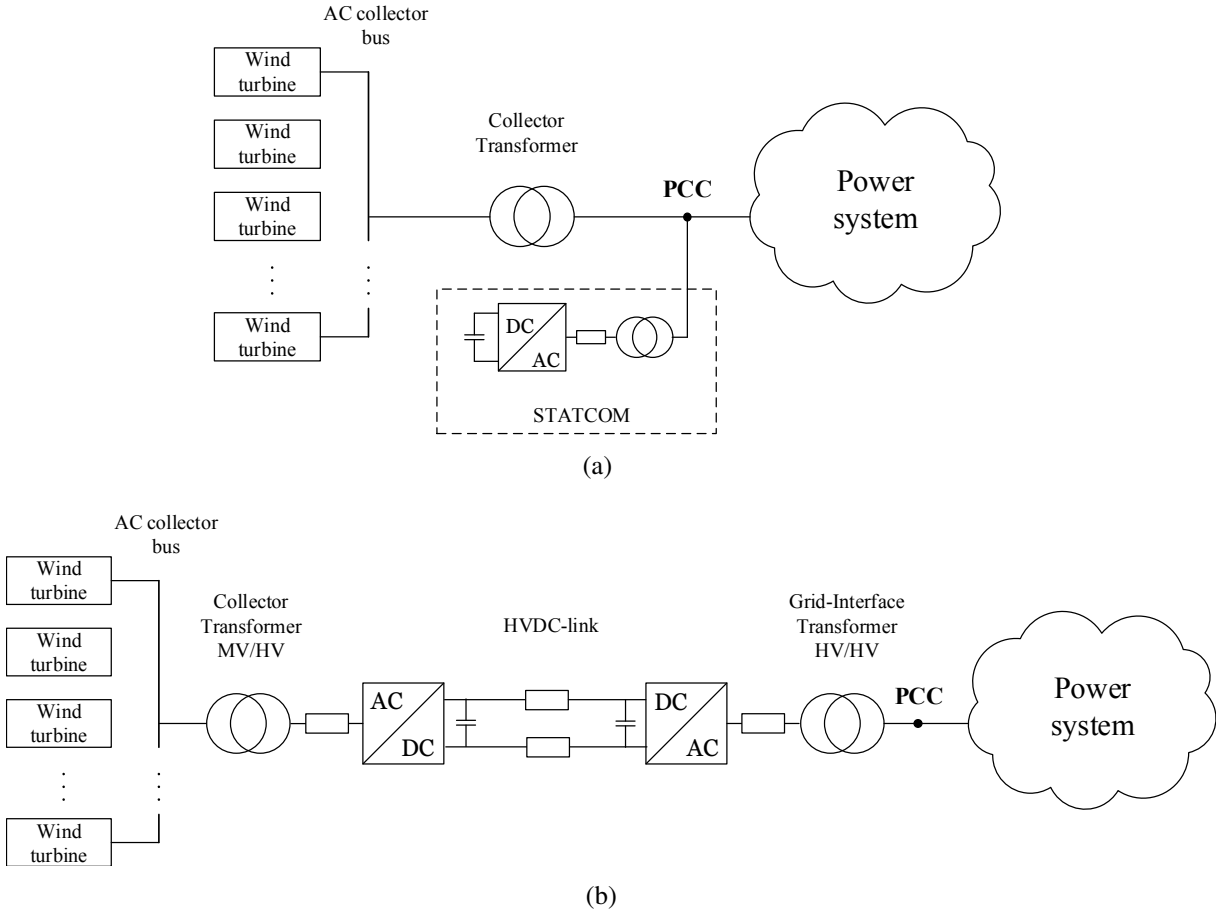

Fig. 2.6 Connection diagram for an on-shore (a) and off-shore (b) wind farm.

defined in its secondary side. Finally, in AC interconnected wind farms, a Static Compensator (STATCOM) can be used to inject or absorb reactive power in order to comply with power factor and voltage support requirements at the connection point with the grid. An example of the connection layout of a STATCOM together with a wind farm is included in Fig. 2.6(a).

2.4 Conclusions

In this chapter, the world wind energy scenario has been briefly discussed, with special focus on onshore and offshore wind power installations. In addition, three main topologies of wind turbine systems have been described. Finally, the schematic for interconnection with the electricity grid of on-shore and off-shore wind power plants has been introduced. In the following, an analysis of the technical requirements included in the selected Grid Codes is given.

Chapter 3

Grid Codes and testing of wind energy systems

3.1 Introduction

In the Grid Codes it is specified how a generating plant should behave under both continuous and dynamic condition of the grid while maintaining a safe and reliable operation. Moreover, requirements for voltage, power and frequency operation range are given in a detailed manner. In addition, typical system disturbances are specified, on which the generating plant should withstand without disconnecting from the grid. In extreme cases, disconnection is also possible when it is allowed by the TSO.

When Grid Code applies specifically to wind farms, the wind turbine manufacturer has to ensure a safe operation of the generating unit by fulfilling the technical requirements for the interconnection of the plant. The requirements that cannot be tested experimentally are verified through software-aided simulation platforms. In the following, an analysis of grid interconnection requirements included in the selected Grid Code is given and Grid Code testing devices are introduced.

3.2 Grid code selection

The Grid Codes considered in this thesis refer to countries that have high penetration of wind power into their national grid [12]. Consequently, these countries have developed detailed technical requirements for grid interconnection of wind power plants [17].

With focus on voltage and frequency operation band, voltage and reactive power dependencies, active power curtailment and LVRT requirements, the selected Grid Codes are: the German (E.ON) [26], [27]; British (National Grid) [28]; Spanish (REE) [29]; Irish (EirGrid) [30]; Danish (Energinet.dk) [31], Swedish (SvK) [32]; Nordic Countries (former Nordel) [33]; and European Network of Transmission System Operators for Electricity (ENTSO-E) [34].

A comparison of the different requirements given in the Grid Codes regarding the interconnection of wind parks is given in [2], [17], [18] and [35]. A dedicated analysis of the German Grid Code is given in [36]. Finally, control strategies developed for meeting Grid Code technical requirements have been documented in [20], [37] and [38].

In this chapter, the main focus of the Grid Code analysis is on the requirements during fault condition of the grid i.e.: comparison of different LVRT and requirements for grid support during a voltage dip. In the following, requirements for normal and abnormal operation of the grid will be briefly described; thus, requirements for fault condition of the grid will be presented.

3.3 Requirements during steady-state operation of the grid

The requirements for steady-state operation of the grid can be mainly categorized in three groups: reactive power requirements for normal voltage operation range; reactive power requirements during nominal active power production; and minimum operation time and active power curtailment during long-term frequency deviations. In the following, these three requirements are briefly explained.

3.3.1 Voltage and reactive power dependencies

A TSO can require reactive power injection from the wind farms to support overall system voltage control during normal operation of the grid. Usually, reactive power requirements are delimited inside a minimum power factor range that goes from 0.95 lagging to 0.925 leading and for an active power set-point between 0.05 pu and 1 pu; and within a nominal voltage that varies between 0.9 pu and 1.15 pu.

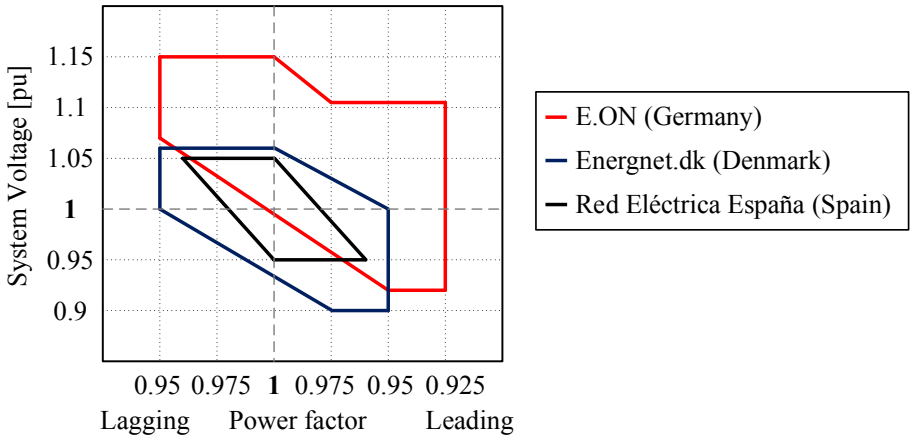

Fig. 3.1 Example of normalized voltage/reactive power dependencies among the selected Grid Codes.

3.3.2 Active and reactive power dependencies

Reactive power requirement are also dependent of the active power production of the wind farm. For instance, the Danish Grid Code states dependencies between voltage and reactive power, and between active and reactive power production [17]. Both requirements shall be complied simultaneously during normal operation of the wind farm. Moreover, reactive power injection can be controlled by either using a voltage control or power factor control [2]. An extra option to define the reactive power production is to manually set the operating point if, for example, a continuous voltage deviation at the connection point is present.

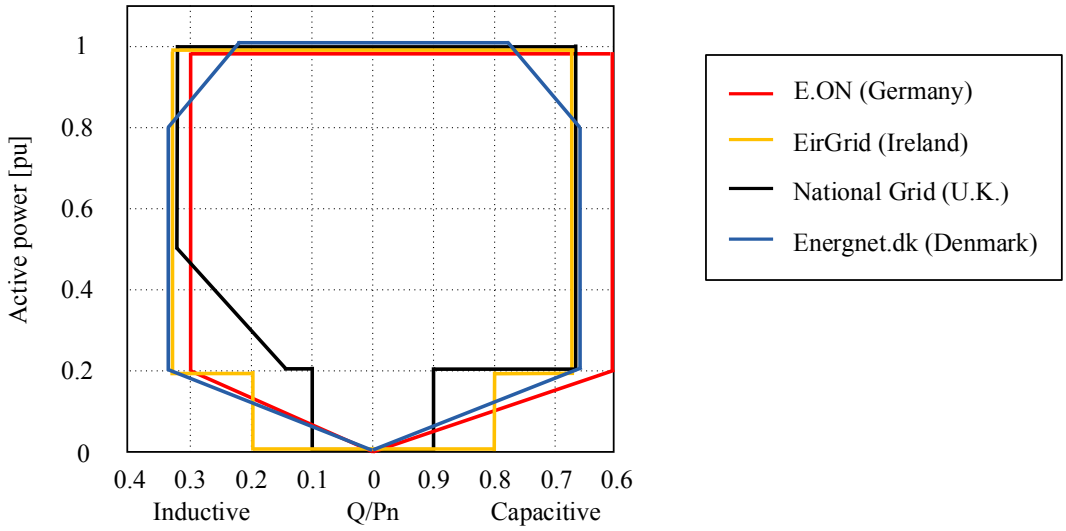

Fig. 3.2 Example of the requirements for active/reactive power operation range given in the selected Grid Codes.

3.3.3 Voltage and frequency dependencies

In Grid Codes, it is specified the steady-state frequency and voltage operation range in which the wind turbine should operate continuously. Normal condition is considered for voltages close to 1.0 pu and frequency around 50/60 Hz, with a deviation of approximately ± 0.1 pu from the rated voltage and ± 0.5 Hz from the rated frequency. Any steady-state grid condition outside these values is defined by a minimum operational time, as shown in Fig. 3.3, and in some cases, by a control action on the active power set-point of the wind farm (explained in the following point), as enforced by e.g.: the Danish [31], Irish [30] and German [26], [27] TSOs.

Minimum operational time during deviations

The strictest requirement among the selected Grid Codes in terms of operation during frequency deviation is imposed by the German TSO E.ON for offshore wind parks, which stipulates that the generating unit should stay connected during minimum 10 seconds when the grid frequency is in the range of 46.5 Hz to 47.5 Hz and 51.5 Hz to 53 Hz. During frequencies away from

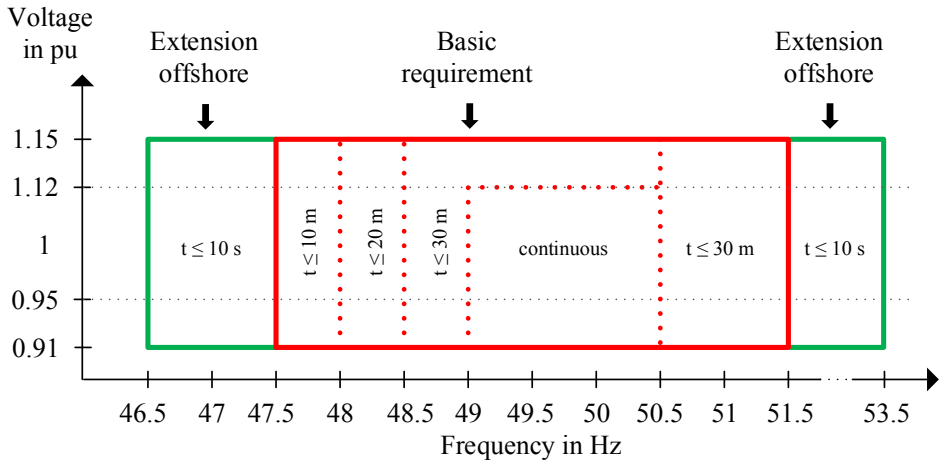

Fig. 3.3 Voltage-frequency requirements enforced by the German Grid Code [27].

nominal frequency, the German Grid Code defines intervals from 10 second to 30 minutes of operation [26], [27]. Another example is the Danish Grid Code [31] that rigorously imposes continuous operation for voltages from 0.9 pu to 1.1 pu, within a frequency range of 47 Hz to 52 Hz where the operational time is defined in seconds for large frequency deviations and in minutes for non extreme cases. The normal operation range is between 49.5 Hz to 50.2 Hz.

Without considering a wide voltage range, another strict requirement is given by the British Grid Code [28], which states that wind park should remain in operation when the grid frequency is in the range of 47.5 Hz to 52 Hz. In this case, the voltage range is from 0.95 pu to 1.05 pu for the 400 kV system.

Other frequency requirement such as the one given in the ENSTO-E Grid Code [34] defines

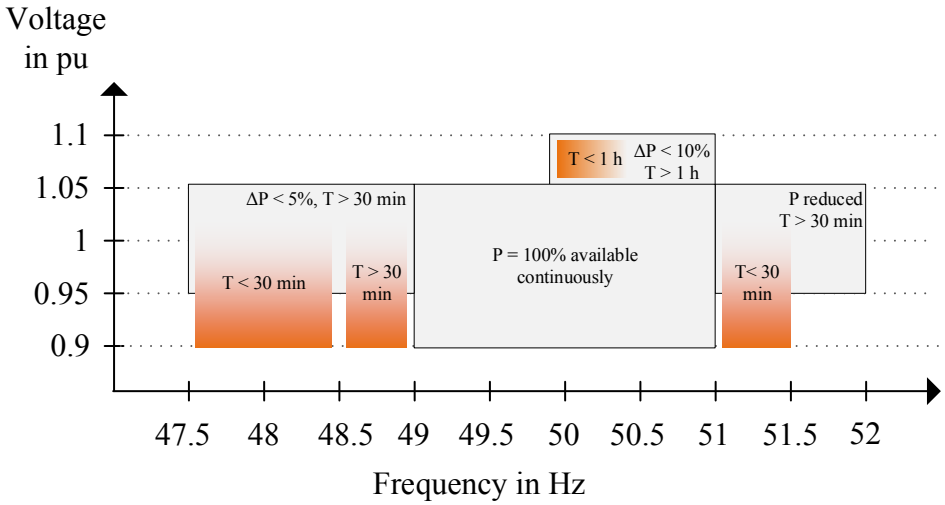

Fig. 3.4 Voltage-frequency requirements enforced by the Swedish Grid Code (grey) over-imposed by the requirements given ENSTO-E Grid Code (orange).

five different ranges with regard to frequency, voltage and minimum time of operation. For example, a voltage/frequency range from 49 Hz to 51 Hz and from 0.9 pu to 1.05 pu is defined as steady-state operation of the grid. The cut-off under-frequency is 47.5 Hz and 51.5 Hz in the over-frequency rage. In between these two frequencies, minimum and maximum voltages, power production levels and ramp/rates of power variations are strictly defined. In Fig. 3.4 it is possible to observe how a local grid code such as the Swedish Grid Code can be modified by the ENSTO-E Grid Code, which entered into force during the recent years.

Active power curtailment during frequency deviation

Frequency deviations can occur when the overall active power production does not match with the overall power system load. An increase of the system frequency is produce by a surplus of the instantaneous active power production compared to the demand of active power of the grid. On the other hand, if a generation plant is disconnected, the frequency drops due to the surplus of the demanded active power.

When active power curtailment is demanded by the TSO in case of frequency deviations, the generation unit must vary its active power output in order to contribute to the overall regulation of the system frequency. In this case, a droop control strategy must be used when the frequency starts to deviate away from a specified dead-band, according to the characteristics given in the specific Grid Code. The active power variation is described as follows: active power must be increased if the system frequency drops from the dead-band, and active power must be reduced if the frequency increases above the dead-band. In a severe case scenario where the system frequency is outside the frequency operation band, the generating plant is allowed to disconnect.

An analysis on the requirements for active power curtailment is given in [17]. A well-documented

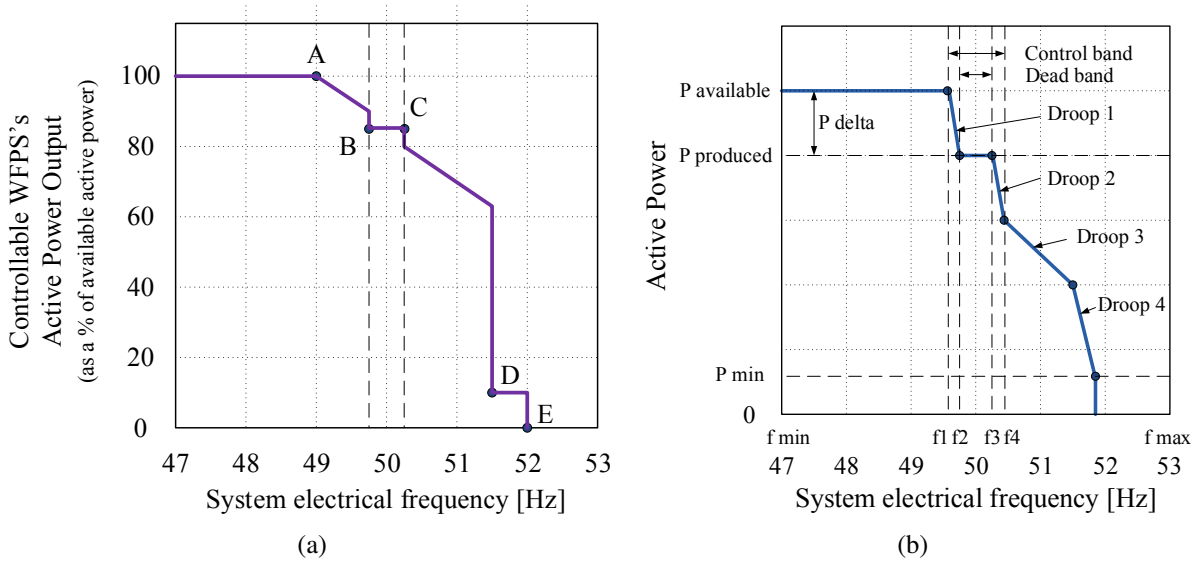

Fig. 3.5 Requirements for active power curtailment given in the (a) Irish Grid Code, and (b) Danish Grid Code.

strategy for frequency control is given in the Irish Grid Code [30], in the Danish Grid Code [31] as well as the German Grid Code [26], [27].

A well-documented strategy for frequency control is given in the Irish Grid Code [30], as shown in Fig. 3.5(a). A normal frequency range is defined between the point “B” and “C”, where any frequency variation within this range does not require compensation. If the frequency drops from the defined dead band, the wind farm should respond according to the segment “AB”. Similarly, if the frequency rises above the dead-band, active power production should varied according to segment “CD”. Segment “DE” refers to maintain a low power set-point during the defined over-frequency range. Interruption of active power production is required when frequency raises the unique frequency where the segment “DE” is defined.

A similar control strategy for frequency response is given by the Danish authority [31], as depicted in Fig. 3.5(b). Values for “f min” and “f max” are settled according to the frequency operation range of the wind farm. The frequencies “f2” and “f3” define the dead-band, where the active power production remains unchanged when frequency variation occurs. Moreover, the control band is defined between the frequencies “f1” and “f4”, where a dedicated frequency control operates by varying the active power production of the plant. Similarly to the Iris Grid Code, “Droop 1” and “Droop 2” have similar purposes of segments “AB” and “CD”, respectively. Finally, “Droop 3” and “Droop 4” define a curve in which the wind farm has to provide critical power-frequency control when needed.

3.4 Requirements during dynamic condition of the grid

In this section, the interconnection requirements during dynamic condition of the grid are introduced. Here, the main focus is on the analysis of the requirements for LVRT and for voltage support in case of a severe voltage dips.

3.4.1 Low voltage ride through (LVRT) requirements

In every Grid Code it is specified a voltage dip profile that the wind turbine should ride through without tripping. An exhaustive comparison of LVRT profiles is given in [2]. Low voltage ride through profiles characterization in terms of fault time, retained voltage and recovery ramp rates can be found in [18]. In Fig. 3.6 is shown a combination of the strictest LVRT profiles among the selected Grid Codes. In particular, the European Grid Code ENTSO-E [34] defines the guidelines to establish the LVRT profiles in each network inside EU.

When it is specified in the Grid Code, wind parks are required to support voltage restoration by injecting reactive power into the grid. In particular, the generating plant must provide voltage support by injecting a specific amount of reactive current during a voltage dip. For example, the Danish Grid Code [31] enforces a specific LVRT with retained voltage of 0.2 pu per 500 ms, as shown in Fig. 3.6, and demands for reactive power support during voltage restoration. Reactive current must be injected when voltage deviates below 0.9 pu. When the system voltage is lower than 0.5 pu, nominal reactive current injection must be reached. Active power production must

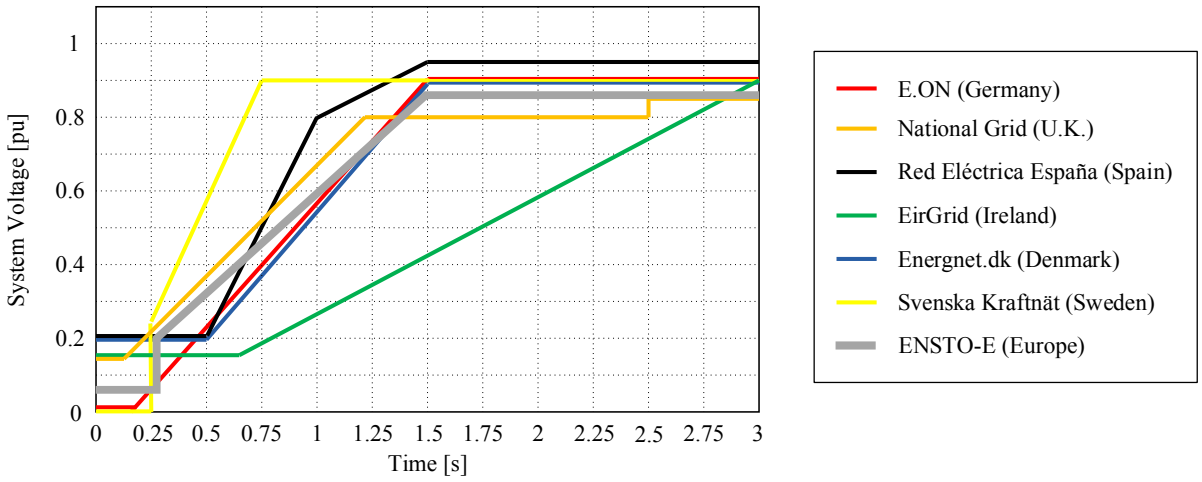

Fig. 3.6 Example of LVRT profiles from the selected Grid Codes.

be restored within 5 seconds after full recovery of the voltage within normal operation range.

A graphical representation of the reactive power requirement given in the Danish grid code during a LVRT event is shown in Fig. 3.7. According to the German Grid Code [26], an automatic voltage control must be activated within 20 ms if the grid voltage deviates more than 0.1 pu, and it must inject at least a reactive current of 0.02 pu for each percent of voltage deviation, as depicted in Fig. 3.8. For offshore wind farms [27], the voltage control must be activated at the PCC when grid voltage deviates 0.05 pu from its nominal value. Full reactive power output must be achieved when the voltage drops more than 0.5 pu, similarly to the Danish Grid Code. After fault clearance, the automatic voltage control must still be active for another 500 ms after the returning of the voltage within the normal operation band, in order to compensate for any voltage

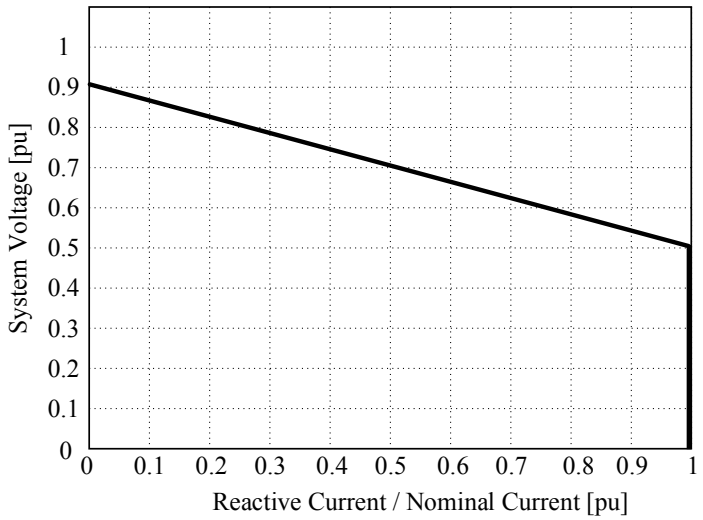

Fig. 3.7 Reactive power requirements during LVRT event enforced by the Danish Grid Code [31].

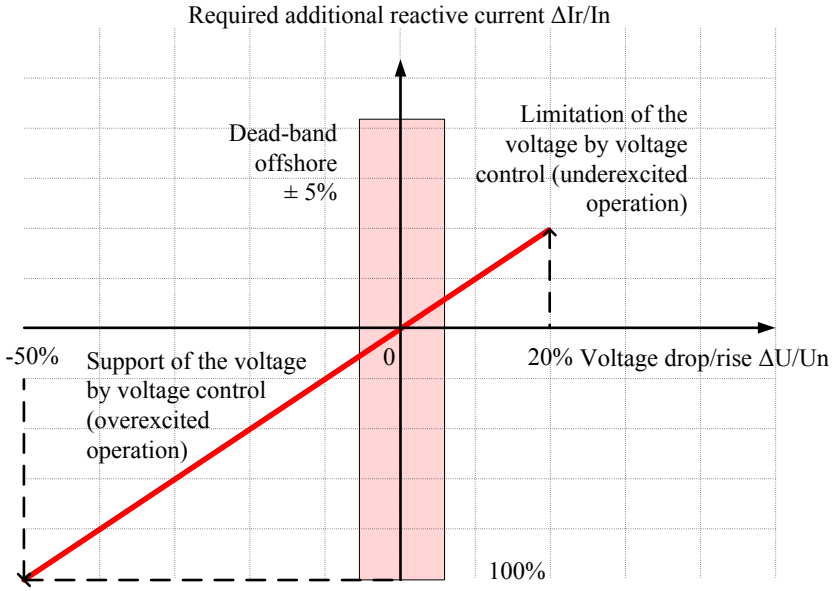

Fig. 3.8 Reactive power requirements during LVRT event enforced by the German Grid Code for offshore wind parks [27].

variation due to the action of an automatic reclosure on an uncleared fault. Finally, the active power production must reach its pre-fault set-point with a gradient of at least 0.2 pu per second after the returning of the voltage within the normal operation range.

A strict LVRT profile is defined in the Irish Grid Code [30], which enforces a minimum retained voltage of 0.15 pu for 650 ms, followed by a voltage recovery ramp for 3 seconds. During the voltage dip, the wind farm shall provide active power in proportion to the retained voltage while maximizing reactive current injection into the grid, for at least 600 ms or until the voltage recovers to its normal operation range. In addition, the wind farm must be able to reach 90% of its available active power production within one second after total voltage recovery. The Irish Grid Code enforces reactive current injection of 0.04 pu, per each percentage of voltage drop when the voltage is lower than 0.9 pu. Maximum reactive power should be injected when the voltage drops below 0.75 pu.

The Swedish Grid Code [32] defines a retained voltage value of 0 pu for 250 ms, followed by voltage step to 0.2 pu and a ramp towards 0.9 pu that lasts 500 ms. The reactive power exchanged between the generating unit and the power system is strictly defined in 0 pu for the whole event.

3.5 Harmonization and future trend in Grid Code requirement

The Grid Code analyses given in [17], [18] and [35] highlight that the interconnection requirements differ substantially between TSOs. These differences are somewhat acceptable due to the fact that each requirement is strictly related to the particular technical and operational characteristic of each power system. For instance, it is acceptable that LVRT recovery ramps of weakly interconnected system such as the Irish or Danish grid are slower than a strongly

interconnected system like the Spanish grid, as illustrated in Fig. 3.6. In this regard, exact levels for what is considered normal or abnormal condition of the grid, such as range limits, dead-bands, set-points, etc., cannot be fully standardized, since they depend on the specific characteristics of each power system e.g.: faster frequency response will be necessary for systems with a low inertia [2].

These natural differences between Grid Codes impose great challenges on wind turbine manufacturers, which are constantly adapting and developing their products according to the latest requirements imposed by the different TSOs [2]. Although this exercise contributes in bringing forward the state of the art of wind turbines technology, a vast diversification of Grid Code requirements creates, at the same time, a narrow market-based development trend among different countries. For this reason, in the last decade TSO associations and power generating facility owners (including wind turbine manufacturers) have joint efforts in order to find standardization in technical and operational requirements [35].

The ENTSO-E Grid Code has been developed in close cooperation of power generating facility owners and manufacturers with their relevant TSO. The code defines a common framework of grid connection requirements for generating plants including synchronous power generating modules, solar and wind power plants, both onshore and offshore installations, with the European electricity grid. In April 14th 2016, the European Grid Code has entered into force laying down the requirements for grid connection of power-generating facilities, e.g.: synchronous power-generating modules, power park modules and offshore power park modules [34]. Similarly, the TSOs in Denmark, Finland, Norway and Sweden have joint efforts in developing a Nordic Grid Code [33] (as members of the Regional Group Nordic defined by ENTSO-E [34]) in which requirements for LVRT and voltage/frequency dependencies are specified, among others.

The European Wind Energy Association (EWEA), or recently called Wind Europe [39], has also urged European TSOs to achieve consistency in their future Grid Codes, in order to guarantee harmonized regulations throughout the global market. This action will allow wind turbine manufacturers to move from market-oriented products to a more generic solution, in order to adapt their hardware and software design with a globally optimized criteria [18], [40]. Alongside, European Stakeholder Committees constituted by consumer organisations, generators, suppliers and many other actors from across the European electricity sector have been pushing for better joint collaboration with their relevant TSO when adopting the European Network Codes [40].

Finally, the trend in Grid Code development for power electronic interfaced generating units will be focused on its contribution in increasing the overall reliability of the power system. As discussed in [18] and [35], future wind farms will be required to provide e.g.: reactive power support during faults, or to emulate the inertia response of synchronous generators, to name a few.

3.6 Grid code testing of wind turbines system

The IEC 61400-21 standard issued by the International Electrotechnical Commission (IEC) defines the methodology to test part of the requirement stated in Grid Codes for interconnection

of wind turbines [25]. In addition, as described in [41], different testing methods exist today to verify the LVRT ability of renewable energy sources. For example, these type of devices include the use of autotransformer with controllable tap changer, controllable shunt reactances to rapidly vary the voltage at the connection point, synchronous generator with a controllable excitation circuit, or series-connected VSC [6], [42].

Moreover, in order to fulfil the standard criteria, specialized testing equipment has been developed. In the following, an introduction of existing solutions for Grid Code testing of wind turbines is given. The most common testing device for LVRT test of wind turbines is the impedance-based voltage dip generator [23], [38], [43] , which will be briefly described in the following section.

3.6.1 Impedance-based testing equipment

A widely used testing equipment for LVRT test of wind turbines is shown in Fig. 3.9. The impedances that constitute the testing device are arranged in order to form a voltage divider at the terminals of the tested object, when the circuit breaker CB is series with Z_{shunt} is closed during the test. By a proper selection of the impedances Z_{grid} and Z_{shunt}, the amplitude and phase angle of the applied voltage can be controlled as desired.

The simple and robust design of this testing device is a great advantage, specially when handling high short-circuit current from the tested object. Moreover, the testing device is modular and can be placed inside a container. It is easy to transport and can be use to perform on-site test of installed wind turbines. A more detailed description of the impedance-based LVRT testing device including field test results of a 2 MW wind turbine is given in [43].

One of the main drawbacks of this testing device is the fact that it is only able to apply voltage steps variations due to the closing-opening action of the circuit breaker, when connecting the shunt impedance at the terminals of the wind turbine. Therefore, is unable to perform the voltage recovery ramp that exist in the majority of the Grid Codes. In addition, when performing the test, the device is highly dependent of the short-circuit power at the grid connection point, which will also impact the resulting wind turbine voltage [43].

Moreover, the use of circuit breakers introduces uncontrollable delays when emulating the

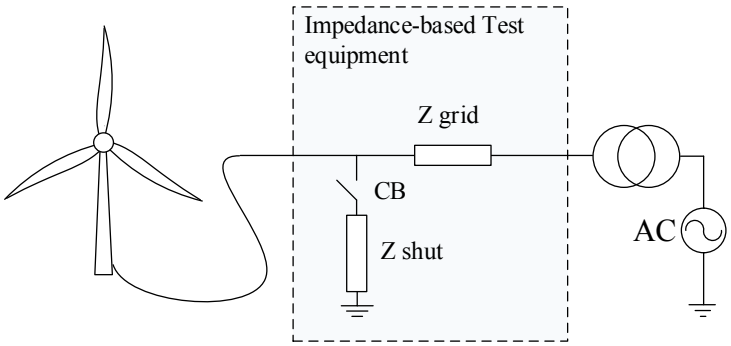

Fig. 3.9 Single-line diagram of the standard LVRT test equipment.

fault and can give rise to high harmonic content into the voltage profile applied to the test object [41], [44]. For these reasons, variant of this device, mainly including the use of power electronic switched shunt impedance, has been proposed in [45]. In this prototype, as a difference of the scheme given in Fig. 3.9, the impedance Z_{shunt} is variable and it is placed in series with a shunt transformer. In addition, the circuit breaker is substituted by a bi-directional power electronic switch. Observe, however, that the use of an extra transformer can lead to undesired inrush current, producing unnecessary stress over the tested system.

3.6.2 Other kind of voltage dip generator

Different kind of voltage sag generators have been proposed in addition to the impedance-based test equipment described in the previous section [41], [44]. Some of these testing devices include the use of transformer with selective voltage output, as shown in Fig. 3.10. In this setup, the primary of the transformer is connected to an AC grid while the generating unit is connected to the secondary side. Observe that the secondary winding is divided into two sets of three-phase transformed voltages. During no-fault operation of the test, the generating unit is connected at rated voltage by closing the switch $CB1$ while $CB2$ remains open. The voltage dip is performed by reconnecting the generating unit to a different transformed voltage for a short period of time. In order to achieve this, $CB1$ is opened and $CB2$ is closed. The recovery of the voltage is performed by bringing both circuit breakers to their previous state.

The benefits of using this kind of dip generator is that is relatively cheap, it uses standard components such as transformer and contactor, in addition to a relatively simple control system. For these reasons, this setup is found to be suitable for laboratory experiment [42].

One of the main drawback of this prototype is that the operation time of the contactors cannot be fully controlled and thus voltage and current transients might occur, damaging, for example, the power electronic converters included in a typical wind turbine system [46]. Similarly to the previous case, a variant of this transformer-based testing device has been proposed in [46], which

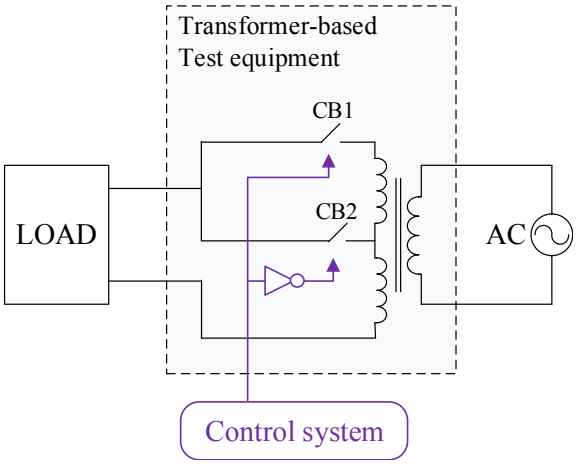

Fig. 3.10 Single-phase diagram of a transformer-based testing device.

includes the use of a power electronic switching stage. This solution is transient-friendly due to the inclusion of fully-controlled Insulated Gate Bipolar Transistors (IGBT). However, the use of only two pre-defined voltage levels at the secondary winding limits the output voltage to be controlled with step variations only. In addition, the testing equipment is coupled directly to the grid, therefore, it is fully dependent on the short-circuit ratio at the point of connection. Given the use of passive components, this testing device is not designed for varying the frequency of the applied voltage, while the use of solely transformers can lead to uncontrolled inrush currents, risking the integrity of the tested system. Finally, for wind power applications, the weigh and scale of a multi-MW transformer can be very bulky, difficulting its transportation when on-site LVRT test is needed.

Finally, in [46] and [47] it is discussed the use of generator-based voltage dip testing device. In order to generate an output voltage of the machine, a diesel motor is mechanically coupled in the rotor shaft. The voltage dip is then performed by varying the excitation field in the rotor circuit. In this setup, the applied frequency can be fully controlled. However, its functionality is basically limited to symmetrical voltage dip with a relatively long response time due to the dynamic of the back-EMF in the generator. Moreover, a bulky multi-MW diesel stand-alone generator system can be very expensive and difficult to transport [47]. For these reasons, this kind of voltage dip generator is unsuitable for on-site LVRT test of wind turbines.

3.6.3 VSC-based testing device

Another solution to realize a voltage dip generator is to use fully-rated VSC in back-to-back configuration. By controlling the turbine-side output of the converter system, the effect of all kind of grid faults can be emulated [42]. Thanks to the full controllability of the applied voltage in terms of magnitude, phase and frequency, the use of VSC-based testing equipment, shown in Fig. 3.11, provides more flexibility as compared with the standard impedance-based test equipment [17], [43], and also brings more advantages in terms of size and weight [41], [47]. In addition, the AC grid is decoupled from the tested object when performing the test; meaning that the strength of the grid is not a major limitation, if a proper control strategy of the grid-side VSC of the test equipment is implemented.

Moreover, the LVRT profile given in the majority of the Grid Codes can be fully tested including the recovery ramp [17]. Similarly, a phase-angle jump can be easily performed by manually adding a phase shift in the applied voltage. In addition, the full controllability of the voltage allows for the emulation of any kind of grid scenario applied to the tested object i.e.: it can emulate either an infinite grid [17], or a grid with a predefined short circuit power, as explored later in this thesis. This particular feature is useful when testing, for example, voltage support capabilities of wind turbines.

Its precise control allows for more possibilities of tests that can be carried out besides what is normally required in the Grid Codes. For example, frequency characterization of wind turbines can be performed by introducing asynchronous frequency content into the applied voltage while observing the equivalence admittance at the PCC. Additionally, frequency support capabilities of the tested object can be evaluated by performing a test where the frequency applied at the PCC

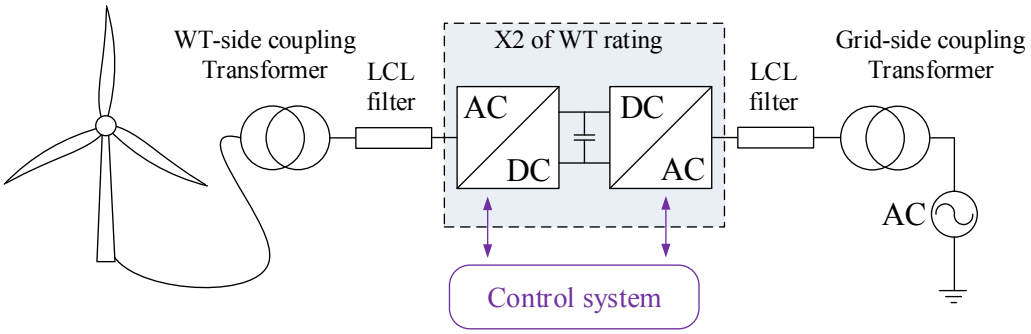

Fig. 3.11 Single line diagram of a VSC-based test equipment.

is varied. In the same way, with a proper emulation of the synchronous generator including its poor mechanical damping, power oscillation damping capabilities of the wind turbine can also be tested.

The main drawback of this technology is the fact that is more expensive than using the standard testing device introduced in the previous section. In addition, the control algorithm needed to implement such arrangement of VSC is more complex and extra attention must be given when dealing with over-currents. Moreover, to emulate a grid fault as realistically as possible, a high dynamic performance of the controller that computes the output voltage of the VSC is necessary [7].

This concept also has been investigated in previous works. For instance, open-loop control for this kind of equipment to test for voltage dip on a wind turbine system has been investigated in [7] and in [8]. In these examples, the VSC-based testing equipment is treated as an infinite bus and no insight on the stability of the system is given. In a different subjects, close-loop control of VSC-HVDC systems with virtual impedance emulation is given in [48] and also discussed in [49]. However, these types of control algorithms have not yet been implemented on testing procedures for wind energy systems. For these reasons, a new approach of wind turbine test by using the VSC-based testing equipment is investigated in this Thesis.

3.7 Conclusion

In this chapter, a comparison of grid requirements regarding interconnection of wind turbine was given. The dependencies between system voltage, grid frequency, and active reactive power production during steady-state operation of the grid were introduced. In addition, requirements for LVRT and voltage support during fault were described in detail. Finally, different Grid Code testing devices have been described including the standard impedance-based testing device and the VSC-based test equipment, which will be further investigated in this thesis.

Chapter 4

Modelling of the FPC-based wind turbine and VSC-based testing device

4.1 Introduction

In this chapter, the derivation of the control algorithms that govern both the testing device and the wind turbine will be described. First, the electrical model of the back-to-back VSC of the testing equipment is shown in detail, with special focus in the control scheme of each VSC. In addition, the mechanical and electrical model of the wind turbine system including the control of both generator-side and grid-side VSC will be described and the implemented LVRT control strategy will be introduced.

4.2 Description of the testing setup

The investigated setup is constituted by a 4 MW FPC wind turbine, similar to the one described in Fig. 2.5, and 8 MW back-to-back VSC system, which resembles the one given in Fig. 3.11. The model presented in this work resembles an actual testing setup located in Gothenburg, Sweden [3].

The wind turbine is rated in 4.5 MVA, 10.5 kV. The stator of the generator, having a voltage rating of 0.69 kV, is directly connected to the back-to-back VSC. Moreover, there is no gearbox in the wind turbine drive-train, meaning that the rotor shaft is directly connected to the hub. The generator-side VSC, here operated in torque control mode, injects the generated power into the wind turbine DC-link capacitor. The grid-side VSC controls the DC-link voltage by exchanging active power with the AC grid. A filtering stage is placed between the VSC and the LV-side of the wind turbine transformer in order to reduce the harmonic content injected into the electricity grid. Finally, the output transformer of the wind turbine steps-up the voltage from 0.69 kV to 10.5 kV.

The test equipment is rated in 8 MVA, 10.5 kV. The wind turbine is coupled to the testing device through a coupling transformer. The secondary of the transformer is rated at 9.35 kV. Similarly, a

filter bank is placed in order to remove the harmonic content produced by the turbine-side VSC. This converter controls the AC voltage imposed to the wind turbine system, while the grid-side converter is controlling the DC-link voltage, in a similar way that the grid-side VSC of the wind turbine does. Finally, the testing equipment is interfaced with the grid means of filter bank and coupling transformer, which grid-side is again 10.5 kV.

4.3 Modelling of the VSC-based testing equipment

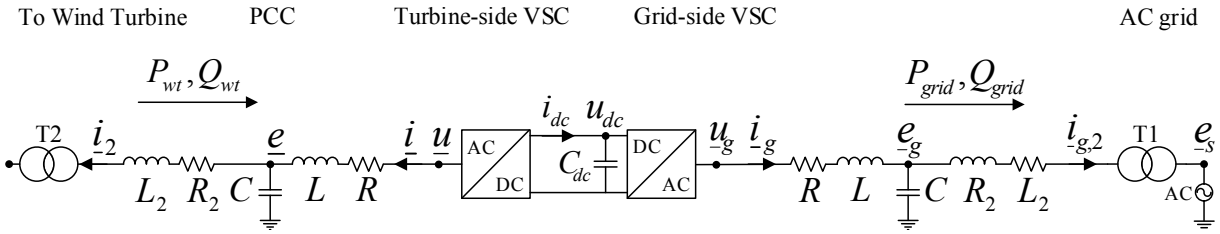

Fig. 4.1 Simplified single-line diagram of the testing equipment.

The circuital scheme of the back-to-back VSC-based testing equipment, including VSC, LCL filter and coupling transformer is given in Fig. 4.1. The secondary side of the grid-coupling transformer $T1$ of the testing equipment is connected to the AC grid, here represented by a infinite bus denoted with the three-phase voltage vector $\underline{e}_{\mathrm{s}}$. The primary three-phase current is denoted $\underline{i}_{\mathrm{g},2}$. An LCL filter is placed between the primary of the transformer and the grid-side VSC of the testing equipment. The voltage at the capacitor bank is here denoted as $\underline{e}_{\mathrm{g}}$, while the current outgoing through the grid-VSC is denoted as $\underline{i}_2$. The inductive and resistive components that constitute the interfacing inductor at the grid-side of the test equipment are here represented by the inductance L in series with its internal resistance R, while on the transformer-side is denoted as L_2, with its internal resistance R_2. Moreover, the filter bank tuned for suppressing the switching harmonics is here represented by its capacitance C. Finally, the grid-side converter a two-level VSC constituted by 6 IGBTs with their corresponding anti-parallel diode. Its terminal three-phase voltage of the converter is labelled as $\underline{u}_{\mathrm{g}}$ and the switching signals are calculated by Pulse Width Modulation (PWM) technique [20].

The DC-link voltage across the capacitor C_{dc} is denoted as u_{dc} and the measured DC current is labelled i_{dc}. No DC filters or DC crowbar have been included in the model of the test equipment.

The turbine-side converter and its interface inductor including the filter bank and coupling transformer are also depicted in Fig. 4.1. The labelling of the electrical variables and components of the turbine-side system resembles the structure given in the previous paragraph. The turbine-side VSC is also a two-level IGBT-based VSC modulated with PWM. The three-phase terminal voltage vector of the turbine-side VSC is denoted as $\underline{u}$ and the three-phase terminal current are labelled as $\underline{i}$. The interface inductor is represented by the series inductive filter L with R its internal resistance. Similarly, a filter bank tuned for suppressing the switching harmonics

has also been modelled and its capacitance is denoted as C. The three-phase PCC voltage vector is measured at the capacitor and it is denoted as $\underline{e}$. The secondary current $\underline{i}_2$ flows through a second inductive filter L_2 of the LCL filter. The turbine-side interface transformer $T2$ steps up the voltage from 9.35 kV to 10.5 kV. Finally, the wind turbine terminals are connected at the primary-side of transformer $T2$, as shown in Fig. 4.1. In the following, the control system of the testing equipment is presented.

4.4 Control of the turbine-side VSC of the testing equipment

The simplified single-line diagram shown in Fig. 4.1 is used to derive the necessary controllers for the wind-turbine side VSC of the testing equipment. Here, the voltage and current dynamic on the capacitor and the interface inductive filter, C and L respectively have been considered for deriving the control law of the VSC. The parameters of the modelled testing equipment are given in Table 4.1.

TABLE 4.1. PARAMETERS OF THE TESTING EQUIPMENT.

Transformer $T1$ and $T2$ power		8 MVA
Transformer $T1$ voltages		9.35 kV / 10.5 kV
Transformer $T2$ voltages		10.5 kV / 9.35 kV
Transformer $T1$ and $T2$ impedances	$X_{\mathrm{T1,T2}}$	8%
Nominal grid angular frequency	ω_{g}, ω_{s}	314 rad/s
Filter inductance	L	0.15 pu
Filter internal resistance	R	0.015 pu
Filter inductance	L_2	0.075 pu
Filter internal resistance	R_2	0.008 pu
Filter capacitor power	C	0.1 pu
DC capacitor time constant	C_{dc}	3 ms
VSC switching frequency	f_{sw}	2000 Hz
Discrete sampling time	T_{s}	0.25 ms
Current control bandwidth	α_{c}	$8\omega_{\mathrm{s}}$
DC voltage control bandwidth	α_{d}	$0.8\omega_{\mathrm{s}}$
AC voltage control bandwidth	α_{e}	$0.8\omega_{\mathrm{s}}$
PLL bandwidth	α_{p}	$0.1\omega_{\mathrm{s}}$

With focus on the turbine-side VSC of the testing equipment, the main control blocks that constitute the implemented discrete controller are shown in Fig. 4.2. The control has been developed in the synchronously rotating dq-frame [50]. In Appendix A is found the adopted amplitude-invariant Clark's Transformation from three-phase to $\alpha\beta$ stationary reference frame, and Park's Transformation from $\alpha\beta$ to dq-rotating reference frame, and vice versa.

In the control algorithm of the turbine-side VSC of the test equipment, a dedicated PCC voltage control is implemented. The role of this controller is to generate the reference current for the inner-current controller of the converter. The structure of the cascaded current controller is shown in Fig. 4.2. The output of the controller is the reference value for the output voltage of the VSC. The calculated voltage is then transformed from the dq-reference frame into three-phase

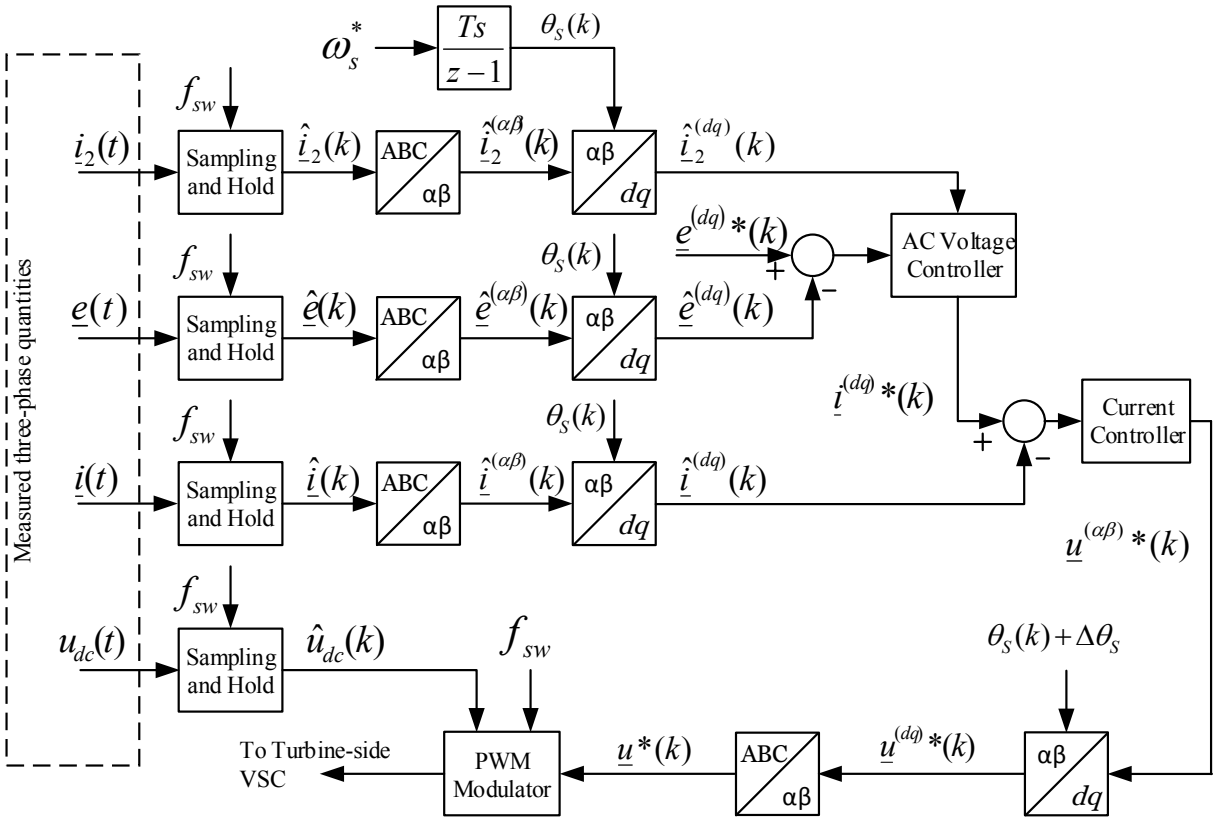

Fig. 4.2 Block diagram of the cascaded vector controller for the turbine-side VSC of the testing equipment.

quantities. Finally, a PWM modulator is used to compute the switching signals of the converter. In the following, the implemented cascaded control strategy will be described in detail.

4.4.1 Inner current controller

Considering the circuit given in Fig. 4.1, the dynamics of the current $\underline{i}$ that flows between the terminals turbine-side VSC and the PCC can be described in the dq-frame as:

$$\frac{d\underline{i}^{(dq)}}{dt}L + j\omega_s L\underline{i}^{(dq)} + R\underline{i}^{(dq)} = \underline{e}^{(dq)} - \underline{u}^{(dq)} \tag{4.1}$$

In order to derive the current control, (4.1) needs to be transformed into Laplace form [19]. Moreover, by rearranging the transformed equation, the open-loop transfer function $G(s)$ is obtained:

$$\frac{\underline{i}^{(dq)}(s)}{\underline{e}^{(dq)}(s) - \underline{u}^{(dq)}(s)} = \frac{1}{R + j\omega_s L + sL} = G(s) \tag{4.2}$$

Derivation of the current controller

The controller has been derived using the Internal Model Control (IMC) method given in [51] and [52]. By assuming perfect knowledge of the system parameters, the effect of the voltage drop across the coupling term $j\omega_{\mathrm{s}}L$ is cancelled in steady-state via feed-forward when deriving the current control loop [52]. The open-loop transfer function $G_{\mathrm{ol}}(s)$ is constituted by the controller $F_{\mathrm{C}}(s)$ in cascade with the decoupled plant $G'(s)$ as

$$G_{\mathrm{ol}}(s) = F_{\mathrm{C}}(s)G'(s) \tag{4.3}$$

where $G'(s)$ in (4.3) is the reduced transfer function of the filter impedance in Laplace form given in (4.2) without the cross-coupling term, expressed in full form as

$$G'(s) = \frac{1}{R + sL} \tag{4.4}$$

In Fig. 4.3 it is found a graphical representation of the derived transfer function. The transfer function of the proportional-integral (PI)-based controller $F_{\mathrm{C}}(s)$ evaluated for the current control is:

$$F_{\mathrm{C}}(s) = k_{\mathrm{p}} + \frac{k_{\mathrm{i}}}{s} \tag{4.5}$$

The closed-loop transfer function $G_{\mathrm{cl}}(s)$ from $\underline{i}^{(\mathrm{dq})^*}$ to $\underline{i}^{(\mathrm{dq})}$ can be expressed as

$$G_{\mathrm{cl}}(s) = \frac{\underline{i}^{(\mathrm{dq})}}{\underline{i}^{(\mathrm{dq})^*}} = \frac{G_{\mathrm{ol}}(s)}{1 + G_{\mathrm{ol}}(s)} \tag{4.6}$$

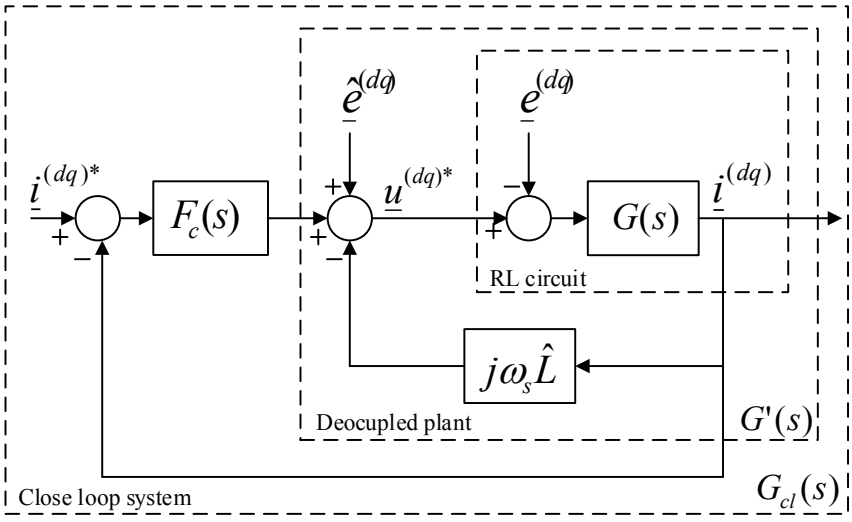

Fig. 4.3 Block diagram of the close-loop current controller.

by substituting (4.4) and (4.5) in (4.6), and shaping the close-loop transfer function as a first order low-pass filter i.e.:

$$G_{\mathrm{cl}}(s) = \frac{F_{\mathrm{c}}(s)G'(s)}{1 + F_{\mathrm{c}}(s)G'(s)} = \frac{\alpha_{\mathrm{c}}/s}{1 + \alpha_{\mathrm{c}}/s} \tag{4.7}$$

where α_{c} is the selected bandwidth of the close-loop system $G_{\mathrm{cl}}(s)$, the control parameters k_{p} and k_{i} can be determined. In Fig. 4.3 it is shown a block diagram representation of the cascaded transfer functions. By arranging (4.7) into the form

$$F_{\mathrm{c}}(s) = \frac{\alpha_{\mathrm{c}}}{s} G'(s)^{-1} \tag{4.8}$$

and further developing (4.8), the PI control parameters $k_{\mathrm{p}} = \hat{L}\alpha_{\mathrm{c}}$ and $k_{\mathrm{i}} = \hat{R}\alpha_{\mathrm{c}}$ are found. Observe that the parameters $\hat{L}$ and $\hat{R}$ are the estimated filter inductance and resistance, respectively. Moreover, when deriving the final control law, the feed-forward of the cross-coupling term $j\omega_{\mathrm{s}}\hat{L}$ allows to independently control the direct and quadrature axis component of the estimated terminal current, $\hat{i}_{\mathrm{d}}$ and $\hat{i}_{\mathrm{q}}$, respectively. Finally, (4.9) shows the implemented controller in Laplace form:

$$\underline{u}^{(\mathrm{dq})^*} = \underline{\hat{e}}^{(\mathrm{dq})} + j\omega_{\mathrm{s}}\hat{L}\underline{\hat{i}}^{(\mathrm{dq})} + (k_{\mathrm{p}} + \frac{k_{\mathrm{i}}}{s})(\underline{i}^{(\mathrm{dq})^*} - \underline{\hat{i}}^{(\mathrm{dq})}) \tag{4.9}$$

where $\underline{\hat{e}}^{(\mathrm{dq})}$ is the estimated grid voltage. The computed voltage $\underline{u}^{(\mathrm{dq})^*}$ is the reference output voltage of the turbine-side VSC. As given in Table 4.1, the sampling frequency of the VSC is 4 kHz corresponding to a bandwidth is $80\omega_{\mathrm{s}}$ rad/s. As suggested in [51], the sampling of the electrical quantities should be much faster than the inner control loop, i.e.: a separation of at least one decade. Thus, the bandwidth of the current control loop α_{c} is selected to be $8\omega_{\mathrm{s}}$ which is approximately 2500 rad/s. The discrete implementation of the current controller is further discussed in Section 4.4.1

Implementation of the anti-windup in the current controller

So far, the current controller has been derived assuming that the VSC has a limitless voltage rating in its output; thus, the controller is able to generate any desired voltage, i.e.: $\underline{u}^{(\mathrm{dq})} = \underline{u}^{(\mathrm{dq})^*}$. Although this approach is useful when calculating for instance the PI parameters, the voltage at the VSC terminals is limited within its rating. When using an integrator term in the control loop, a windup of the integrator output might occur in case of saturation, i.e.: $\underline{u}^{(\mathrm{dq})^*} > \underline{u}^{(\mathrm{dq})}_{\mathrm{max}}$. In this case, the error input of the integrator must be limited. By calculating a current error $\underline{\epsilon}^{(\mathrm{dq})}$ as

$$\underline{\epsilon}^{(\mathrm{dq})} = (\underline{i}^{(\mathrm{dq})^*} - \underline{\hat{i}}^{(\mathrm{dq})}) \tag{4.10}$$

and substituting (4.10) in (4.9), assuming a non saturation of the controller, the unlimited reference voltage is obtained:

$$\underline{u}^{(\mathrm{dq})^*} = \underline{\hat{e}}^{(\mathrm{dq})} + j\omega_\mathrm{s}\hat{L}\underline{\hat{i}}^{(\mathrm{dq})} + k_\mathrm{p}\underline{\epsilon}^{(\mathrm{dq})} + \frac{k_\mathrm{i}}{s}\underline{\epsilon}^{(\mathrm{dq})} \tag{4.11}$$

When the controller requests a voltage that is greater than the converter rating, the saturated output voltage reference becomes

$$\underline{u}_\mathrm{sat}^{(\mathrm{dq})^*} = \underline{\hat{e}}^{(\mathrm{dq})} + j\omega_\mathrm{s}\hat{L}\underline{\hat{i}}^{(\mathrm{dq})} + k_\mathrm{p}\underline{\epsilon}_\mathrm{sat}^{(\mathrm{dq})} + \frac{k_\mathrm{i}}{s}\underline{\epsilon}_\mathrm{sat}^{(\mathrm{dq})} \tag{4.12}$$

where $\underline{\epsilon}_\mathrm{sat}^{(\mathrm{dq})}$ is the extra error signal added into the integrator when the controller is saturated. Subtracting (4.11) from (4.12), the term $\underline{\epsilon}_\mathrm{sat}^{(\mathrm{dq})}$ is found:

$$\underline{\epsilon}_\mathrm{sat}^{(\mathrm{dq})} = \underline{\epsilon}^{(\mathrm{dq})} + \frac{\underline{u}_\mathrm{sat}^{(\mathrm{dq})^*} - \underline{u}^{(\mathrm{dq})^*}}{k_\mathrm{p}} \tag{4.13}$$

Observe in (4.13) that when the controller is not saturated, $\underline{\epsilon}_\mathrm{sat}^{(\mathrm{dq})} = \underline{\epsilon}^{(\mathrm{dq})}$ and the VSC is operated within its limits.

Discrete implementation

In the previous section the current controller has been derived in the frequency domain. However, in applications such as discrete-time simulation and implementation of a digital control in a laboratory environment, the control law given in (4.13) needs to be discretized. In order to derive the current controller in discrete form, the following assumptions are made:

- The capacitor voltage $\underline{\hat{e}}^{(\mathrm{dq})}$ changes slowly and can be considered to be constant over the sampling period T_s, thus:

$$\frac{\underline{\hat{e}}^{(\mathrm{dq})}(k+1) + \underline{\hat{e}}^{(\mathrm{dq})}(k)}{2} = \underline{\hat{e}}^{(\mathrm{dq})}(k) \tag{4.14}$$

- The variation of the current $\underline{\hat{i}}^{(\mathrm{dq})}$ across the filter inductor L is linear over the sampling period T_s:

$$avg(\underline{\hat{i}}^{(\mathrm{dq})}(k, k+1)) = \frac{\underline{\hat{i}}^{(\mathrm{dq})}(k+1) + \underline{\hat{i}}^{(\mathrm{dq})}(k)}{2} \tag{4.15}$$

- The voltage $\underline{u}^{(\mathrm{dq})}$ delivered by the VSC is, in average, equal to the reference value $\underline{u}^{(\mathrm{dq})^*}$ during the period T_s

$$\frac{\underline{u}^{(\mathrm{dq})}(k+1) + \underline{u}^{(\mathrm{dq})}(k)}{2} = \underline{u}^{(\mathrm{dq})^*}(k) \tag{4.16}$$

Under these assumptions, equation (4.11) can be expressed in discrete form as:

$$\underline{u}^{(\mathrm{dq})^*}(k) = \underline{\hat{e}}^{(\mathrm{dq})}(k) + j\omega_\mathrm{s}\hat{L}\underline{\hat{i}}^{(\mathrm{dq})}(k) + k_\mathrm{p}\underline{\epsilon}^{(\mathrm{dq})}(k) + \underline{I}(k) \tag{4.17}$$

with

$$\underline{\epsilon}^{(\mathrm{dq})}(k) = \underline{i}^{(\mathrm{dq})^*}(k) - \underline{\hat{i}}^{(\mathrm{dq})}(k) \tag{4.18}$$

as the current error in discrete form at the instant k. Moreover, $\underline{\hat{e}}^{(\mathrm{dq})}(k)$ and $\underline{\hat{i}}^{(\mathrm{dq})}(k)$ are the grid voltage and filter current, respectively, at the sampling instant k . The term $\underline{u}^{(\mathrm{dq})^*}(k)$ is the reference converter voltage at instant k, and $\underline{I}(k)$ is the integrator state during the instant k. With forward-Euler method, the integrator function in discrete form is calculated as:

$$\underline{I}(k+1) = \underline{I}(k) + k_\mathrm{i}T_\mathrm{s}\left(\underline{\epsilon}^{(\mathrm{dq})}(k) + \frac{\underline{u}_\mathrm{sat}^{(\mathrm{dq})^*}(k) - \underline{u}^{(\mathrm{dq})^*}(k)}{k_\mathrm{p}}\right) \tag{4.19}$$

Equations (4.17), (4.18) and (4.19) summarize the implemented discrete current controller for the turbine-side of the back-to-back VSC-based testing equipment. In Fig. 4.4 it is shown a step response of the current controller. Here, the simulation platform PSCAD/EMTDC v4.2 [53] has been used.

Observe the similarities between the response of the transfer function $G_\mathrm{cl}(s)$ and the sampled current $\hat{i}_\mathrm{d}$. With a bandwidth of $8\omega_\mathrm{s}$ equals 2500 rad/s approximately, a rise time 0.9 ms is expected, as shown in the figure.

4.4.2 PCC voltage controller

The PCC voltage control is in the outer loop of the turbine-side VSC control shown in Fig. 4.2. The input of the controller is the reference PCC voltage denoted as $\underline{e}^{(\mathrm{dq})^*}$ and it calculates the necessary current reference $\underline{i}^{(\mathrm{dq})^*}$, which are sent into the current controller.

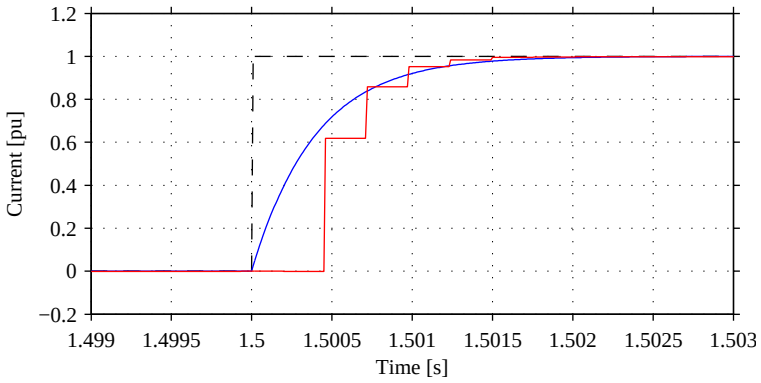

Fig. 4.4 Normalized step response of the current controller: current reference (black dashed), response of system $G_\mathrm{cl}(s)$ (blue) and sampled current $\hat{i}_\mathrm{d}$ (red).

With reference to Fig. 4.1, the current that flows in the capacitor C can be derived by applying Kirchhoff's law at the PCC

$$\underline{i}_{\mathrm{c}}^{(\mathrm{dq})} = \underline{i}^{(\mathrm{dq})} - \underline{i}_{2}^{(\mathrm{dq})} \tag{4.20}$$

Similarly, the dynamic of the current $\underline{i}_{\mathrm{c}}^{(\mathrm{dq})}$ is expressed in (4.21)

$$C\frac{d\underline{\mathrm{e}}^{(dq)}}{dt} + j\omega_{\mathrm{s}}C\underline{e}^{(dq)} = \underline{i}_{\mathrm{c}}^{(\mathrm{dq})} \tag{4.21}$$

By simply combining (4.20) and (4.21), the dependency of the PCC voltage $\underline{\mathrm{e}}^{(dq)}$ with the converter terminal current $\underline{i}^{(\mathrm{dq})}$ and the outer current $\underline{i}_{2}^{(\mathrm{dq})}$ can be obtained:

$$C\frac{d\underline{\mathrm{e}}^{(dq)}}{dt} + j\omega_{\mathrm{s}}C\underline{e}^{(dq)} = \underline{i}^{(\mathrm{dq})} - \underline{i}_{2}^{(\mathrm{dq})} \tag{4.22}$$

The transfer function needed to derive the voltage controller is obtained by transforming (4.22) into Laplace form:

$$\frac{\underline{\mathrm{e}}^{(dq)}(s)}{\underline{i}^{(\mathrm{dq})}(s) - \underline{i}_{2}^{(\mathrm{dq})}(s)} = \frac{1}{sC + j\omega_{\mathrm{s}}C} = G(s) \tag{4.23}$$

where $G(s)$ now describes the open-loop transfer function of the impedance across the capacitor C. By applying the same methodology (ICM) given in Section 4.4.1. The voltage controller can be derived.

Proportional controller

The close-loop transfer function for the voltage control loop can be expressed as

$$G_{\mathrm{ol}}(s) = F_{\mathrm{c}}(s)G'(s) \tag{4.24}$$

where $F_{\mathrm{c}}(s)$ is the transfer function of the controller and $G'(s)$ is the transfer function of the modified plant which does not include the cross-coupling term $j\omega_{\mathrm{s}}C$ in (4.23). By shaping the close-loop transfer function of the voltage controller into a first-order system, i.e.:

$$G_{\mathrm{cl}}(s) = \frac{F_{\mathrm{c}}(s)G'(s)}{1 + F_{\mathrm{c}}(s)G'(s)} = \frac{\alpha_{\mathrm{e}}/s}{1 + \alpha_{\mathrm{e}}/s} \tag{4.25}$$

and further rearranging (4.25) into the form

$$F_{\mathrm{c}} = \frac{\alpha_{\mathrm{e}}}{s}G'(s)^{-1} \tag{4.26}$$

and evaluating $F_{\mathrm{c}} = k_{\mathrm{p}}$ as a proportional (P)-based controller with bandwidth $\alpha_{\mathrm{e}} \leq 0.1\alpha_{\mathrm{c}}$ [51], where $\hat{C}$ is the estimated filter capacitance given in Table 4.1, the gain of the P-based controller is found to be $k_{\mathrm{p}} = \alpha_{\mathrm{e}}\hat{C}$ with α_{e} set to $0.8\omega_{\mathrm{s}}$ (250 rad/s approximately). Finally, the control law can be written as

$$\underline{i}^{(\mathrm{dq})^*} = k_{\mathrm{p}}\underline{\epsilon}^{(\mathrm{dq})} + j\omega_{\mathrm{s}}\hat{C}\underline{\hat{e}}^{(\mathrm{dq})} + \hat{\underline{i}}_2^{(\mathrm{dq})}\left(\frac{\alpha_{\mathrm{f}}}{s+\alpha_{\mathrm{f}}}\right) \tag{4.27}$$

with the voltage error defined as

$$\underline{\epsilon}^{(\mathrm{dq})} = \underline{e}^{(\mathrm{dq})^*} - \underline{\hat{e}}^{(\mathrm{dq})} \tag{4.28}$$

In order to reject high frequency disturbances, a low pass filter (LPF) with bandwidth $\alpha_{\mathrm{f}} = \alpha_{\mathrm{c}}$ has been added when feed-forwarding the measured current $\hat{\underline{i}}_2^{(\mathrm{dq})}$ in (4.27). For a digital implementation, the voltage controller given in (4.27) needs to be written in discrete form. With similar approach given in Section 4.4.1, (4.29) shows the discretized voltage controller based on proportional controller and LPF filter:

$$\underline{i}^{(\mathrm{dq})^*}(k) = k_{\mathrm{p}}\underline{\epsilon}^{(\mathrm{dq})}(k) + j\omega_{\mathrm{s}}C\underline{\hat{e}}^{(\mathrm{dq})}(k) + \hat{\underline{i}}_{2,\mathrm{f}}^{(\mathrm{dq})}(k) \tag{4.29}$$

where the discrete voltage error signal is

$$\underline{\epsilon}^{(\mathrm{dq})}(k) = \underline{e}^{(\mathrm{dq})^*}(k) - \underline{\hat{e}}^{(\mathrm{dq})}(k) \tag{4.30}$$

and the filtered outer current $\hat{\underline{i}}_{2,\mathrm{f}}^{(\mathrm{dq})}(k)$ is calculated as

$$\hat{\underline{i}}_{2,\mathrm{f}}^{(\mathrm{dq})}(k+1) = (1 - T_{\mathrm{s}}\,\alpha_{\mathrm{f}})\,\hat{\underline{i}}_{2,\mathrm{f}}^{(\mathrm{dq})}(k) + T_{\mathrm{s}}\,\alpha_{\mathrm{f}}\,\hat{\underline{i}}_2^{(\mathrm{dq})}(k) \tag{4.31}$$

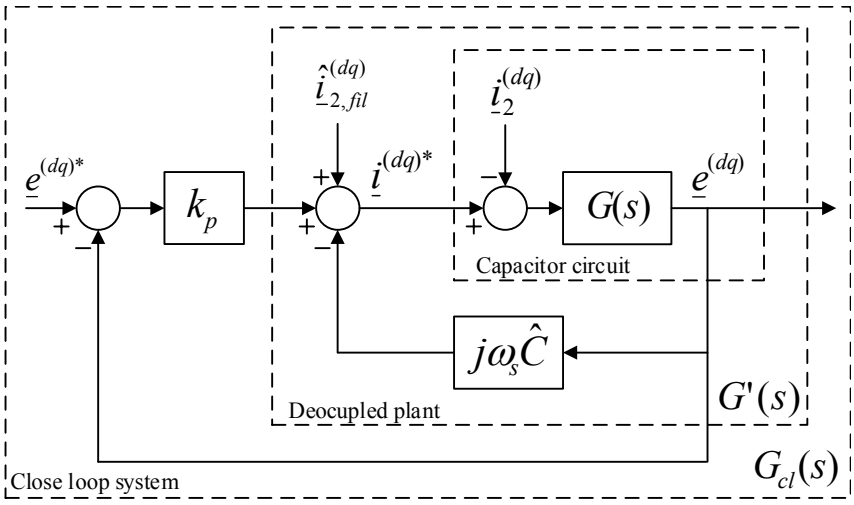

Fig. 4.5 Block diagram of the PCC voltage control based on proportional controller with LPF.

Finally, in Fig. 4.5 it is shown a graphical representation of the implemented PCC.

Proportional and integral controller with active damping

The capacitor C in Fig. 4.1 can represent the capacitive properties of a filter bank connected to the VSC. A non-accurate knowledge of the filter parameters i.e.: actual capacitance, filter losses, etc, can lead to a steady-state error between the reference voltage $\underline{e}^{(\mathrm{dq})^*}$ and the measured voltage $\hat{\underline{e}}^{(\mathrm{dq})}$ at the PCC. For this reason, an integral term can be included in the control law described in (4.27). In order to derive a suitable gain k_i for the integrator and at the same time increase the robustness of the control system against voltage disturbances, an active damping term, as suggested in [50] and [52] has been introduced. The principle of active damping is to include a virtual resistor G_A in (4.22); while an integral part is included in the control algorithm to preserve the bandwidth of the close-loop transfer function. The modified equation becomes:

$$C\frac{d\underline{e}^{(dq)}}{dt} + j\omega_\mathrm{s}C\underline{e}^{(dq)} + G_\mathrm{A}\underline{e}^{(dq)} = \underline{i}^{(\mathrm{dq})} - \underline{i}_2^{(\mathrm{dq})} \tag{4.32}$$

By transforming (4.32) into Laplace form, the open-loop transfer function of the capacitor voltage including the active damping term G_A can be formulated as

$$G_\mathrm{A}(s) = \frac{1}{sC + j\omega_\mathrm{s}C + G_\mathrm{A}/\hat{C}_\mathrm{f}} \tag{4.33}$$

when introducing the decoupling term $j\omega_\mathrm{s}\hat{C}_\mathrm{f}$ in the control law, as shown in Fig. 4.6, a decoupled plant $G'(s)$ can be derived. As suggested in [52], it is desired that the plant $G'(s)$ has the same bandwidth as the voltage regulator, previously selected as α_e equal to $0.8\omega_\mathrm{s}$, i.e.:

$$G'(s) = \frac{1}{sC + G_\mathrm{A}/C} = K\frac{\alpha_\mathrm{e}}{s + \alpha_\mathrm{e}} \tag{4.34}$$

with K as the gain of $G'(s)$, yielding to

$$G_\mathrm{A} = \alpha_\mathrm{e}\hat{C}_\mathrm{f} \tag{4.35}$$

Similarly, with the approach given in Section 4.4.2, i.e.: deriving the close-loop transfer function of the voltage controller and shaping it into a first-order system, the following equivalence can be established:

$$G_\mathrm{cl}(s) = \frac{F_\mathrm{c}(s)G'(s)}{1 + F_\mathrm{c}(s)G'(s)} = \frac{\alpha_\mathrm{e}/s}{1 + \alpha_\mathrm{e}/s} \tag{4.36}$$

which can be rearranged as

$$F_\mathrm{c} = \frac{\alpha_\mathrm{e}}{s}G'(s)^{-1} \tag{4.37}$$

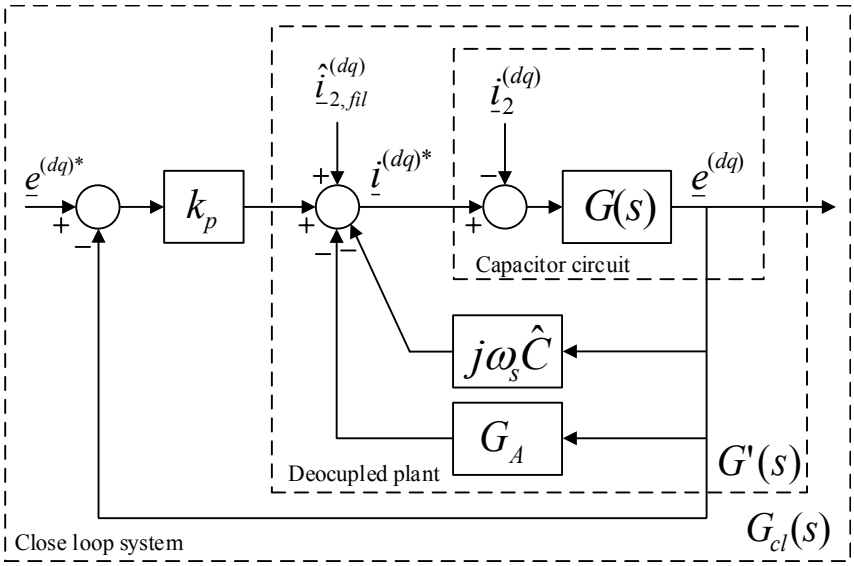

Fig. 4.6 Block diagram of the PCC voltage control based PI controller and active damping.

By evaluating (4.37) with $F_{\mathrm{c}} = k_{\mathrm{p}} + k_{\mathrm{i}}/s$, the parameter of the PI controller are found to be $k_{\mathrm{p}} = \alpha_{\mathrm{e}}\hat{C}$ and $k_{\mathrm{i}} = \alpha_{\mathrm{e}}^2\hat{C}$. Finally, the control law of the voltage controller in Laplace form including integrator and active damping is written as follow:

$$\underline{i}^{(\mathrm{dq})^*} = (k_{\mathrm{p}} + \frac{k_{\mathrm{i}}}{s})\underline{\epsilon}^{(\mathrm{dq})} + (j\omega_{\mathrm{s}}\hat{C}_{\mathrm{f}} - G_{\mathrm{A}})\underline{\hat{e}}^{(\mathrm{dq})} + \underline{\hat{i}}_2^{(\mathrm{dq})}\left(\frac{\alpha_{\mathrm{f}}}{s+\alpha_{\mathrm{f}}}\right) \tag{4.38}$$

where the voltage error $\underline{\epsilon}^{(\mathrm{dq})}$ is defined in (4.28). Similarly, in order to implement the derived control law in a digital controller, (4.38) must be written in discrete form. Equation (4.39) shows the PI-based discrete voltage controller, including active damping and filtering of the outer current.

$$\underline{i}^{(\mathrm{dq})^*}(k) = k_{\mathrm{p}}\underline{\epsilon}^{(\mathrm{dq})}(k) + \underline{I}(k) + (j\omega_{\mathrm{s}}\hat{C}_{\mathrm{f}} - G_{\mathrm{A}})\underline{\hat{e}}^{(\mathrm{dq})}(k) + \underline{\hat{i}}_{2,\mathrm{f}}^{(\mathrm{dq})}(k) \tag{4.39}$$

Observe that in (4.39), the discrete voltage error $\underline{\epsilon}^{(\mathrm{dq})}(k)$ is defined in (4.30), and the filtered current $\underline{\hat{i}}_{2,\mathrm{f}}^{(\mathrm{dq})}(k)$ is defined in (4.31). The integral term $\underline{I}(k)$, including the needed anti-windup function, is given by:

$$\underline{I}(k+1) = \underline{I}(k) + k_{\mathrm{i}}T_{\mathrm{s}}\left(\underline{\epsilon}^{(\mathrm{dq})}(k) + \frac{\underline{i}_{\mathrm{t,sat}}^{(\mathrm{dq})^*}(k) - \underline{i}^{(\mathrm{dq})^*}(k)}{k_{\mathrm{p}}}\right) \tag{4.40}$$

where $\underline{i}_{\mathrm{t,sat}}^{(\mathrm{dq})^*)}$ is the reference current limited within the ratings of the converter. Finally, in Fig. 4.6 is shown a graphical representation of the implemented PCC voltage controller, based on PI controller and active damping and LPF.

Open loop control

Another option in controlling the imposed voltage at the terminals of the wind turbine is to directly select the output voltage of the testing equipment. That is, by manually varying the voltage $\underline{u}^{(\mathrm{dq})^*}(k)$ according to the LVRT profiles given in the Grid Codes. In order to avoid step variation of the modulation index, a predefined ramp-rate limiter can be used when calculating the reference voltage of the converter.

$$\underline{u}^{(\mathrm{dq})^*} = \underline{e}^{(\mathrm{dq})^*} \tag{4.41}$$

Optionally, by taking into consideration the voltage equation given in (4.1). The steady-state voltage drop over L and R can be easily compensated. This allows for an accurate open-loop control of the PCC voltage $\underline{e}$ in steady-state instead of controlling only $\underline{u}$ depicted in Fig. 4.1. In order to avoid feeding high-frequency current transients into the reference voltage when calculating the voltage drop over the interface inductor, a LFP can be placed when feed-forwarding the terminal current. In this control mode, the terminal voltage of the converter can be calculated as:

$$\underline{u}^{(\mathrm{dq})^*} = \underline{e}^{(\mathrm{dq})^*} + \hat{\underline{i}}^{(\mathrm{dq})}\left(\frac{\alpha_\mathrm{f}}{s+\alpha_\mathrm{f}}\right)(\hat{R} + j\omega_\mathrm{s}\hat{L}) \tag{4.42}$$

where α_f is the bandwidth of the LPF. Similarly, a discrete form of the open-loop voltage controller including filter compensation is written as follows:

$$\underline{u}^{(\mathrm{dq})^*}(k) = \underline{e}^{(\mathrm{dq})^*}(k) + \hat{\underline{i}}_\mathrm{f}^{(\mathrm{dq})}(k)(\hat{R} + j\omega_\mathrm{s}\hat{L}) \tag{4.43}$$

where $\hat{\underline{i}}_\mathrm{f}^{(\mathrm{dq})}(k)$ is the estimated converter terminal current passed through a low bandwidth LPF set at α_c, (see Section 4.4.2 for the derivation of a discrete first-order LPF).

Observe that when the parameters of the interface inductor are used in (4.43), the voltage is controlled where the PCC is defined in Fig. 4.1, thus, upstream from the terminal voltage $\underline{u}$. Moreover, if the current $\underline{i}_2$ is measured, the same approach can be used when the voltage at the secondary of the transformer $T2$ needs to be controlled in steady-state by compensating the voltage drop over L_2 . For simplicity, (4.41) will be used later in this thesis when open-loop control is adopted.

Comparison of the derived PCC voltage controllers

In Fig. 4.7 it is given a graphical comparison between the step responses of the derived close-loop voltage control transfer functions when using both P and PI based controller with active damping, as depicted in Fig. 4.5 and in Fig. 4.6, respectively. The results shown in this section are obtained by using the simulation software PSCAD/EMTDC v4.2 [53]. From Fig. 4.7, it is noticeable that ideally both controller shows the same response. This is expected, as both controllers were derived by shaping the close-loop system into a first order system with bandwidth α_e, as given in (4.25) and in (4.36) as for the control law with P-based and PI-based controllers, respectively.

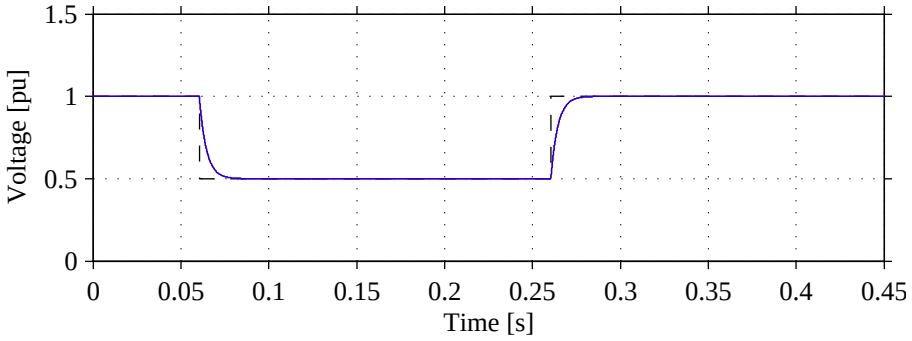

Fig. 4.7 Step response of an ideal close-loop voltage controller transfer functions: reference voltage (dashed black); controlled voltage using P-based controller (blue); and controlled voltage using PI controller with active damping (red).

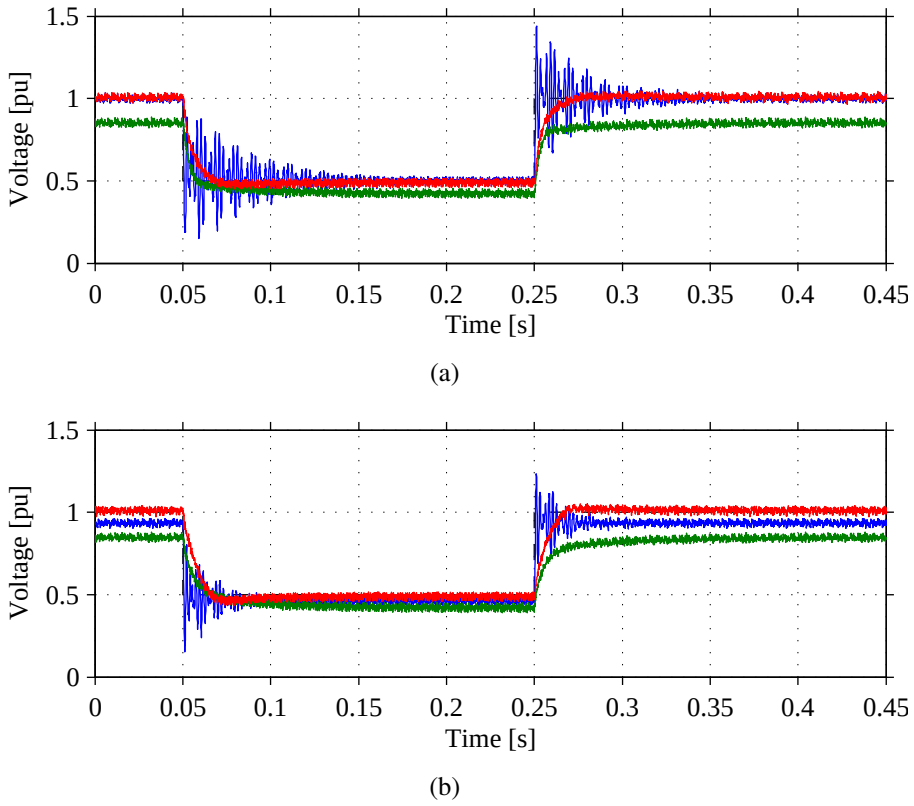

Fig. 4.8 Step response of the PCC voltage when using discrete voltage controller with: (a) no load at the collector-VSC ($\underline{i}_2 = 0$) and (b) an RL load ($\underline{i}_2$ is nominal). In plots: reference voltage (dashed black); controlled voltage using open-loop control (blue); controlled voltage using P-based controller (green); and controlled voltage using PI controller with active damping (red).

Moving now to a more realistic scenario, in Fig. 4.8(a) is given the step response of the implemented PCC voltage controller when the test equipment is operating with no load ($\underline{i}_2$ = 0 pu). The blue traces in Fig. 4.8(a) represent the PCC voltage when the open-loop voltage controller given in Section 4.4.2 is used. Observe that in order to give a step reference to the

voltage controller, no LPF or ramp-rate limiter are used over the reference voltage $\underline{e}^*$. When using open-loop control directly in the collector-VSC of the test equipment, the three-phase current $\underline{i}$ defined in Fig. 4.1 flows freely across the interface inductor L without any control action from the VSC. On the other hand, the filter bank at the PCC is constituted by two arrays of RLC circuits tuned to suppress the harmonic content introduced by the VSC. For these reasons, the interaction between the inductive and capacitive components at turbine-side circuit leads to a poorly damped oscillatory response at 700 Hz approximately in the PCC voltage, as shown with blue traces in Fig. 4.8(a).

With reference to Fig. 4.8(a), the green traces correspond to the response of the PCC voltage when the P-based controller given in (4.39) is used. It is of interest to observe that the pre-event and post-event PCC voltage does not reach 1 pu, evidencing the need of an integrator function in the close-loop controller. Note that when controlling a non lossless system, the assumptions made when modelling the system in Section 4.4.2 when deriving a pure P-based controller are not necessarily representing the actual physical system. Moreover, the step response of the voltage at 0.05 s and at 0.25 s are not as expected to be, taking more than 20 ms to reach steady-state compared with the theoretical value of 9 ms (given for a controller bandwidth of $\alpha_{\mathrm{e}} = 0.8\omega_{\mathrm{s}}$).

The red traces in Fig. 4.8(a) correspond of the step response of the PCC voltage when the PI controller and active damping G_{A} given in (4.39) is implemented. The use of the integrator removes the steady-state error, fixing the actual voltage to its reference in steady-state. Moreover, the step response has a rise time of 12 ms, which is close to the theoretical value of 9 ms. This difference is due to the fact that the controller has no knowledge of the filter losses present in the filter bank connected at the PCC. The use of integrator and virtual resistor terms in the control-loop result in a more accurate first order step response.

In the following, an RL load is connected at the turbine-side VSC of the test equipment. Here, the effect of the feed-forward of the outer current $\hat{\underline{i}}_2$ is investigated. The response of the PCC voltage when an RL load is connected at the primary of the transformer $T2$ (see Fig. 4.1) is depicted in Fig. 4.8(b). The RL load is set in order to demand rated current from the VSC, according to the data given in Table 4.1. Observe that both the P and the PI based controller show slightly different response as compared with Fig. 4.8(a) when RL load is not connected. These 3 to 5 extra milliseconds in the rise-time of the response of the PCC voltage are due to the delay introduced by the filtering of the current $\hat{\underline{i}}_2$ before reaching the voltage controller, as written in (4.29) and (4.39). Observe that the filtered current becomes part of the current reference for the inner current controller, which also introduces a delay when controlling the actual current.

When using open-loop control, the resonance is still present in the dynamic response of the voltage. However, the resonance is much more damped as compare with the no-load test. Here, it is expected that the current needed to charge the capacitor C is small compared to the currents $\underline{i}$ and $\underline{i}_2$ that flow into the load. Moreover, the resistive part of the load also contributes to the damping at the LCL equivalent circuit formed between the filter capacitance C and the inductive elements in the turbine-side circuit of testing device.

It is of interest to observe in Fig. 4.8(b) that the P-base controller exhibits the same steady-state error as in Fig. 4.8(a). Finally, note that when implementing the open-loop controller (blue traces) without steady-state filter compensation, a steady-state error is seen at the PCC voltage. The sign

of the error is strictly dependent of the power flow at the collector-VSC. If the current $\underline{i}_2$ changes direction, a slight over-voltage is expected at the PCC.

4.5 Control of the grid-side VSC of the testing equipment

In this section the focus is on the grid-side VSC of the testing equipment. The main blocks that constitute the implemented discrete controller are the DC voltage control and the inner current controller together with the phase-locked loop (PLL). Similar to the previous section, the controller has been developed in the synchronously rotating dq-reference frame [50] by applying the IMC method.

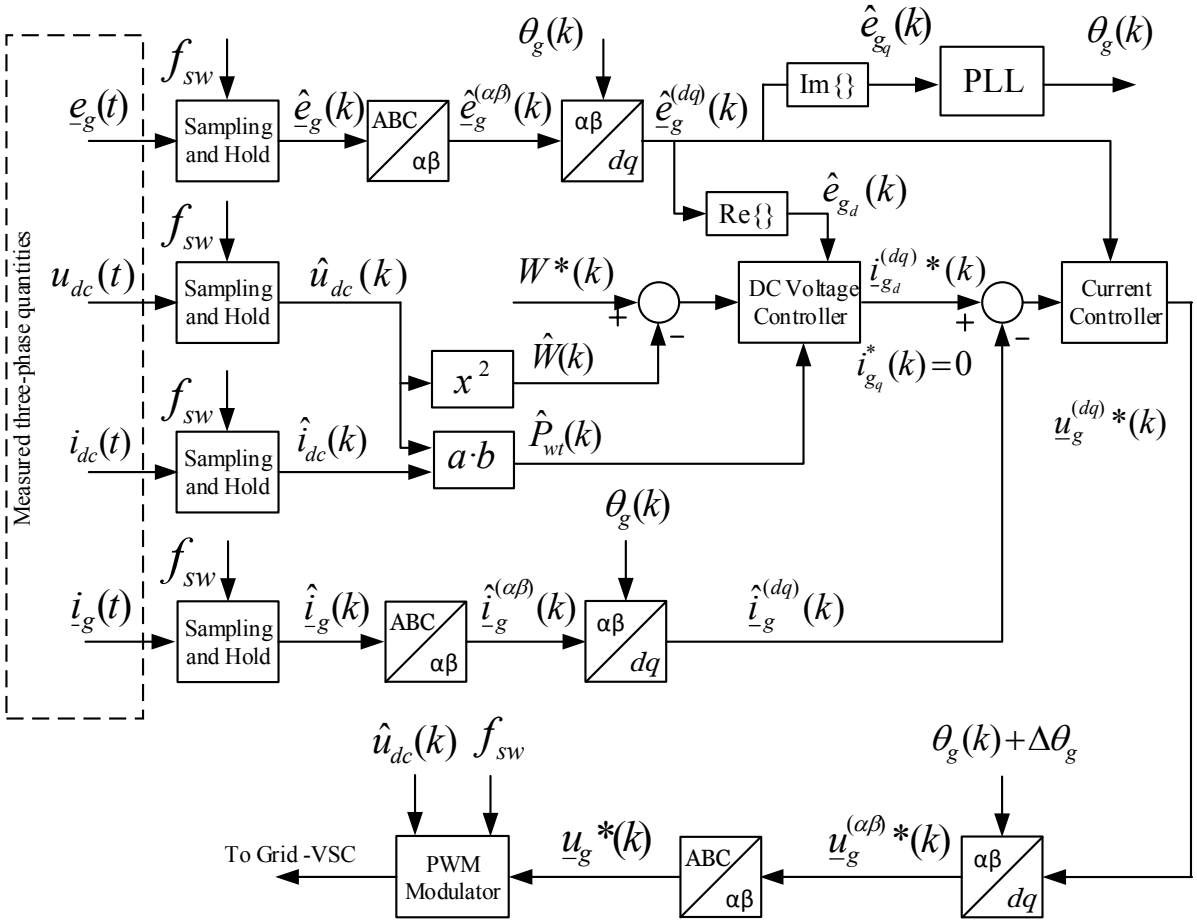

Fig. 4.9 Block diagram of the cascaded vector controller for the grid-VSC of the testing equipment.

The structure of the cascaded controller is shown in Fig. 4.9. In this case, a DC voltage control generates the reference current for the inner-current controller of the converter. Similarly, the output of the current controller is the reference value for the output voltage of the grid-side VSC. In the following, the implemented cascaded control strategy will be described in detail.

4.5.1 Current control

The current control in the grid-side VSC share the same structure of the current control for the turbine-side VSC. Similar to (4.1), the dynamics of the current that flows in the filter L can be expressed as

$$\frac{d\underline{i}_{\mathrm{g}}^{(dq)}}{dt}L + (j\omega_{\mathrm{g}}L + R)\,\underline{i}_{\mathrm{g}}^{(dq)} = \underline{e}_{\mathrm{g}}^{(dq)} - \underline{u}_{\mathrm{g}}^{(dq)} \tag{4.44}$$

from (4.44), and by applying the same IMC method including discretization of the controller and anti-windup function for the integrator, as described in Section 4.4.1, the following control law is found:

$$\underline{u}_{\mathrm{g}}^{(\mathrm{dq})^*}(k) = \underline{\hat{e}}_{\mathrm{g}}^{(\mathrm{dq})}(k) + j\omega_{\mathrm{g}}\hat{L}\underline{\hat{i}}_{\mathrm{g}}^{(\mathrm{dq})}(k) + k_{\mathrm{p}}\underline{\epsilon}^{(\mathrm{dq})}(k) + \underline{I}(k) \tag{4.45}$$

with $\underline{I}(k)$ as the state at instant k of the integrator present in the current control law. Moreover, the current error is here defined.

$$\underline{\epsilon}^{(\mathrm{dq})}(k) = \underline{i}_{\mathrm{g}}^{(\mathrm{dq})^*}(k) - \underline{\hat{i}}_{\mathrm{g}}^{(\mathrm{dq})}(k) \tag{4.46}$$

as the current error in discrete form at the instant k, where $\underline{u}_{\mathrm{g}}^{(\mathrm{dq})^*}$ is the reference grid-side converter voltage and $\underline{\hat{e}}_{\mathrm{g}}^{(\mathrm{dq})}$ is the estimated grid voltage at the primary of the grid-coupling transformer $T1$, at the capacitor filter C. Finally, the PI controller gain are $k_{\mathrm{p}} = \alpha_{\mathrm{c}}L$ and $k_{\mathrm{i}} = \alpha_{\mathrm{c}}R$, with $\alpha_{\mathrm{c}} = 8\omega_{\mathrm{s}}$ equivalent to 2500 rad/s approximately.

4.5.2 Phase-locked loop

In the grid-VSC of the testing device, a PLL such as the one described in [50] is used to synchronize the VSC with the grid voltage $\underline{e}_{\mathrm{g}}^{(dq)}$. With reference to the system shown in Fig. 4.1 and calling $\omega_{\mathrm{g}}^* = 2\pi 50$ rad/s the reference angular frequency of the grid, the equations that governs the PLL in Laplace form can be formulated as

$$\theta_{\mathrm{g}} = \frac{1}{s}(\omega_{\mathrm{g}}^* + \Delta\omega_{\mathrm{g}}) \tag{4.47}$$

where θ_{g} is the instantaneous position of the estimated grid voltage vector $\underline{\hat{e}}_{\mathrm{g}}^{(dq)}$, and $\Delta\omega_{\mathrm{g}}$ is expressed as

$$\Delta\omega_{\mathrm{g}} = \left(k_{\mathrm{p}} + \frac{k_{\mathrm{i}}}{s}\right)\hat{e}_{\mathrm{g_q}} \tag{4.48}$$

As suggested in [50], the parameter of the PI controller are selected as $k_{\mathrm{p}} = 2\alpha_{\mathrm{p}}$ and $k_{\mathrm{i}} = \alpha_{\mathrm{p}}^2$, where $\alpha_{\mathrm{p}} = 0.1\omega_{\mathrm{g}}^*$. Observe that the selection of the bandwidth of the PLL is a trade-off between fast detection of the voltage angle and the ability of rejecting grid disturbances.

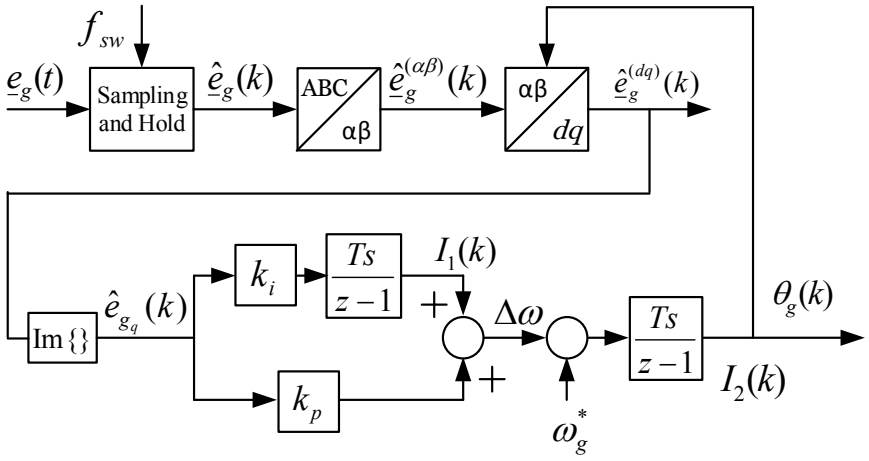

Fig. 4.10 Block diagram of the implemented PLL in the grid-side VSC of the test equipment.

The discrete calculation of the instantaneous position θ_{g} is written as follows:

$$\theta_{\mathrm{g}}(k) = I_2(k) \tag{4.49}$$

$$I_2(k+1) = I_2(k) + Ts(\omega_{\mathrm{g}}^* + \Delta\omega_{\mathrm{g}}(k)) \tag{4.50}$$

where I_2 is the result of the discrete integration of the angular reference frequency, as described in (4.47), added to the output of the PI controller $\Delta\omega_{\mathrm{g}}(k)$ expressed as

$$\Delta\omega_{\mathrm{g}}(k) = k_{\mathrm{p}}\hat{e}_{\mathrm{g_q}}(k) + I_1(k) \tag{4.51}$$

with I_1 as output of the discrete integrator of the PI controller given in (4.48), described as

$$I_1(k+1) = I_1(k) + T_{\mathrm{s}}k_{\mathrm{i}}\hat{e}_{\mathrm{g_q}}(k) \tag{4.52}$$

The block scheme of the implemented PLL is shown in Fig. 4.10.

4.5.3 DC voltage control

The DC voltage controller of the test equipment is placed at the grid-side VSC. The DC-link voltage v_{dc} is controlled by exchanging active power with the AC grid. The voltage across the capacitor C_{dc} is controller by varying the energy stored E_{dc} [50]. The stored energy can be formulated as

$$E_{\mathrm{dc}} = \frac{1}{2}C_{\mathrm{dc}}v_{\mathrm{dc}}^2 \tag{4.53}$$

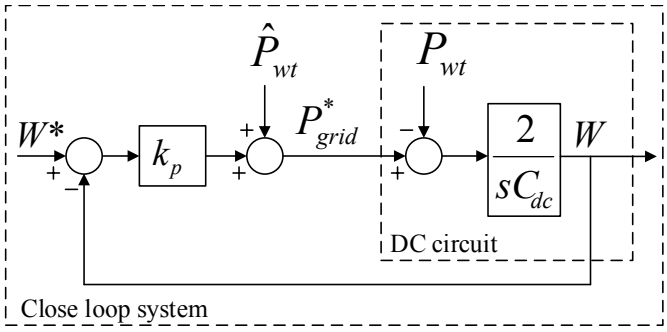

Fig. 4.11 Block diagram of the implemented DC-link voltage controller in the grid-side VSC of the test equipment.

By deriving (4.53), it is possible to define the variation of the energy stored in the capacitor in terms of the difference between the input and output power that flows in the DC-link. Hence, the variation of the energy content will depend on the transferred power from the turbine-side VSC of the test equipment P_{wt} into the DC-link, and the active power P_{grid} delivered from the DC-link into the AC network. Substituting $W = v_{\mathrm{dc}}^2$ in (4.53), we get:

$$\frac{1}{2}C_{\mathrm{dc}} = \frac{dW}{dt} = P_{\mathrm{wt}} - P_{\mathrm{grid}} \tag{4.54}$$

By transforming (4.54) into Laplace form, the transfer function between the capacitor power and W can be written as:

$$\frac{W(s)}{P_{\mathrm{wt}}(s) - P_{\mathrm{grid}}(s)} = \frac{2}{sC_{\mathrm{dc}}} \tag{4.55}$$

As suggested in [50], a P-based controller is used to keep the close-loop transfer function as a first order system. The error is defined as the difference between the square of the reference voltage i.e.: $W^* = (v_{\mathrm{dc}}^*)^2$ and the square of the estimated capacitor voltage $\hat{W}$. By applying the IMC method, the complete control law is found to be:

$$P^*_{\mathrm{grid}} = (W^* - \hat{W})k_{\mathrm{p}} + \hat{P}_{\mathrm{wt}} \tag{4.56}$$

where P^*_{grid} is the active power reference of the testing equipment, $\hat{P}_{\mathrm{wt}} = \hat{v}_{\mathrm{dc}}\hat{i}_{\mathrm{dc}}$ and $k_{\mathrm{p}} = -\alpha_{\mathrm{d}}\hat{C}_{\mathrm{dc}}/2$. As suggested in [51], the bandwidth of the DC voltage controller is selected to be 10 times smaller than the bandwidth of the current controller α_{c}, thus $\alpha_{\mathrm{d}} = 0.8\omega_{\mathrm{s}}$. A block diagram of the implemented DC voltage controller is given in Fig. 4.11. Finally, the direct-axis current reference of the grid-side VSC using amplitude-invariant Clark's Transformation (see Appendix A) is calculated as:

$$i^*_{\mathrm{g_d}} = \frac{2}{3}\frac{P^*_{\mathrm{grid}}}{\hat{e}_{\mathrm{g_d}}} \tag{4.57}$$

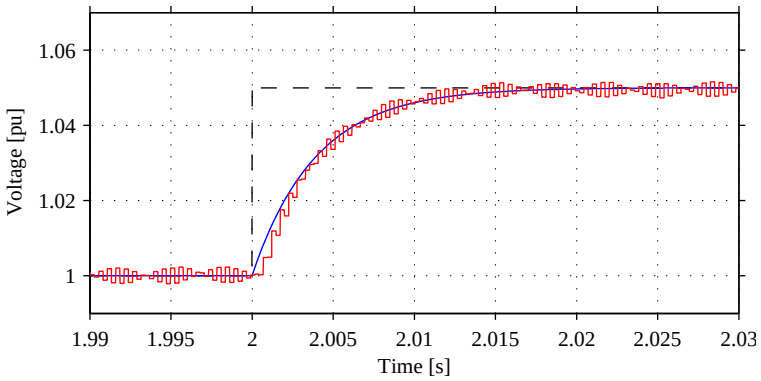

Fig. 4.12 Normalized step response of the DC-link voltage controller: voltage reference (black dashed); voltage output of the mathematical model (blue); and simulated voltage $\hat{v}_{\mathrm{dc}}$ of the test equipment (red).

where $\hat{e}_{\mathrm{g_d}}$ is the direct component of the estimated grid voltage vector $\underline{\hat{e}}_{\mathrm{g}}^{(dq)}$.

The discretization of the DC voltage controller has been done with the same procedure given in Section 4.4.1 and Section 4.4.2. The discrete control law is written as follows.

$$P^*_{\mathrm{grid}}(k) = (W^*(k) - \hat{W}(k))k_{\mathrm{p}} + \hat{P}_{\mathrm{wt}}(k) \tag{4.58}$$

and

$$i^*_{\mathrm{g_d}}(k) = \frac{2}{3}\frac{P^*_{\mathrm{grid}}(k)}{\hat{e}_{\mathrm{g_d}}(k)} \tag{4.59}$$

Figure 4.12 shows the step-response of the estimated voltage $\hat{v}_{\mathrm{dc}}$. From the figure, it is observable that the mathematical model is accurate, and that the actual voltage follows the reference accordingly. Finally, the reactive current reference of the grid-side VSC is controlled at zero, thus, $i^*_{\mathrm{g_q}}(k) = 0$ pu.

4.6 Wind turbine modelling

In this section, the modelling of the wind turbine is presented. A general description of an FPC wind turbine is found in Section 2.2.3. A complete model of the wind turbine has been considered for mathematical analysis. The model includes a two-mass mechanical system, a PMSG, the control law for the generator-side VSC and all the relevant grid-side components of the wind turbine. On the other hand, for time-domain simulation, only the DC-link and the grid-side system of the wind turbine has been modelled. A schematic of the full wind turbine model is shown in Fig. 4.13 while system parameters data is given in Table 4.2.

4.6.1 Modelling of the drive-train dynamics and PMSG

With reference to Fig. 4.13, the torsional stiffness and mechanical damping are denoted as K_{s} and D_{s}, respectively. The inertia of the turbine blades and hub are represented by the equivalent inertia J_{h} while the rotor inertia of the PMSG is labelled as J_{r}. The terms B_{h} and B_{r} are the friction coefficients for the hub and rotor, respectively. Similarly, Ω_{h} and ω_{r} are the hub mechanical speed and rotor electrical speed, respectively, T_{w} is the input torque calculated from an equivalent incoming wind power, T_{e} is the electro-dynamical torque produced by the PMSG, and the pole pairs of the PMSG is denoted by n_{p} . The relevant mechanical parameters are given in [16]. The equations of the mechanical system are here given by

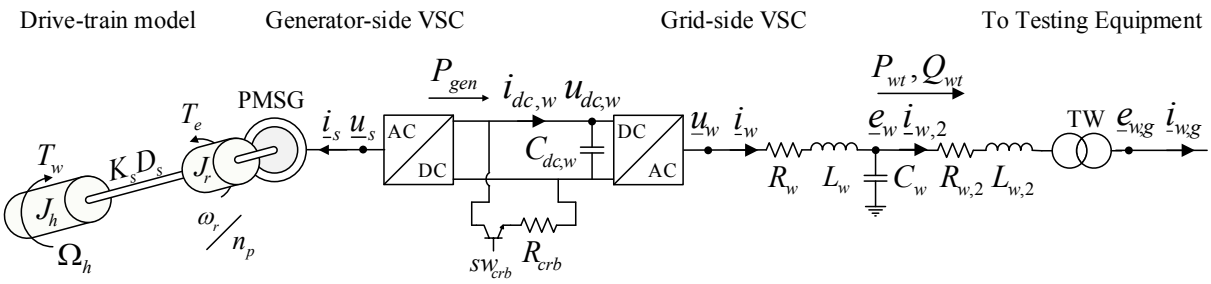

Fig. 4.13 Single-line diagram of the modelled FPC wind turbine.

TABLE 4.2. PARAMETERS OF THE WIND TURBINE SYSTEM.

Transformer TW power		4.5 MVA
Transformer TW voltages		0.69 kV / 10.5 kV
Transformer TW impedance	X_{tw}	6%
Filter inductance	L_{w}	0.15 pu
Filter internal resistance	R_{w}	0.015 pu
Filter inductance	$L_{\mathrm{w,2}}$	0.07 pu
Filter internal resistance	$R_{\mathrm{w,2}}$	0.007 pu
Filter capacitor power	C_{w}	0.1 pu
DC capacitor time constant	C_{dc}	7 ms
DC crowbar resistor	R_{crb}	1 pu
Stator inductance	L_{s}	0.08 pu
Stator resistance	R_{s}	0.01 pu
Magnet flux	Ψ_{m}	1 pu
VSC switching frequency	f_{sw}	2500 Hz
Discrete sampling time	T_{s}	0.2 ms
Current control bandwidth	$\alpha_{\mathrm{c,w}}$	$5\omega_{\mathrm{s}}$
Dc voltage control bandwidth	$\alpha_{\mathrm{d,w}}$	$0.5\omega_{\mathrm{s}}$
PLL bandwidth	$\alpha_{\mathrm{p,w}}$	$0.1\omega_{\mathrm{s}}$

$$
\begin{aligned}
J_{\mathrm{h}}\frac{d\Omega_{\mathrm{h}}}{dt} &= -T_{\mathrm{w}} + K_{\mathrm{s}}\Delta\Omega_{\mathrm{r,h}} + D_{\mathrm{s}}\Delta\dot{\Omega}_{\mathrm{r,h}} - B_{\mathrm{h}}\Omega_{\mathrm{r}} \\
\frac{J_{\mathrm{r}}}{n_{\mathrm{p}}}\frac{d\omega_{\mathrm{r}}}{dt} &= T_{\mathrm{e}} - K_{\mathrm{s}}\Delta\Omega_{\mathrm{r,h}} - D_{\mathrm{s}}\Delta\dot{\Omega}_{\mathrm{r,h}} - B_{\mathrm{r}}\frac{\omega_{\mathrm{r}}}{n_{\mathrm{p}}} \\
\Delta\dot{\Omega}_{\mathrm{r,h}} &= \frac{\omega_{\mathrm{r}}}{n_{\mathrm{p}}} - \Omega_{\mathrm{h}}
\end{aligned}
\tag{4.60}
$$

The electrical system of the PMSG is modelled as

$$
\underline{u}_{\mathrm{s}} = R_{\mathrm{s}}\underline{i}_{\mathrm{s}} + L_{\mathrm{s}}\frac{d\underline{i}_{\mathrm{s}}}{dt} + j\omega_{\mathrm{r}}L_{\mathrm{s}}\underline{i}_{\mathrm{s}} + j\omega_{\mathrm{r}}\Psi_{\mathrm{m}} \tag{4.61}
$$

where R_{s} is the stator resistance, L_{s} is the total stator inductance and Ψ_{m} is the exciter magnet flux given in Table 4.2. The link between (4.60) and (4.61) is given by the torque expression

$$
T_{\mathrm{e}} = \frac{3}{2}n_{\mathrm{p}}\Psi_{\mathrm{m}}i_{\mathrm{s_q}} \tag{4.62}
$$

while the current $i_{\mathrm{s_d}}$ is controlled at 0 pu.

4.6.2 Current controller in generator-side VSC

The current control strategy for the system given in (4.61) is here derived by using the ICM method given in [19]. The resulting control law is expressed as

$$
\underline{u}_{\mathrm{s}}^{*} = \big(k_{\mathrm{p}} + \frac{k_{\mathrm{i}}}{s}\big)(\underline{i}_{\mathrm{s}}^{*} - \hat{\underline{i}}_{\mathrm{s}}) + j\omega_{\mathrm{r}}\hat{L}_{\mathrm{s}}\hat{\underline{i}}_{\mathrm{s}} + j\omega_{\mathrm{r}}\hat{\Psi}_{\mathrm{m}} \tag{4.63}
$$

where k_{p}=$\alpha_c\hat{L}_{\mathrm{s}}$ are k_{i}=$\alpha_c\hat{R}_{\mathrm{s}}$ are the gains of the PI controller implemented in (4.63), with $\alpha_{\mathrm{c}} = 5\alpha_{\mathrm{s}}$ as the bandwidth of the close-loop current controller. Observe that the hat accent is used to differentiate estimated values from measured ones. In order to produce the necessary torque T_{e}, the reference current vector $\underline{i}_{\mathrm{s}}^{*}$ for the generator-side VSC can be calculated by measuring the rotor speed in the machine, as

$$
\underline{i}_{\mathrm{s}}^{*} = 0 - j|\underline{i}_{\mathrm{s}}^{\mathrm{nom}}|\big(\frac{\omega_{\mathrm{r}}}{\omega_{\mathrm{r}}^{\mathrm{nom}}}\big)^{3} \tag{4.64}
$$

where the superscript “nom” relates to values obtained from (4.61) and (4.62) evaluated at nominal conditions. Wind turbine system equation such as (4.60), (4.61), (4.62) and (4.66) and control law equations such as (4.63), (4.64) are later included in the mathematical model analysed in Chapter 5. In the following, a reduced model of the wind turbine for time-domain simulation and laboratory implementation is described.

4.6.3 Reduced model of the FPC wind turbine

Reference [14] provides actual measurements of the 4 MW FPC wind turbine rotor speed with its corresponding wind speed over a 300 s window. The generated power is also measured over the same time period. Here it is assumed that, due to the large rotor inertia, the rotational speed of the wind turbine is kept constant if a voltage dip occurs at its terminals [14]. For this reason, the generator and generator-side VSC are modelled as a current source in parallel with the DC-link capacitor. The reference of the controlled current source is set according to an equivalent generated power P^*_{gen} delivered by the generator-VSC into the DC-link. The magnitude of the DC current source can be calculated by the simple expression

$$i^*_{\mathrm{dc,w}} = \frac{P^*_{\mathrm{gen}}}{\hat{v}_{\mathrm{dc,w}}} \tag{4.65}$$

where P^*_{gen} is the reference generator power, and $v_{\mathrm{dc,w}}$ is the voltage across the wind turbine DC-link capacitor $C_{\mathrm{dc,w}}$. A crowbar constituted by the power electronic switch sw_{crb} in series with the crowbar resistor R_{crb} is placed between the two poles of the DC bus. When the incoming power P_{gen} exceeds P_{wt}, the excess of instantaneous power is redirected through this circuit.

The grid-side converter of the wind turbine is modelled with a 3-phase VSC with 6 IGBTS and their corresponding anti-parallel diodes. The gates are triggered using a PWM, as shown in Fig. 4.14. The converter is interfaced with the imposed AC grid through an LCL filter and a step-up transformer. The inductor L_{w} is connected at the terminals of the grid-side VSC of the wind turbine. The internal resistance of the inductive filter is denoted as R_{w}. The shunt capacitor C_{w} represents the capacitive effect of a filter bank tuned to suppress undesired harmonic content. The voltage $\underline{e}_{\mathrm{w}}$ is measured at its terminals while the voltage $\underline{u}_{\mathrm{w}}$ denotes the terminal voltage of the VSC. The current that flows between these two voltages is labelled $\underline{i}_{\mathrm{w}}$. Similar to how the testing equipment is layout, the second inductive filter of the LCL filter is here denoted as $L_{\mathrm{w,2}}$ with $R_{\mathrm{w,2}}$ as its internal resistance. The current that flows through this filter into the primary-side of the transformer TW is labelled as $\underline{i}_{\mathrm{w,2}}$. Additionally, the generating unit is interconnected with the test equipment in the secondary side of TW. Here, the voltage $\underline{e}_{\mathrm{w,g}}$ and the current $\underline{i}_{\mathrm{w,g}}$ are defined.

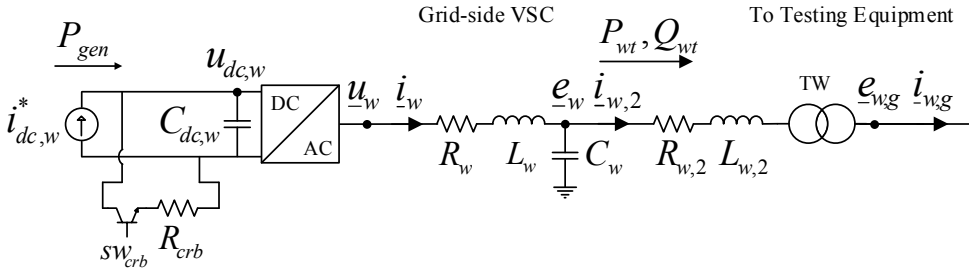

Fig. 4.14 Simplified single-line diagram of the modelled FPC wind turbine.

4.7 Control of the grid-side VSC of the wind turbine

With reference to Fig. 4.14, the controller has been developed in the synchronously rotating dq-reference frame and the control structure is shown in Fig. 4.15. The control is constituted by a DC voltage controller that maintains the DC-voltage to its reference value, and a LVRT control strategy that reacts by injecting reactive current in case of a voltage dip. In the inner loop there is the classical current controller also described in Section 4.4.1. A PLL similar to the one described in Section 4.5.2 is used to maintain synchronism with the imposed voltage. The parameters of the modelled wind turbine are given in Table 4.2. The derived AC current control and DC voltage control strategies for the modelled wind turbine, including LVRT control strategy during voltage dips, are briefly discussed in the following.

4.7.1 Current control

The current control of the wind turbine model including discretization and anti-windup for the integrator function have been also implemented with the same methodology given in Section 4.4.1. In (4.66) is written the discrete form of the wind turbine current controller.

$$\underline{u}_{\mathrm{w}}^{(\mathrm{dq})^*}(k) = \underline{\hat{e}}_{\mathrm{w}}^{(\mathrm{dq})}(k) + j\omega_{\mathrm{s}}\hat{L}_{\mathrm{w}}\underline{\hat{i}}_{\mathrm{w}}^{(\mathrm{dq})}(k) + k_{\mathrm{p}}\underline{\epsilon}^{(\mathrm{dq})}(k) + \underline{I}(k) \tag{4.66}$$

with the current error expressed as

$$\underline{\epsilon}^{(\mathrm{dq})}(k) = \underline{i}_{\mathrm{w}}^{(\mathrm{dq})^*}(k) - \underline{\hat{i}}_{\mathrm{w}}^{(\mathrm{dq})}(k) \tag{4.67}$$

for the control signal of the derived PI controller.

By using the same methodology when deriving the current control given in the previous section, the PI controller gains are found to be $k_{\mathrm{p}} = \alpha_{\mathrm{c,w}}L_{\mathrm{w}}$ and $k_{\mathrm{i}} = \alpha_{\mathrm{c,w}}R_{\mathrm{w}}$, with $\alpha_{\mathrm{c,w}} = 5\omega_{\mathrm{s}}$, which is 1500 rad/s approximately. Finally, the reference voltage of the grid-side VSC of the wind turbine $\underline{u}_{\mathrm{w}}^{(\mathrm{dq})^*}(k)$ is transformed into three-phase quantities and sent into a PWM modulator to calculate the switching signal of the converter.

4.7.2 DC voltage control

The discrete control of the DC voltage controller has been derived with the same procedure given in Section 4.5.3. Calling $W_{\mathrm{w}} = v_{\mathrm{dc,w}}^2$, the power reference $P_{\mathrm{wt}}^*(k)$ of the wind turbine converter is:

$$P_{\mathrm{wt}}^*(k) = (W_{\mathrm{w}}^*(k) - \hat{W}_{\mathrm{w}}(k))k_{\mathrm{p}} + P_{\mathrm{gen}}(k) \tag{4.68}$$

The active current reference $i_{\mathrm{w_d}}^*(k)$ is calculated as

$$i^*_{\mathrm{w_d}}(k) = \frac{2}{3}\frac{P^*_{\mathrm{wt}}(k)}{\hat{e}_{\mathrm{w_d}}(k)} \tag{4.69}$$

where P^*_{gen} is the active power reference used to calculate the reference current $i^*_{\mathrm{dc,w}}$ in (4.65). The P-based controller gain is $k_{\mathrm{p}} = -\alpha_{\mathrm{d,w}}\hat{C}_{\mathrm{dc,w}}/2$, and the bandwidth of the DC voltage controller is set to ten times smaller than the bandwidth of the current control, thus, $\alpha_{\mathrm{d,w}} = 0.5\omega_{\mathrm{s}}$ or 150 rad/s approximately. Finally, the complete control scheme is shown in Fig. 4.15.

4.7.3 Phase-locked loop

In the grid-VSC of the wind turbine, a PLL similar to the one described in Section 4.5.2 is also implemented. Here, the PLL is used to synchronize with the imposed voltage $\underline{e}^{(dq)}_{\mathrm{w}}$. The reference grid angular frequency is $\omega^*_{\mathrm{s}} = 2\pi 50$ rad/s while the actual frequency is set by the testing equipment.

Similar to the PLL structure given in Fig. 4.10, the integrator $I_2(k)$ outputs instantaneous position $\theta_{\mathrm{s}}(k)$ and it is updated every time step as given in (4.70).

$$I_2(k+1) = I_2(k) + Ts(\omega^*_{\mathrm{s}} + \Delta\omega_{\mathrm{s}}(k)) \tag{4.70}$$

The input of the integrator I_2 is the reference angular frequency in addition to the control signal $\Delta\omega_{\mathrm{g}}(k)$ delivered by the PI controller. The error signal for the PI controller is the q axis component of the measured wind turbine voltage $\hat{e}_{\mathrm{w_q}}(k)$

$$\Delta\omega_{\mathrm{g}}(k) = k_{\mathrm{p}}\hat{e}_{\mathrm{s_q}}(k) + I_1(k) \tag{4.71}$$

with I_1 as output of the discrete integrator of the PI controller given in (4.48), described as

$$I_1(k+1) = I_1(k) + T_{\mathrm{s}}k_{\mathrm{i}}\hat{e}_{\mathrm{w_q}}(k) \tag{4.72}$$

Here, the gains of the PI controller are $k_{\mathrm{p}} = 2\alpha_{\mathrm{p,w}}$ and $k_{\mathrm{i}} = \alpha^2_{\mathrm{p,w}}$, where $\alpha_{\mathrm{p,w}} = 0.1\omega^*_{\mathrm{s}}$.

4.7.4 LVRT control strategy

When a grid fault occurs in the power system resulting in a sudden voltage variation at the connection point of the wind power plant, modern wind turbines must be capable to ride-through the corresponding voltage dip seen at its terminals, if the disturbance is within the specification of the LVRT profile given in the Grid Code. In this scenario, the TSO requires that the wind power plant remains in service.

The control strategies implemented in modern wind turbines can be classified in two main actions: hardware protection of the converter, and AC voltage support by current control [20].

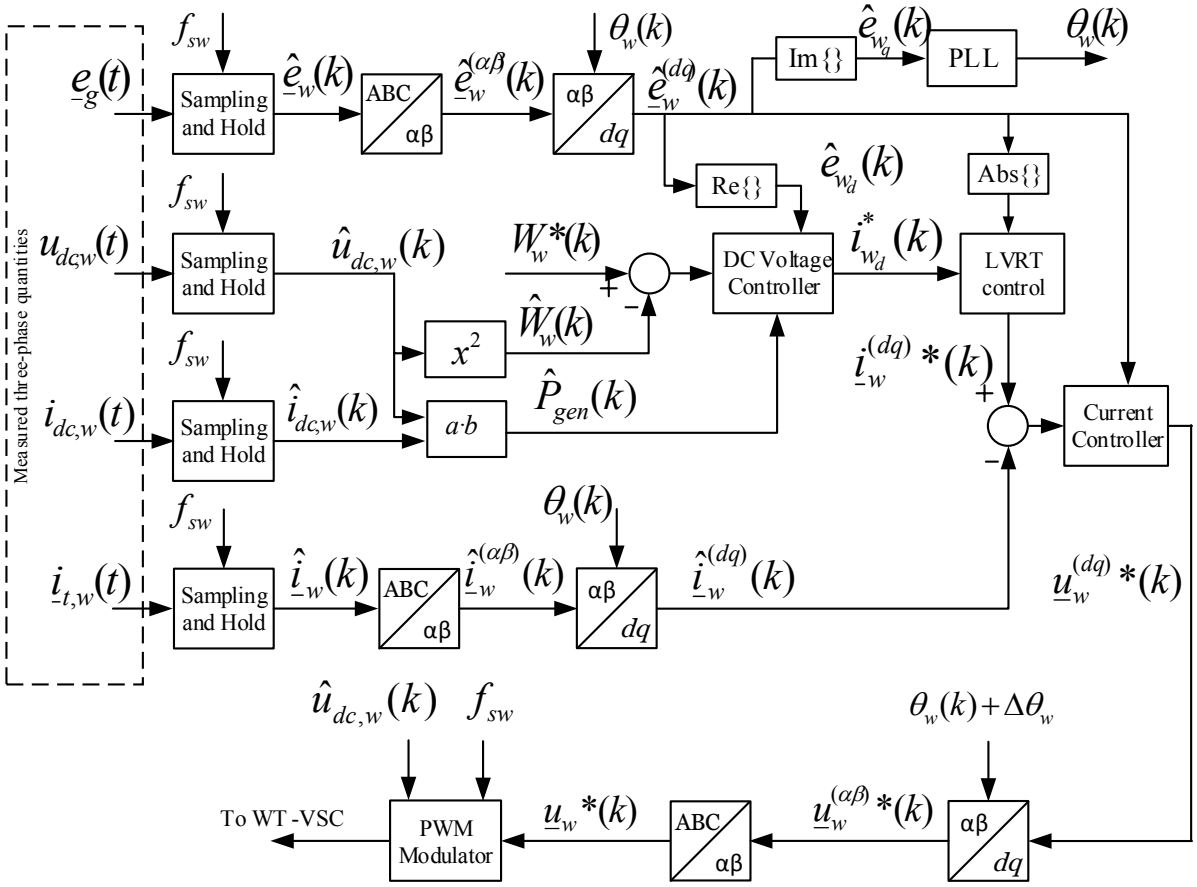

Fig. 4.15 Block diagram of the cascaded vector controller for the modelled wind turbine.

Current control during LVRT

The wind turbine modelled in this thesis is equipped with a current control strategy that provides reactive current support during a voltage dip. Depending on the retained voltage at the PCC, the active current reference $i^*_{\mathrm{w_d}}$ can be limited in order to give room for the pre-calculated reactive current $i^*_{\mathrm{w_q}}$. In case of a severe voltage dip, the current contribution into the fault can be rapidly controlled by the grid-side VSC of the FPC wind turbine.

Here, a predefined voltage/current profile is used to calculate the reactive current reference. The set value of the current is dependent on the retained voltage at the terminals of the wind turbine. For instance, in the German Grid Code [26] and Danish Grid Code [31] it is specified that 1 pu of reactive current must be injected when the system voltage is below 0.5 pu.

When the voltage is restored within the normal operation range, voltage support must be maintained for an additional 500 ms, for example, according to the German Grid Code [26]. Once the reactive current reference is set to its pre-fault value, the LVRT control slowly removes the limitation in the active current, restoring normal active power production of the wind turbine. Finally, in case that reactive power production is not allowed by the TSO during a voltage

dip [32], the active current must be controlled within the current limits of the wind turbine VSC.

Hardware protection

Hardware protection is used to limit the energy stored in the DC capacitor in the wind turbine back-to-back converter, thus, preventing dangerous over-voltages in the DC-link of the wind turbine [20]. The protection system is provided by crowbars connected to the DC-link, as shown in Fig. 4.14.

The crowbar, also called DC chopper, is constituted by a braking resistor which dissipates the excess of energy delivered by the generator into the DC-link. A power electronic switch (typically, a set of IGBTs) allows the current $i_{\mathrm{dc,w}}$ to deviate through the resistor R_{crb}.

An hysteresis control is used to generate the gate signal of the power electronic switch. The protection system of the wind turbine is constantly monitoring the instantaneous voltage $\hat{v}_{\mathrm{dc,w}}$. A control signal is enabled when the voltage exceeds its maximum safe value (typically 1.2 pu) [20], closing the switch and allowing the capacitor $C_{\mathrm{dc,w}}$ to be immediately discharged into the resistor. By this means, the capacitor $C_{\mathrm{dc,w}}$ can be protected against overvoltages.

The resistor is dimensioned in such way that it can dissipate full power production of the wind turbine for approximately one to two seconds [54]. Here, its impedance is calculated so the current that flows through the switch is in proximity to 1 pu.

4.8 Conclusion

In this chapter the control functions of the wind turbine and the test equipment have been described in detail, with special focus on the AC voltage control of the applied voltage at the PCC, and on the LVRT control strategy implemented in the wind turbine model.

Finally, it is of importance to ensure a safe interaction between the wind turbine and the test equipment. For this reason, a stability analysis of the system in steady-state condition is presented in Chapter 5, while the dynamics experienced when carrying out the tests are discussed throughout the rest of the thesis.

Chapter 5

Stability analysis

5.1 Introduction

In the investigated testing setup, the VSC-based testing equipment is a controllable voltage source that must present a stable operation both dynamically and under steady-state conditions. This is of high importance, especially when considering that different wind turbine manufacturers have implemented their own control settings as well as control strategies for operation during a voltage dip.

A potential risk of interaction does not only relate to unstable condition of the system, but also to situations where poorly damped resonances can be triggered under a specific operating condition. For this reason, it is of interest to investigate the stability of the investigated system. First, the passivity of the wind turbine system is studied by the analysis of its input admittance.

In the second part of this chapter, the stability of the complete system is addressed by root-locus analysis. Observe that this analysis is strictly dependent on the system parameters and on the control structure of the tested object. Here, the analysis is focused on the risk of interaction between the two investigated controllers of the wind turbine and the testing equipment, and on the identification of the control parameters that mainly impact the location of the system poles.

5.2 Analysis of the input admittance of the modelled wind turbine

In order to analyse the input impedance of the converter based wind turbine only, the model given in Fig. 4.13 is under consideration. The wind turbine model parameters such as the bandwidth of the implemented controllers for the wind turbine system are given in Table 4.2. As mentioned earlier, the dynamics of the mechanical system shown in Fig. 4.13 have been included in this investigation. Similarly, the dynamics of the grid-side circuit of the wind turbine system including the LCL filter and the inductance of the transformer TW have been also considered. The differential equations that describe both the mechanical system and the electrical system

including the control strategies given in Section 4.6 have been linearised around an operating point and represented in state-space form as:

$$\begin{aligned} \dot{\underline{x}}(t) &= A\underline{x}(t) + B\underline{u}(t) \\ \underline{y}(t) &= C\underline{x}(t) + D\underline{u}(t) \end{aligned} \tag{5.1}$$

where the matrices A, B, C and D are dependent on the systems parameters, on the control algorithms and on the operating conditions. The input vector $\underline{u}(t)$ in (5.1) is expressed as

$$\underline{u}(t) = \begin{bmatrix} \underline{e}^*_{\mathrm{w,g}} \\ i^*_{\mathrm{w_q}} \\ W^*_{\mathrm{dc,w}} \\ i^*_{\mathrm{s_d}} \\ T_{\mathrm{h}} \end{bmatrix} \tag{5.2}$$

where T_{h} refers to the input mechanical torque produced by an incoming wind and $\underline{e}^*_{\mathrm{w,g}}$ refers to the wind turbine grid voltage transferred into the primary-side of the transformer TW.

The state vector $\underline{x}(t)$ is here represented with vector quantities as:

$$\underline{x}(t) = \begin{bmatrix} \underline{i}_{\mathrm{w,2}} \\ \underline{e}_{\mathrm{w}} \\ \underline{i}_{\mathrm{w}} \\ W_{\mathrm{dc,w}} \\ \underline{i}_{\mathrm{s}} \\ \omega_{\mathrm{r}} \\ \omega_{\mathrm{h}} \\ \dot{\Omega}_{\mathrm{r,h}} \\ \theta_{\mathrm{w}} \\ I_{\mathrm{pll,wt}} \\ \underline{I}_{\mathrm{i,w}} \\ \underline{I}_{\mathrm{i,s}} \end{bmatrix} \tag{5.3}$$

The state-space representation of the wind turbine system shown in (5.1) can be expressed as an equivalent transfer function by

$$H(s) = \frac{B(s)}{A(s)} = C(sI - A)^{-1}B + D \tag{5.4}$$

here I is the identity matrix and s is the Laplace operator in (5.4).

The use of the characteristic polynomial of the system as in (5.4) is a powerful tool to investigate the stability of the system [55]. Another approach to understand the susceptibility of the turbine at the different frequencies is based on the derivation of the its frequency-dependent impedance, as described in [51] and [56]. In this case, the system described in (5.1) can be expressed as

frequency dependent transfer functions that relate the voltage applied to the turbine with its output current, as

$$\begin{bmatrix} -i_{\mathrm{w,2_d}} \\ -i_{\mathrm{w,2_q}} \end{bmatrix} = \begin{bmatrix} Y_{\mathrm{dd}}(s) & Y_{\mathrm{dq}}(s) \\ Y_{\mathrm{qd}}(s) & Y_{\mathrm{qq}}(s) \end{bmatrix} \begin{bmatrix} e_{\mathrm{w,g_d}} \\ e_{\mathrm{w,g_q}} \end{bmatrix} \tag{5.5}$$

Equation (5.5) describes in full the dynamics of the modelled wind turbine through a multiple-input multiple-output system. If the resulting admittance matrix is symmetrical, the system can be easily expressed as a single-input single-output system [57]. However, due to the different control loops (especially due to the DC voltage control loop and the PLL), the admittance matrix in (5.5) becomes unsymmetrical [51]. For this reason, proper stability investigation must be carried out with focus on the response from each input to each output. However, this approach can sometimes be bulky [58]. For a quick investigation of the stability properties of the system, (5.5) can be simplified by deriving an equivalent phase impedance $Z_{\mathrm{w}}(j\omega)$ [57], [59].

Evaluating (5.5) with $s = j(\omega - \omega_{\mathrm{s}})$ where ω is the frequency of interest and ω_{s} is the fundamental angular frequency given in Table 4.2, reference [57] suggests that the phase impedance $Z_{\mathrm{s}}(j\omega)$ can be computed as

$$Z_{\mathrm{w}}(j\omega) = \frac{1}{Y_{\mathrm{w}}(j\omega)} = R_{\mathrm{w}} + jX_{\mathrm{w}} \tag{5.6}$$

where the phase admittance $Y_{\mathrm{s}}(j\omega)$ is calculated as

$$\begin{aligned} Y_{\mathrm{w}}(j\omega) = \frac{1}{2}\big[&Y_{\mathrm{dd}}(j(\omega-\omega_{\mathrm{s}})) + Y_{\mathrm{qq}}(j(\omega-\omega_{\mathrm{s}})) \\ &+ j\big(Y_{\mathrm{qd}}(j(\omega-\omega_{\mathrm{s}})) - Y_{\mathrm{dq}}(j(\omega-\omega_{\mathrm{s}}))\big)\big] \end{aligned} \tag{5.7}$$

Observe that the phase admittance $Y_{\mathrm{w}}(j\omega)$ in (5.7) is strictly valid in the sub-synchronous frequency range only. This is due to the fact that in this frequency range, any excitation appears as a positive sequence component and thereby the contribution of the different matrix components is averaged as in the final expression. This is however not necessarily valid in systems where the negative sequence terms have a larger impact on the system dynamics. In such a case, the overall admittance must be separated into its independent positive and negative sequence terms and these must be investigated separately, as explained in [51] and [56]. Here, for simplicity of the analysis and under the consideration that the aim of the investigation is to highlight the possibility of using the test equipment for frequency scan purposes, the derivation of the positive sequence admittance through (5.7) is considered. Here, the response of the turbine is evaluated only in the sub-synchronous frequency range. The interested reader can expand the analysis to higher frequencies using the approach described in [51], [60], [61] and [62] .

The complete model of the wind turbine has been first implemented and verified in Matlab Simulink [63]. Subsequently, the model has been linearized in Wolfram Mathematica [64] to obtain the transfer functions of the admittance matrix in (5.5), that allow for frequency characterization of the analytical wind turbine model.

5.2.1 Evaluation of the admittance matrix and phase admittance

First, the wind turbine is operated with the control parameters given in Table 4.2 (hereafter referred to as "nominal control parameters"). The real part of the resulting admittances $Y_{\mathrm{dd}}(j\omega)$, $Y_{\mathrm{dq}}(j\omega)$, $Y_{\mathrm{qd}}(j\omega)$ and $Y_{\mathrm{qq}}(j\omega)$ are plotted in Fig. 5.1. From the figure, it is possible to observe the asymmetry of the components of the admittance matrix across the sub-synchronous range.

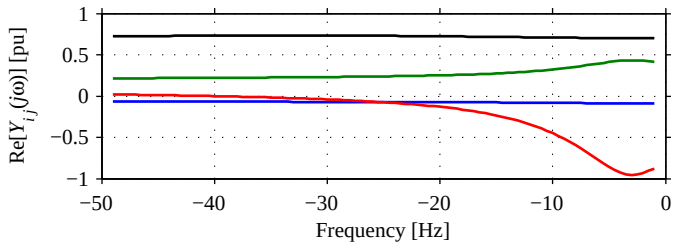

Fig. 5.1 Evaluation of admittances $Y_{\mathrm{dd}}(j\omega)$ (black), $Y_{\mathrm{dq}}(j\omega)$ (blue), $Y_{\mathrm{qd}}(j\omega)$ (green) and $Y_{\mathrm{qq}}(j\omega)$ (red) in the dq-frame of the linearized wind turbine model, when operating at full power production.

In Fig. 5.2 it is shown the real part of $Y_{\mathrm{w}}(j\omega)$ evaluated as in (5.7) for the same frequency range. The admittance component $Re\{Y_{\mathrm{w}}(j\omega)\}$ evaluated with nominal controller gains shows that the admittance increases its magnitude towards the positive region with the increasing of power production, reaching a maximum of 0.44 pu in proximity to 0 Hz. The admittance crosses 0 pu at 45 Hz, increasing towards the negative region in proximity to 50 Hz.

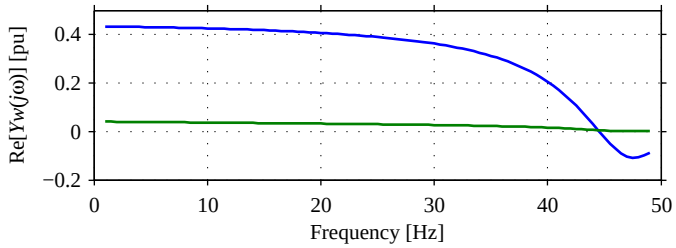

Fig. 5.2 Evaluation of the phase admittance $Y_{\mathrm{w}}(j\omega)$ in the abc-frame of the linearized wind turbine model, when operating at full power production (blue) and at reduced power production (green).

Here it can be noticed that for most of the sub-synchronous range, the real part of the admittance is positive, meaning that the system is passive for that frequency range and that perturbations at these frequencies can be dissipated [51], [60], [65]. Observe, however, that when operated at low power and for most of the analysed frequency range, the wind turbine admittance is in proximity to 0 pu; meaning that the ability of exhibiting passive behavior is substantially reduced. On the other hand, the impact of the system components and control bandwidths (as later discussed in this chapter) in $Y_{\mathrm{w}}(j\omega)$ is more noticeable when P=0.9 pu, in the studied frequency range. In addition, since the generating unit is expected to operate in proximity to rated operation, the input admittance of the wind turbine is here evaluated only at full power production.

5.2.2 Impact of the control parameters of the linearized wind turbine model

It is of interest to observe the effect of the PLL bandwidth on the input admittance of the wind turbine. As discussed in [65], [51] and [66], inverter systems can exhibit a negative input admittance, mainly due to the implemented grid synchronizing method. A simple verification can be carried out by increasing the PLL bandwidth $\alpha_{\mathrm{p,w}}$ from $0.1\omega_{\mathrm{s}}$ to $0.3\omega_{\mathrm{s}}$. The resulting real part of the input admittance $Y_{\mathrm{w}}(j\omega)$ of the linearized wind turbine model is shown in Fig. 5.3 in blue traces.

A negative admittance is observable from 35 Hz when $\alpha_{\mathrm{p,w}}$ is increase to $0.3\omega_{\mathrm{s}}$. A negative peak of -0.1 pu is seen at 43 Hz, while the maximum admittance of 0.4 pu is observed at 1 Hz. Increasing the bandwidth of the PLL means that the controller is capable of tracking faster any change in the grid voltage phase-angle. However, poorly damped resonances can be experienced within the frequency range where the real part of $Y_{\mathrm{w}}(j\omega)$ is negative. This can be dangerous if, for example, an FPC wind turbine is located in proximity to another object that can exhibit a resonance in this frequency range. On the other hand, decreasing $\alpha_{\mathrm{p,w}}$ to $0.05\omega_{\mathrm{s}}$ brings the admittance towards positive values for the majority of the frequency range, as shown in dashed-blue lines in Fig. 5.3. Note that reducing the PLL bandwidth is beneficial for the passivity of the system [56] at the same time that increases the ability of the system in reject grid disturbances [50].

Two more case scenarios are also shown in Fig. 5.3. First, the bandwidth of the current control loop α_{c} is increased from $5\alpha_{\mathrm{s}}$ to $7.5\alpha_{\mathrm{s}}$. It can be noticed from the green curve that the selection of $\alpha_{\mathrm{c,w}}$ barely affect the shape of $Re\{Y_{\mathrm{w}}(j\omega)\}$. Similar behavior can be seen when varying the bandwidth of the DC voltage controller $\alpha_{\mathrm{d,w}}$ from $0.5\alpha_{\mathrm{s}}$ to $1.0\alpha_{\mathrm{s}}$, as shown with a red curve. Both curves are somewhat superimposing the black curve, which corresponds to the real part of the admittance of the wind turbine system when operated at nominal power with nominal control parameters. Thus, the selection of $\alpha_{\mathrm{c,w}}$ and $\alpha_{\mathrm{d,w}}$ have a relatively small impact on the real part of $Y_{\mathrm{w}}(j\omega)$ in the investigated frequency range.

The configuration of the interconnecting system between the grid-side VSC of the wind turbine and the grid can also affect the input admittance of the generating unit. For this reason, it is of interest to analyse the impact of system parameters, such as the capacitor C_{w} and the inductance $L_{\mathrm{w,2}}$ placed at the grid-side of the LCL filter, on the admittance of the modelled wind turbine.

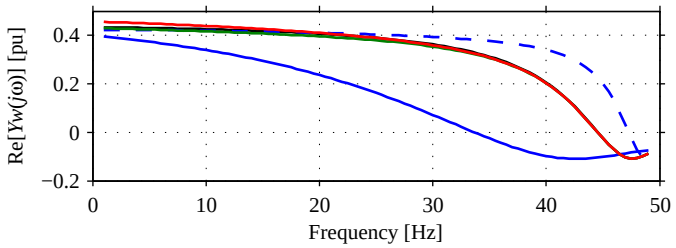

Fig. 5.3 Evaluation of $Re\{Y_{\mathrm{w}}(j\omega)\}$ of the linearized wind turbine model operated at 0.9 pu, with nominal parameters (black), $\alpha_{\mathrm{p,w}}$ set at $0.2\omega_{\mathrm{s}}$ (blue), $\alpha_{\mathrm{p,w}}$ set at $0.05\omega_{\mathrm{s}}$ (dash-blue), $\alpha_{\mathrm{c,w}}$ set at $7.5\omega_{\mathrm{s}}$ (green), $\alpha_{\mathrm{d,w}}$ set at ω_{s} (red).

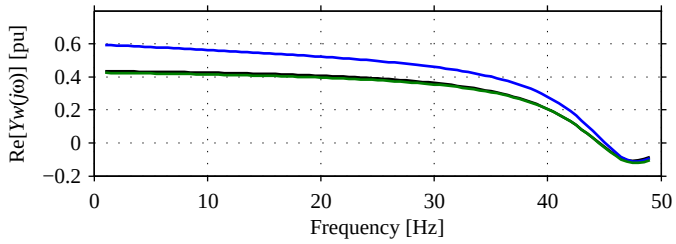

Fig. 5.4 Evaluation of $Re\{Y_{\mathrm{w}}(j\omega)\}$ of the linearized wind turbine model operated at 0.9 pu, evaluated with nominal parameters (black), with C_{w} increased two times (blue), and with $L_{\mathrm{w},2}$ increased two times (green).

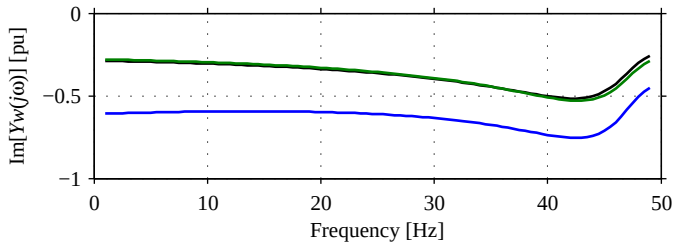

Fig. 5.5 Evaluation of $Im\{Y_{\mathrm{w}}(j\omega)\}$ of the linearized wind turbine model operated at 0.9 pu, evaluated with nominal parameters (black), with C_{w} increased two times, and with $L_{\mathrm{w},2}$ increased two times (green).

In blue traces, Fig. 5.4 shows the waveform of $Re\{Y_{\mathrm{w}}(j\omega)\}$ when the reactive power of the capacitor bank, represented by the capacitor C_{w} in the mathematical model, is increased by a factor of two.

The main difference as compared with nominal system parameters (black traces) is that the admittance curve is displaced towards the positive region. Increasing the capacitance between the grid and the grid-side VSC of the wind turbine means that the imposed voltage becomes more stiff against grid voltage variations, increasing the overall passivity of the system.

Moreover, depicted in green traces, Fig. 5.4 also shows the resulting waveform of $Re\{Y_{\mathrm{w}}(j\omega)\}$ when $L_{\mathrm{w},2}$ is increased from 0.1 pu to 0.2 pu, together with its corresponding internal resistance $R_{\mathrm{w},2}$. Here, the inductive effect of an increased inductor or a subsequent collector transformer is being studied. The admittance seems to be reduced in a small portion when increasing the overall interfacing impedance. It is somewhat expected that, as comparison with a strong gird connection, if a weaker grid connection is encountered at the terminals of the wind turbine, the overall system can be less passive.

Finally, The effect of C_{w} and $L_{\mathrm{w},2}$ over the imaginary part of the admittance $Y_{\mathrm{r}}(j\omega)$ can be observed in Fig. 5.5. Naturally, these reactive elements of the circuit affect the cross-coupling between the d and the q axis, contributing to a great variation in the imaginary part of (5.7). Increasing the value of C_{w} leads to a decrease of the susceptance $Im\{Y_{\mathrm{w}}(j\omega)\}$, while increasing $L_{\mathrm{w},2}$ creates a slight opposites effect. The counter-effect can be easily explained by the contribution the complex variable j when including, for example, the reactances $X_{\mathrm{C}} = -1/\omega C_{\mathrm{w}}$ and $X_{\mathrm{L}} = \omega L_{\mathrm{w},2}$ in the circuit equations. Observe that variations in the cross-coupling impedance also affects the real part of the admittance, as discussed in the previous paragraph.

5.3 Stability of the testing setup

In the following, the stability of the testing system constituted by the generating unit and the testing device, is investigated. As a difference with the previous section, here, the wind turbine and test equipment are combined in a single state-space model. In order to represent the main equations that govern the system dynamics, a reduced electrical model of the testing setup has been derived. As shown in Fig. 5.6, only the grid-side converter of the wind turbine and the turbine-side VSC of the test equipment have been considered for this analysis. The DC current source of the wind turbine model and the interface impedance between the testing device and the generating unit have been also included. Moreover, the inductor $L_{\mathrm{w},2}$, the output transformer of the wind turbine TW, the AC cable, the coupling transformer $T1$ and the inductance L_2 of the testing equipment have been represented by the equivalent inductance and resistance L_{eq} and R_{eq}, respectively. The testing equipment VSC is sourced by a fix DC voltage at its DC bus, meaning that the DC-link voltage controller of the grid-VSC of the test equipment is considered ideal and infinitely fast.

With reference to Fig. 5.6, the system parameters are reported in Table 5.1, while the rest of the model parameters such as bandwidth of the implemented controllers in test equipment and wind turbine system are given in Table 4.1 and Table 4.2, respectively.

TABLE 5.1. PARAMETER OF THE REDUCED SYSTEM MODEL.

Base values		4.5 MVA, 10 kV
Filter inductance	L_{w}	0.15 pu
Filter internal resistance	R_{w}	0.02 pu
Filter capacitor power	C_{w}	0.1 pu
Equivalent interface inductance	L_{eq}	0.14 pu
Equivalent interface resistance	R_{eq}	0.014 pu
Filter inductance	L	0.08 pu
Filter internal resistance	R	0.01 pu
Filter capacitor power	C	0.2 pu

Similarly to the previous section in this chapter, the differential equations that describe the physical system shown in Fig. 5.6, including the control strategies given in the previous chapter have been again linearised around an operating point and represented in state-space form as given

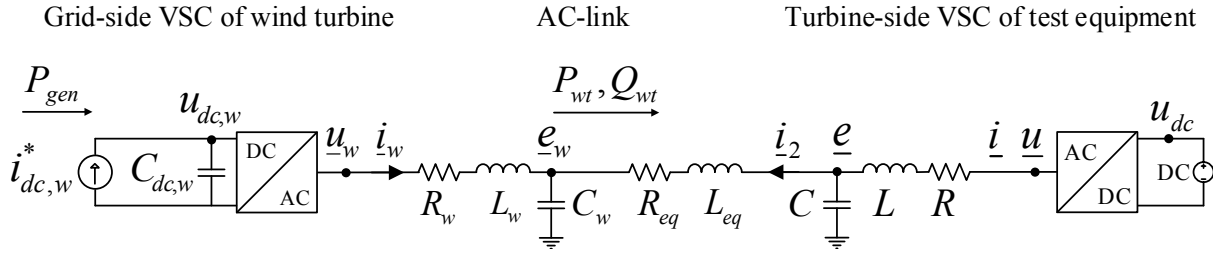

Fig. 5.6 Reduced electrical model of the testing setup.

in (5.1). Observe that when evaluating (5.1) for the reduced testing system shown in Fig. 5.6, the matrices A, B, C and D are now dependent on the systems parameters, on the control algorithms and on the operating conditions of both the testing equipment and wind turbine model. Moreover, the determinant of A has been considered for evaluating the stability of the system by means of root-locus analysis [55]. For this analysis, the wind turbine system model is reduced and only the DC-link and the grid-side VSC circuit dynamics have been considered, as modelled in Section 4.6.3. For this reason, the input vector $\underline{u}(t)$ is now defined as

$$\underline{u}(t) = \begin{bmatrix} \underline{e}^* \\ P_{\mathrm{gen}} \\ W^*_{\mathrm{dc,w}} \\ i^*_{\mathrm{w_q}} \end{bmatrix} \tag{5.8}$$

where P_{gen} is the input DC-link power used when deriving (4.68) and that $\underline{e}^*$ is the reference voltage of the PCC, controlled by the testing equipment. The state vector $\underline{x}(t)$ is here represented with vector quantities as:

$$\underline{x}(t) = \begin{bmatrix} \underline{i} \\ \underline{e} \\ \underline{i}_2 \\ \underline{i}_{2,\mathrm{f}} \\ \underline{e}_{\mathrm{w}} \\ \underline{i}_{\mathrm{w}} \\ W_{\mathrm{dc,w}} \\ \underline{I}_{\mathrm{c,t}} \\ \underline{I}_{\mathrm{e,t}} \\ \underline{I}_{\mathrm{c,w}} \\ \theta_{\mathrm{w}} \\ I_{\mathrm{p_1,w}} \\ I_{\mathrm{p_2,w}} \end{bmatrix} \tag{5.9}$$

where the subscript t and w denotes for variables related to the testing equipment for the wind turbine, respectively, and the subscript c and p denotes for current control and PLL integrators, respectively.

Similarly, two operating point $\underline{x}_0$ are found after evaluating the mathematical model of the system shown Fig. 5.6, when the reference generator power defined in (4.65) is set at P^*_{gen} = 0 pu and P^*_{gen} = 0.9 pu (4 MW). The reference voltage of the PCC voltage controller $\underline{e}^*$ is set at 1 pu. The reference for the DC-link voltage controller $W^*_{\mathrm{dc,w}}$=$(v^*_{\mathrm{dc,w}})^2$ is set at 1 pu (DC) while the reference for the reactive current $i^*_{\mathrm{w_q}}$ of the grid-side VSC of the wind turbine is set at 0 pu.

The output vector $\underline{y}(t)$ includes information about the value of all states, including the reference active power and active current of the wind turbine, P^*_{wt} and $i^*_{\mathrm{w_d}}$, respectively, and the reference current $\underline{i}^*_{\mathrm{t}}$ for the current control of the test equipment. Since the testing setup is constituted by two controllable objects, the impact of the variation of system parameters on the location of the system poles will be analysed and discussed [55].

Here, the linearised model has been obtained through the software Wolfram Mathematica [64] and evaluated in the simulation software MATLAB [63]. In the plots, the star represent the initial location of the system poles and the trace represents its displacement when a selected parameter is varied.

5.4 Dependency of system poles with respect to control parameters of the test equipment

The bandwidth of the closed-loop AC voltage controller of the test equipment α_e sets the speed of response of the overall system when varying the PCC voltage. Moreover, as described in Section 4.4.2, the close-loop PCC voltage control can either be based on P or PI controller. Thus, it is of interest to identify the pole location when selecting a particular control with a given bandwidth α_e.

5.4.1 Impact of the topology of the PCC voltage controller

In (4.27) is given the control law of the PCC voltage controller based on proportional controller with gain $k_p = \alpha_e \hat{C}$. Similarly, in (4.34) is given the control law of the PCC voltage controller based on PI controller with gains $k_p = \alpha_e \hat{C}$ and $k_i = \alpha_e^2 \hat{C}$, and active damping $G_A = \alpha_e \hat{C}_f$. In the following, the bandwidth α_e of the voltage controller is varied while the current control bandwidth α_c is kept constant at $8\omega_s$. Observe that this analysis is valid in the case that a faster voltage controller is needed without necessarily modifying α_c.

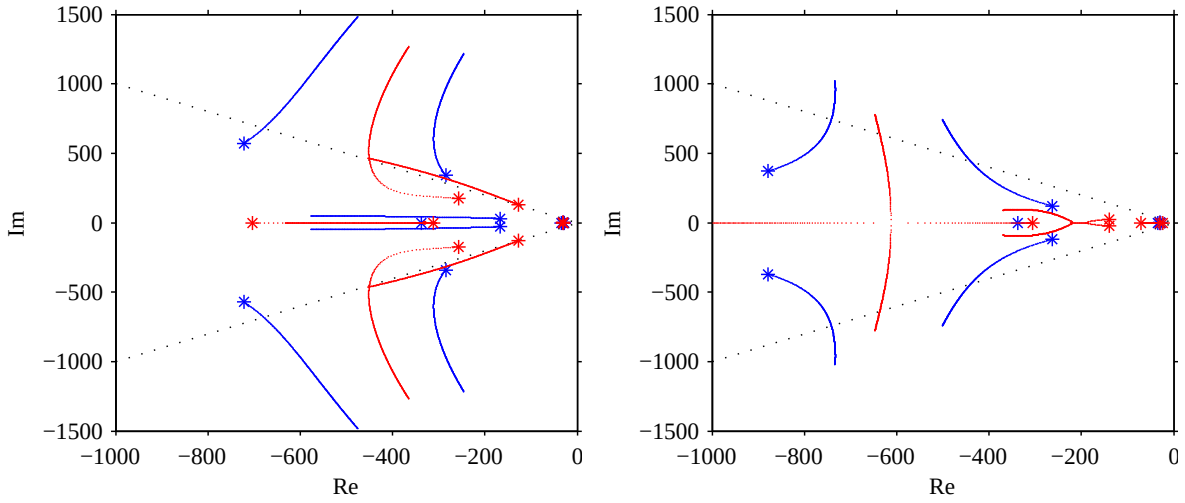

Fig. 5.7 Pole displacement when increasing the bandwidth α_e from $0.8\omega_s$ to $2.5\omega_s$ while α_c is kept constant : Plot (a): using PI-Ga controller; Plot (b): using P controller; when the testing equipment is with no load (blue traces) and full load (red traces).

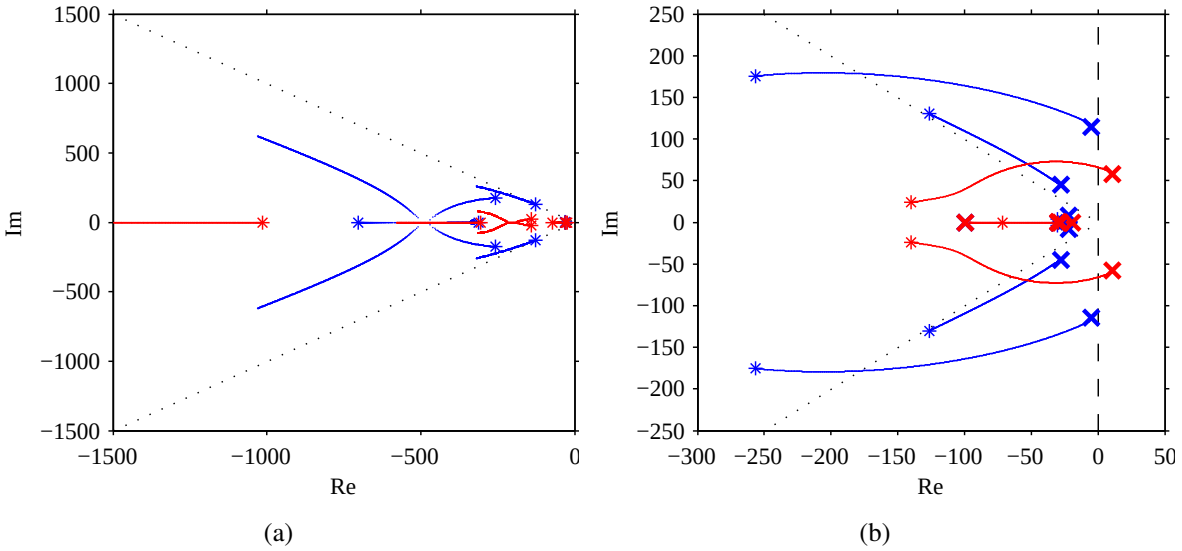

Fig. 5.8 Plot (a): Pole displacement when increasing α_c from $8\omega_s$ to $16\omega_s$; Plot (b): Pole displacement when decreasing α_c from $8\omega_s$ to $2.5\omega_s$. In plots: ratio $\alpha_e = 0.1\alpha_c$ is kept constant while using PI-based controller (blue), P-based controller (red) and poles location of the system with $\alpha_{c,w}$ and $\alpha_{d,w}$ reduced (X in plot b).

Figure 5.7(a) shows the pole displacement of the investigated system when using PI-based controller and the bandwidth of the voltage controller of the test equipment α_e is varied from its nominal value of $0.8\omega_s$ to $2.5\omega_s$. The plot show the resulting pole location for two different operating point of the wind turbine: the blue traces correspond to the operating point P^*_{gen}= 0 pu, and the red traces correspond to the operating point when P^*_{gen}= 0.9 pu. When increasing the bandwidth α_e while maintaining P^*_{gen} at 0 pu, two pair of complex poles immediately become poorly damped. Observe at the red traces that these two complex poles located in the proximity to the 45 degrees line are shifted to near the origin when the wind turbine operates at full power output. The results in Fig. 5.7(a) also shows that these two poles are within the well damped area when P^*_{gen}= 0.9 pu for values α_e below $2.5\omega_s$. Due to the cascaded structure of the implemented controller illustrated in Fig. 4.2, two complex poles appear to move toward the non-damped region when $\alpha_e$increases. while two complex-poles moves across the real axis when the bandwidth increases in both scenarios.

In Fig. 5.7(b) it is shown the pole location of the system when using P-based controller (with $G_A = 0$) for the same sweeping of the bandwidth α_e. Observe that for α_e = $0.8\omega_s$, the location of the poles for P^*_{gen} = 0 pu and P^*_{gen} = 0.9 pu is always below the 45 degrees line. For no-load operation of the turbine (blue traces), two pair of complex poles moves away from the well damped area when α_e increases. For full power operation of the wind turbine at α_e = $0.8\omega_s$, the system poles are located in proximity of the origin, changing their characteristic frequency and damping. However, when α_e increases, two of complex pole become poorly damped and continue to move in parallel to the imaginary axis. Finally, it is of interest to observe that for values of α_e close to $0.8\omega_s$, the use of P-based controller gives a more damped system as compared with PI controller, for the two selected operating point of the wind turbine. However, as later discussed

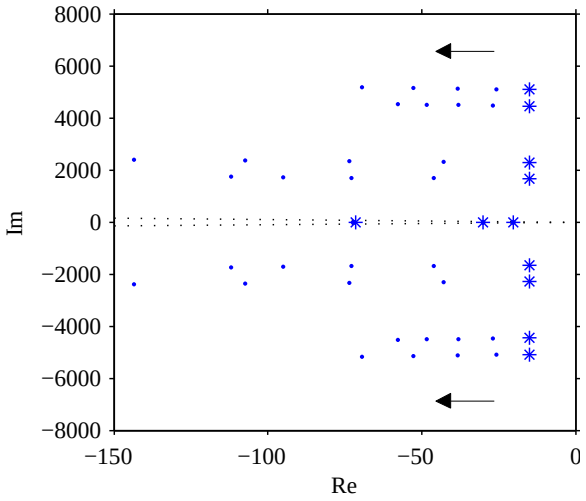

Fig. 5.9 Pole displacement when increasing the power of the wind turbine from 0 pu to 1 pu using open-loop controller in collector-VSC.

in Section 5.5.1, the high frequency poles are not greatly affected by the selection of the structure of the PCC voltage control.

In the following, both controller bandwidth α_c and α_e are varied simultaneously while keeping the ratio $\alpha_e = 0.1\alpha_c$ constant. Here, the wind turbine operates at nominal active power production and the overall speed of the testing equipment control action is increased. First α_c has been increase from $8\omega_s$ to $16\omega_s$ while at the same α_e is increased from $0.8\omega_s$ to $1.6\omega_s$. The displacement of the system poles is given in Fig. 5.8(a). Observe that when PI-based controller is used (blue traces), two complex poles move towards the left-hand side of the map, meaning that the system becomes more damped. On the other hand, then P-control is used (red traces), the poles located in proximity to the origin remain almost unvaried, while two real poles moves across the real axis towards the negative region. In this case, increasing the bandwidth of the outer and inner loop improves the stability of the system.

On the other hand, it is of interest to observe the location of the system poles if a slower control-loop is implemented in the testing equipment. In Fig. 5.8(b) it is shown the displacement of the poles when α_c is reduced from $8\omega_s$ to $3\omega_s$ under the same conditions ($\alpha_e = 0.1\alpha_c$). Observe that when PI-based controller is implemented, two complex poles approach the imaginary axis, while when the P-based controller is in use, two complex poles cross towards the positive region of the map, meaning that the system becomes unstable. Finally, Fig. 5.8(b) shows with X-marks the pole location when $\alpha_{c,w}$ and $\alpha_{d,w}$ are reduced to $3\omega_s$ and $0.3\omega_s$, respectively, after reducing both the current controller and AC voltage controller bandwidths on the testing equipment. The latter scenario corresponds when a testing equipment with a reduced close-loop control bandwidth is in presence of a VSC-interfaced wind turbine with similar (reduced) bandwidths. Note that the stability is maintained only when the PI-controller is used. The impact of the wind turbine control bandwidths is later discussed in Section 5.5.1.

The open-loop control strategy for the PCC voltage has been presented in Section 4.4.2. Observe that for this analysis, the cascaded control structure shown in Fig. 4.2 is not implemented.

Therefore, the input vector $\underline{e}^{(\mathrm{dq})^*}$ of the state-space model is here fed as the VSC terminal voltage $\underline{u}^{(\mathrm{dq})}$ shown in Fig. 5.6. The location of the system poles is computed for different operating points of the wind turbine from P^*_{gen} = 0 pu to P^*_{gen} = 0.9 pu (4 MW). The results are shown in Fig. 5.9.

As seen from the figure, the number of poles has been reduced as compared with the use of close-loop controller, decreasing the order of the system. Observe that for non-load operation, 4 pair of high-frequency complex pole parallel to the imaginary axis appear. When the wind turbine increases its power output, these poles move toward the left-hand side, meaning that the system becomes more damped. This result goes in hand with the results given in Fig. 4.8, where the three topologies of PCC voltage controllers are compared. Observe that in both analyses, the system becomes more damped when the current $\underline{i}_2$ (see Fig. 5.6) is nominal.

5.4.2 Impact of the active damping term in PI-based PCC voltage controller

The active damping term contributes to the controllability of the PCC voltage by improving the performance of the controller against voltage disturbances. At the same time, the addition of the virtual resistor G_{A} in the control-loop leads to an increment of the gain of the integrator term in the PI controller. In this section, the impact of the active damping term G_{A} on the location of the system poles is investigated.

In Fig. 5.10(a) it is shown the pole location when the term G_{A} is varied from 0 to $\alpha_{\mathrm{e}}\hat{C}_{\mathrm{f}}$. Observe in the figure that all the poles of the system are displayed and that only one visible real pole is moved towards the negative side. In addition, the high-frequency poles located in proximity to the imaginary axis are unvaried with respect to the selection of G_{A}.

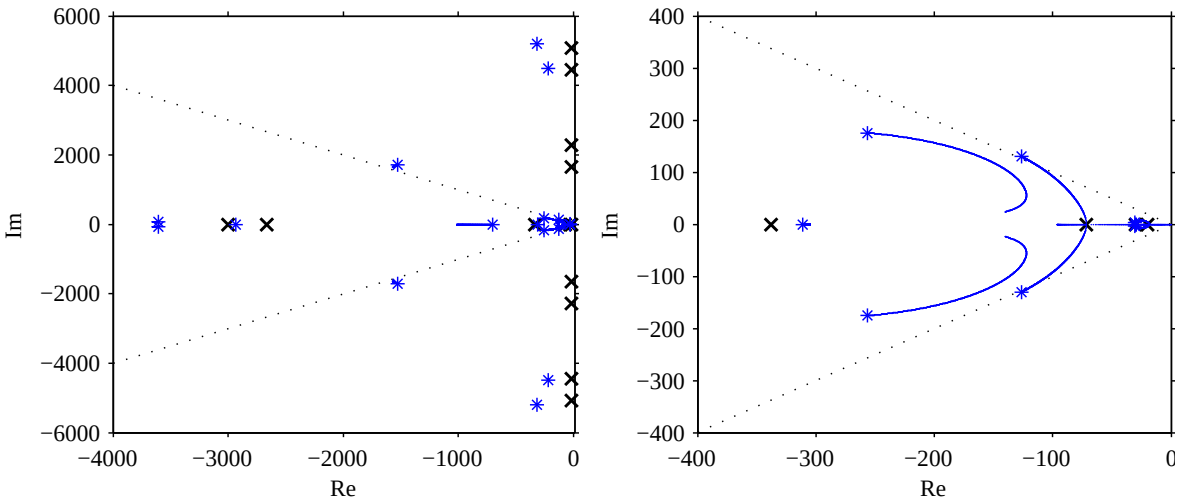

Fig. 5.10 Location of the system poles when the active damping term G_{A} is varied from 0 to $\alpha_{\mathrm{e}}\hat{C}_{\mathrm{f}}$ (blue). System poles when PCC is controlled in open-loop (black X). Plot (a): complete pole map. Plot (b): location of the low-frequency poles

With focus on the low frequency poles located in the well-damped region shown in Fig. 5.10(b), only to pair of complex poles become more damped when increasing G_{A} towards its nominal value of $\alpha_{\mathrm{e}}\hat{C}_{\mathrm{f}}$. From the figures, it is possible to conclude that the system is stable for any given value of active damping between 0 and $\alpha_{\mathrm{e}}C_{\mathrm{f}}$.

As a comparison, in the figures it is also shown the poles of the system when the PCC is controlled in open-loop (black X marks in Fig. 5.10(a) and Fig. 5.10(b)). Observe that there is no major difference, in particular, on the location of the high-frequency poles, meaning that in this control mode the stability of the system is also maintained. However, as discussed in Section 4.4.2, the virtual resistor plays a key role when deriving an integrator term capable of removing the steady-state error while controlling the PCC voltage in close-loop. For this reason, a virtual resistor of $G_{\mathrm{A}} = \alpha_{\mathrm{e}}C_{\mathrm{f}}$ is recommended when using close-loop controller of the PCC voltage.

5.4.3 Impact of the feed-forward of the outer current in close-loop

The filtering stage applied to the feed-forward of the estimated outer current $\hat{\underline{i}}_2$ in the close-loop voltage control is required to be fast enough to guarantee good system dynamics. In Fig. 5.11 is shown the displacement of the system poles when increasing the low-pass filter bandwidth α_{f} in (4.27) and in (4.38) corresponding to P-based and PI-based controller, respectively, from $0.8\omega_{\mathrm{s}}$ (α_{e}) to 10 times this value (α_{c}).

In Fig. 5.11(a) it is shown the displacement of the low-frequency poles when varying α_{f} while the P-controller is implemented in the test equipment. The blue curves correspond to the pole location when the wind turbine power is set at 0 pu. Observe that all poles are well-damped, independent of the selection of α_{f}. Moreover, wind turbine at 0 pu power means that the outer

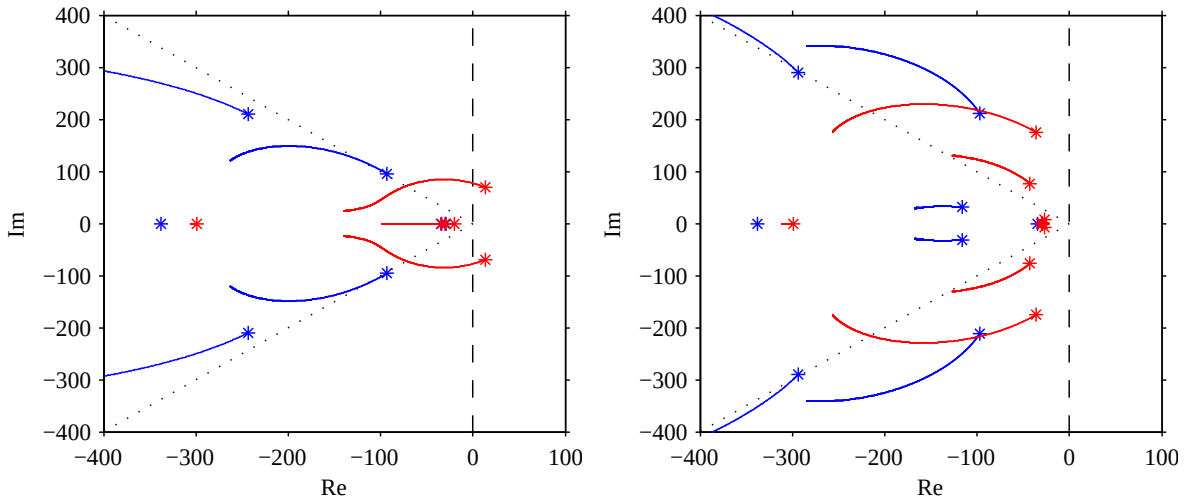

Fig. 5.11 Pole displacement when increasing the LPF bandwidth α_{f} from $0.8\omega_{\mathrm{s}}$ to $8\omega_{\mathrm{s}}$ using Plot (a): P-controller; and Plot (b): PI-controller with active damping; for P^{*}_{gen} set at 0 pu (blue traces) and P^{*}_{gen} set at 0.9 pu (red traces).

current $\underline{i}_2$ is also 0 pu, meaning that the impact of the filter α_f in the dynamics of the system can be unnoticed. Note from the red curves that when the power of the wind turbine is set at 0.9 pu, the system becomes unstable when $\alpha_\mathrm{f} = \alpha_\mathrm{e}$. A reduced bandwidth of the LPF over the current $\underline{i}_2$ introduces a considerable delay when calculating the current reference $\underline{i}^*$ for the cascaded inner current controller. In this scenario, it is crucial to have fast filtering on the feed-forward of the gird current, especially if a pure P-controller is used. The poles become well damped when α_f is set above $4\omega_\mathrm{s}$, while better damping is achieved when $\alpha_\mathrm{f} = \alpha_\mathrm{c}$.

Figure 5.11(b) shows the location of the low-frequency poles when using PI-based controller with active damping for the same sweeping of α_f. Observe that in this scenario, all the low-frequency poles are located in the left-hand side of the plane, independently of the wind turbine power set-point P_gen. When the wind turbine is set to 0 pu (blue traces), two pair of complex poles moves towards the left while still being poorly damped. If the turbine operates at full power (red traces), the two pair of complex poles become well damped when increasing α_f to α_c. Note that for small values of α_f, the integrator term of the PI controller and the active damping term G_A have a beneficial effect on the system performance.

5.5 Dependency of system poles with respect to wind turbine parameters

Different wind turbine manufacturers have implemented their own control settings as well as control strategies for operation during a voltage dip. For this reason, the stability of the test system must also be investigated for variation on external parameters which are not related to the control settings of the testing equipment. In the investigated setup, two main parameters have been identified: the bandwidth of the DC-link voltage controller together with the bandwidth of the inner current control of the wind turbine, which governs the power flow between the wind turbine and the grid, and the interface impedance between the tested object and the testing device. In the following, a sensitivity analysis is carried out, focused on the parameters previously mentioned.

5.5.1 Impact of the control loop bandwidths of the wind turbine

In this section, the focus is on the impact of the bandwidth of the DC voltage controller of the tested wind turbine. The main control parameter that governs the power flow between the wind turbine and the grid is the bandwidth of the DC voltage controller $\alpha_\mathrm{d,w}$. Here the wind turbine is set to full power operation.

In Fig. 5.12(a) it is shown the pole movement when the $\alpha_\mathrm{c,w}$ is varied from its nominal value of $5\omega_\mathrm{s}$ to $10\omega_\mathrm{s}$ while maintaining a constant ratio on the bandwidth of DC voltage control $\alpha_\mathrm{d,w} = 0.1\alpha_\mathrm{c,w}$, for the two investigated close-loop PCC voltage controllers. It is clearly shown that the control bandwidth of the test object mainly impacts the characteristic frequency of two high-frequency complex poles, and that the trajectory of the poles is independent of the topology of the PCC voltage control. Moreover, the damping of the poles located in proximity to the real

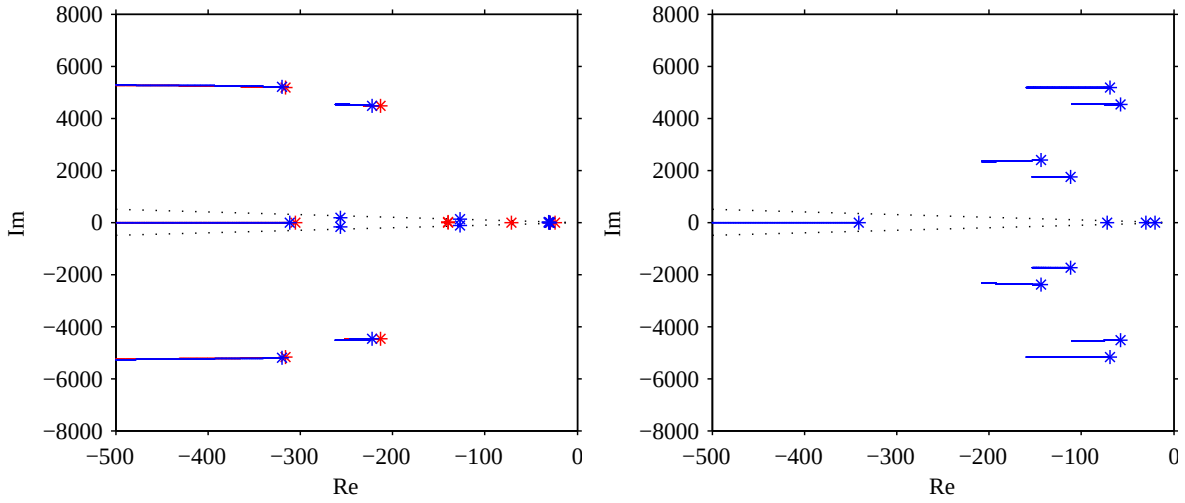

Fig. 5.12 Pole displacement when increasing the bandwidth $\alpha_{c,w}$ from $5\omega_s$ to $10\omega_s$ while maintaining $\alpha_{d,w} = 0.1\alpha_{c,w}$ when using Plot(a): PI (blue) and with P (red) based close-loop controller; and Plot (b) open-loop control in turbine-side VSC of test equipment.

axis is not affected, while two real poles are displaced towards the negative region.

In Fig. 5.12(b) it is shown the pole movement when varying $\alpha_{c,w}$ and $\alpha_{d,w}$ in the same fashion as previously mentioned, when using open-loop control for the test equipment. Observe that in this scenario, only the high-frequency poles are mainly affected when varying the bandwidths on the wind turbine system. Similar to the previous case, one real pole is displaced toward the negative side of the map. Note that, by comparing the location of the high-frequency poles, system is slightly more damped against variation of the wind turbine system when close-loop controller is used.

However, the result given in Fig. 5.12 also suggests that for the selected (nominal) bandwidths of the test system, the location of the high-frequency poles is not considerably affected by the selection of the topology of the PCC voltage controller, meaning that the overall damping of the system is not significantly improved. It is also observable that the order of the system is reduced when open-loop control is selected. However, only the poles that are located within the well-damped region of the map are mainly affected, while the high-frequency poles existing in the system are not removed. Finally, note that the overall stability of the system is maintained for both open-loop and close-loop controllers.

5.5.2 Impact of the interface impedance

As mentioned earlier, the total inductance and resistance between the wind turbine and the test equipment is here represented by an equivalent series branch R_{eq} and L_{eq}. Observe that if the layout of the tested system is unknown, the total impedance between the two controllable objects can be considerable. For this reason, it is of interest to investigate the impact of the interface

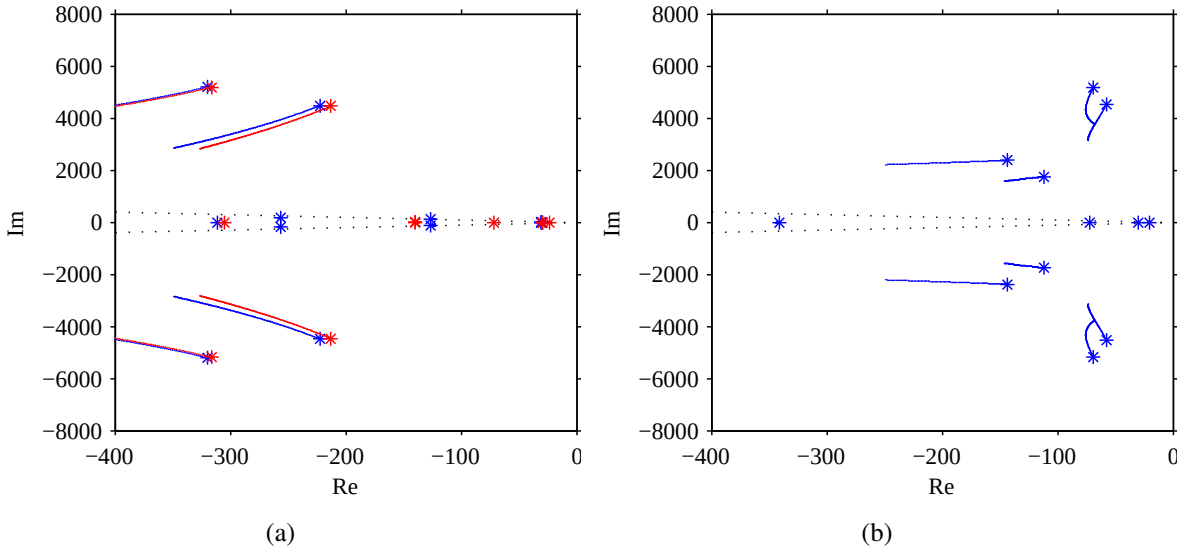

Fig. 5.13 Pole displacement when increasing the interface impedance R_{eq} and L_{eq} from 0.1 pu to 0.25 pu, when using Plot(a): PI (blue) and with P (red) based close-loop controller; and Plot (b) open-loop control in turbine-side VSC of test equipment.

impedance between the wind turbine under test and the testing equipment in the location of the system poles. Observe that under the assumption that the test equipment is in the proximity of the wind turbine, the impact of the connecting cables can be neglected. Thus, only the total impedance of the two transformers TW and $T2$, together with the outer inductive filters $L_{\text{w},2}$ and L_2 and their corresponding internal resistance are considered in this analysis. In the following, the magnitude of R_{eq} and L_{eq} is varied for the case when the PCC voltage is controlled in close-loop (P-based and PI-based controller) and in open-loop. Here, the wind turbine is operated at full power.

Figure 5.13(a) shows the poles displacement of the system when varying the impedance from 0.1 pu to 0.25 pu. Observe that the selection of the close-loop controller (red traces for P-controller and blue traces for PI-controller) has a minor impact on the location of the poles. In this regard, the high-frequency poles are the most affected, becoming more damped as the impedance increases. Note in Fig. 5.13(b) that when open-loop controller is used, two high-frequency complex poles in proximity to the imaginary axis tend to approach the real axis, while the other two affected complex-poles become more damped. Finally, as shown in Fig. 5.13(a) and Fig. 5.13(b), the displacement of the low-frequency well damped poles is negligible.

In practice, increasing the impedance means to create more physical decoupling between the test equipment and the wind turbine system. Instead of using a direct coupling between the two devices, a reasonable impedance level brings the whole test system more stable. However, it is important to keep in mind that high impedance means high voltage drop between the two devices, affecting the resulting voltage at the terminals of the wind turbine when testing for LVRT.

5.6 Conclusion

In this chapter, the impact of the control settings and the system parameters on the input admittance of the wind turbine, as well as on the overall system stability, have been investigated through small-signal stability analysis.

The input admittance of the modelled wind turbine has been computed by using state-space analysis. Among different parameters of the implemented controller, the PLL has a mayor effect in the input admittance of the wind turbine. A negative real-part is seen for a great part of the sub-synchronous range when the bandwidth is set relatively high, meaning that the risk of interaction with another object that can exhibit resonances at these frequencies is increased.

The selection of the bandwidth of the controllers determine the pole position, and thus, has a mayor impact on the stability of the system. When using a P-based controller in the PCC voltage control, the system poles located in the well-damped area become even more damped, as compare with PI-based controller. However, the lack of integrator term does not necessarily benefits the performance of the system. In addition, the stability of the system is compromised if a strong filter is applied when feed-forwarding the outer current in the outer control-loop of the test equipment. In this regard, the PI-based controller is found to be more robust against different bandwidth of the LPF applied to the outer current. Moreover, a fast filtering of the this current is always beneficial for the stability of the system.

The use of PI controller with active damping increases the order of the system. As also discussed in the previous chapter, the addition of the virtual resistor and integrator term gives a better dynamic performance, allowing to remove steady-state error due to inaccurate system modelling. In this analysis it has been found that the size of the virtual resistor (represented by the active damping term G_{A}) can be reduced while maintaining stability. Observe, however, that the ability of the controller in rejecting voltage disturbances can be compromised.

On the other hand, without considering the poles that are located in the well-damped region, the location of the high-frequency poles are not significantly affected by the selection of the PCC voltage controller, meaning that the use of open-loop controller could be equally beneficial for the stability of the system.

External parameters such as controller bandwidth of the tested object, or interface impedance between the tested object and the testing equipment will also impact the position of the poles. However, if these parameters are kept within its nominal range, the stability of the system is maintained, again, independently of the topology of the controller implemented on the testing equipment. Finally, time-domain simulations must be carried out to guarantee the stability of the system in case of large disturbances. Thus, in the following section, a verification of the testing methodology is presented.

Chapter 6

Simulation verification of the proposed testing methodology

6.1 Introduction

In the previous chapters, the overall control strategy for the VSC-based testing equipment and for the wind turbine including the control algorithm for LVRT have been discussed. Hence, a verification of the investigated testing methodology is presented in this section.

First, an evaluation of different ramp rates when varying the PCC voltage with open-loop control is given. Afterwards, the different PCC voltage controllers including open-loop, P-based and PI-based close-loop controllers are compared in terms of effectiveness in controlling the applied voltage. In addition, the simulation results of the complete test when testing for LVRT are analysed, including when testing for unbalanced voltage dips, among other simulated case scenarios.

Moreover, the algorithm for short-circuit impedance emulation and the capability of the testing equipment in representing different grid scenarios is investigated. Finally, the results for frequency scan on the modelled wind turbine are presented. The electrical system has been modelled in the simulation platform PSCAD/EMTDC v4.2 [53].

6.2 Simulation verification

This section is dedicated to the simulation of the test system shown in Fig. 3.11. A schematic of the simulation model, which combines both the derived wind turbine model and the testing equipment model, is shown in Fig. 6.1. The parameters of the testing setup are given in Table 4.1 and Table 4.2, for the test equipment and wind turbine system models, respectively.

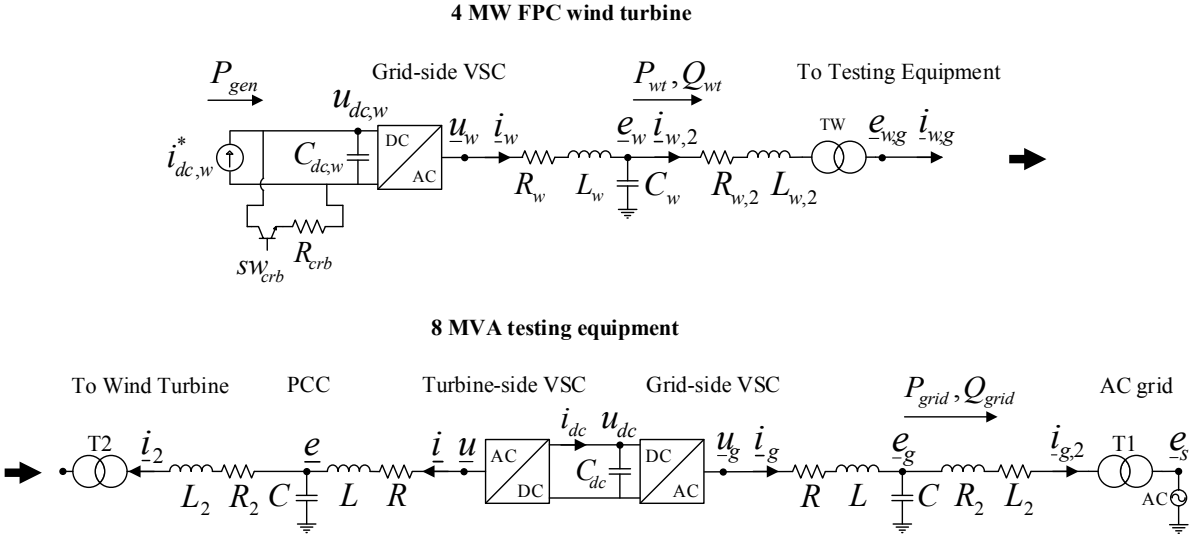

Fig. 6.1 Test system simulation model implemented in PSCAD/EMTDC

6.2.1 Impact of different ramp-rates for open-loop control of the PCC voltage

The open-loop control is relatively simple to implement. Here, the first approach in controlling the PCC voltage is to manually control the modulation index of the turbine-side VSC. However, as shown in Fig. 4.8 and also discussed in Section 5.4.1, when given a step-change directly at the reference voltage the VSC, the system presents an oscillatory response. For this reason, the effect of different ramp-rates applied to the voltage reference will be investigated.

Zero voltage ride through test by VSC has been successfully performed using open-loop control of the VSC in [7], [8] and [67] by setting the modulation index to zero. To cope with zero-voltage ride through, here the controller on the wind turbine needs to be further improved by limiting (to non-zero) the feed-forward of the grid voltage $\hat{\underline{e}}_{\mathrm{w}}^{(\mathrm{dq})}$ in the DC voltage controller, in the PLL and in the LVRT control among other modifications. On the other hand, the LVRT profile of the majority of the selected Grid Codes are defined within a minimum dip between 0 pu to 0.2 pu, as shown in Fig. 3.6. For these reasons, in order to demonstrate the performances of the different controllers when conducting the tests, here the minimum dip has been set to 0.2 pu, similar to the minimum voltage dip given in the Danish Grid Code. In the following, the open-loop control given in Section 4.4.2 has been implemented in the turbine-side VSC of the test equipment. The voltage is reduced from 1 pu to 0.2 pu and maintained for 250 ms.

When the wind turbine is connected (and thus, $\underline{i}_2 \neq 0$), the system is more damped, mainly due to the fact that the majority of the current comes from the wind turbine and not from the resonant path introduced by the filters. Furthermore, in order to mitigate the transient behavior produced by the resonance, a predefined rate limiter on the VSC voltage can be implemented. For this reason, it is of interest to investigate the effect of different ramp-rates applied to the voltage reference $\underline{u}^*$ when testing for voltage dip using open-loop control of the PCC. In the simulated

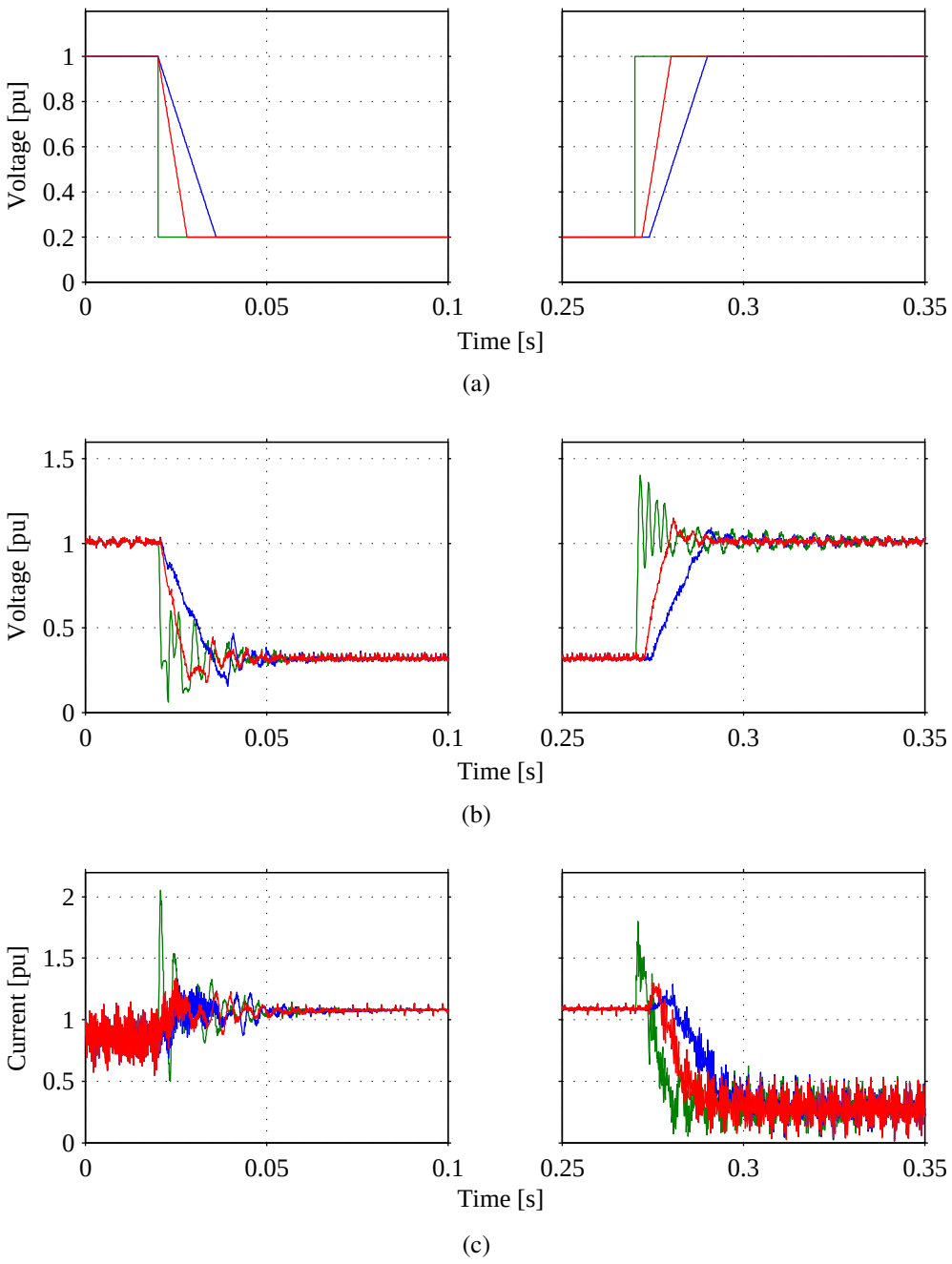

Fig. 6.2 Ramp-rate comparison when using open-loop control of PCC voltage: step function (green), voltage dip with rate of 0.1 pu/ms (red), and voltage dip with 0.05 pu/ms (blue). Plot (a): voltage reference $|\underline{u}^*|$; Plot (b): magnitude of PCC voltage $|\underline{e}|$; Plot (c): magnitude of converter current $|\underline{i}|$.

scenario, the wind turbine is operating at full power production and the LVRT control strategy described in Section 4.7.4 has been implemented.

In Fig. 6.2(a) it is shown the waveforms for different rate of change of the voltage reference $|\underline{u}^*|$ for the turbine-side VSC. Observe that green traces correspond to a step variation, while red and

blue traces correspond to a ramp-rate of 0.1 pu/ms and 0.05 pu/ms, respectively. The resulting PCC voltage magnitude $|\underline{e}|$ is shown in Fig. 6.2(b), and the magnitude of the converter terminal current $|\underline{i}|$ is shown in Fig. 6.2(c).

As shown in Fig. 6.2(b), when using a step function in the reference converter voltage, the PCC voltage reaches a minimum peak of approximately 0.08 pu when the voltage is reduced, while at the recovery peaks at 1.4 pu. The frequency of the oscillations depicted in green traces is 830 Hz, similar to the average resonant frequency of the high-frequency poles given in Fig. 5.13(b). Moreover, according to Table 5.1, the resonant frequency of the LCL filter of the testing equipment (see Table 4.1) is in proximity to 700 [Hz].

The current shown in Fig. 6.2(b) presents a similar transient response, reaching 2 pu when the voltage is reduced with a step function and 1.7 pu when the voltage is increased back to normal condition. This uncontrollable transient response can lead to tripping of both devices due to the action of the protection system. Moreover, over-voltages and over-current can damage the power electronic devices and negatively impact the lifetime of the capacitors and inductors present in the electrical circuit [41], [44]. For this reason, the use of step variation in the reference voltage is not recommended when performing LVRT test.

When using a ramp rate of 0.05 pu/ms (corresponding to the blue traces in Fig. 6.2), the PCC voltage responds in a safer way and no over-currents or over-voltages are induced. Although a smooth response of the system can be obtain, the PCC voltage requires 20 ms to reach steady-state during the voltage dip and during the recovery.

In [68] it is shown in detail the simulation and field test results of a LVRT test for certification process of a DFIG wind turbine using the impedance-based test equipment shown in Fig. 3.9. The resulting rate of change of the voltage at the terminals of the wind turbine is found to be 0.05 pu/ms. Similarly, the rate of change at the LV side of the coupling transformer is 0.03 pu/ms.

As compared with the case scenario given in [68], here the system benefits from a wider controllability of the system voltage when using VSC-based testing equipment. In order to have an acceptable transient dynamic behavior, the maximum ramp-rate is here selected to be 0.1 pu/ms. Observe that for the red traces in Fig. 6.2, the resulting voltage and current magnitudes are within the rated values. Finally, it is of importance to stress that the selected ramp-rate is valid only for this particular setup. Other testing setup, which can include different wind turbine systems or different filtering stage configuration in the test equipment, might require a different limitation on the voltage derivative.

6.2.2 Impact of the topology of the PCC voltage control

As previously discussed, the use of open-loop control can introduce undesired transients in the system, if the use of a suitable ramp-rate is not considered. In addition, if the current of the turbine-side VSC is not controlled in close-loop, these transients can be propagated into the DC-link producing undesired stress in the hardware. For these reasons, as proposed in Section 4.4.2, two type of close-loop PCC voltage controllers have been investigated in this thesis: a P-based controller and a PI-based controller.

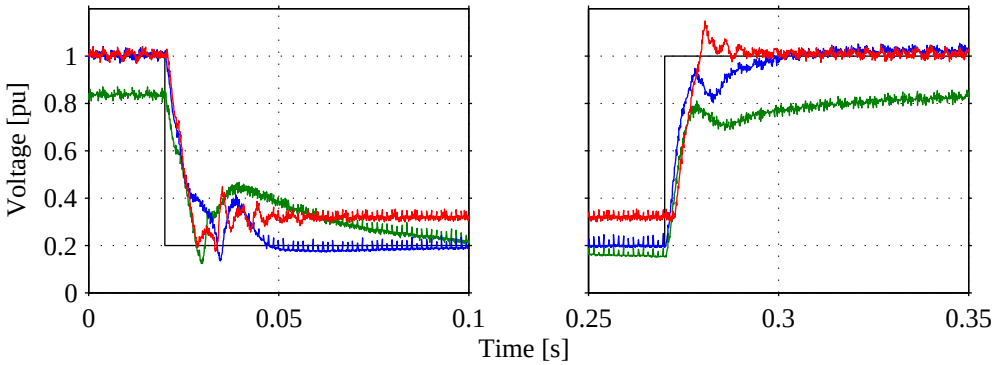

Fig. 6.3 Impact of the topology of the PCC voltage controller. In plots: voltage reference $\underline{e}^*$ (black), response of the PCC voltage $\underline{e}$ when it is controlled by a PI-based controller (blue), P-based controller (green), and open-loop control (red) during voltage drop and voltage recovery.

Here, a comparison of the performance of the open-loop control (without compensation of the voltage drop across the interface inductor) and both close-loop controllers is given. The focus is on the dynamic of the waveform of the PCC voltage $\underline{e}$ and the converter current $\underline{i}$. The voltage reference is a voltage dip with a retained voltage of 0.2 pu maintained for 250 ms. In the case of open-loop control, the reference is reduced with a ramp-rate of 0.1 pu/ms, while for close-loop control, the reference is varied with a step function. Note that with this selection of references, the PCC voltage exhibits the same rate of change regardless of the topology of the voltage controller. Thus, allowing for a fair comparison between the derived control strategies. The wind turbine is equipped with the LVRT control strategy described in Section 4.7.4 and it is operated at full power production with unity power factor.

In Fig. 6.3 is shown the transient response of the PCC voltage when the wind turbine is tested by the testing equipment using the three investigated voltage control topologies (see Section 4.4.2). In particular, a zoom of the transient during the voltage dip and during the recovery is given in the figure. Observe that the PCC voltage is controlled in proximity of 1 pu when open-loop control (red traces) as well as when PI-based close-loop (blue traces) controllers are used. For P-based controller (green traces), the pre-fault voltage is 0.85 pu. As expected, the P-based controller cannot remove the steady-state error present in the voltage. These results confirm what has been found in Section 4.4.2 where the three controllers have been compared when connecting an RL load to the testing equipment (see Fig. 4.8(a)).

At the moment of the dip, the LVRT response of the wind turbine creates a transient when reducing its active power output and immediately injecting reactive current to support the voltage. When open-loop controller is used, the steady-state PCC voltage during the dip is boosted, reaching a maximum of 0.3 pu, due to the reactive current injected by the wind turbine. For the case when PI-controller is used, the PCC voltage is controlled at 0.2 pu within 20 ms after the dip. However both the open-loop and PI controller show a transient at 0.03 s mainly due to the control action of the wind turbine when detecting the voltage dip. Observe at the green traces that when the P-based controller is implemented, the steady-state voltage during the dip is in proximity to 0.2 pu only due to the reactive current support from the wind turbine. If the reactive

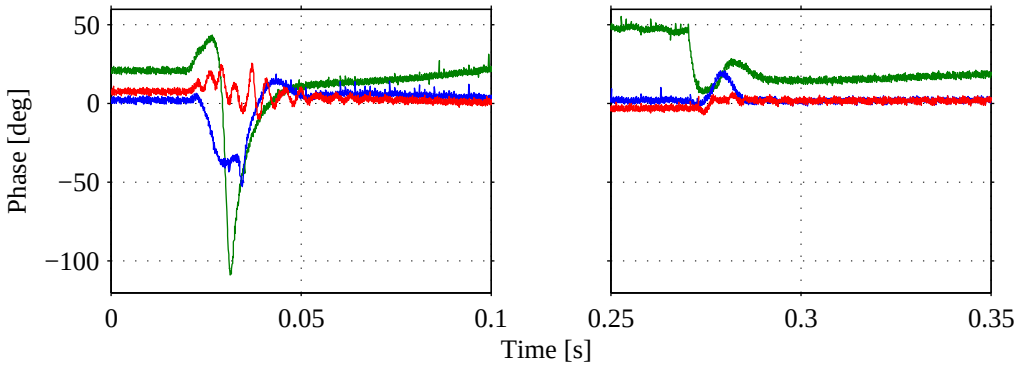

Fig. 6.4 Impact of the topology of the PCC voltage controller on the phase-angle of the voltage $\underline{e}$ when it is controlled by a PI-based controller (blue), P-based controller (green), and open-loop control (red) the voltage drop and the voltage recovery.

current from the generating unit is set to zero, the response would be similar to the one presented in Fig. 4.8(a), showing a considerable deviation from the reference voltage.

The transient response of the PCC voltage when recovering from the dip is also shown in Fig. 6.3. When the voltage reference is back to 1 pu, the PCC voltage presents a small overshoot when open-loop control is used. However, steady-state is achieved at 0.28 s. When the PI-controller is used, the integrator takes approximately 10 ms extra to bring the voltage up to 1 pu. On the other hand, when a P-based controller is used, the post-fault PCC voltage reaches only 0.8 pu, while continues to vary over time.

The response of the phase-angle of the voltage $\underline{e}$ when using the three investigated controllers is shown in Fig. 6.4. Observe in the figure that when the voltage is reduced, the P-controller (green traces) and PI-controller (blue traces) actively vary the angle of the PCC voltage in order to remove the stored energy in the capacitor C connected at the PCC, which is also being affected by the reactive current injected by the wind turbine. Observe that, since the P-controller lacks of an integrator and active damping term, the angle reaches a minimum of -110 degrees when reducing the voltage, as shown with green traces in Fig. 6.4. When using PI-based controller, the angle of the voltage reaches -50 degrees. This transient is also affected by the fact that the wind turbine is rapidly varying its active and reactive current output as soon as the voltage dip is detected at its terminals. Observe that when open-loop is implemented (red traces), the angle oscillates with an amplitude of 15 degrees and a mean value of 5 degrees approximately. All controllers seems to damp the phase-angle deviation at $t = 0.05$ s.

The transients on the phase-angle during the recovery of the voltage is also shown in Fig. 6.4. The open-loop control seems to have the best performance in maintaining the phase angle in proximity to 0 degrees. A small variation is seen only due to the power flow across the inductive filter L of the test equipment. The PI-based controller manages to set the angle at 0 degrees. However, a small deviation of 15 degrees is experienced at $t = 0.275$ s. The P-based controller seems to have a poor performance in controlling the phase of the applied voltage. In this case, the angle is varied 30 degrees when the recovering of the PCC voltage occurs.

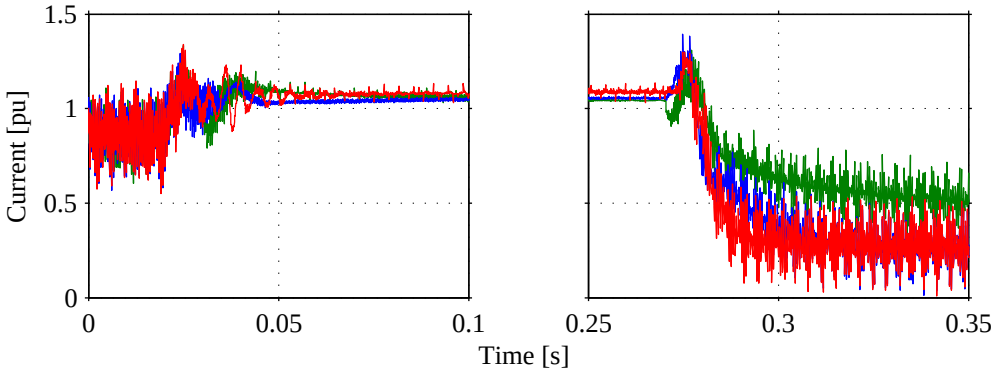

Fig. 6.5 Response of the turbine-side VSC current $|\underline{i}|$ when it is controlled by a PI-based controller (blue), P-based controller (green), and open-loop control (red) during voltage drop and voltage recovery.

The response of the current $\underline{i}$ is shown in Fig. 6.5. The pre-fault current is controlled in 0.9 pu (corresponding to 4 MW) by the wind turbine current controller. When the voltage dip occurs at 0.02 s, before the LVRT control strategy comes into place, the DC voltage controller will immediately maximize the current output in order to deliver the produced power. For this reason, the current peaks at $t = 0.025$ s. Subsequently, the LVRT control reacts by injecting reactive current into the system at 0.03 s. The fast variation of the voltage at the filter capacitor C also contributes to the transient seen in the current, especially in the case of open-loop control, where nor the current $\underline{i}$ or the voltage $\underline{e}$ are controlled. In this case, the current reaches a maximum value of 1.3 pu, as shown in red traces in Fig. 6.5. The current transient is reduced to 1.25 pu when a PI-based PCC voltage controller is used (blue traces). When the P-controller is implemented, the current reaches a peak value of 1.2 pu (green traces). Moreover, a difference of 0.05 pu between PI-based and open-loop controller seems not be significant; however, an oscillation is seen at 0.04 s when the open-loop control is used, as compared with a small variation when PI-bases controller is implemented.

For the recovery of the voltage shown in Fig. 6.5, the resulting current waveform for the three implemented controllers are similar, meaning that the selection of the PCC voltage controller has no mayor impact in the current $|\underline{i}|$ when recovering from the voltage dip. Here, the wind turbine is not producing active power while it is reducing the reactive current as the retained voltage increases. The maximum peak during the recovery is 1.4 pu for the PI-based voltage controller, while for the P-based and open-loop voltage control topologies, the current peaks at 1.3 pu. Note that this current is plotted using the base power of the wind turbine (4.5 MVA), meaning that 1.4 pu is below the current rating of the testing equipment (8 MVA).

It is of interest to observe the response of the DC voltage u_{dc} of the test equipment when varying the topology of the PCC voltage controller in the turbine-side VSC. The waveform of the DC-link voltage is shown in Fig. 6.6. When applying a voltage dip, the active power transferred from the wind turbine to the test equipment is drastically reduced. With reference to (4.54), during the first 20 ms of the voltage dip, the input power P_{wt} is lower than the output power P_{grid}. The unbalance between these two powers affects the DC voltage of the test equipment, as shown in Fig. 6.6 at $t = 0.03$ s. The maximum voltage drop in the DC-link is achieved when the PCC

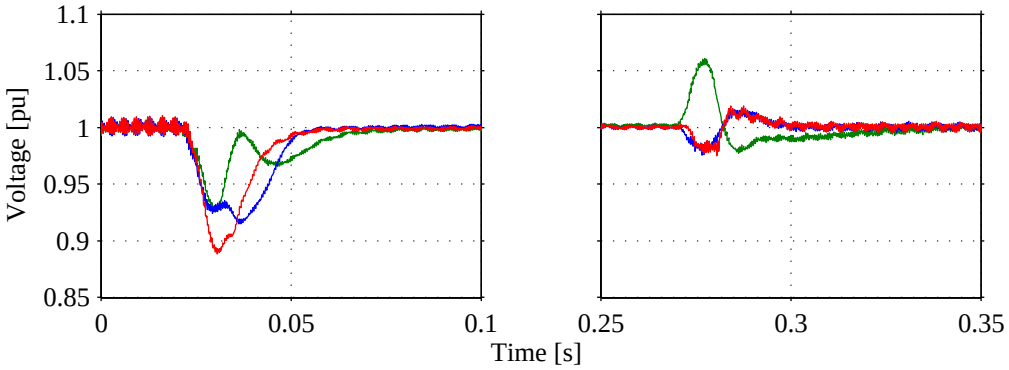

Fig. 6.6 Response of the response of the DC voltage u_{dc} of the test equipment when the PCC voltage it is controlled by a PI-based controller (blue), P-based controller (green), and open-loop control (red) during voltage drop and voltage recovery.

voltage is controlled in open-loop (red traces), while the minimum deviation occurs when the P-based controller is used (green).

Moreover, according to Section 4.7.4, the wind turbine is not producing active power during the recovery of the PCC voltage at 0.28 s. Hence, the transients shown in Fig. 6.6 for open-loop and PI-based controller are mainly due to the interaction between the DC capacitor of the test equipment and the energy delivered into the AC-link when increasing rapidly the applied voltage. Observe that when the P-based controller is used, the DC voltage experiences a rise up to 1.06 pu. A small amount of power being injected into the DC-link at the moment of the recovery can be explained by phase angle variation seen in green traces in Fig. 6.4. Observe that the dynamic performance of the DC-link control loop of the testing equipment can be improved if a more aggressive control strategy is implemented. As compared with the P-based controller derived in Section 4.5.3, a PI-based control with active damping can be derived for the direct voltage control-loop, as given Section 4.4.2.

From the previous simulation results it is found that the response of the PCC voltage is acceptable when the open-loop control and PI-based control with active damping are implemented. In order to avoid an oscillatory response in both current and voltage at the PCC, an acceptable rate of change of 0.1 pu/ms in the voltage reference is found to be sufficient to perform the LVRT test, when open-loop control is used. In this scenario, the transients in the voltage and current at the PCC are somewhat damped. Similar performance can be achieved if close-loop control is implemented in the turbine-side of the test equipment. In the following, the PI-based PCC voltage controller has been selected for further investigation, while the benefits together with the simplicity of the open-loop control is later discussed in this chapter.

6.3 Close-loop control on the PCC voltage

6.3.1 LVRT test

In this section, as compared to the previous section, the complete voltage dip event is analysed in detail. The focus will be on the controllability of the PCC voltage, on the response of the wind turbine system when detecting a voltage dip, and on the impact of the test on the DC-link voltage of the test equipment and on the AC grid where the testing device is interconnected. For this simulation, the PI-based close-loop controller given in (4.39) has been implemented in the testing equipment. The PCC voltage is first controlled at 1 pu when a step variation is applied on its reference. A retained voltage of 0.2 pu is maintained for 250 ms. In the following, the electrical quantities of both the testing equipment and the wind turbine are analysed in detail.

The three-phase terminal voltage of the wind turbine filter $\underline{u}_{\mathrm{w}}$ is shown in Fig. 6.7(a). During the voltage dip, the wind turbine output current $\underline{i}_{\mathrm{w}}$ depicted in Fig. 6.7(b) is maintained in 1 pu. Observe in Fig. 6.7(c) that the active power output is reduced to 0 pu in order to give room to the reactive power to be injected in the grid. The excess of produced power boosts the DC-link voltage immediately after the dip, as shown in Fig. 6.8(a). However, the DC crowbar reacts by redirecting the power into the braking resistor. By this means, the DC-link voltage is maintained at a safe value.

Moreover, as depicted in Fig. 6.8(b), a maximum of 1 pu of reactive current is injected during the voltage dip, boosting the local wind turbine voltage $\underline{u}_{\mathrm{w}}$ up to 0.28 pu. Hence, the maximum reactive power during the fault is 0.28 pu. At the moment when the voltage is recovering from the fault, the LVRT control strategy in the wind turbine maintains the reactive current, giving a fast rising of the reactive power at 0.36 s. The reactive current is reduce once the voltage has reached 1 pu at 0.375 s. Furthermore, the AC voltage is monitored for additional 500 ms, as enforced by the German and Danish Grid Codes. The wind turbine resumes active power production 100 ms after the recovery of the voltage.

Moving the focus on the testing equipment, the reference and actual PCC voltage are shown in Fig. 6.9(a). The transient in the PCC voltage and wind turbine filter voltage is due to the sudden exchange between active and reactive power; however, the test equipment manages to control the voltage back to its reference value of 0.2 pu. Moreover, the recovery of the voltage is controlled in a smooth way. The reference and estimated d and q voltage components are depicted in Fig. 6.9(b) and Fig. 6.9(c), respectively. Note that the controller in the turbine-side VSC of the test equipment lacks of a PLL, meaning that it generates its own reference frequency ω_{s}^{*} and thus its self generated dq-transformation angle θ. As shown in the plots, each voltage component is tracked and controlled at their reference values. Observe in Fig. 6.9 at 0.12 s that when wind turbine is varying its current output, a transient is seen in both components of the voltage. During this short moment, the phase-angle of the PCC voltage reaches 50 degrees of phase-shift, as shown in Fig. 6.4.

The reference and estimated d and q axis components of the current vector $\underline{i}^{(\mathrm{dq})}$ are depicted in Fig. 6.10(b) and Fig. 6.10(c), respectively. The actual tree-phase VSC current $\underline{i}$ is shown in Fig. 6.10(a). During normal operation, the effect of the switching of the VSC and the reactive

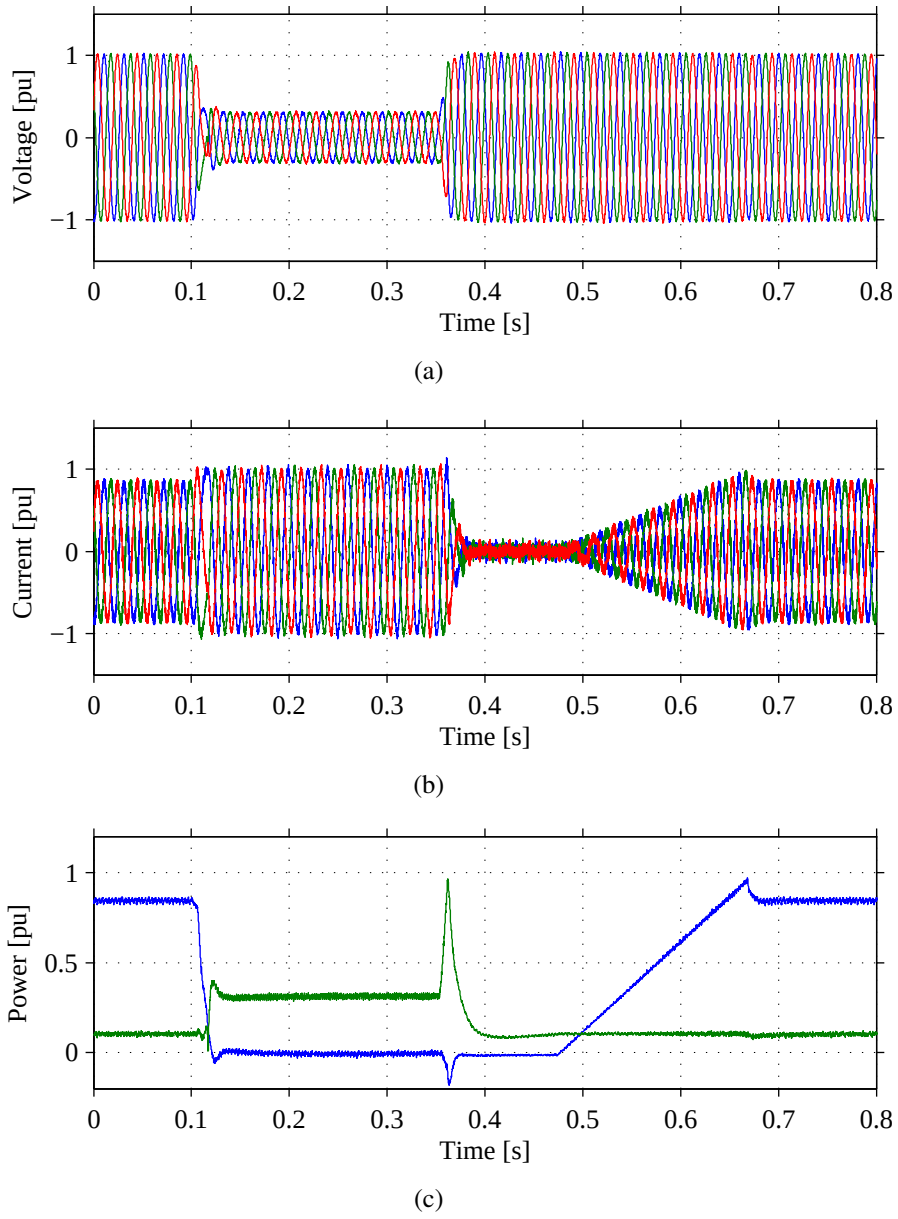

Fig. 6.7 Wind turbine response under a voltage dip. Plot (a): three-phase voltage $\underline{e}_{\mathrm{w}}$; Plot (b): three-phase current $\underline{i}_{\mathrm{w}}$; Plot (c): active power P_{wt} (blue) and reactive power Q_{wt} (green) output.

current introduced by the capacitor filter banks both in the wind turbine and test equipment increases the actual peak value of the three-phase current slightly above 1 pu (see Table 4.2 for wind turbine base values). The current at the test equipment reaches a peak value of 1.25 pu in the first transient and 1.4 pu at the recovery of the voltage. This current peak is the result of the response of the current control on the wind turbine when a fast voltage variations occurs at its terminals. However, the rating of the test equipment, given in Table 4.1, is two times larger than the rating of the wind turbine. For this reason, a 1.4 pu transient current is not harmful for the test equipment. Observe that if the wind turbine is large enough, the transient experienced in the current would be in proximity to the current rating of the testing equipment. In this case, special

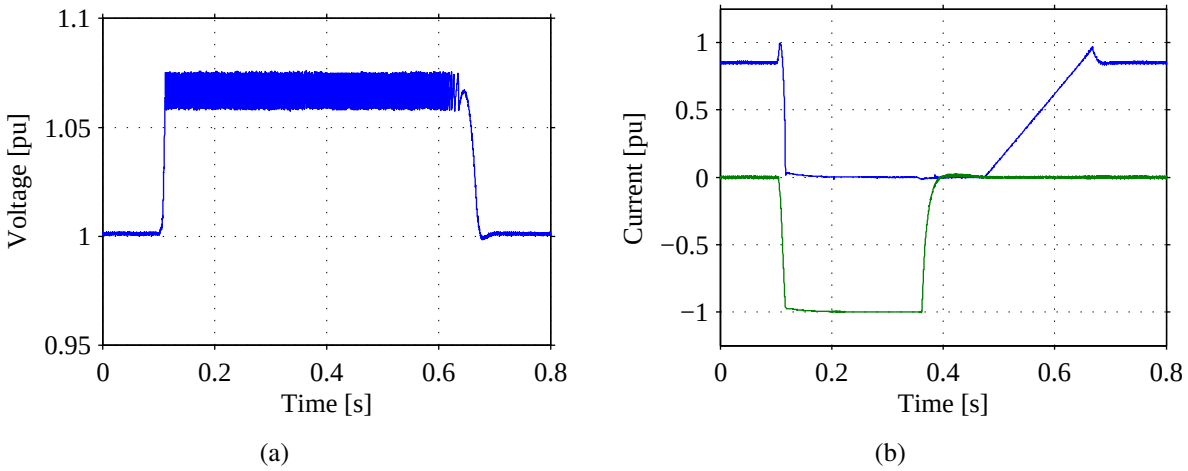

(a) (b)

Fig. 6.8 Wind turbine LVRT control under a voltage dip. Plot (a): DC voltage $\underline{u}_{\mathrm{dc,w}}$; Plot (b): active current $\hat{i}_{\mathrm{w_d}}$ (blue) and reactive current $\hat{i}_{\mathrm{w_q}}$ (green).

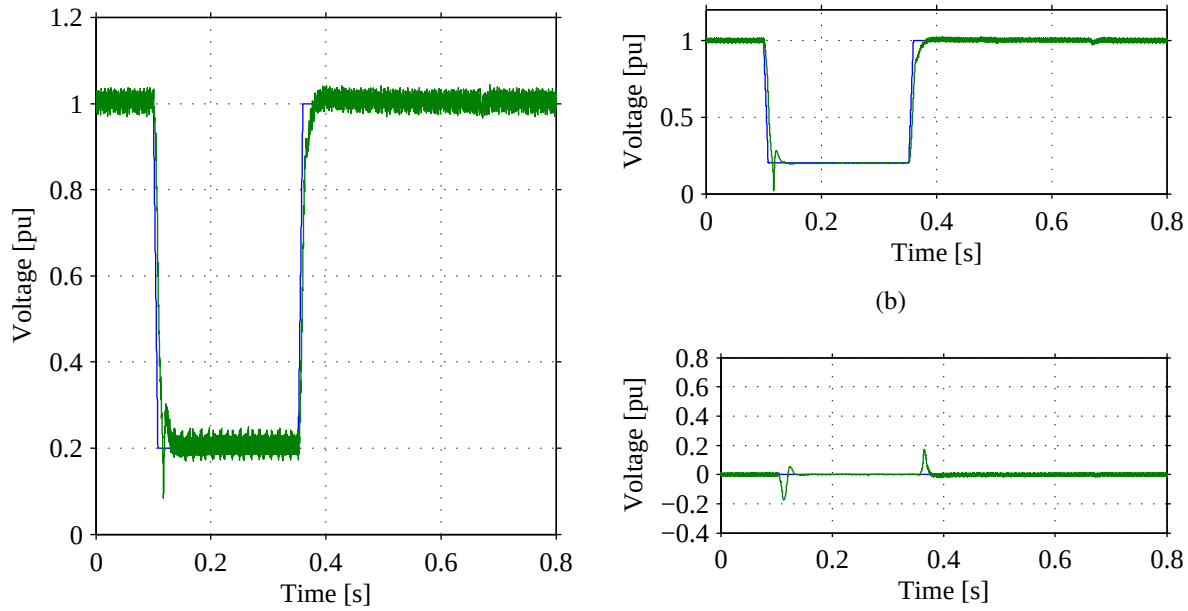

(a) (b) (c)

Fig. 6.9 PCC voltage control. Plot (a): reference voltage $|\underline{e}^*|$ (blue) actual magnitude of the PCC voltage $|\underline{e}|$ (green); Plot (b): d-axis PCC reference voltage e_{d}^* (blue) and estimated voltage $\hat{e}_{\mathrm{d}}$ (green); Plot (c) q-axis PCC reference voltage e_{q}^* (blue) and estimated voltage $\hat{e}_{\mathrm{q}}$ (green).

consideration bust be taken on the selection of a minimum dip and on the selection of a suitable ramp-rate in the voltage reference, even if the voltage is controlled in close-loop.

Finally, it is of interest to analyse the response of the grid-VSC of the test equipment. Here, the focus is on the DC voltage control, and the impact of the testing towards the AC grid. In Fig. 6.11(a) is shown the DC-link voltage u_{dc}. From the figure, it is possible to observe that the DC voltage deviates from its reference for a short period of time. From Fig. 6.11(b) is shown

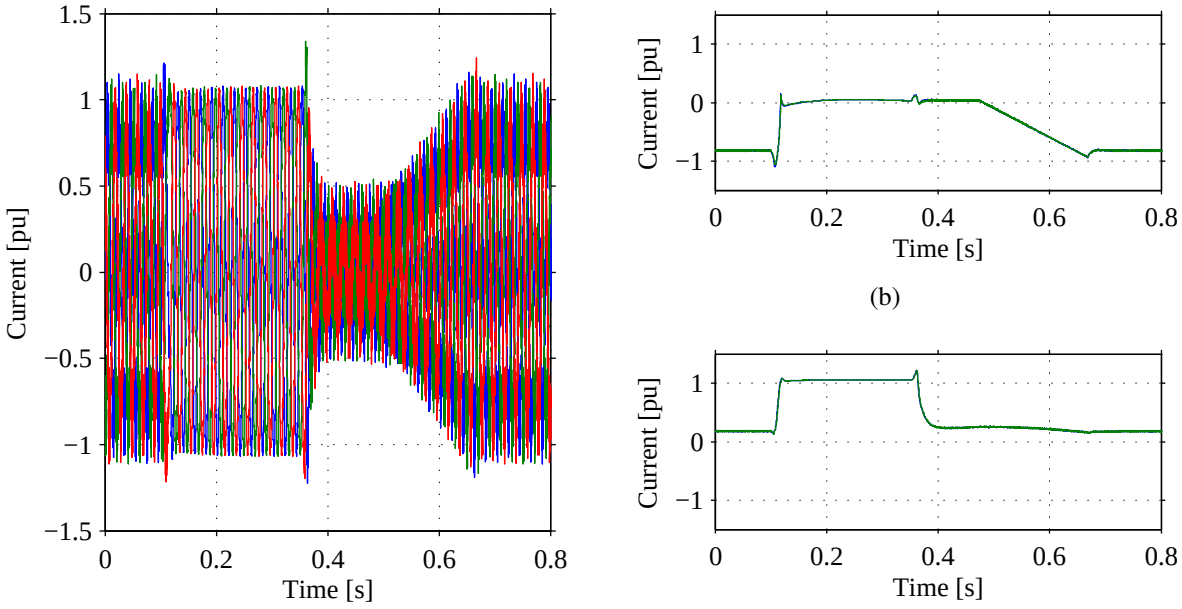

Fig. 6.10 Current control in test equipment. Plot (a): actual three-phase current $\underline{i}$; Plot (b): d-axis current reference i_{d}^{*} (blue) and estimated current component $\hat{i}_{\mathrm{d}}$ (green); Plot (c): q-axis current reference i_{q}^{*} (blue) and estimated current component $\hat{i}_{\mathrm{q}}$ (green).

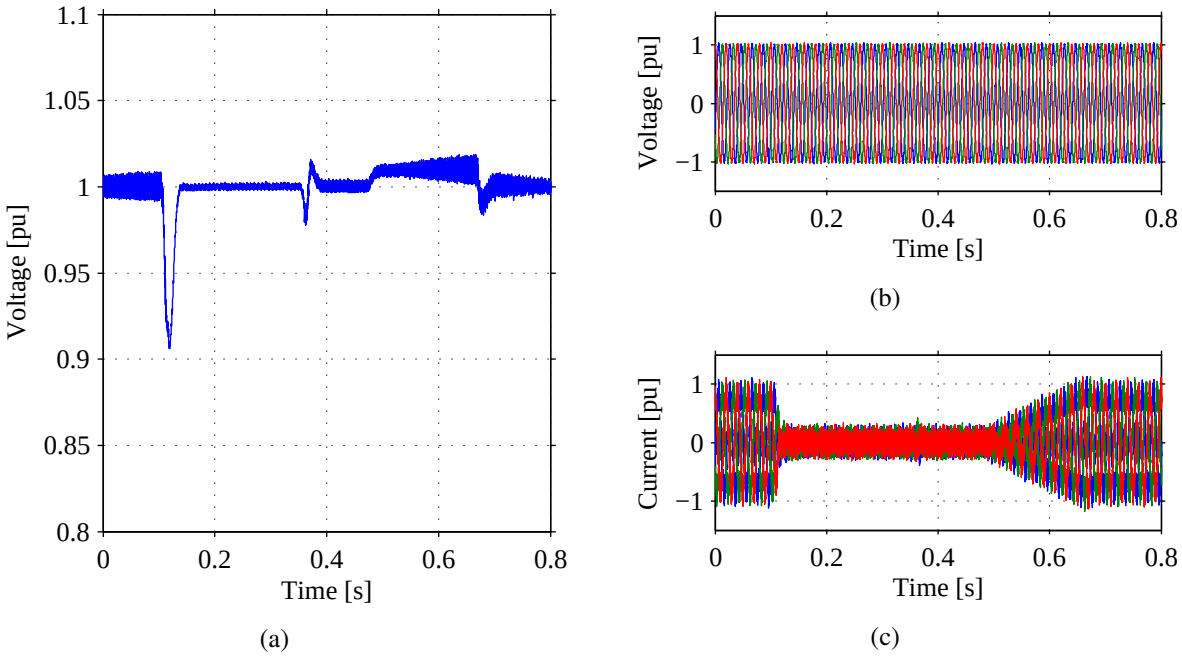

Fig. 6.11 Grid-side VSC in test equipment. Plot (a): DC link voltage U_{dc}; Plot (b): actual three-phase grid filter voltage $\underline{e}_{\mathrm{g}}$; Plot (c): actual three-phase grid-VSC terminal current $\underline{i}_{\mathrm{g}}$.

the voltage at the grid connection point of the testing equipment $\underline{e}_{\mathrm{g}}$. As seen from the figure, the voltage is unaffected by the performance of the test. Although the current is varied according

to the active power variation of the wind turbine, as shown in Fig. 6.11(c), the current does not present any transients, and is controlled by the grid-side VSC during the complete event.

Given the power rating of the tested wind turbine, the PCC voltage is controlled in a stiff manner, meaning that the reactive power injected by the wind turbine does not significantly affect the set-point of the PCC voltage. Hence, an interesting alternative could be to include the dynamics of a virtual impedance when testing for LVRT, thus having the ability to emulate the short-circuit impedance of a grid. This concept will be explored in the following section.

6.3.2 Grid emulation algorithm in close-loop

A control feature to emulate the impact of the grid short-circuit power during LVRT operations has been implemented. Under the assumption that the test equipment is operated within its voltage limits, both active and reactive power production of the test object will now impact the set-point of the system voltage $\underline{e}$, if the grid emulation algorithm is enabled.

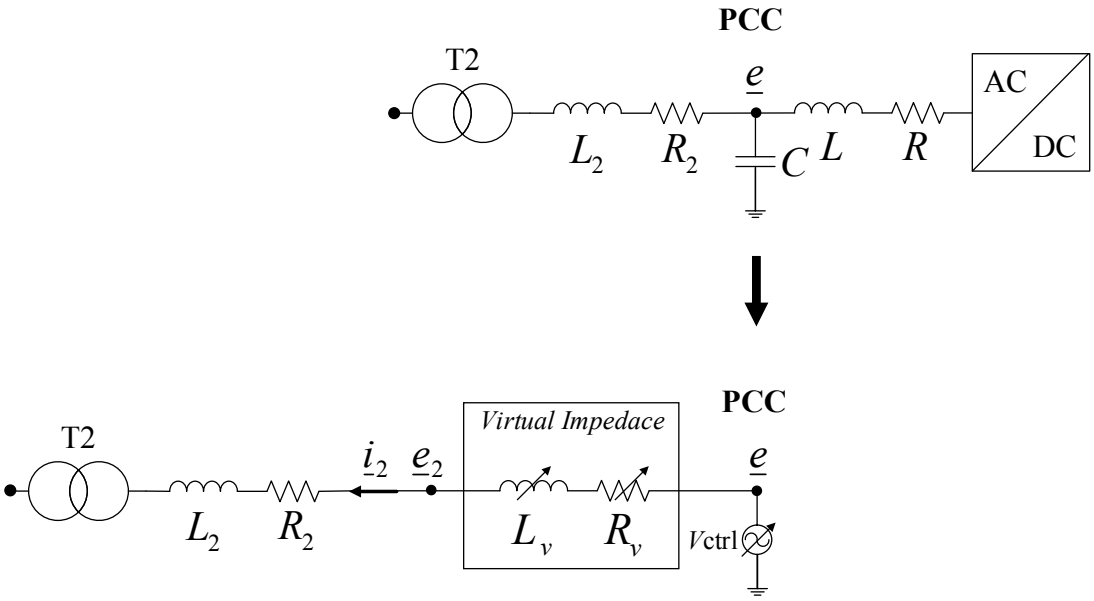

Fig. 6.12 Equivalent representation of the grid-side VSC of the test equipment for grid impedance emulation.

In Fig. 6.12 it is shown an equivalent representation of the test equipment when used to emulate the short-circuit power of the grid at the connection point. The upper part of the figure corresponds to the actual circuit, while the lower part corresponds to the effect of the regulation of the grid voltage (V_{ctrl}) with the virtual impedance in cascade. The dynamic of the current $\underline{i}_2$ in the dq-frame can be described by the expression:

$$\underline{e}^{(\text{dq})} - \underline{e}_2^{(\text{dq})} = L_{\text{v}} \frac{d\underline{i}_2^{(\text{dq})}}{dt} + \underline{i}_2^{(\text{dq})}(R_{\text{v}} + j\omega_{\text{s}} L_{\text{v}}) \tag{6.1}$$

with R_{v} and L_{v} as the inductive and resistive part, respectively, of the virtual grid impedance shown in Fig. 6.12. The voltage $\underline{e}^{(\mathrm{dq})}$ can be a selected as a LVRT profile controlled in a stiff way, as shown in the previous section. Observe, however, that this representation is only valid as long as the rating of the wind turbine is lower than the testing equipment. Meaning that if the rating of both systems is similar, the representation of the testing equipment by the infinitely strong controllable voltage source V_{ctrl} might not hold true. The voltage $\underline{e}_2^{(\mathrm{dq})}$ is, therefore, the PCC voltage evaluated after the voltage drop over the virtual impedance.

The inductor L_{v} in Fig. 6.12 contributes as a smoothing factor on the dynamics of the current $\underline{i}_2$. Observe that L_{v} also impacts the amount of voltage drop across the virtual impedance in (6.1), especially if the derivative term is included when calculating the reference voltage $\underline{e}_2^*$ for the PCC voltage controller. When implementing (6.1) in a digital controller, the discrete calculation of the derivative term when sampling the current $\hat{\underline{i}}_2$ can be very sensitive to noise, especially if the sampling time is relatively small [48], [69].

In order to investigate impact of the derivative term on the dynamics of the voltage $\underline{e}_2^{(\mathrm{dq})}$ in (6.1), the ideal system shown in Fig. 6.12 has been simulated, with the exception of the inductor L_2, R_2 and the transformer $T2$. In this study, the reference voltage vector $\underline{e}^{(\mathrm{dq})^*}$ of the test equipment is sent as a reference for the voltage source V_{ctrl}. The voltage is here varied in order to represent a stiff grid voltage. In addition, an RL load has been connected where the voltage $\underline{e}_2$ is measured, in order to set the current denoted as $\underline{i}_2$ at nominal value. Three different case scenarios have been simulated in continuous time domain, described in the following.

First, an actual impedance is placed where R_{v} and L_{v} are depicted, in order to interconnect the RL load and the AC voltage source. A voltage dip test has been performed to the load: the voltage $\underline{e}^{(\mathrm{dq})}$ at the AC source is varied from 1 pu to 0.5 pu for 200 ms. The phase a of the resulting three-phase load voltage $\underline{e}$, which includes the dynamics produced by the actual impedance, is plotted in blue traces in Fig. 6.13.

As a second test scenario, the actual impedance is removed and a virtual impedance R_{v} and L_{v} is considered when calculating the voltage $\underline{e}^{(\mathrm{dq})^*}$ according to the following expression:

$$\underline{e}_2^{(\mathrm{dq})^*} = \underline{e}^{(\mathrm{dq})^*} - \frac{d\underline{i}_2^{(\mathrm{dq})}}{dt} L_{\mathrm{v}} - \underline{i}_2^{(\mathrm{dq})}(R_{\mathrm{v}} + j\omega_{\mathrm{s}} L_{\mathrm{v}}) \tag{6.2}$$

Note that (6.2) is (6.1) rearranged in order to obtain the reference voltage $\underline{e}_2^{(\mathrm{dq})^*}$, which includes the complete dynamics of the voltage drop across the virtual impedance. Here, the same voltage dip has been applied to the load. The resulting load voltage $\underline{e}$ is plotted in red traces in Fig. 6.13.

Third and final case scenario. Here the dynamics of the voltage drop across the virtual impedance is removed from the reference voltage $\underline{e}_2^{(\mathrm{dq})^*}$; thus, only a steady-state voltage drop is emulated as

$$\underline{e}_2^{(\mathrm{dq})^*} = \underline{e}^{(\mathrm{dq})^*} - \underline{i}_2^{(\mathrm{dq})}(R_{\mathrm{v}} + j\omega_{\mathrm{s}} L_{\mathrm{v}}) \tag{6.3}$$

The waveform of the load voltage $\underline{e}_2$ for the third scenario is shown in green traces in Fig. 6.13.

As expected, it is possible to observe from Fig. 6.13(a) that for steady-state conditions, there is no

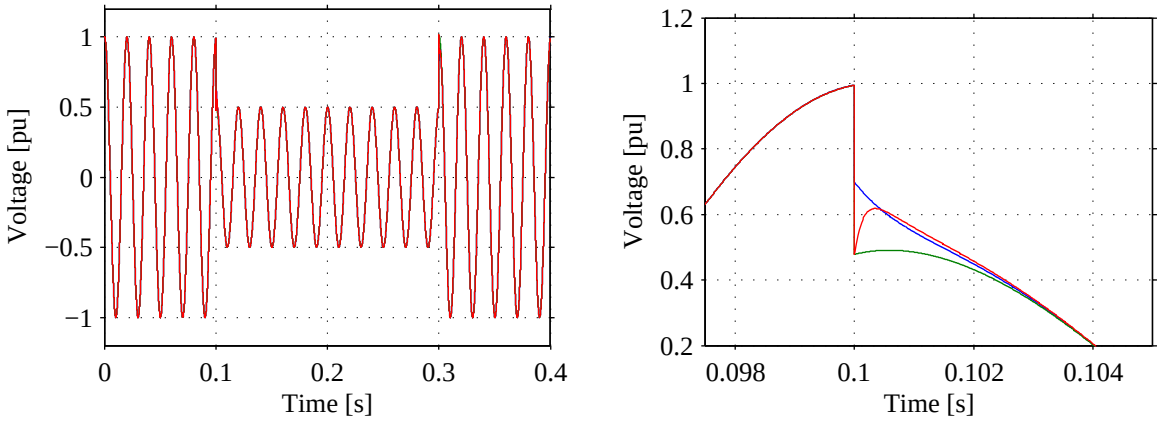

Fig. 6.13 Response of the load voltage $\underline{e}_2$ when a voltage dip is applied. In plots: load voltage when interconnecting an actual grid impedance (blue); when using dynamic voltage drop (red) and when using steady-state voltage drop (green) of an equivalent virtual impedance. Plot (a): Resulting voltage waveform of phase a during the complete event; Plot (b): Zoom of phase a during the voltage dip.

difference in the voltage waveform when connecting the load through an actual grid impedance or when emulating the voltage drop both dynamically or in steady-state. During the transient, however, a mismatch between the emulated and actual voltages is clearly visible, as shown in Fig. 6.13(b). Note that when the derivative term of the voltage drop in L_v is included in (6.2) (red traces), the effect of the short-circuit impedance is emulated accurately within less than 0.5 ms. On the other hand, when the derivative term is not included (green traces), thus, using steady-state voltage drop as in (6.3), the emulated voltage drop takes 2 ms to recreate the effect of an actual impedance.

It is important to note that when a stiff regulation of the PCC voltage is applied i.e.: in Fig. 6.9(a), the voltage takes 12 ms approximately to reach steady-state during the dip. This means that if the derivative term is included when calculating the reference PCC voltage, the voltage controller will not be able to reproduce the dynamics that are below the time constant of the control-loop. For this reason, and in order to enhance the stability of the system, the derivative term (6.4) is chosen to be neglected. To emulate the effect of the grid impedance only by using steady-state voltage drop, the calculated voltage reference in Laplace form can be formulated as:

$$\underline{e}_2^{(\mathrm{dq})*} = \underline{e}^{(\mathrm{dq})*} - \left(\frac{\alpha_\mathrm{fil}}{s+\alpha_\mathrm{fil}}\right)\hat{\underline{i}}_2^{(\mathrm{dq})}(R_\mathrm{v} + j\omega_\mathrm{s}L_\mathrm{v}) \tag{6.4}$$

with $\alpha_\mathrm{f} = \alpha_\mathrm{e}$ (equal to $0.8\omega_\mathrm{s}$) as the bandwidth of a LPF used to remove high-frequency content in the estimated outer current $\hat{\underline{i}}_2^{(\mathrm{dq})}$. Given that the measured current $\hat{\underline{i}}_{2,\mathrm{f}}$ is used to perform a control action on the PCC voltage controller, the bandwidth α_f in (6.4) has to be selected at least one decade below the bandwidth of the sampling frequency while keeping in mind that the dynamics of the emulated voltage drop in the virtual impedance is here constrained by the bandwidth of the voltage controller. Finally, the discrete implementation of the short-circuit

impedance emulation algorithm is written as

$$\underline{e}_2^{(\mathrm{dq})^*}(k) = \underline{e}^{(\mathrm{dq})^*}(k) - \hat{\underline{i}}_{2,\mathrm{f}}^{(\mathrm{dq})}(k)(R_\mathrm{v} + j\omega_\mathrm{s} L_\mathrm{v}) \tag{6.5}$$

with $\hat{\underline{i}}_{2,\mathrm{f}}$ calculated in (4.31).

In the following, a virtual impedance of 0.1 pu corresponding a short-circuit power of 10 pu (45 MVA) is simulated. Here, the focus will be on the dependency of the controlled PCC voltage

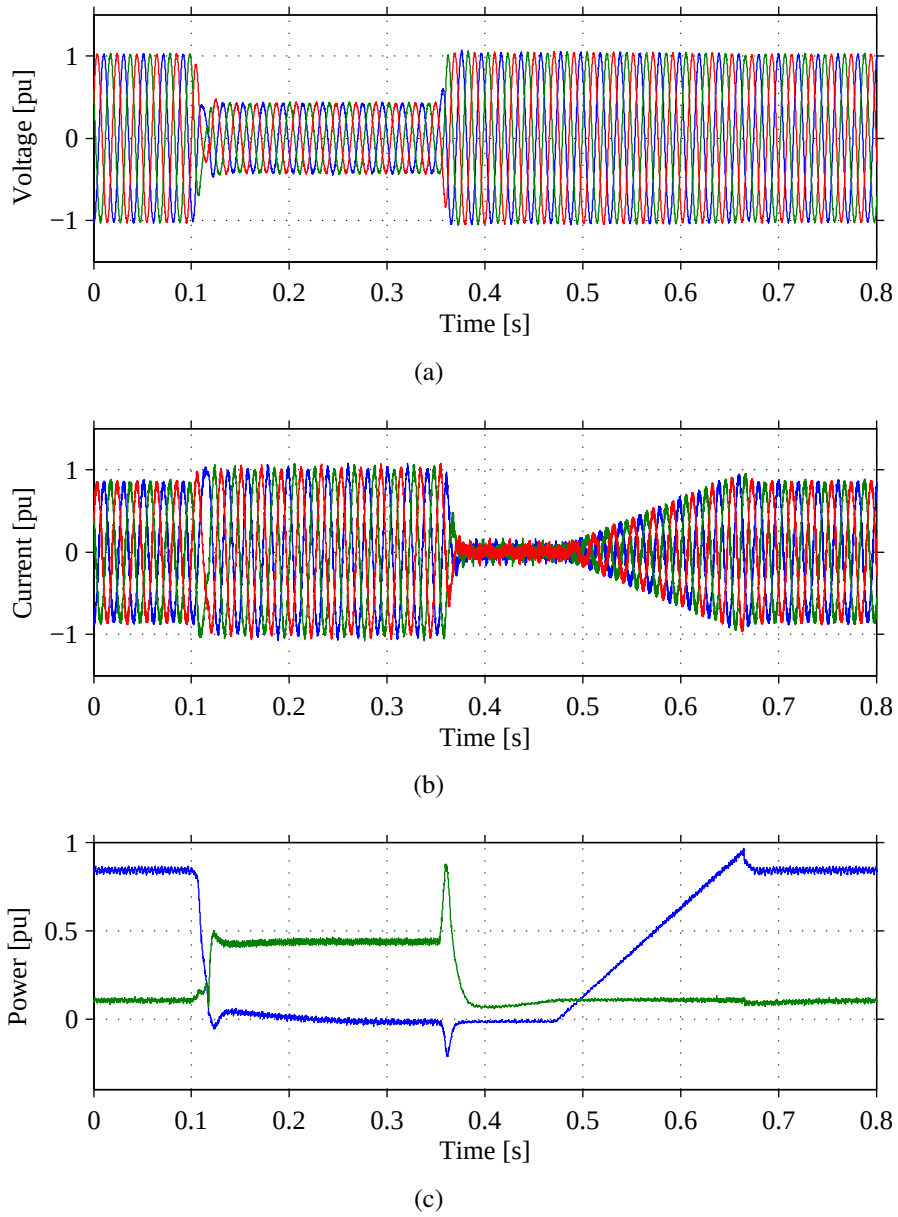

Fig. 6.14 Wind turbine response under a voltage dip with emulated short-circuit power of 10 pu. Plot (a): three-phase voltage $\underline{e}_\mathrm{w}$; Plot (b): three-phase current $\underline{i}_\mathrm{w}$; Plot (c): active power P_wt (blue) and reactive power Q_wt (green) output.

(using PI-based close-loop controller) with respect to the reactive power exchanged between the wind turbine and the test equipment.

The pre-fault voltage is 1 pu, and the retained voltage reference is 0.2 pu for 250 ms. The resulting three-phase wind turbine voltage and output current is shown in Fig. 6.14(a) and Fig. 6.14(b), respectively. When the short-circuit impedance emulation is enabled, the active and reactive power output from the wind turbine shown in Fig. 6.14(c), affect the set-point of the voltage reference in the test equipment, according to the discrete voltage reference calculation given in (6.5). In Fig. 6.14(a) it is possible to see that the wind turbine voltage $\underline{e}_{\mathrm{w}}$ reaches a peak of 0.45 pu during the dip, as compared with 0.28 pu in Fig. 6.7(a), when a stiff regulation of the PCC is applied. Similarly to the previous case, the wind turbine is injecting 1 pu of reactive current during the dip, thus, the maximum injected reactive power is 0.45 pu, as depicted in Fig. 6.14(c).

The resulting PCC voltage is boosted up to 0.33 pu during the dip, as shown in Fig. 6.15(a), due to the action of the wind turbine. Observe that there is a difference of 0.13 pu between the actual PCC voltage and the LVRT profile. This is due to the effect of the static voltage drop across the virtual impedance $R_{\mathrm{v}} + j\omega_{\mathrm{s}}L_{\mathrm{v}}$ when calculating the reference signal $\underline{e}_2^{(\mathrm{dq})^*}$ for the voltage controller, according to (6.5). The d and q component of the current $\hat{\underline{i}}_2$ are plotted in Fig. 6.15(b) and Fig. 6.15(c), respectively. Observe that for both plots, the non-filtered and filtered currents components are shown in blue and green traces, respectively. According to (6.5), the filtered current $\hat{\underline{i}}_{2,\mathrm{f}}^{(\mathrm{dq})}$ is used to modify the voltage reference $\underline{e}^{(\mathrm{dq})^*}$. Moreover, the pre-fault and post-fault PCC voltage is also increased due to the reactive power injected by the wind turbine and test

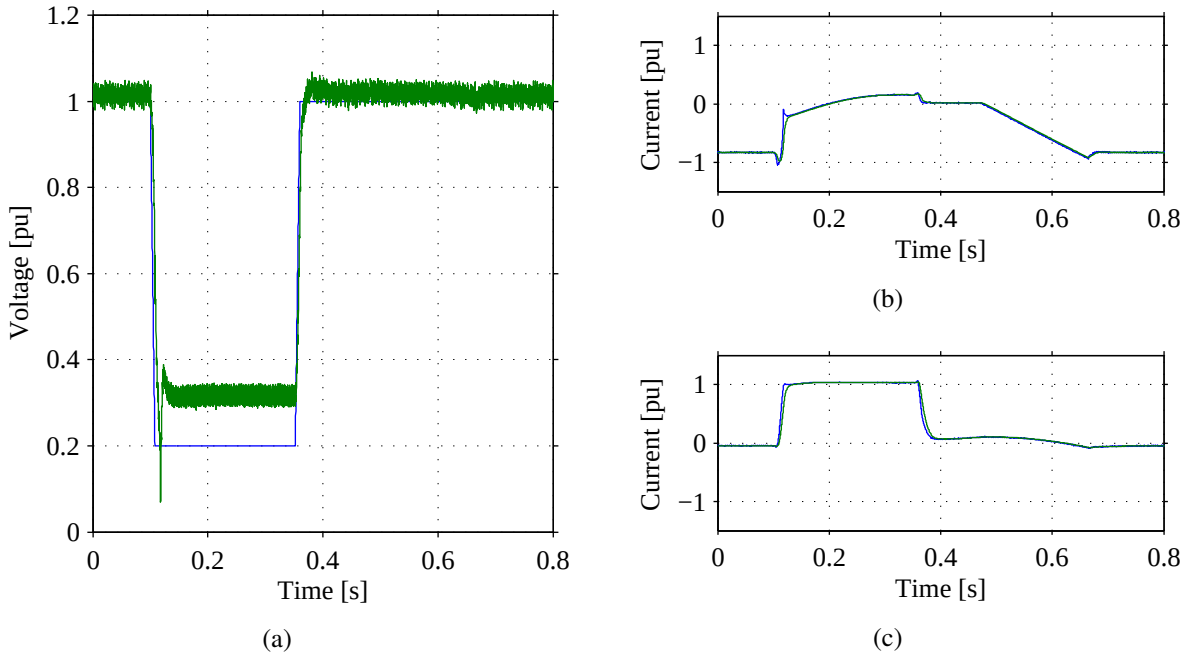

Fig. 6.15 PCC voltage control with emulated short-circuit power of 10 pu. Plot (a): LVRT reference $|\underline{e}^*|$ (blue) actual magnitude of the PCC voltage $|\underline{e}|$ (green); Plot (b): estimated d-axis grid current $\hat{i}_{\mathrm{g_d}}$ (blue) and filtered current $\hat{i}_{\mathrm{g_{d,fil}}}$ (green); Plot (c): estimated q-axis current $\hat{i}_{\mathrm{g_q}}$ (blue) and filtered current $\hat{i}_{\mathrm{g_{q,fil}}}$ (green).

equipment filter banks.

In the following, the interest is on the wind turbine response when a typical recovery ramp given in the Grid Codes is included in the voltage reference of the test equipment.

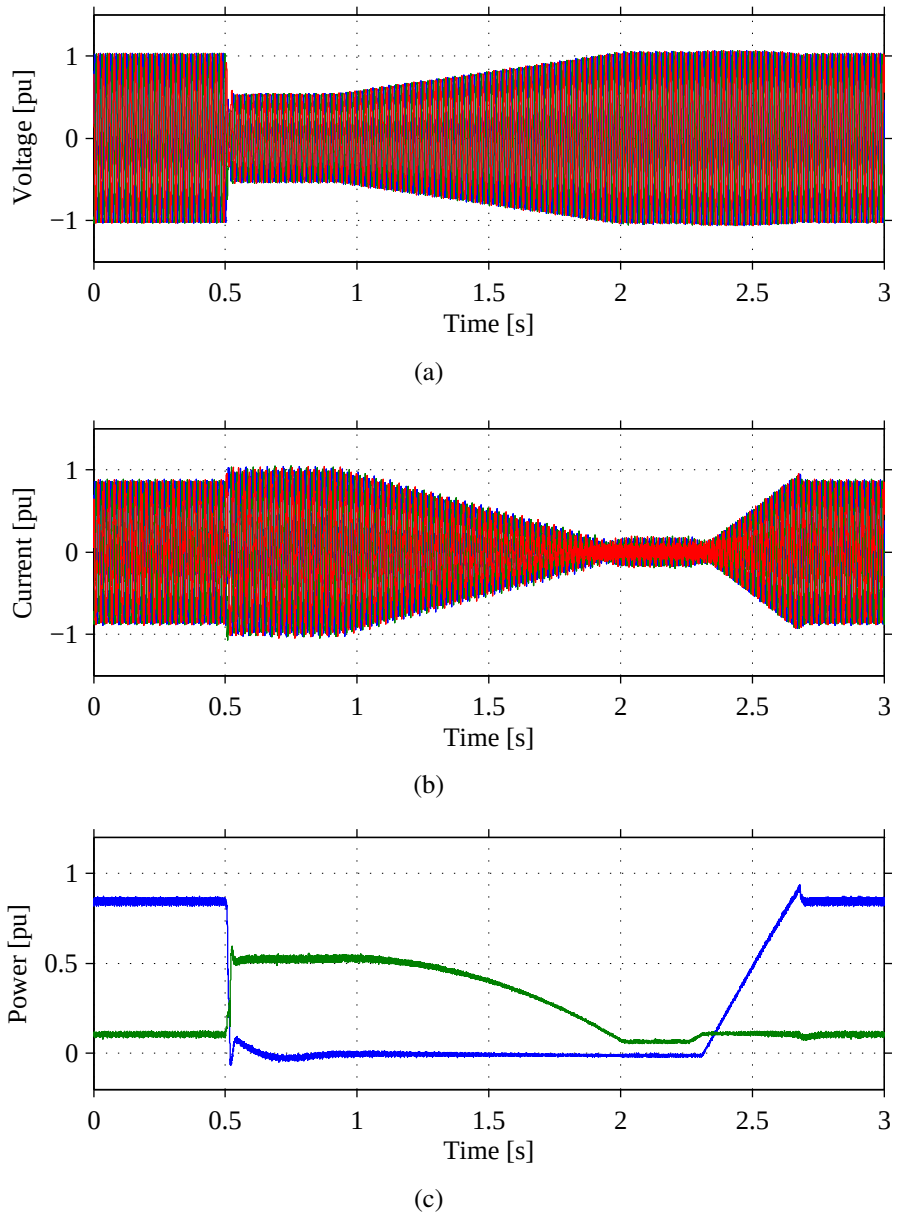

Fig. 6.16 Wind turbine response under a voltage dip and recovery ramp. Plot (a): three-phase voltage $\underline{e}_{\mathrm{w}}$; Plot (b): three-phase current $\underline{i}_{\mathrm{w}}$; Plot (c): active power P_{wt} (blue) and reactive power Q_{wt} (green) output.

6.3.3 LVRT test including recovery ramp

Here, the wind turbine operates at full-power and at unity power factor. The virtual short-circuit impedance is set to 0.2 pu, corresponding a short-circuit power of 5 pu (20 MW) at the PCC. The selected Grid Code LVRT profile is given in the German off-shore Grid Code [27]. The LVRT profile corresponds to a retained voltage of 0.2 pu for 450 ms, and a recovering ramp to 1 pu during 1 second.

The resulting three-phase wind turbine voltage $\underline{e}_{\mathrm{w}}$ is shown in Fig. 6.16(a). From the figure, it is possible to observe that the magnitude of the voltage reaches 0.5 pu during the dip, while the current output of the wind turbine $\underline{i}_{\mathrm{w}}$, shown in Fig. 6.16(b), is controlled within 1 pu. The injected reactive power is 0.5 pu, as depicted in Fig. 6.16(c). Observe in Fig. 6.18(a) that the resulting PCC voltage is controlled above 0.4 pu, when the LVRT profile is set to 0.2 pu.

As soon as the wind turbine voltage is recovering above 0.5 pu at 1 s, the reactive current $\hat{i}_{\mathrm{w_q}}$ shown in Fig. 6.17(b) is decreasing. For this reason, the resulting reactive power also decreases. Due to the reduction of reactive current between 1 s and 2 s, the actual PCC voltage approaches the LVRT profile. The active power output is maintained in zero during the voltage dip and increases after 500 ms of the complete returning of the wind turbine voltage, at 2.3 s approximately.

The DC-link voltage of the wind turbine $\underline{u}_{\mathrm{dc,w}}$ is depicted in Fig. 6.17(a). The voltage increases rapidly when the wind turbine current $\hat{i}_{\mathrm{w_d}}$ is reduced to zero, as shown in Fig. 6.17(b). The crowbar protection of the wind turbine maintains the DC voltage below 1.075 pu. As soon as the limitation in the active current is removed, at 2.5 s approximately, the DC voltage controller manages to bring the DC-link voltage back to its reference.

Finally, the voltage at the grid connection point of the test equipment $\underline{e}_{\mathrm{g}}$ is depicted in Fig. 6.18(b). The three-phase current of the grid-VSC of the test equipment is also show in Fig. 6.18(b). Observe that when performing the test, there are no transients in the voltage nor the current. This

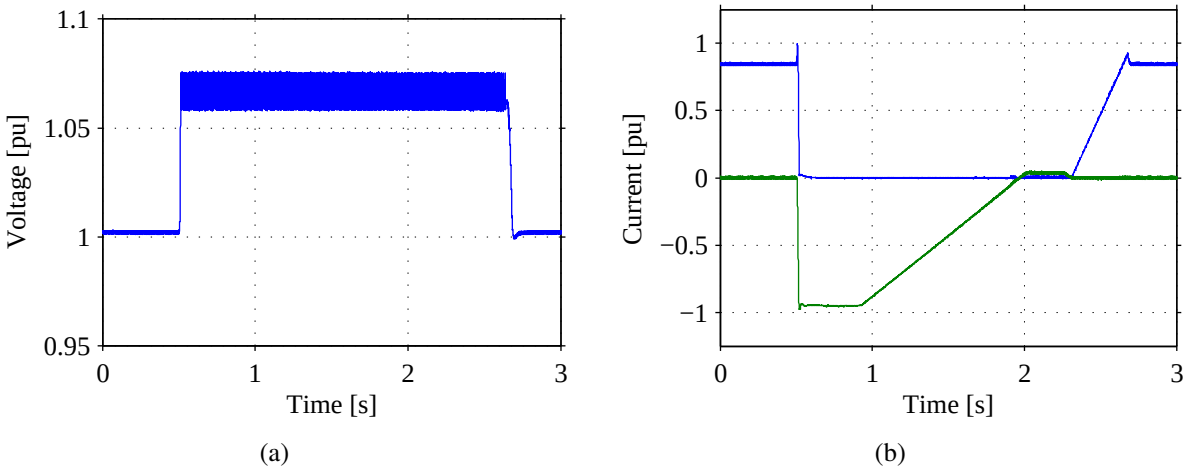

Fig. 6.17 Wind turbine LVRT control under a voltage dip. Plot (a): DC voltage $\underline{u}_{\mathrm{dc,w}}$; Plot (b): active current $\hat{i}_{\mathrm{w_d}}$ (blue) and reactive current $\hat{i}_{\mathrm{w_q}}$ (green).

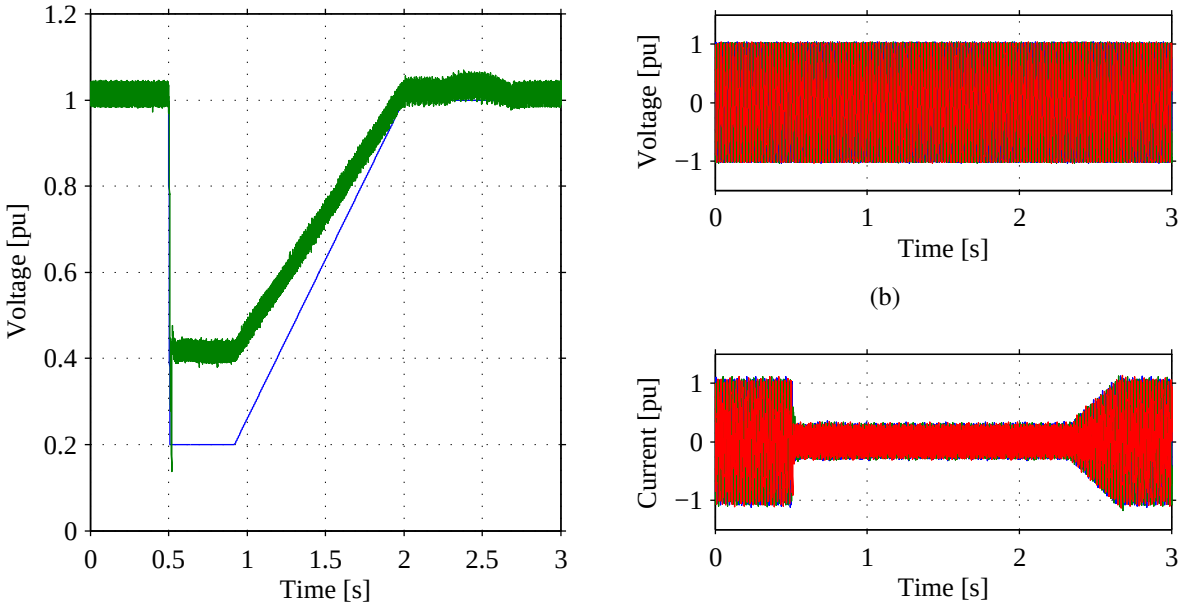

Fig. 6.18 PCC voltage control. Plot (a): reference voltage $|\underline{e}^*|$ (blue) actual magnitude of the PCC voltage $|\underline{e}|$ (green); Plot (b): actual three-phase grid filter voltage $\underline{e}_{\mathrm{g}}$; Plot (c): actual three-phase grid-VSC terminal current $\underline{i}_{\mathrm{g}}$.

is expected due to the decoupling that exists between the grid-side and turbine-side VSCs in the testing device. As seen in the figure, the grid voltage is practically unaffected during the whole LVRT test. The current is mostly active current, resulting of the active power production of the wind turbine. The small amount of current between 0.5 and 2.5 s is due to the reactive power injection by the filter bank at the grid-side of the test equipment.

6.3.4 Test for phase-angle jump during voltage dip

In this simulation, the ability of the test equipment in varying the phase angle of the PCC voltage during a voltage dip test is investigated. Here, the voltage is controlled in close-loop, at 1 pu and at 0.1 s it is dropped to 0.5 pu for 300 ms approximately. The angle of the reference voltage vector $\underline{e}^*$ is varied from 0 degrees to 30 degrees during the dip. Here, the d and q voltage components are controlled independently in order to reproduce the phase-angle jump. The results are shown in Fig. 6.19.

Observe in Fig. 6.19(a) that the actual three-phase voltage $\underline{e}$ is zoomed during the dip and during the recovery. From the figure it is possible to observe that the voltage actually changes its phase. In Fig. 6.19(b) it is shown the d and q components of the PCC reference voltages $\hat{e}_{\mathrm{d}}$ (blue) and $\hat{e}_{\mathrm{q}}$ (green), respectively and also its references (black). The d component is controlled at its reference within 10 ms. The q is affected by the reaction of the wind turbine and it is controlled at its reference within 15 ms. In order to create a phase shift, the q component must be controlled at a value different than 0 pu, as compared with the case shown in Fig. 6.9 where only the d

component is varied. Figure 6.19(c) shows the reference (blue traces) and the actual (green traces) phase-angle of the PCC voltage. The actual phase-angle of the voltage is controlled at its reference within 10 ms. An overshoot is seen at 0.11 s due to the dynamics of the voltage component $\hat{e}_{\mathrm{q}}$ shown in Fig. 6.19(b). The variation of the angle θ_{w} tracked by the wind turbine PLL measured at the voltage $\underline{\hat{e}}_{\mathrm{w}}$ is also shown in red traces in Fig. 6.19(c). Observe that as soon as the reference phase-angle is varied, the PLL of the wind turbine takes 180 ms approximately to track the varied voltage vector $\underline{\hat{e}}_{\mathrm{w}}$.

The magnitude of the wind turbine voltage is shown in Fig. 6.20(a) in blue traces. The magnitude of the PCC voltage and its reference value are also plotted in the figure in green and black traces, respectively. The PCC voltage is controlled at its reference within 12 ms after applying the dip and also after the recovery. The wind turbine d and q currents are shown in Fig. 6.20(b) in blue and green traces, respectively. Observe that the d and q currents are controlled properly to 0.8 pu and -0.85 pu, respectively, and that the magnitude of the current (black) is controlled to 1 pu during the dip, meaning that the wind turbine controller is able to control the current during the phase shift. However, when a phase shift is applied in the AC-link, the rotating dq-frame of the wind turbine controller is not in synchronism with the angle of the voltage $\underline{e}_{\mathrm{w}}$ due to the delay introduced by the PLL. Although the current controller on the wind turbine manages to control the current in steady-state 3 ms after detecting the voltage dip, the current $\hat{i}_{\mathrm{w_d}}$ does

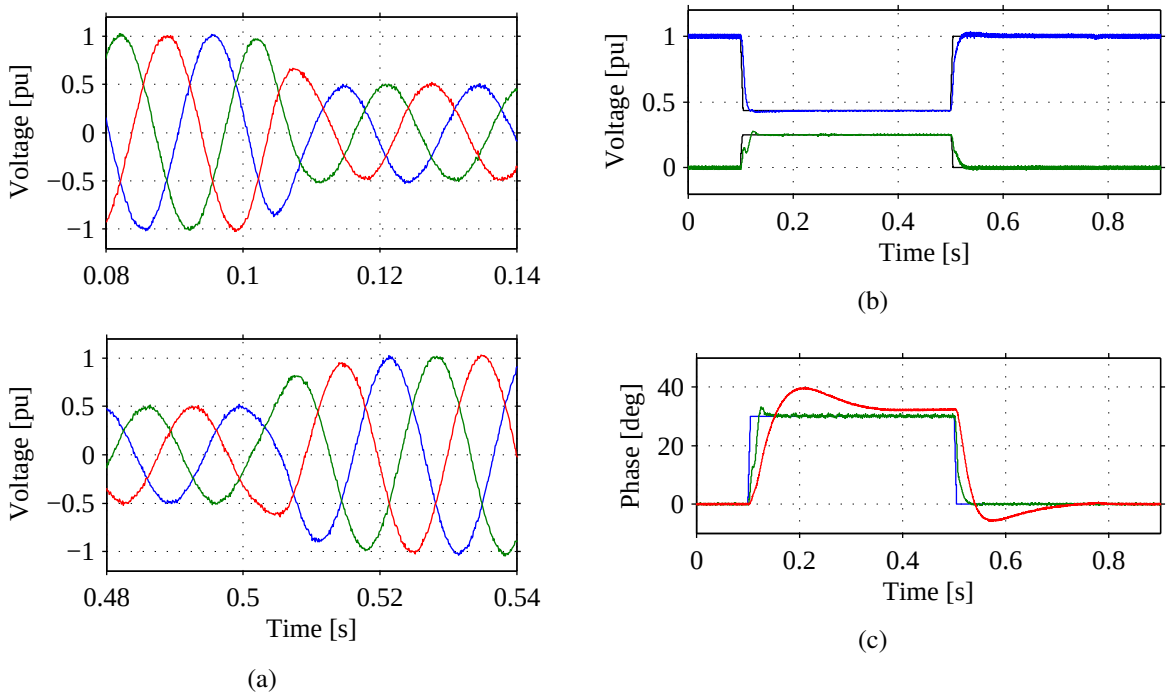

Fig. 6.19 Test equipment performance when testing for phase-angle jump during voltage dip: Plot (a): three-phase voltage $\underline{e}^{\mathrm{abc}}$; Plot (b) d and q PCC reference voltages $\hat{e}_{\mathrm{q}}$ (blue) and $\hat{e}_{\mathrm{q}}$ (green), respectively, and its references (black). Plot (c): reference (blue) and actual (green) phase-angle in PCC voltage $\underline{e}$. Variation of the angle θ_{w} during the voltage dip, tracked by wind turbine PLL (red) at the voltage $\underline{\hat{e}}_{\mathrm{w}}$.

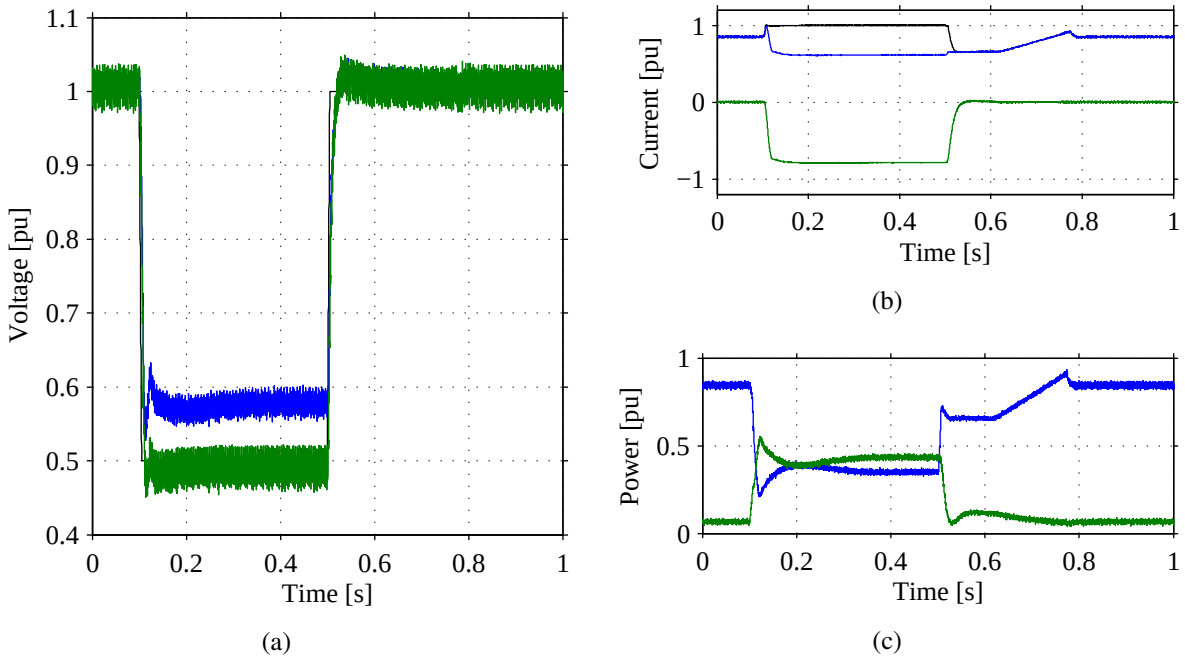

Fig. 6.20 Wind turbine test for phase-angle jump during voltage dip: Plot (a): reference voltage $|\underline{e}^*|$ (black) actual magnitude of the PCC voltage $|\underline{e}|$ (blue) and actual magnitude of the wind turbine voltage $\underline{e}_{\mathrm{w}}$ (blue); Plot (b): active current $\hat{i}_{\mathrm{w_d}}$ (blue), reactive current $\hat{i}_{\mathrm{w_q}}$ (green) and current magnitude $|\hat{\underline{i}}_{\mathrm{t,w}}|$ (black); Plot (c): active power P_{wt} (blue) and reactive power Q_{wt} (green) output.

not represent the active current and the current $\hat{i}_{\mathrm{w_q}}$ does not represent the reactive current, at least for the first 140 ms after the phase shift. The effect of the transitory asynchronism of the dq-frame is clearly shown in Fig. 6.20(c) where an undershoot can be seen in the active power (blue traces) while the reactive power experiences an overshoot (green traces). As a comparison, observe for example Fig. 6.16(c) where the resulting active and reactive power are constant almost immediately during the voltage dip. Here, the active power is decreased to 0.25 pu and that the reactive power peaks at 0.55 pu at $t = 0.12$ s while the d and q components of the wind turbine currents are controlled without transients.

Finally, the resulting wind turbine voltage is boosted by the reactive power injected by the wind turbine, as shown in Fig. 6.20(a). Moreover, the active and reactive power set-point impact the resulting phase-angle of the wind turbine voltage, which is dependent of the impedance across the AC-link. For this reason, the angle variation measured by the PLL of the wind turbine is greater than 30 degrees, as shown in red traces in Fig. 6.19(c). At 0.5 s the angle is restored to 0 degrees and the wind turbine increases the active power output to 0.65 pu while decreasing the reactive power to 0 pu. Observe that the d and q currents are controlled at 0.65 pu and 0 pu respectively while the active and reactive power output experience again a small deviation at $t = 0.5$ s.

6.4 Open-loop control on the PCC voltage

6.4.1 Test for single-phase voltage dip

In addition to the three-phase LVRT requirement given in the majority of Grid Codes, some of the most elaborated Grid Code require wind turbines to withstand asymmetric voltage dips. For instance, the Danish Grid Code [31] states that the wind turbine unit must be tested against single-phase and two-phase voltage dip for a duration of 150 ms. In [10] it is given a methodology to replicate phase-to-ground faults by feed-forwarding a pre-calculated zero sequence voltage. Note that in Fig. 4.1, the testing equipment is here interfaced by a delta-star transformer $T2$, decoupling the zero sequence equivalent circuit between the PCC and the wind turbine circuit. For this reason, only the positive and negative sequence voltage can be effectively regulated by the VSC in the investigated setup. In order to demonstrate the flexibility of the VSC-based testing equipment in reproducing unbalance voltage dips, a single-phase voltage dip test is presented in this section. Here, the open-loop control given in Section 4.4.2 has been implemented in three-phase form, meaning that the magnitude of each phase voltage is selected independently [9]. In this simulation, only phase c of the turbine-side VSC voltage is dropped to 0.5 pu for 150 ms while phase a and b are maintained at 1 pu. The resulting three-phase voltage at the PCC and three-phase current output of the wind turbine system are shown in Fig. 6.21.

As experted, the unbalanced voltage at the turbine-side VSC leads to an unbalanced PCC voltage $\underline{e}$ and an unbalanced wind turbine current output $\underline{i}_{\mathrm{w},2}$ as shown Fig. 6.21(a) and Fig. 6.21(b), respectively. Moreover, due to the unbalanced voltage drop across the filter inductance of the turbine-side VSC, the resulting PCC voltage in phase a (blue) and b (green) are slightly phase-shifted and the peak values are reduced to 0.97 pu, while phase c (red) drops to 0.6 pu. As expected, the wind turbine current $\underline{i}_{\mathrm{w},2}$ in the LV side of the output transformer is also unbalanced.

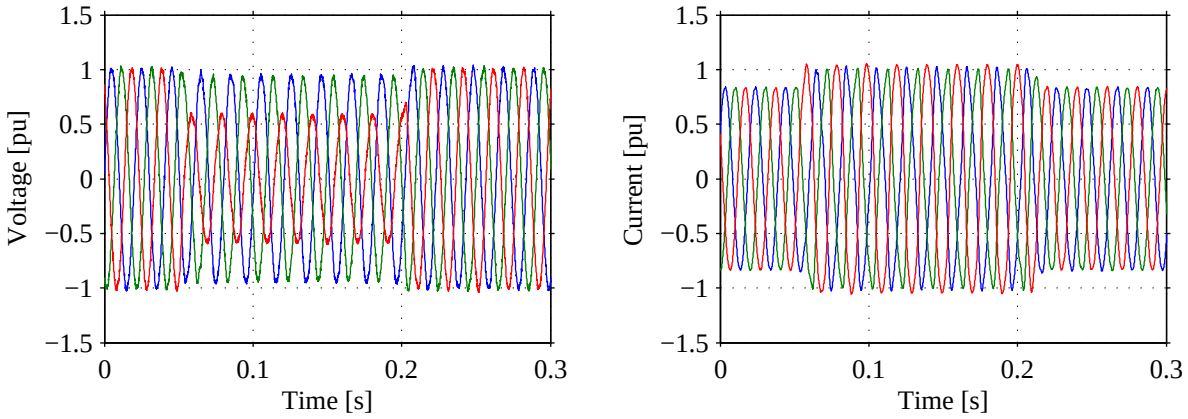

Fig. 6.21 Test for single-phase voltage dip: Plot (a): three-phase PCC voltage $\underline{e}^{(\mathrm{abc})}$. Plot (b): three-phase current $\underline{i}_{\mathrm{w},2}^{(\mathrm{abc})}$.

The RMS magnitude of the wind turbine voltage $\underline{e}_{\mathrm{w}}$ and the PCC voltage are shown in blue and green traces, respectively, in Fig. 6.22(a). Observe that the LVRT control action of the wind turbine boosts the RMS value of the voltage to 0.77 pu and the RMS value of the PCC voltage is at 0.71 pu. Since the implemented open-loop control imposes the voltage only at the terminals of the turbine-side VSC of the test equipment, both the PCC voltage and wind turbine voltage are boosted. The active and reactive current output are depicted in Fig. 6.22(b) in blue and red traces, respectively, and its references are shown in black. As shown in the figure, in case of unbalanced condition of the grid, the current and also the voltage will show an oscillatory component at frequency equal to double the grid frequency. This is due the fact that the three-phase current and voltage vectors have a negative-sequence component which rotates in the opposite direction with respect to the synchronously rotating dq-reference frame. An alternative to improve the performance of the controller of the VSC during unbalance condition is to modify the control system in order to control separately positive sequence and negative sequence current. These modifications are presented, for example, in [70], [71] and [72].

Observe that the active and reactive power output shown in Fig. 6.22(c) in blue and green traces, respectively, exhibit an oscillatory response. In the figure it is also shown the average value of both powers. Note that even during an unbalance voltage dip, the modelled wind turbine can still provide reactive power support. Moreover, since the resulting voltage dip at the terminals of the wind turbine is not severe, the generating unit can sill deliver active power into the grid.

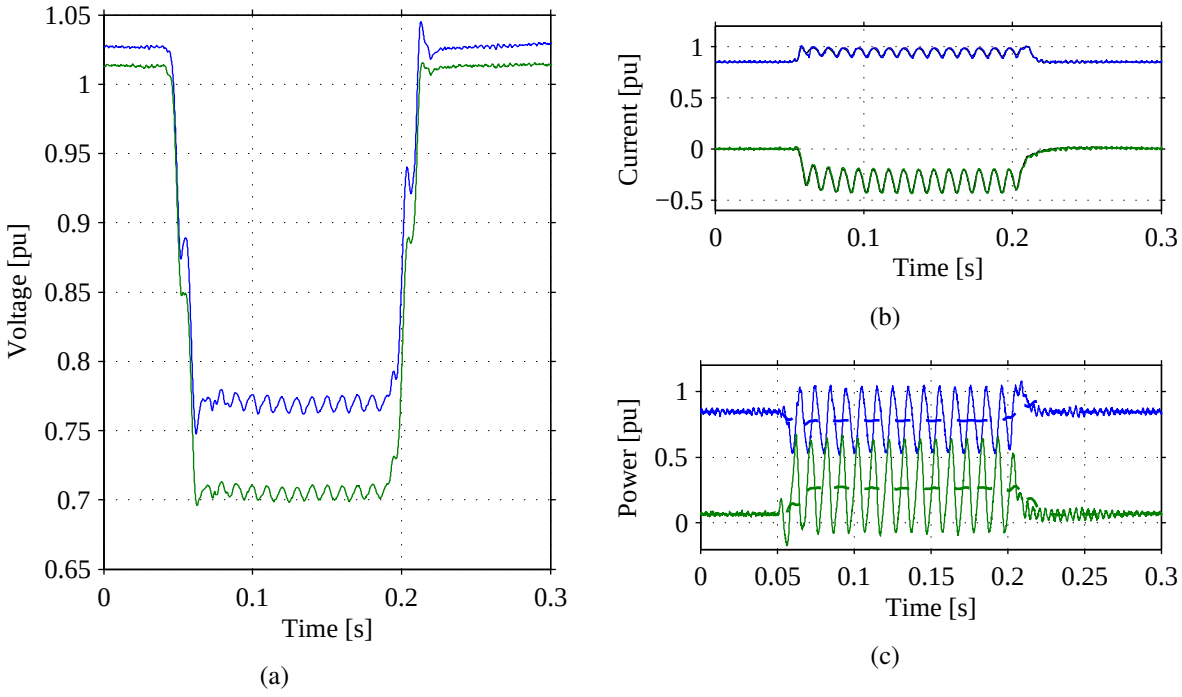

Fig. 6.22 Wind turbine performance during single-phase voltage dip: Plot (a): WT voltage (blue) and PCC voltage (green) RMS values. Plot (b): active current $\hat{i}_{\mathrm{w_d}}$ (blue), reactive current $\hat{i}_{\mathrm{w_q}}$ (green) and references (black); Plot (c): active power P_{wt} (blue) and reactive power Q_{wt} (green) output and their average values (dashed).

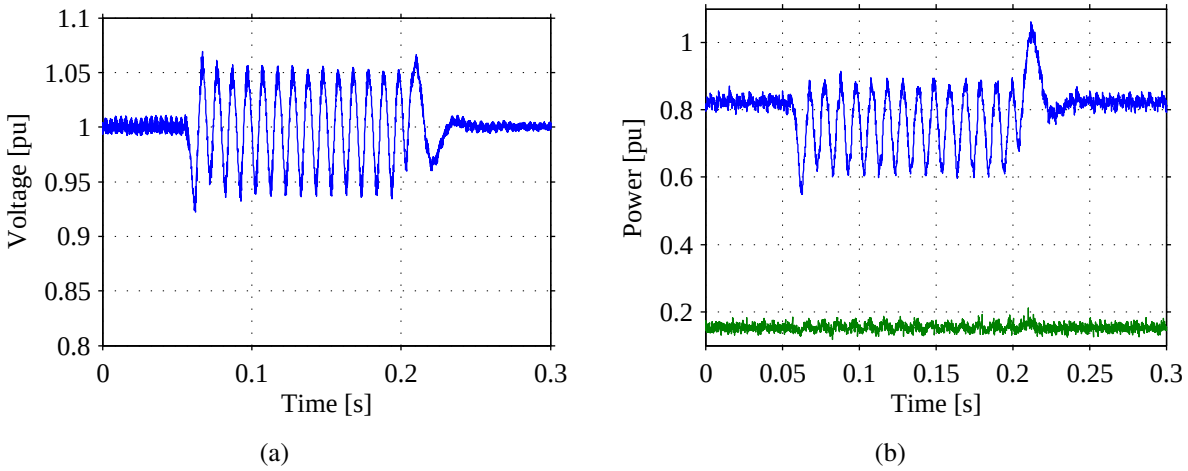

(a) (b)

Fig. 6.23 Grid-side VSC performance during single-phase voltage dip: Plot (a): three-phase PCC voltage u_{dc}. Plot (c):active power P_{grid} (blue) and reactive power Q_{grid} (green) output of test equipment towards the the AC grid.

Finally, it is of interest to analyse the effect of the oscillatory power across the AC-link and how this uncontrolled power can affect both the DC-link and the grid-side the test equipment. In Fig. 6.23(a) it is shown the DC-link voltage u_{dc} of the testing equipment. From the figure it is possible to observe that the power oscillation experienced by the wind turbine leads to a second harmonic oscillatory response of the DC voltage [73]. Note that the amplitude of the oscillation is strictly related to the operating conditions of the wind turbine and to the nature of the unbalance and that they can introduce an extra stress on the capacitors of the testing device. In Fig. 6.23(b) it is shown the oscillatory response of the active power output P_{grid} (blue traces) and reactive power output Q_{grid} (green traces) respectively, of the test equipment. From the figure it is possible to observe that the power oscillation is propagated into the AC grid.

6.4.2 Test for two consecutive two-phase voltage dips

A TSO can also require to wind turbines manufactures to withstand two consecutive voltage drops at the point of common coupling of the wind power plant. Note that if the fault in the AC system is not cleared, the action of an automatic reclosure at the point of the fault will lead to a second voltage drop at the wind turbine terminals. The requirements given in the Danish Grid Code [31] specifically says that the wind power plant must be designed to withstand recurring faults. In particular, two consecutive single-phase to ground and two-phase (with and without earth contact) voltage drops of 150 ms each, separated by 0.5 to 3 seconds

The impact of a single-phase voltage dip test in the testing equipment and wind turbine system has been covered in the previous section. In this scenario, the test equipment is used to generate two recurring two-phase voltage dips. Similarly to the previous case, the three-phase open-loop control given in [9] has been implemented. Here, phase a is controlled at 1, and phases b and c are dropped to 0.3 pu for 150 ms. In order to show the dynamic behavior of the system within a reasonable time resolution, the second voltage dip is programmed 150 ms after the first voltage

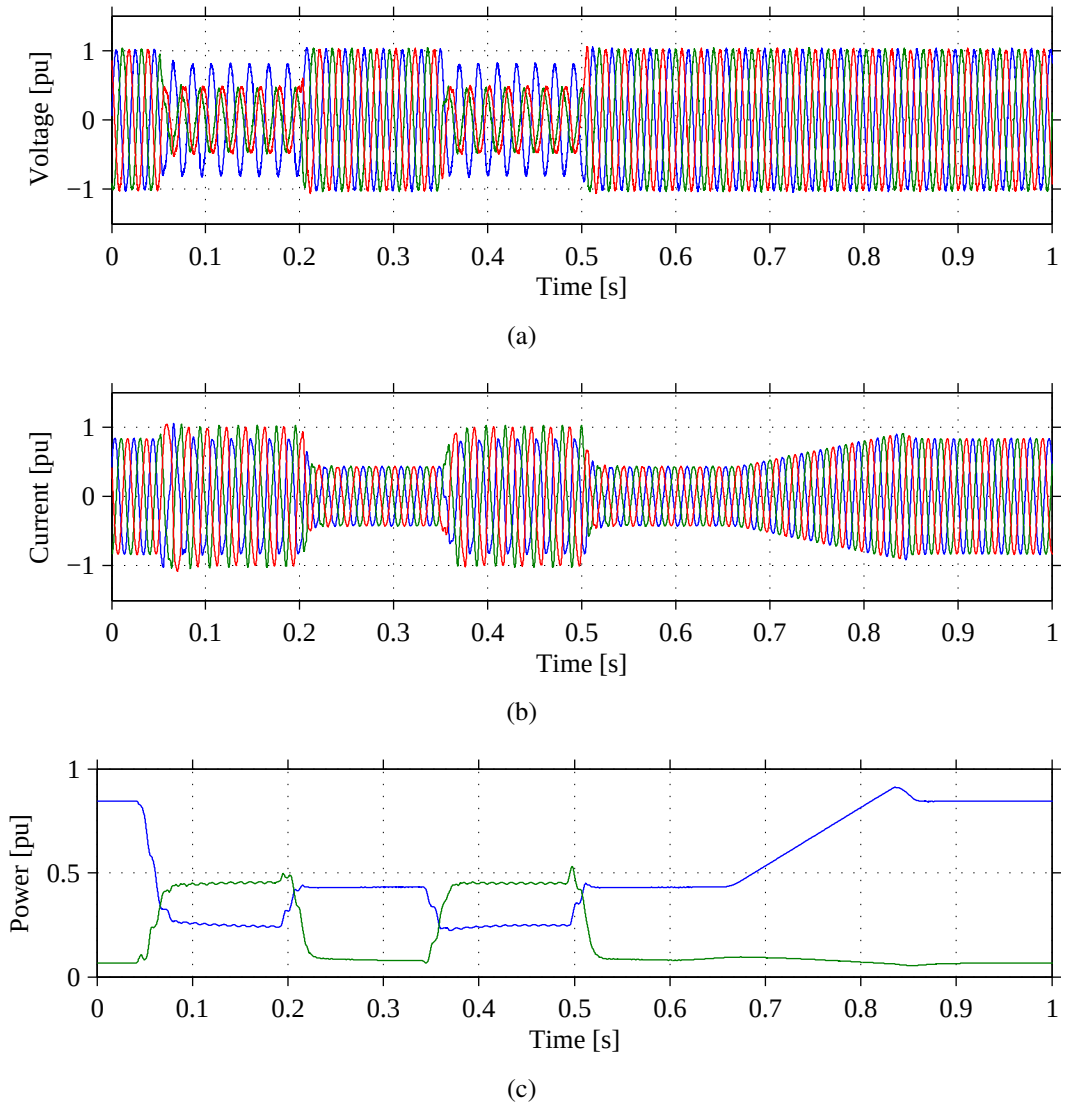

Fig. 6.24 Test for two-phase voltage dip: Plot (a): three-phase PCC voltage $\underline{e}^{(\mathrm{abc})}$. Plot (b): three-phase current $\underline{i}_{\mathrm{w},2}^{(\mathrm{abc})}$; Plot (c): filtered active power P_{wt} (blue) and reactive power Q_{wt} (green) output.

dip is restored. The wind turbine is injecting 0.9 pu of active power into the AC-link. The resulting three-phase PCC voltage is given Fig. 6.24(a) and the current output of the wind turbine system is shown in Fig. 6.24(b). In the figure it is possible to observe that both the current and the voltage become severely unbalanced. Observe that under an two-phase voltage dip, the wind turbine manage to control the current below 1 pu.

The power output from the wind turbine is also heavily distorted, similar to the waveforms shown in Fig. 6.22(c). For this reason, only the average of the active and reactive power output has been plotted in Fig. 6.24(c), in blue and red traces, respectively. Note that the LVRT control strategy manages to reduce active power production and increase the injection of reactive power during the voltage dip. The resulting RMS value of the PCC voltage $\underline{e}$ and wind turbine voltage $\underline{e}_{\mathrm{w}}$ are shown in Fig. 6.25(a), in green and blue traces, respectively. Observe that due to the control

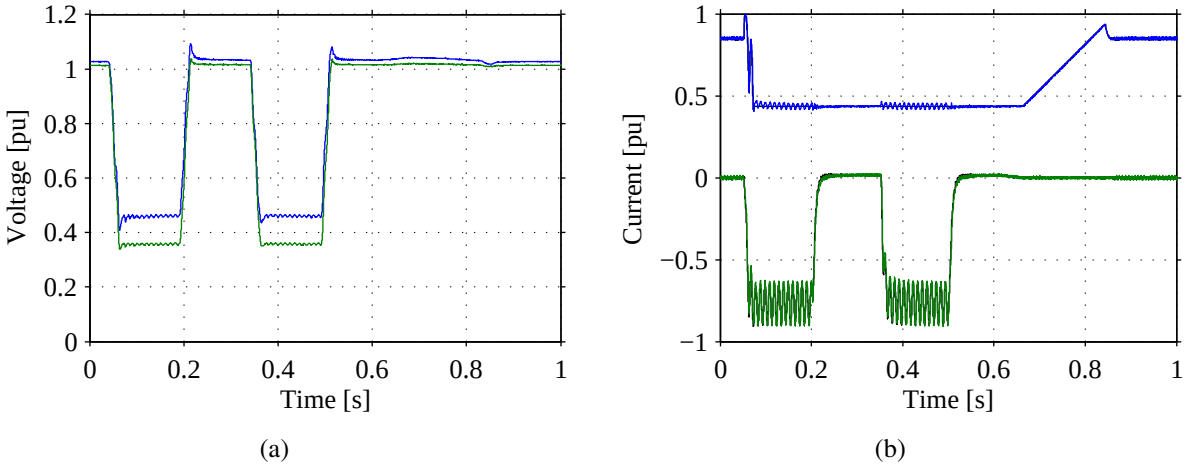

(a) (b)

Fig. 6.25 Grid-side VSC performance during single-phase voltage dip: Plot (a): magnitude of wind turbine voltage $\underline{e}_{\mathrm{w}}$ (blue) and PCC voltage $\underline{e}$ (green). Plot (b): active current $\hat{i}_{\mathrm{w_d}}$ (blue), reactive current $\hat{i}_{\mathrm{w_q}}$ (green) and references (black).

action of the wind turbine during dip, the voltage at the wind turbine is 0.48 pu and the PCC voltage is 0.35 pu.

The active and reactive current are shown Fig. 6.25(b) in blue and green traces, respectively. The LVRT control strategy varies the reactive current according to the magnitude of the voltage dip, while the active current is maintained at 0.45 pu. The reference current is shown in black traces in the figure. Observe that the controller manages to control both d and q currents during unbalanced conditions. The 100 Hz oscillation in both actual d and q currents due to the negative sequence component seen in the dq-frame. The reference q-current also oscillates because is calculated in the LVRT control block based on $\hat{e}_{\mathrm{w_d}}$ which also contains negative sequence oscillation. On the other hand, the current reference in the d axis is limited by the LVRT control; therefore, it remains invariant during the voltage dip, as seen in Fig. 6.25(b).

Finally, due to the reactive power injected by the AC filters at 0.3 s, the reactive power is maintained at a minimum value of 0.1 pu when the voltage is restored between the dips. Moreover, the q-current is set to zero. The second voltage dip is produced by the test equipment at 0.36 s. A similar behavior of the system is expected. Observe that the wind turbine injects 0.4 pu of reactive power, until the recovery of the voltage at 0.5 s. After 150 ms, the wind turbine starts to resume active power production with a smooth ramp function. At 0.89 s, the generating unit resumes normal operation.

6.4.3 Grid emulator algorithm in open-loop

The virtual impedance algorithm discussed in Section 6.3.2 is here implemented in open-loop in order to represent different short-circuit power of the interconnecting grid. The reference voltage of the turbine-side VSC $\underline{u}^{(dq)^*}$ is no longer varied according to (4.41), but instead, the voltage drop over the virtual impedance $R_{\mathrm{v}} + j\omega_{\mathrm{s}}L_{\mathrm{v}}$ is added.The control law in discrete form is given

as:

$$\underline{u}^{(\mathrm{dq})^*}(k) = \underline{e}^{(\mathrm{dq})^*}(k) + \hat{\underline{i}}_{\mathrm{f}}^{(\mathrm{dq})}(k)(R_{\mathrm{v}} + j\omega_{\mathrm{s}}L_{\mathrm{v}}) \tag{6.6}$$

where $\hat{\underline{i}}_{\mathrm{f}}^{(\mathrm{dq})}(k)$ is the estimated converter terminal current passed through a low bandwidth LPF (see Section 4.4.2 for the derivation of a discrete first-order LPF), in order to avoid feeding of high-frequency content directly into the PWM. Note that in open-loop operation, the grid-emulation algorithm does not have the limitation of the cascaded PCC voltage control and the inner current control; meaning that the derivative term in (6.1) can be included. In this control mode, the only limiting factor is the switching frequency while the interface inductor L provides a natural derivative voltage drop when the current $\underline{i}$ varies. However, in order to have a point of comparison with the previously developed grid emulation algorithm in close-loop, the derivative term has been, again, removed.

When enabling the grid emulator function, the voltage $\underline{u}$ will be dependent on the wind turbine operating point, according to (6.6). In order to obtain 1 pu at the PCC at different emulated grid impedances, the reference voltage has been slightly adjusted in order to counteract both the voltage drop over L and R, and L_{v} and R_{v} at pre-fault condition.

In the following, a voltage dip down to 0.2 pu for 150 ms is applied to the simulated wind turbine system. For different levels of stiffness, curves for the resulting voltage and wind turbine

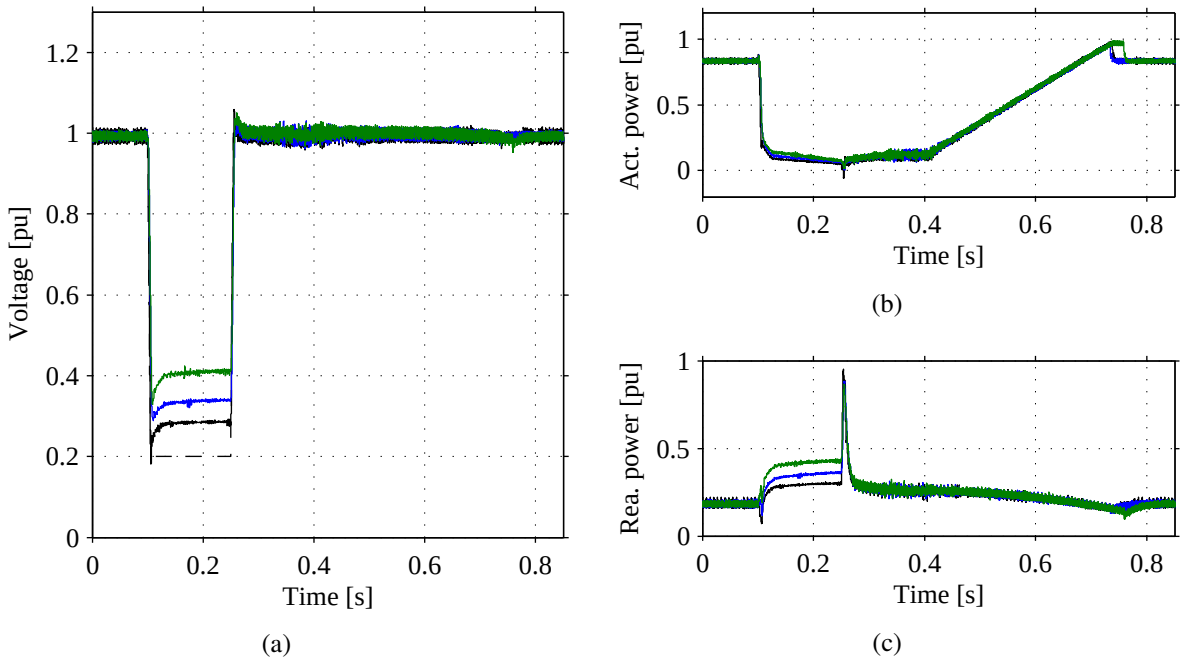

Fig. 6.26 Test equipment performance when testing for voltage dip including grid emulator: Plot (a): three-phase voltage magnitude $|\underline{e}|$; Plot (b): active power (P_{wt}); and Plot(c): reactive power (Q_{wt}) output of the wind turbine. In plots: dashed-black: reference voltage, black: open-loop with impedance emulation disabled; blue: emulated grid of 10 pu (45 MVA), green: emulated grid of 4 pu (18 MVA).

operating point are combined and shown in Fig. 6.26. Starting with a stiff regulation in open-loop, the resulting voltage and wind turbine active (Q_{wt}) and reactive (Q_{wt}) power output are depicted in black traces in Fig. 6.26(a), Fig. 6.26(b) and Fig. 6.26(c), respectively.

The minimum voltage experienced by the wind turbine system is 0.28 pu at 0.5 s measured at the PCC. The voltage is here being boosted by both the wind turbine grid capacitor C_{w} and the testing equipment capacitor C. The maximum reactive power output is 0.25 pu. By increasing the virtual impedance to 10 pu (45 MVA), shown in blue traces in Fig. 6.26, the resulting voltage is 0.35 pu with a reactive power of 0.3 pu. Finally, a short-circuit power of 4 pu is emulated, shown in green traces in Fig. 6.26. The maximum voltage set-point reaches 0.41 pu with a reactive power output of 0.45 pu.

Observe, however, that the active power given in Fig. 6.26(b) is somewhat the same for all simulated grid scenarios. The increasing effect of the retained voltage at 0.1 s for all cases is between the range of 0.3 to 0.4 pu. The resulting voltage at the terminals of the wind turbine is also in proximity to this voltage range. For this reason, the LVRT control calculates a retained current $i^{*}_{\mathrm{w_d}}$ in proximity to 0 pu during the voltage dip, giving similar values of the wind turbine power output shown in Fig. 6.26(b) for all cases.

6.5 Frequency scan on the modelled FPC wind turbine

A wind turbine system analysis is mainly dependent on the mathematical model of the generating unit and on its implemented control strategy. In addition, the model must be verified not only at the fundamental frequency but also for a wider frequency range in which the wind turbine can interact with other existing elements present in the interconnected grid [62]. Since wind turbine data is not always available, the investigated testing equipment can be of used to obtain more information from an actual wind turbine system [74]. In this regard, this section deals with the use of the testing device to characterize the input admittance of the modelled wind turbine unit. For this reason, a practical approach for frequency scanning is discussed in this section. As previously discussed in Section 5.2, this analysis is limited to the sub-synchronous range only.

6.5.1 Practical implementation

In order to perform a frequency scan on a generating unit (i.e.: a wind turbine system), a dedicated controller must be implemented in the testing equipment. In particular, on the turbine-side converter of the back-to-back VSC shown in Fig. 6.1. Depending on the control strategy that is selected for implementation, the converter can either inject a small voltage signal at the desired frequency over-imposing the fundamental voltage, as shown in Fig. 6.27(a), or it can vary the incoming current from the tested object, as depicted in Fig. 6.27(b). The first option requires only a open-loop voltage controller; while the latter option requires a current control loop in the test equipment in order to vary its input current and thus varying the total current that flows outward the wind turbine. Observe, however, that the inner and outer loops of a close-loop controller on the test equipment can impact the admittance of the measured system. For this reason, an

open-loop control is preferred. The magnitude of the signal must be controlled within a safe margin in such way that the system under test can respond naturally against the perturbation, while maintaining a proper steady-state operating condition [75].

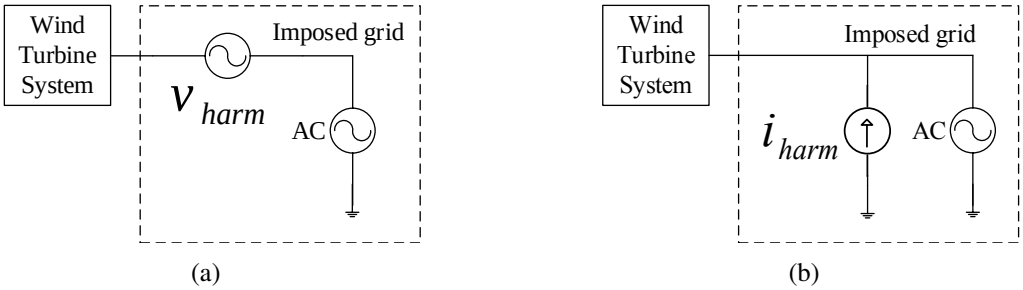

Fig. 6.27 Example of interconnection between wind turbine and testing equipment for frequency scan test. (a) Equivalent diagram for voltage harmonic injection. (b) Equivalent diagram for current harmonic injection.

A sinusoidal excitation signal with a single-frequency component can be used to determine the impedance at that specific frequency [65]. It is clear that, however, the frequency of the excitation signal is limited by the frequency range that a dedicated controller implemented on the testing equipment can operate. In the case for open-loop control, a digital controller capable of injecting the excitation signal can be easily programmed [62] while the frequency of excitation will be limited by the switching frequency of the VSC. The simplicity of an open-loop controller can be of advantage especially for experimental verification, as later demonstrated in this thesis. In addition, the computational time used when calculating the impedance off-line can be reduced if fast Fourier transformation (FFT) is used. For this reason, sinusoidal excitation has been preferred for implementation.

6.5.2 Control of the testing equipment for frequency scan

In order to perform a frequency scan in the abc-frame on the connected wind turbine, the testing equipment must first supply 50 Hz, 1 pu voltage. Once the system has reached steady-state, a 3-phase voltage vector $\underline{u}_{\mathrm{h}}^{(\mathrm{abc})}$ is added into the reference voltage $\underline{u}^{(abc)^*}$ of the turbine-side converter of the testing equipment.

The magnitude of the frequency content is increased with a ramp function from 0 pu to 0.025 pu. The voltage at the wind turbine connection point $\underline{e}^{(abc)}$ and the current $\underline{i}^{(abc)}$ are later recorded when the system reaches steady-state against the excitation voltage. The 3-phase harmonic current $\hat{\underline{i}}_{\mathrm{h}}^{(\mathrm{abc})}$ and voltage $\hat{\underline{e}}_{\mathrm{h}}^{(\mathrm{abc})}$ are retrieved off-line by FFT analysis.

The input admittance $Y_{\mathrm{w,h}}(j\omega)$ of the wind turbine is calculated as:

$$Y_{\mathrm{w,h}}(j\omega) = \frac{1}{Z_{\mathrm{w,h}}(j\omega)} = \frac{1}{R_{\mathrm{w,h}} + jX_{\mathrm{w,h}}} \tag{6.7}$$

for each harmonic h. The impedance $Z_{\mathrm{w,h}}(j\omega)$ is calculated as an average of each phase

impedance as

$$Z_{\mathrm{w,h}}(j\omega) = \frac{1}{3}\left(\frac{\hat{\underline{e}}_{\mathrm{h_a}}}{\hat{\underline{i}}_{\mathrm{h_a}}} + \frac{\hat{\underline{e}}_{\mathrm{h_b}}}{\hat{\underline{i}}_{\mathrm{h_b}}} + \frac{\hat{\underline{e}}_{\mathrm{h_c}}}{\hat{\underline{i}}_{\mathrm{h_c}}}\right) \tag{6.8}$$

with subscript a, b, c corresponding to each voltage and current phase evaluated at the harmonic h.

In Fig. 6.28 it is shown a combined frequency response of the modelled wind turbine tested for frequencies between 2 Hz and 48 Hz. Observe that the magnitude of the voltage imposed by the testing equipment is somewhat constant, as shown in blue traces in Fig. 6.28(a), and that the current magnitude varies across the scanned frequency range, as shown in green traces in the same figure. The phase of the current, however, presents larger variations depending of the frequency of excitation, as shown in green traces in Fig. 6.28(b). The phase crosses 180 degrees at 45 Hz, meaning that the turbine is reacting non-passively for frequencies above this value. In the following, different parameters of the simulation model are varied and the admittance of the wind turbine is evaluated.

Impact of the control parameters of the modelled wind turbine

The wind turbine model is scanned between the frequency range of 1 Hz and 49 Hz with a voltage amplitude of 0.025 pu. The first scenario corresponds to the evaluation of $Re\{Y_{\mathrm{w}}(j\omega)\}$ against variation of control parameters of the wind turbine. Here, the impact of $\alpha_{\mathrm{p,w}}$, $\alpha_{\mathrm{c,w}}$ and $\alpha_{\mathrm{d,w}}$ is studied, in a similar fashion as discussed in Section 5.2. First, the bandwidth $\alpha_{\mathrm{p,w}}$ is increased to $0.2\omega_{\mathrm{s}}$ and later decreased to $0.05\omega_{\mathrm{s}}$. The resulting waveforms are shown in Fig. 6.29 with blue and dashed-blue lines, respectively.

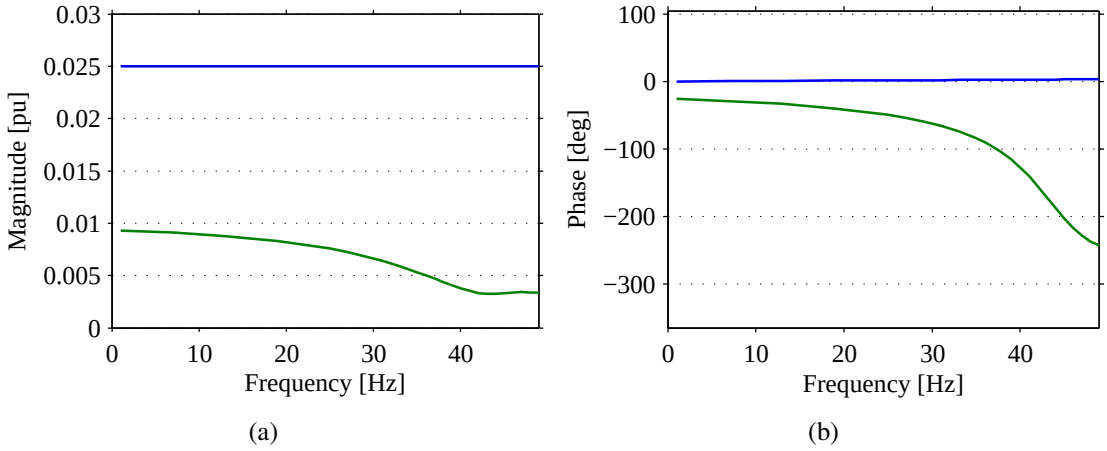

Fig. 6.28 Combined results at different excitation frequencies applied to the wind turbine model evaluated with nominal parameters. Plot (a): magnitude, and Plot(b): phase angle of the measured voltage (blue) and current (green) in phase a.

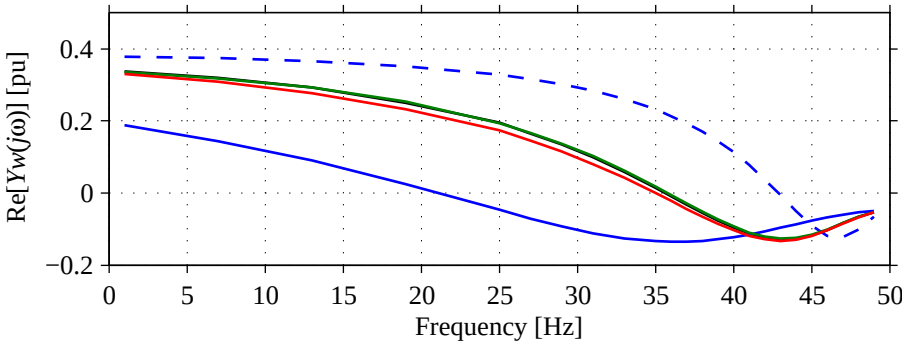

Fig. 6.29 Evaluation of $Re\{Y_{\mathrm{w}}(j\omega)\}$ of the time-domain simulation model operated at 0.9 pu, with nominal parameters (black), $\alpha_{\mathrm{p,w}}$ set at $0.2\omega_{\mathrm{s}}$ (blue), $\alpha_{\mathrm{p,w}}$ set at $0.05\omega_{\mathrm{s}}$ (dashed-blue), $\alpha_{\mathrm{c,w}}$ set at $7.5\omega_{\mathrm{s}}$ (green), $\alpha_{\mathrm{d,w}}$ set at ω_{s} (red).

Observe that the waveform shown in Fig. 6.29 is in line to what have been found in Fig. 5.3 where the analytical model is used. Moreover, the selection of the PLL speed impacts both the mathematical model and the time-domain simulation model in a similar way. When $\alpha_{\mathrm{p,w}}$ is increased, $Re\{Y_{\mathrm{w}}(j\omega)\}$ is drastically reduced, with minimum peak of -0.25 pu at 35 Hz and a maximum value of 0.12 pu at the minimum frequency. The system becomes non-passive for a wide frequency range between 20 Hz to 49 Hz, increasing the risk of interaction with other objects that can exhibit non-passivity at this range. On the contrary, a reduce value of $\alpha_{\mathrm{p,w}}$, shown in dashed-blue lines, brings the system passive for the majority of the studied frequency range. In this scenario, the non-passivity is exhibited only for a narrow frequency range in proximity the 50 Hz. Finally, a variation of the bandwidth of the current control and dc voltage control, $\alpha_{\mathrm{c,w}}$ and $\alpha_{\mathrm{d,w}}$, respectively, have a slight impact on $Re\{Y_{\mathrm{w}}(j\omega)\}$, as depicted in Fig. 6.29 with green and red traces, respectively, similar to the results presented in Section 5.2 where the analytical model has been studied.

Impact of the size of interconnecting LCL filter of the wind turbine

In the third scenario, impact of the capacitor C_{w}, included as depicted in Fig. 4.14 is studied. Subsequently, C_{w} is replaced by two filter banks of power 0.07 pu tuned at the switching frequency, and 0.03 pu tuned at twice the switching frequency. All parameters and control settings are kept at nominal value as listed in Table 4.2.

The resulting real and imaginary parts of the wind turbine admittance $Y_{\mathrm{w}}(j\omega)$ are plotted in Fig. 6.30 with solid traces and dashed traces, respectively. Observe that there is no mayor difference between using each of the two filter models. However, the use of tuned filters gives a more realistic approach for the simulation.

In the next case study, the impact of the filter inductance $L_{\mathrm{w,2}}$ on the wind turbine admittance is studied. First, the system is scanned at nominal conditions. With reference to Fig. 6.31, the component $Re\{Y_{\mathrm{w}}(j\omega)\}$ is depicted with black solid lines. The blue curve corresponds of the evaluation of $Re\{Y_{\mathrm{w}}(j\omega)\}$ when the $L_{\mathrm{w,2}}$ is increased to 0.05 pu. It can be noticed that when a larger filter is used, $Re\{Y_{\mathrm{w}}(j\omega)\}$ tends to move towards the negative region, crossing 0 pu at 33 Hz. A decreased value of the admittance suggests that the system becomes less passive against

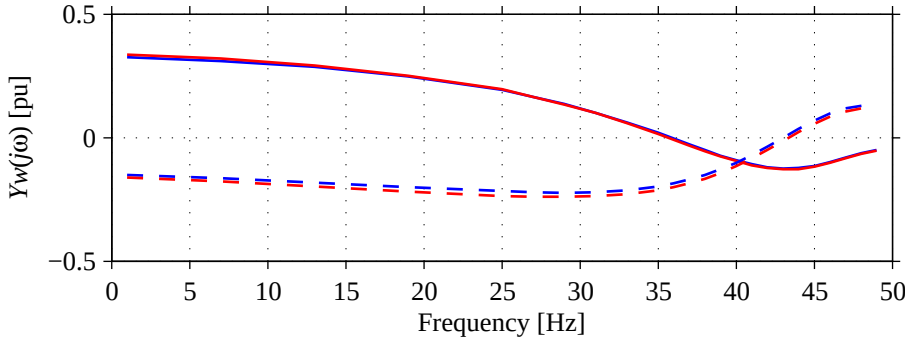

Fig. 6.30 Evaluation of $Re\{Y_{\mathrm{w}}(j\omega)\}$ (solid lines) and $Im\{Y_{\mathrm{w}}(j\omega)\}$ (dashed lines) of the time-domain simulation model, when using C_{w} (blue) and tuned filter banks (red).

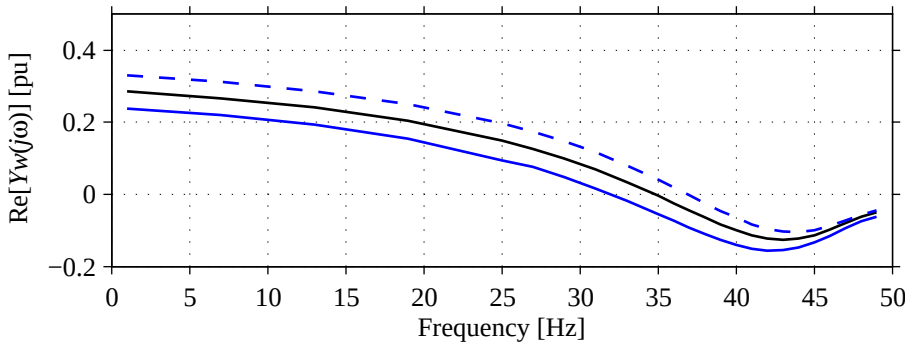

Fig. 6.31 Evaluation of $Re\{Y_{\mathrm{w}}(j\omega)\}$ of the time-domain simulation model, when setting $L_{\mathrm{w},2}$ at nominal value (black), $L_{\mathrm{w},2}$ is increased to 0.05 pu (blue) and when $L_{\mathrm{w},2}$ is removed (dashed-blue).

resonances.

The blue-dashed curve corresponds to the admittance of the system when only an LC filter is used. The waveform shows that when $L_{\mathrm{w},2}$ is removed, $Re\{Y_{\mathrm{w}}(j\omega)\}$ tends to move towards the positive region in the sub-synchronous range. Removing completely $L_{\mathrm{w},2}$ leads to a tighter coupling between the wind turbine and the grid. Hence, the imposed voltage is stiffer than the previous case, which can result in a increase of the passivity of the system.

6.5.3 Frequency scan in the dq-reference frame

In order to perform the frequency scan in the dq-frame, a similar excitation signal $\underline{u}_{\mathrm{h}}^{(\mathrm{dq})}$ of 0.025 pu is added to the reference voltage $\underline{u}^{(\mathrm{dq})}$. Each voltage component is excited separately. The voltage vector $\hat{\underline{e}}^{(\mathrm{dq})}$ and output current $\hat{\underline{i}}^{(\mathrm{dq})}$ enclose the excitation voltage $\hat{\underline{e}}_{\mathrm{h}}^{(\mathrm{dq})}$ and current $\hat{\underline{i}}_{\mathrm{h}}^{(\mathrm{dq})}$, respectively, which can be retrieved off-line by FFT analysis.

The excitation signal $\underline{u}_{\mathrm{h}}^{(\mathrm{dq})}$ can be decomposed in

$$\underline{u}_{\mathrm{h}}^{(\mathrm{dq})} = u_{\mathrm{h_d}} + j u_{\mathrm{h_q}} \tag{6.9}$$

In particular, $\underline{u}_{\mathrm{h}}^{(\mathrm{dq})} = u_{\mathrm{h_d}}$ when scanning for Y_{dd} and Y_{qd} and $\underline{u}_{\mathrm{h}}^{(\mathrm{dq})} = j u_{\mathrm{h_q}}$ when retrieving Y_{dq}

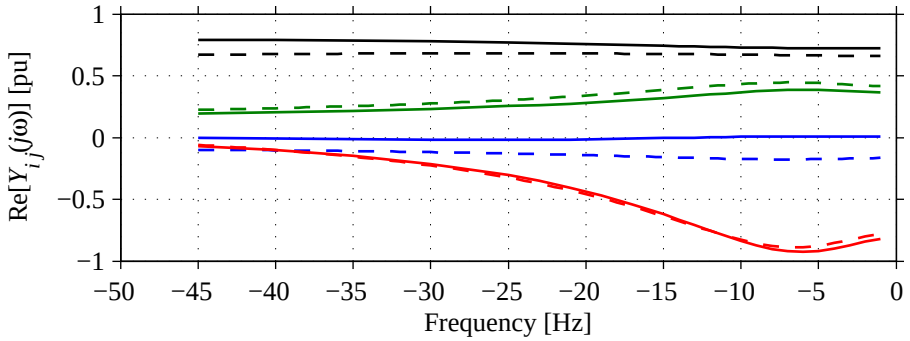

Fig. 6.32 Evaluation of the real part of the admittances $Y_{\mathrm{dd}}(j\omega)$ (black), $Y_{\mathrm{dq}}(j\omega)$ (blue), $Y_{\mathrm{qd}}(j\omega)$ (green) and $Y_{\mathrm{qq}}(j\omega)$ (red) in the dq-frame of the linearized wind turbine model, when operating at full power production. Solid traces: simulation results. Dashed traces: matched mathematical model (see Fig. 5.1 as reference).

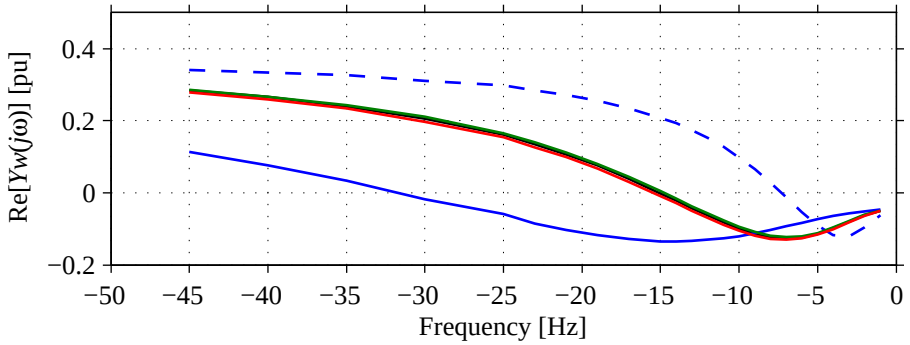

Fig. 6.33 Evaluation of $Re\{Y_{\mathrm{w}}(j\omega)\}$ of the time-domain wind turbine model operated at 0.9 pu, with nominal parameters (black), $\alpha_{\mathrm{p,w}}$ set at $0.3\omega_{\mathrm{s}}$ (blue), $\alpha_{\mathrm{p,w}}$ set at $0.05\omega_{\mathrm{s}}$ (dash-blue), $\alpha_{\mathrm{c,w}}$ set at $20\omega_{\mathrm{s}}$ (green), $\alpha_{\mathrm{d,w}}$ set at ω_{s} (red).

and Y_{qq} in (5.5). Figure 6.32 shows in solid traces the matrix component measured by the testing equipment and in dashed traces the ones calculated by the mathematical model introduced in Section 5.2 evaluated in a similar operating point and with an slightly increased value for $L_{\mathrm{w,2}}$ and $R_{\mathrm{w,2}}$ (see Fig. 5.1 as reference), resembling higher losses in particular on the wind turbine output transformer.

Observe that for the admittance Y_{dd} and Y_{qq}, which encloses the response of the DC voltage controller and PLL transfer function [51], both mathematical model and time-domain simulation model resembles one another. However, a small deviation is seen in the figure, which can be explained by the use of tuned filters as well as a more detailed T-model of the wind turbine output transformer, implemented only in the time-domain simulation model.

Adjusting the mathematical model allow for a better simplification of complex system such as a wind turbine system. Here, the admittance calculated by the use of the adjusted linearized model seems to match the admittance calculated by frequency scan on the time-domain simulation model, for most of the investigated frequencies.

As previously discussed, the admittance is drastically varied when different PLL bandwidth $\alpha_{\mathrm{p,w}}$ are set. This effect can be seen both in the abc-frame and also in the dq-frame, as shown

in Fig. 6.33. The scan performed in the dq-frame for the simulated wind turbine model shows that varying the current control bandwidth $\alpha_{\mathrm{c,w}}$ and the DC voltage control bandwidth $\alpha_{\mathrm{d,w}}$ also has a small effect on the real part of the wind turbine admittance $Re\{Y_{\mathrm{w}}(j\omega)\}$ in the scanned frequency range.

6.6 Conclusions

In this chapter, the investigated wind turbine testing methodology has been verified through time-domain simulations. Here, three different topologies for PCC voltage control have been compared. On one side, the open-loop control shows to be a simple and robust way of controlling the PCC voltage by means of controlling directly the terminal voltage of the turbine-side VSC of the testing device. In order to avoid an oscillatory response of the system, an appropriate ramp-rate has been selected when varying the converter voltage. On the other side, the PI-based close-loop controller seems to effectively control the PCC voltage while taking care of the filter losses and at the same time controlling the current that flows between the turbine-side converter and the PCC, thus, preventing an oscillatory response of the system. Moreover, focusing on the dynamics of both wind turbine and testing equipment during the test, an analysis of the performance of the overall system has been given. The open-loop and P-based and PI-based close-loop controllers have been verified through simulations and a control algorithm to emulate different grid scenarios has been derived and verified. The use of PI-based controller gives a smooth response when controlling the PCC voltage, while the open-loop control gives a similar response, with the addition that it is more simple and easy to implement, especially when testing for unbalanced voltage dips. For these reasons, the open-loop control has been selected for further verification through laboratory experiment.

The testing equipment, in open-loop control mode, is also capable of controlling the voltage in such way that the wind turbine can be excited at different frequencies, aside from the fundamental frequency. By using FFT analysis on the measured current and voltage, it is possible to retrieve the input admittance of the tested wind turbine. Simulation results have shown that the passivity of wind turbine system at sub-synchronous frequencies is mainly dependent of the PLL bandwidth. If a proper selection of this parameter is made, the passivity of the turbine can be maintained for the majority of the scanned frequency range. Moreover, the wind turbine has been scanned not only in the abc-frame but also in the dq-frame. The three-phase frequency scan algorithm is easy to implement and requires less post-processing effort to retrieve the system admittance. In addition, the admittance is easier to calculate given that it is not dependent of the transformation angle, as compared with the dq-frame scanning method. For this reason, this technique has been chosen for implementation in the laboratory.

Chapter 7

Experimental verification of the proposed testing methodology

7.1 Introduction

The aim of this chapter is to validate experimentally part of the simulation results obtained in the previous section. Thus, a description of the testing setup implemented in the laboratory together with the obtained experimental results is presented. The circuit diagram of the testing setup is given in Fig. 7.1 while the actual test-bench is shown in Fig. 7.2 and Fig. 7.3. The experimental setup is located at the Power System Laboratory at the Department of Energy and Environment of Chalmers University of Technology, Gothenburg, Sweden. The tests presented in this chapter were carried out between January of 2015 and October of 2016.

7.2 Laboratory setup and verification of the control algorithms

The testing equipment comprises two independently controlled VSC connected in back-to-back. The wind turbine model is here represented by the DC-sourced VSC. In order to replicate independently the operation and control of the two systems, the switching signals of each converter are generated by two dedicated dSPACE boards.

The power flows from the DC source into the AC-link through the wind turbine model VSC. This VSC is operated in current control mode in order to inject active power into the AC-link imposed by the test equipment. The turbine-side VSC of the testing equipment imposes the voltage to the wind turbine model and receives the produced power P_{wt}. The power is then transferred into the grid-side VSC through the DC-link of the testing equipment. The grid-side VSC maintains the DC voltage at its reference value by controlling the power that flows between the grid and the testing equipment.

The voltage applied to the wind turbine model is here controlled in open-loop. This control mode offers the flexibility that is needed when performing different test on the wind turbine model. Moreover, the grid-connected side of the wind turbine model and the testing equipment model

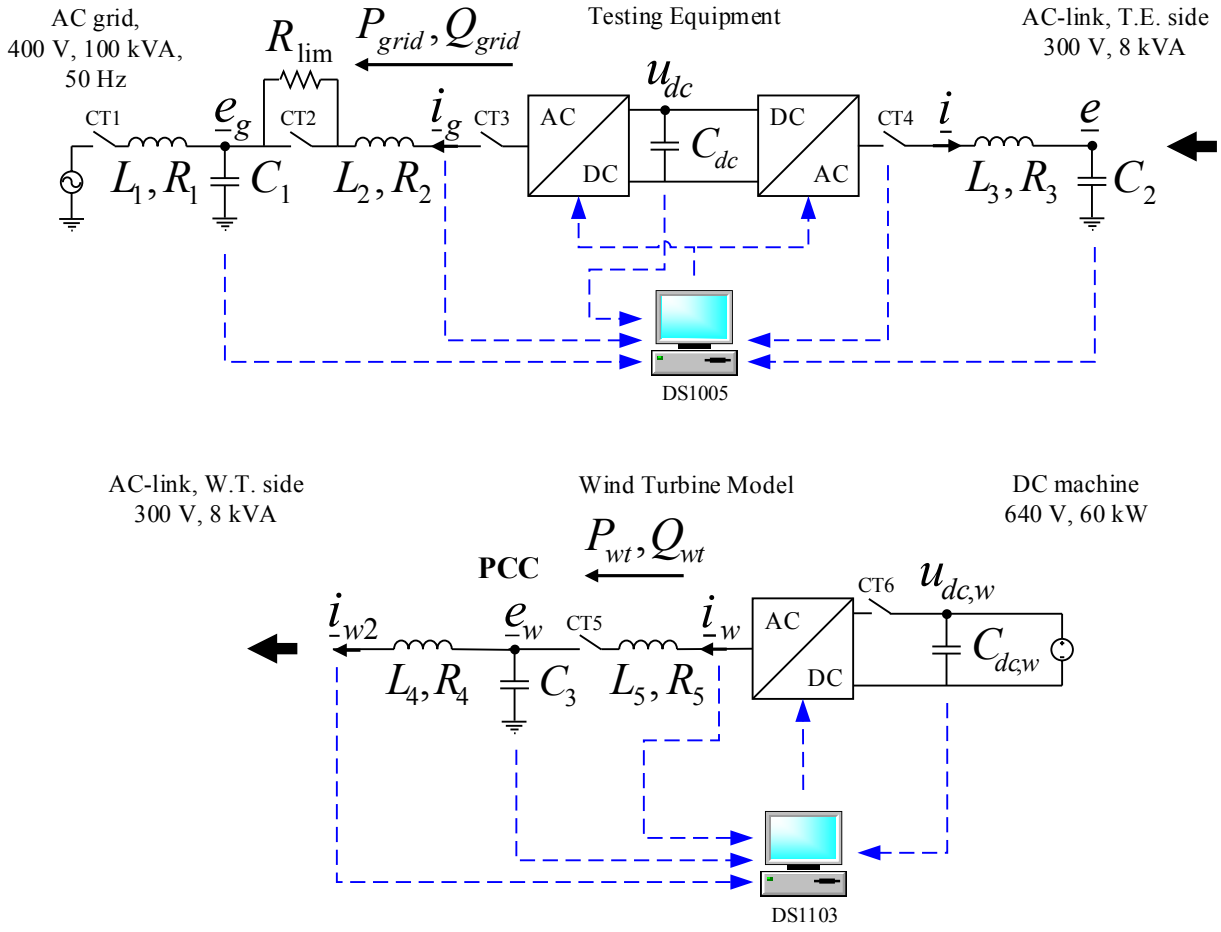

Fig. 7.1 Single line diagram of the laboratory setup constituted by the wind turbine model and the VSC-based testing equipment.

are controlled in close-loop.

The system is energized first by closing the contactor $CT6$ and supplying voltage into the wind turbine model by the use of a voltage-controlled the DC machine. Afterwards, the grid connection of the testing setup is enabled by closing the contactor $CT1$. The DC-link of the testing equipment is energized by closing the grid contactor $CT3$. The pulses of the grid-VSC are blocked and the DC capacitor is charged through the inner diode-rectifier. In order to limit the current that flows into the capacitor C_{dc} when energizing the system, the resistor R_{lim} has been placed between the 400 V AC grid and the grid-side VSC of the testing equipment. When the DC-link voltage reaches 550 V, the contactor $CT2$ parallel to R_{lim} is closed and therefore the resistor is bypassed. At this instance, the grid-VSC is directly connected to the 400 V grid and the resulting DC-link voltage is imposed at 580 V approximately.

Afterwards, the grid-VSC is deblocked and the DC-link voltage is incremented to 680 V with a smooth ramp function. At this moment, the testing equipment is controlled in STATCOM

TABLE 7.1. PARAMETERS OF THE LABORATORY SETUP.

Gird, filters and VSC rating		400 V, 100 kVA
Rating AC-link (also for plots)		300 V, 8 kVA
Frequency		50 Hz
DC voltage (Machine)		640 V
DC voltage (T.E.)		680 V
Filter inductance	L_1	2.1 mH
Filter capacitance	C_1	51 μF
Limiting resistor	R_{lim}	45 Ω
Filter inductance	L_2	3 mH
DC capacitor T.E.	C_{dc}	6.6 mF
Filter inductance	L_3	3 mH
Filter capacitance	C_2	30 μF
Filter inductance	L_4	2.1 mH
Filter capacitance	C_3	51 μF
Filter inductance	L_5	2.1 mH
DC capacitor W.T.	$C_{\text{dc,w}}$	4.4 mF
Base angular frequency	ω_{s}	314 rad/s
Current control bandwidth in T.E.	α_{c}	$2.5\omega_{\text{s}}$
DC voltage control bandwidth in T.E.	α_{d}	$0.25\omega_{\text{s}}$
Current control bandwidth in W.T.	$\alpha_{\text{c,w}}$	$2.0\omega_{\text{s}}$
Switching frequency in all VSC	f_{s}	5 kHz
Discrete sampling time	T_{s}	0.2 ms

operation. Subsequently, the contactor $CT4$ is closed and the turbine-side VSC is deblocked. The AC-link is here controlled at 300 V. The wind turbine contactor $CT5$ is closed and the VSC is deblocked once the PLL has acquire the correct phase-angle. Finally, the power reference of the wind turbine model is increased to the desired level.

In the following, all the sub-modules that constitute the laboratory setup are first verified independently. Afterwards, the sub-system and controllers are integrated in one complete test-bench as shown in Fig. 7.1.

The physical implementation of the laboratory setup is shown in Fig. 7.2, where the main parts that constitute the test system are highlighted. Similarly, in Fig. 7.3 it is shown the inductive and capacitive filters used to interface the wind turbine model with the test equipment.

7.2.1 Current control in grid-connected VSC

In this section, an experimental verification of the derived current controller given in Chapter 4 is given. The dynamic performance of the current control is evaluated with special focus on the step response as well as in the decoupling of both d and q axis. Observe that the implemented current controller is used in both the testing equipment and in the wind turbine model.

The grid-VSC of the testing equipment of the laboratory setup shown in Fig. 7.1 is used to verify the dynamic performance of the discrete current controller derived in Section 4.4.1 in conjunction with the PLL derived in Section 4.5.2. Here, the converter system including the capacitor C_1 and

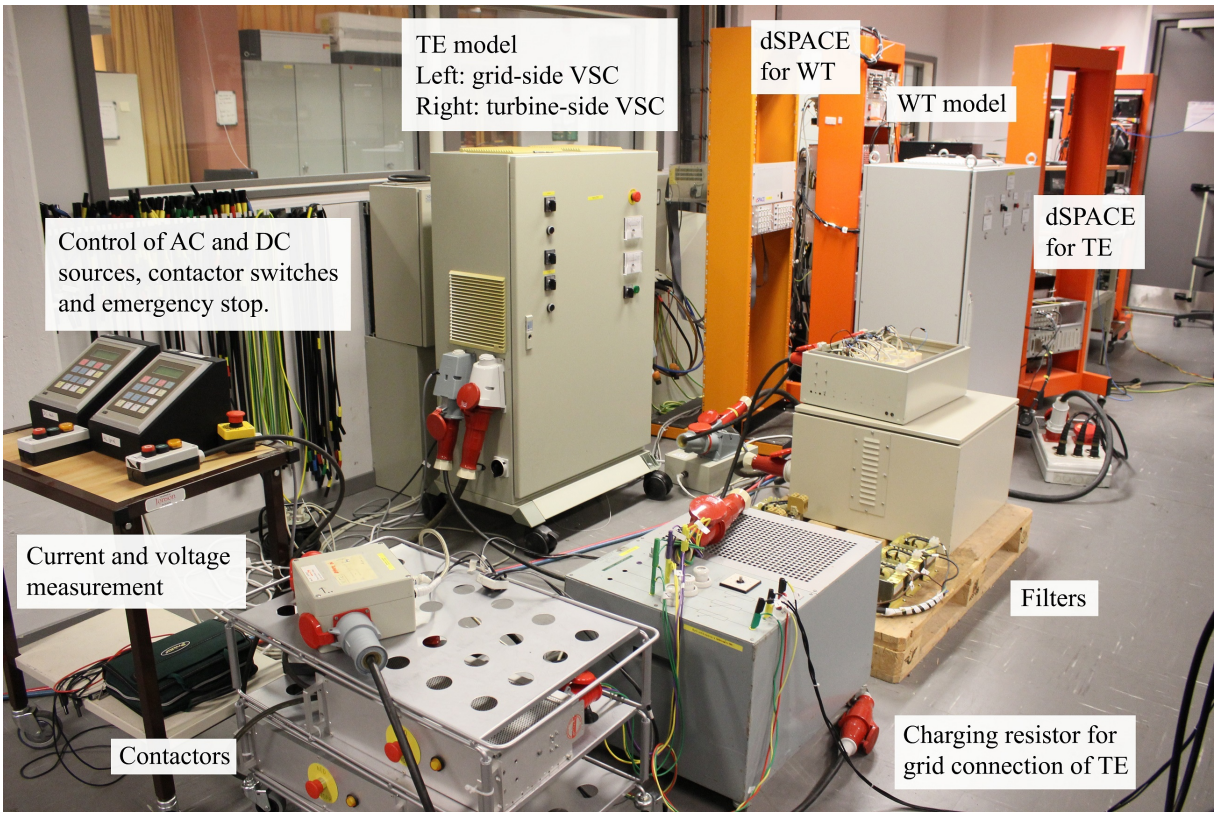

Fig. 7.2 Physical implementation of the laboratory setup.

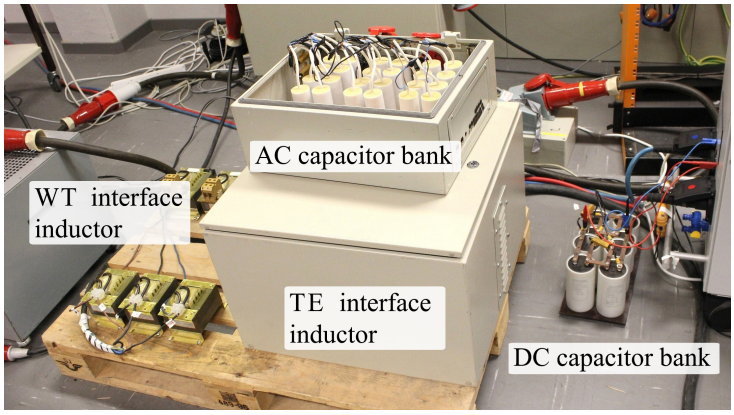

Fig. 7.3 AC and DC filter banks in the laboratory.

inductors L_1 and L_2 are connected directly to the 400 V AC system. The converter is a two-level VSC with 6 IGBTS, where the DC-link is fed by a DC machine rated in 700 V, 64 A, giving the possibility for the VSC to inject active power into the grid. Moreover, the DC voltage at the terminals of the machine is controlled to 650 V by an external drive system connected in its shaft. The converter is controlled by a DS1103 dSPACE system [76]. The discrete controller is built and compiled in Matlab R2011a [63]. The PWM switching frequency is set to 5 kHz and the

TABLE 7.2. CONTROL PARAMETERS FOR TESTING THE DIFFERENT CONTROL-LOOPS

Base values		400 V, 3 kVA
Base angular frequency	ω_s	314 rad/s
DC voltage		620 V
Current control bandwidth	α_c	$10\omega_\mathrm{s}$
DC voltage control bandwidth	α_d	ω_s
PLL bandwidth	α_p	$0.1\omega_\mathrm{s}$
Switching frequency of VSC	f_sw	5 kHz
Sampling time	t_s	0.2 ms

sampling time is 0.2 ms. For this test, the system parameters of the laboratory setup is given in Table 7.2. To evaluate the performance of the current controller, the reference current in both d and q axis is varied with a step function. Here, the peak value of the current is limited to 6.2 A. The resulting waveform of each current component is shown in Fig. 7.4.

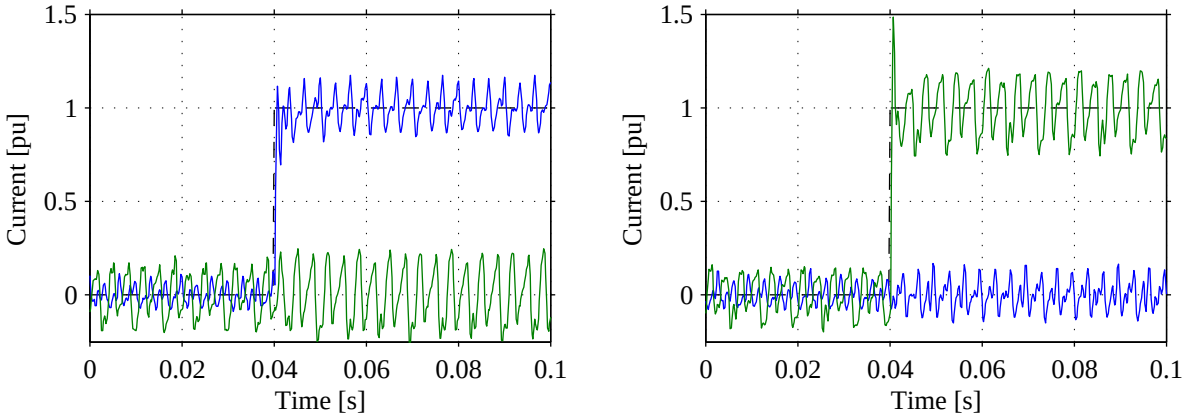

Fig. 7.4 Experimental validation of the implemented current controller. In plots: estimated active current $\hat{i}_{\mathrm{g,d}}$ (blue) and estimated reactive current $\hat{i}_{\mathrm{g,q}}$ (green). Plot (a): step response when reference current $i^*_{\mathrm{g,d}}$ (black-dashed) is varied. Plot (b): step response when reference current $i^*_{\mathrm{g,q}}$ (black-dashed) is varied.

From Fig. 7.4(a) and Fig. 7.4(b) it is possible to observe that the d-axis component of the current is decoupled from the q axis component, meaning that when the d-current is varied, the q-current remains unchanged and vice-versa. Moreover both step responses have similar rise times of about 1 ms. Observe, however, that due to the harmonic distortion present in the grid voltage at the moment of the test, as shown in Fig. 7.5(a), a large amount of harmonic content is seen also in the current, as depicted in Fig. 7.5(b). These harmonics are shown as an oscillatory component when the current vector is represented in a 50 Hz synchronously rotating dq-reference frame. The weakness introduced by the LCL filter of the wind turbine model in conjunction to the increased selected bandwidth of α_c of $10\omega_\mathrm{s}$ account for the fast overshoot seen when stepping the q-current. Moreover, since the controller is implemented in a digital system, delays due to discretization and computational time in the control system result in a phase shift between the actual grid voltage $\underline{e}_\mathrm{g}$ and the feed-forwarded grid voltage $\hat{\underline{e}}_\mathrm{g}^{(\mathrm{dq})}$ in the control scheme shown in

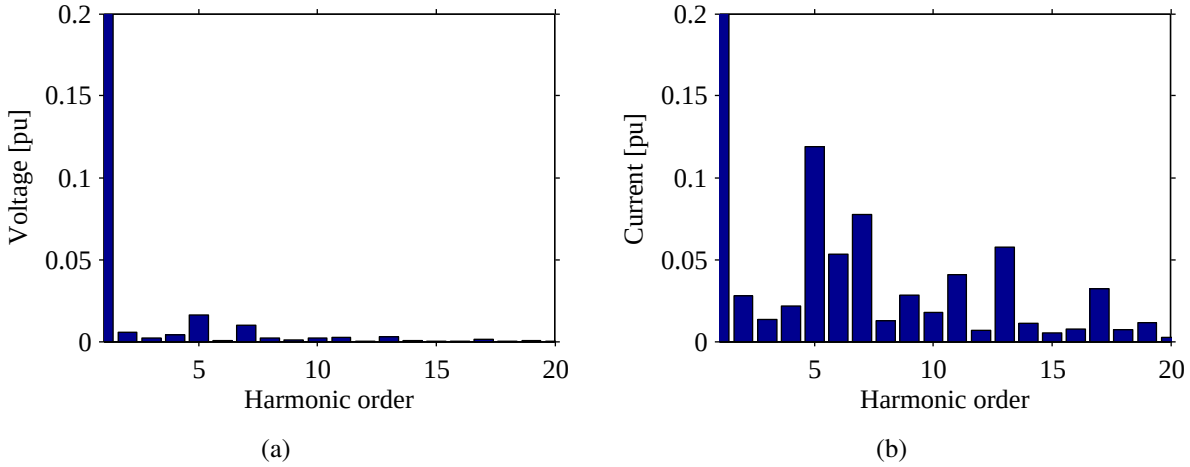

Fig. 7.5 FFT on the measured three-phase voltage (a) and current (b) when testing current control.

Fig. 4.2. In [77] and [78] it is discussed the use of an improved harmonic-compensated current controller in order to deal with harmonic disturbances. Note that the harmonics on the current are reduced when the voltage is imposed by the testing equipment, as later shown on this chapter. Moreover, in order to deal with the harmonics present in the grid, a LPF has been placed when feed-forwarding the grid voltage $\underline{\hat{e}}_{\mathrm{w}}^{(\mathrm{dq})}$ and $\underline{\hat{e}}^{(\mathrm{dq})}$ in both the current controller of the small-scale wind turbine model and on the grid-side VSC of the testing equipment, respectively. Here, the performance of the implemented current controller is found to be sufficient in controlling the d and q components of the current vector. Observe, however, that the final selected value of α_{c} is $2.5\omega_{\mathrm{s}}$ for the testing equipment and $2.0\omega_{\mathrm{s}}$ for the wind turbine model, as shown in Table 7.1. Finally, this example verifies the ability of the grid-connected VSC in controlling the current by using the discrete controller derived in Section 4.4.1.

7.2.2 DC voltage control in STATCOM operation

In this section, the implemented DC voltage controller given in Section 4.5.3 is validated laboratory experiment. With reference to Fig. 7.1, for this experiment, the DC voltage supply is disconnected from the grid-side VSC of the testing equipment, meaning that the converter is operated as a STATCOM [78]. The DC voltage reference is set to 660 V and varied with a step function to 680 V. In Fig. 7.6 is shown the step response of the implemented controller.

As shown in the figure, the voltage across the DC-link capacitance of the VSC is controlled in an smooth way. Observe that the shape of the step response resembles a first order system, as previously designed in Section 4.5.3.

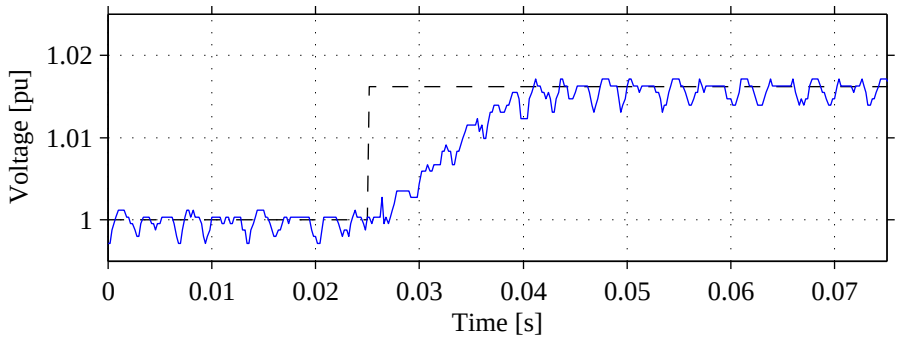

Fig. 7.6 Normalized step response of the implemented DC-link voltage controller: voltage reference (black dashed) and sampled voltage $\hat{u}_{\mathrm{dc}}$ of the VSC (blue).

7.3 Wind turbine model tested for LVRT in the laboratory

In the previous section the independent controllers for the grid-VSC of the test equipment have been verified. The wind turbine controller including PLL, current control and DC voltage control have been also tested in a similar way. Here, all the sub-modules that constitute the testing bench are integrated in one setup as shown in Fig. 7.1. In the following, the wind turbine model is tested against voltage dips including the recovery ramp, by means of the investigated VSC-based testing equipment.

7.3.1 LVRT test

In this scenario, the AC voltage at the terminals of the collector-VSC is reduced from 1 pu to 0.2 pu and maintained for approximately 400 ms. Afterwards, the voltage is restored back to 1 pu.

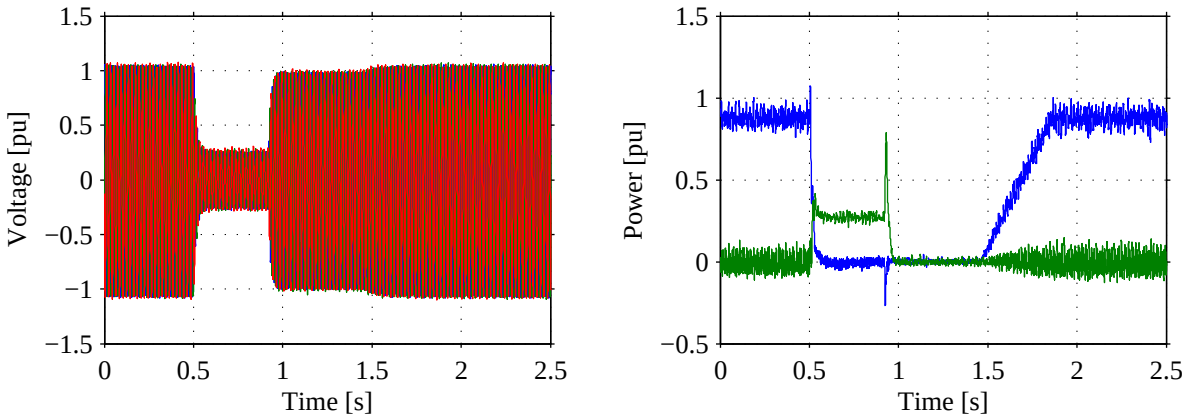

Fig. 7.7 Voltage dip test in laboratory setup: Plot (a): Three-phase voltage $\underline{e}_{\mathrm{w}}^{(\mathrm{abc})}$; Plot (b): active power P_{wt} (blue) and reactive power Q_{wt} (green) output of the wind turbine model.

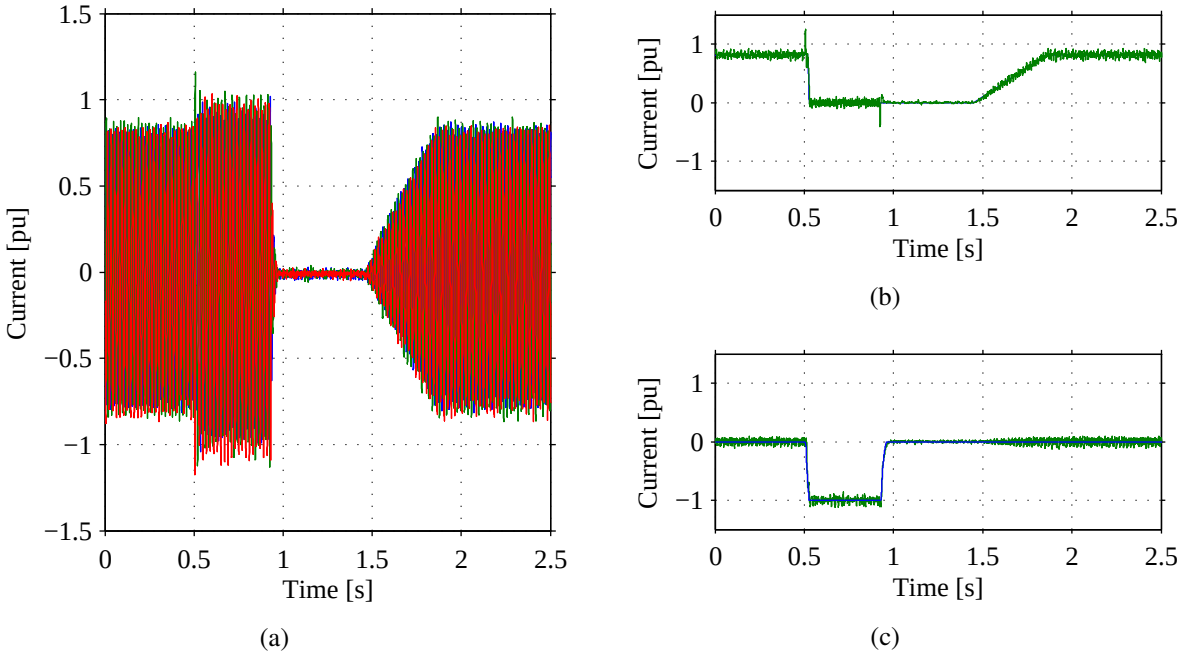

Fig. 7.8 Voltage dip test in laboratory setup. Plot (a): Three-phase current $\underline{i}_{\mathrm{w}}^{(\mathrm{abc})}$; Plot (b): Active reference current $i_{\mathrm{w_d}}^{*}$ (blue) and actual current $\hat{i}_{\mathrm{w_d}}$ (green); Plot (c): Reactive reference current $i_{\mathrm{w_q}}^{*}$ (blue) and actual current $\hat{i}_{\mathrm{w_q}}$ (green).

The three-phase voltage at the PCC is shown Fig. 7.7(a).

The pre-fault active power output is set to 0.9 pu with at unity power factor, as depicted in Fig. 7.7(b). Hence, three-phase current $\underline{i}_{\mathrm{w}}^{(\mathrm{abc})}$ and the active current $\hat{i}_{\mathrm{w_d}}$ are controlled in 0.9 pu, as shown in Fig. 7.8(a) and Fig. 7.8(b) respectively. The reactive current $\hat{i}_{\mathrm{w_q}}$ shown in Fig. 7.8(c) is set to 0 pu prior the emulated fault. The wind turbine model is equipped with the LVRT current control strategy similar to the one given in the German grid code.

Observe that it is the terminal voltage $\underline{u}$ of the testing equipment shown in Fig. 7.1 that is controlled at 1 pu before applying the voltage dip, meaning that the reference voltage is directly applied to the PWM. The excess of voltage drop across the inductances L_3, L_4 and L_5 implemented in the laboratory setup are not being compensated in the open-loop voltage controller. Moreover, the operating condition of the wind turbine model affects the PCC voltage in steady-state. For this reason, with reference to Fig. 7.7 at 0 s, the resulting PCC voltage $\underline{e}^{(\mathrm{abc})}$ shown in Fig. 7.7(a) is found to be 1.03 pu, approximately.

At 0.5 s the terminal voltage $\underline{u}$ is dropped to 0.2 pu. The PCC voltage is also in proximity to 0.2 pu slightly boosted by the reactive power injected by the wind turbine model. In order to increase the reactive current to 1 pu after detecting the fault, the active current must be kept at 0 pu during the dip, as shown in Fig. 7.8(b). Observe in Fig. 7.8(c) that the reactive current is controlled at 1 pu. The maximum reactive power injected reaches 0.3 pu approximately during the period where the voltage is minimum. When the voltage is restored at 0.9 s, the wind turbine model cease of injecting reactive power into the grid; however, the algorithm of voltage/reactive power compensation is still active for 500 ms after the voltage is back to normal operation. As discussed

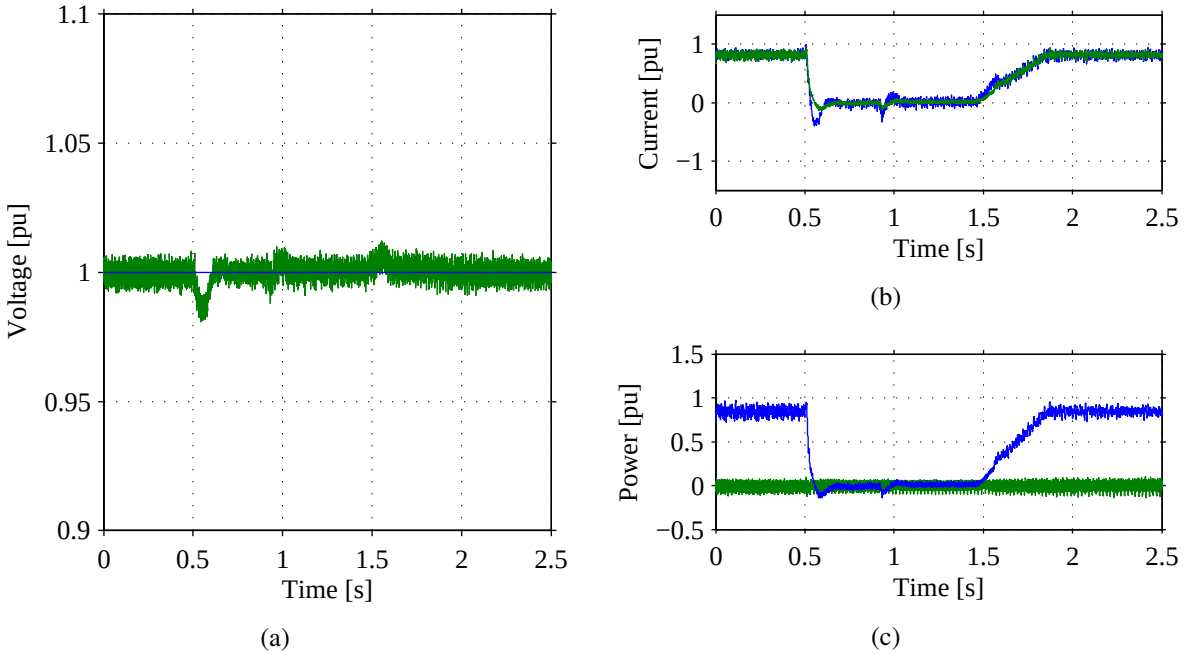

Fig. 7.9 Voltage dip test in laboratory setup. Plot (a): DC voltage in testing equipment $\underline{u}_{\mathrm{dc}}$; Plot (b): Active reference current $i^*_{\mathrm{g_d}}$ (blue) and actual current $\hat{i}_{\mathrm{g_d}}$ (green) of gird-side VSC of testing equipment; Plot (c): Active power P_{grid} (blue) and reactive power Q_{grid} (green) output of the testing equipment.

in the previous chapter, two voltage dips can be experienced at the terminals of the wind turbine in case of automatic reclosure if a grid fault in the power system is not cleared. For this reason, the active current is still set to 0 pu while the LVRT control strategy actively monitors the PCC voltage in order to supply reactive current if a second voltage dip is experienced. After 500 ms it is assumed that the system is back into normal operation. At 1.5 s active power production is restored by slowly removing a limiter in the active current set-point. Finally, within the next 400 ms the active current is restored back to its pre-fault value.

The effectiveness of the testing equipment in controlling the DC voltage during the test while maintaining a reliable operation is analysed as follows. The DC voltage of the back-to-back converter $\underline{u}_{\mathrm{dc}}$ is shown in Fig. 7.9(a). The active current reference $i^*_{\mathrm{g_d}}$ and actual current $\hat{i}_{\mathrm{g_d}}$ of gird-side VSC of testing equipment are plotted in Fig. 7.9(b) with blue and green traces, respectively. Finally, the active power P_{grid} and reactive power Q_{grid} output of the testing equipment is shown in Fig. 7.9(c), with blue and green traces, respectively.

Observe that, when the active power of the wind turbine P_{wt} is varied rapidly from 0.9 pu to 0 pu in less than 50 ms, the voltage u_{dc} of the testing equipment is controlled at 1 pu, with a small variation of 0.03 pu during the execution of the voltage dip. The AC system, in which the grid-side VSC of the testing equipment is connected to, imposes the voltage $\underline{e}_{\mathrm{g}}$ at 1 pu. Finally, the current output $\underline{i}_{\mathrm{g}}$ is controlled within the rated values.

In the following, the testing equipment performs a voltage dip with the inclusion of the recovery ramp as given in the selected Grid Codes.

7.3.2 LVRT test including recovery ramp

In this scenario, the wind turbine model is tested for LVRT including the recovery ramp, similar to the one given in the German Grid Code. The voltage profile is described as follows: first, the voltage is reduced from 1 pu to 0.2 pu and maintained for 500 ms. Afterwards, the voltage is brought back to 1 pu with a ramp function that lasts for 1 second. The LVRT control strategy is also implemented in the wind turbine model and the initial conditions are maintained (full active power production at unity power factor). The results from this experiment are given in Fig. 7.10.

The PCC voltage shown in Fig. 7.10(a) follows the LVRT voltage profile, which is given as a reference in the turbine-side VSC of the testing equipment. As shown in Fig. 7.10(b), at 0.5 s when the voltage is reduced, the wind turbine model injects the required reactive power. Moreover, the reactive current $\hat{i}_{\mathrm{w_q}}$ shown in Fig. 7.10(d) is controlled at 1 pu at the moment of the voltage dip while the active current is $\hat{i}_{\mathrm{w_d}}$ set to 0 pu. As a result, the PCC voltage is boosted

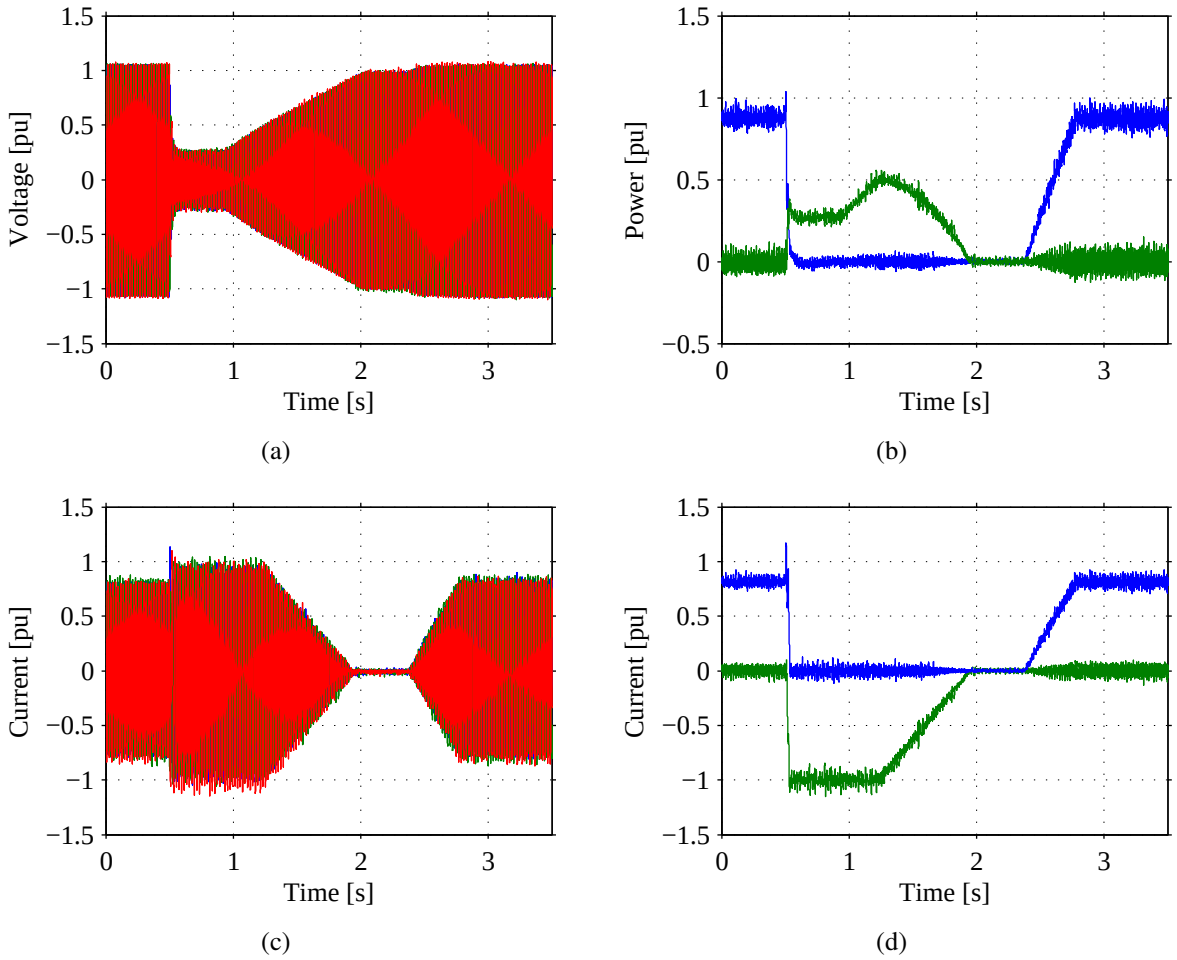

Fig. 7.10 LVRT test in laboratory setup: Plot (a): Three-phase voltage $\underline{e}_{\mathrm{w}}^{(\mathrm{abc})}$; Plot (b): Active power P_{wt} (blue) and reactive power Q_{wt} (green) output of the wind turbine model. Plot (c): Three-phase current $\underline{i}_{\mathrm{w}}^{(\mathrm{abc})}$; Plot (b): Active current $\hat{i}_{\mathrm{w_d}}$ (blue) and reactive current $\hat{i}_{\mathrm{w_q}}$ (green).

by the reactive power injected by the wind turbine model, reaching a minimum value of 0.3 pu during the fault, while the three-phase current $\underline{i}_{\mathrm{w}}^{(\mathrm{abc})}$ is maintained at 1 pu.

The recovery of the voltage start at $t = 1$ s when the voltage is ramped from 0.2 pu to 1.0 pu for 1 second. Observe that the reactive current reference is maintained at 1 pu when the PCC voltage is still below 0.5 pu. For this reason, the reactive power is increasing with the voltage, reaching its maximum of 0.5 pu at 1.25 s. Afterwards, the reactive current $\hat{i}_{\mathrm{w_q}}$ is linearly reduced, as depicted in Fig. 7.10(d), according to the retained voltage at the PCC when this is above 0.5 pu. As a consequence, the reactive power decreases when the voltage increases towards 1 pu.

At 2 s the reactive current is set to 0 pu, meaning that the PCC voltage is recovered from the fault. After 500 ms, the wind turbine model resumes active power production by removing a limitation over $\hat{i}_{\mathrm{w_d}}$ with a controlled ramp function. Full active power production is achieved at 2.75 s.

Finally, in this example the active power production is brought to 0 pu resembling the action of a crowbar protection placed at the DC-link of the FPC wind turbine which can redirect the produced power into a chopper resistor (see Section 6.3.1). Other alternative control actions such as pitch control [24] have not been mimicked by the wind turbine model.

In the next experiment, the response of the modelled wind turbine is studied when no LVRT control strategy is implemented and the power reference is maintained during the complete event.

7.3.3 LVRT test with constant power output

Not all the Grid Codes require that wind turbines must support the grid by injecting reactive current in case of voltage dip. For this reason, it is of interest to investigate the case where a wind turbine that controls the reactive current at 0 pu during LVRT. For this experiment, the wind turbine is operating with a power reference of 0.6 pu. The voltage is controlled at 1 pu and it is reduced to 0.6 pu for 1.3 s, followed by a recovery ramp for 700 ms towards 1 pu. The results of this experiment are given in Fig. 7.11.

The resulting voltage is shown in Fig. 7.11(a). The minimum voltage is 0.65 pu slightly boosted by the capacitor bank C_3. From Fig. 7.11(b) it is possible to observe that the active power is kept at 0.6 pu during the voltage dip. In order to deliver the generated power during a voltage reduction, the active current $\hat{i}_{\mathrm{w_d}}$ plotted in Fig. 7.11(c) must increase to its maximum permitted value of 1 pu. From the figure it is possible to observe that there is no reactive current injection ($\hat{i}_{\mathrm{w_d}}$ = 0 pu), meaning that the reactive power is set at 0 pu during the whole event.

Finally, at 1.3 s the voltage starts to increase. The active current is decrease accordingly so the power output P_{wt} is kept constant during the recovery. The voltage reaches 1 pu at 2 s. The active current is set to its pre-fault value of 0.6 pu. The variation of the active current allows that the active power is kept constant during the whole event. This control feature on wind turbines is useful when disconnection of the wind turbine is not allowed if a steady-state voltage reduction is present in the grid.

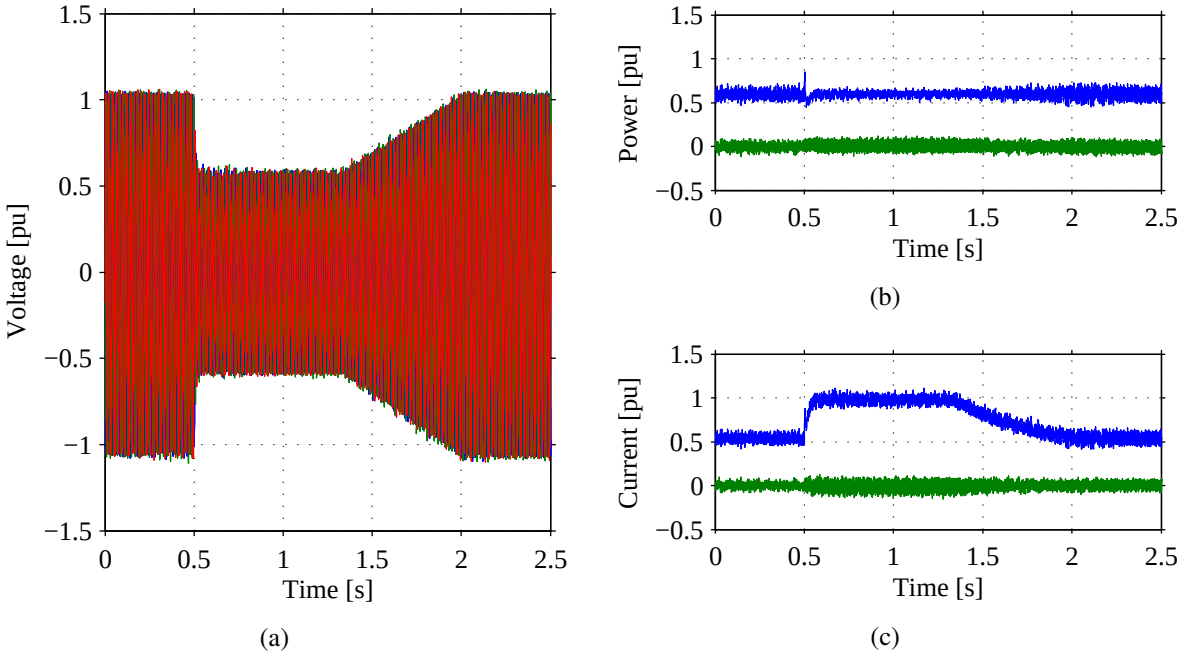

Fig. 7.11 LVRT test with constant power in laboratory setup: Plot (a): Three-phase voltage $\underline{e}_{\mathrm{w}}^{(\mathrm{abc})}$; Plot (b): Active power P_{wt} (blue) and reactive power Q_{wt} (green) output of the wind turbine model. Plot (c): Active current $\hat{i}_{\mathrm{w_d}}$ (blue) and reactive current $\hat{i}_{\mathrm{w_q}}$ (green).

7.4 Testing for consecutive three-phase voltage dips

In this test, the wind turbine model is tested against two consecutive voltage dips. Here, the testing equipment reproduces the reclosure action of a circuit breaker in the presence of an uncleared fault. The result is given in Fig. 7.12. The resulting wind turbine voltage is shown in Fig. 7.12(a). At $t = 5$ s the voltage is dropped to 0.2 pu for 100 ms. Subsequently, the voltage is restored to 1 pu and maintained for an extra 200 ms when another voltage dip is reproduced for an extra 100 ms. In order to stress the system even more and to simulate a fault in the vicinity of the wind turbine system, the ramp-rate limiter has been increased. For this reason, a transient is experienced at each voltage dip, as shown in Fig. 7.12.

As previously discussed, the wind turbine reacts by injecting reactive current. Observe in Fig. 7.12(b) that the current $\underline{i}_{\mathrm{w},2}$ peaks to 1.5 pu due to the fast change over the capacitor C_3 (where the voltage $\underline{e}_{\mathrm{w}}$ is measured). The LVRT control strategy quickly controls the active current $\hat{i}_{\mathrm{w_d}}$ to 0 pu while increasing the reactive current $\hat{i}_{\mathrm{w_q}}$ to -1 pu, busting the voltage to 0.3 pu with 0.3 pu reactive power shown in green traces in Fig. 7.12(c)

The second voltage dip occurs only 250 ms after the recovery of the first one ($t = 0.45$ s). For this reason, the implemented control strategy maintains the active current $\hat{i}_{\mathrm{w_d}}$ at 0 during the second event. As a result, the current does not peak as compared from the first event. After the second voltage dip is cleared, the wind turbine control strategy maintains the limitation in the active power for 500 ms. Since no more voltage variation are experienced, the active power is ramped to 0.9 pu.

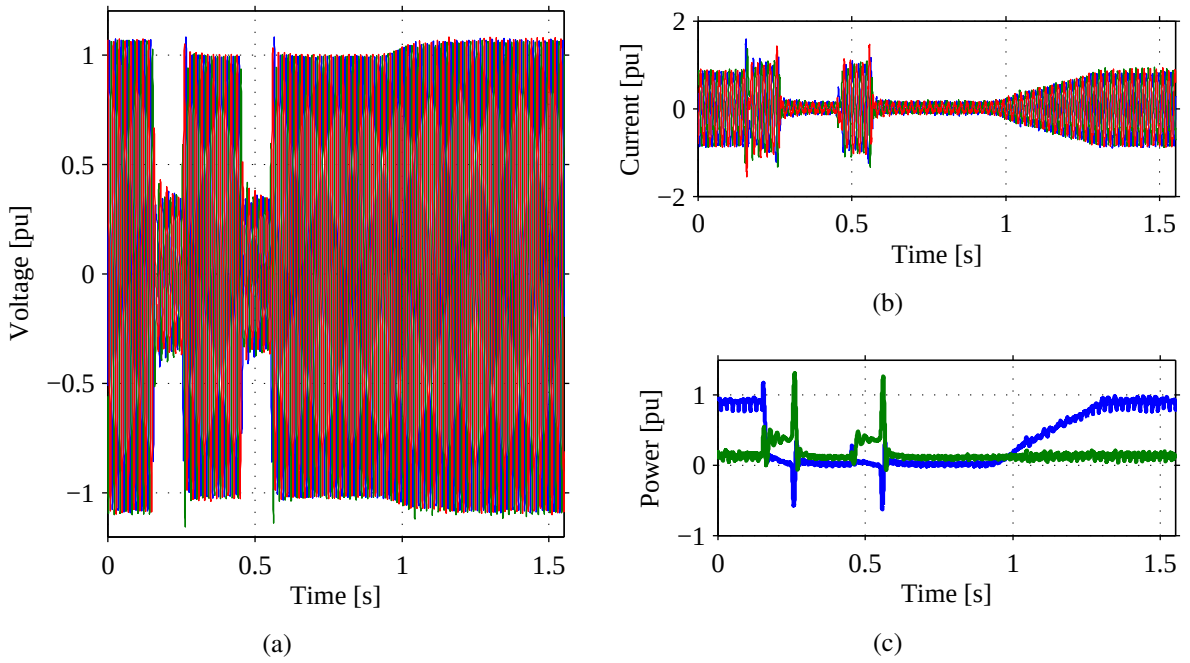

Fig. 7.12 Consecutive voltage dip test in laboratory setup. Plot (a): Three-phase voltage $\underline{e}_{\mathrm{w}}$; Plot (b): Three-phase current $\underline{i}_{\mathrm{w},2}$; Plot (c): Active power P_{wt} (blue) and reactive power Q_{wt} (green) output of the testing equipment.

7.5 Testing for unbalanced voltage dip

In this section, the testing equipment is used to create an unbalanced voltage dip. The unbalanced condition at the output of the turbine-side VSC of the testing equipment is achieved by varying independently each phase component of the reference voltage $\underline{u}^{(\mathrm{abc})*}$, before being sent into the PWM block. In the following, test results from two-phase and consecutive single-phase voltage dip tests are presented.

7.5.1 Single-phase voltage dip

The first scenario corresponds to a single-phase voltage dip applied to the wind turbine model. The test is performed by varying phase a of the voltage vector $\underline{u}^{(\mathrm{abc})*}$ from 1 pu to 0.2 pu for 100 ms. The results of this experiment are first shown in Fig. 7.13.

Given the interfacing impedance existing between the testing equipment and the wind turbine, the resulting magnitude of voltage $\underline{e}_{\mathrm{w}}$ is dropped to 0.75 pu, as shown Fig. 7.13(a) in black traces. The mean value of the wind turbine output active and reactive power are highlighted in Fig. 7.13(b) in blue and green traces, respectively. Observe in the figure that the active power dropped to 0.5 pu, mainly due to the high retained voltage at the wind turbine terminals.

The frequency of the oscillatory component of the d and q wind turbine currents plotted in Fig. 7.13(d) is 100 Hz, which corresponds to the negative sequence at fundamental frequency seen on the dq-reference frame. Note that these oscillations are also present in the d and q voltage

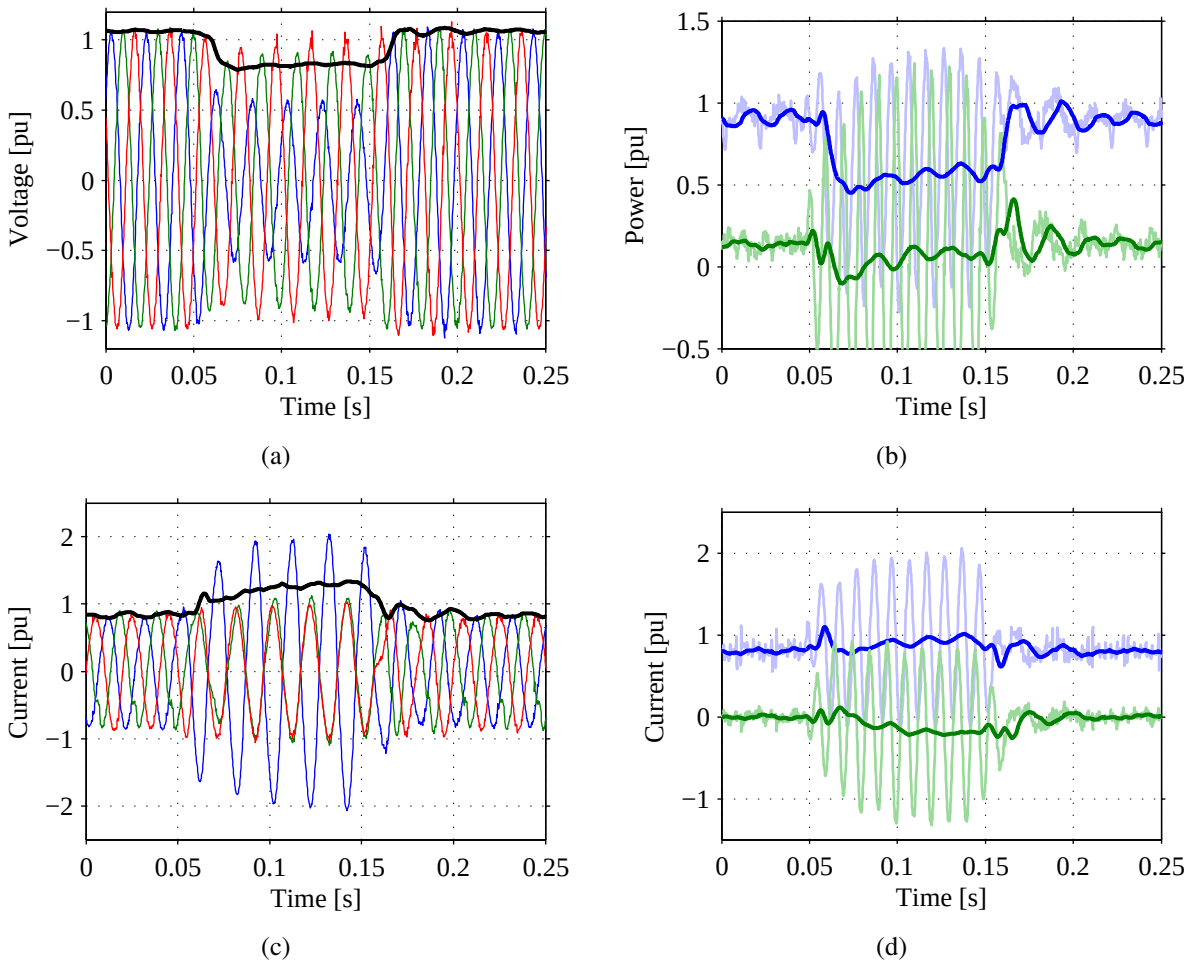

Fig. 7.13 Single-phase voltage dip in laboratory setup : Plot (a): Three-phase voltage $\underline{e}_{\mathrm{w}}$ and its magnitude (black); Plot (b): Active power P_{wt} (blue) and reactive power Q_{wt} (green) output of the wind turbine model and their mid values. Plot (c): Three-phase current $\underline{i}_{\mathrm{w}}$ and its magnitude (black); Plot (d): Active current $\hat{i}_{\mathrm{w_d}}$ (blue) and reactive current $\hat{i}_{\mathrm{w_q}}$ (green) with their mid values.

components of $\underline{e}_{\mathrm{w}}^{(\mathrm{dq})}$ which also affects the performance of both the current control and the LVRT control. For this reason, the current $\hat{i}_{\mathrm{w_d}}$ and $\hat{i}_{\mathrm{w_q}}$ are not properly controlled during the unbalanced voltage dip. Note that the actual rating of the testing setup shown in Fig. 7.1 is 400 V, 100 kVA, while the value of the base power utilized on the control of the VSCs and on the plotting of the results is selected at 300 V, 8 kVA (see Table 7.1). In addition, the protection system of the laboratory setup has not been downscaled. For these reasons, this particular setup allows for a 2 pu transient current, as shown in Fig. 7.13(d).

As discussed during this section, testing for unbalanced voltage dip is one of the most stressful test that can be carried out on the generating unit, especially if the wind turbine under test can experience an oscillatory response. Although it has been shown that the turbine-side of the testing equipment is capable of reproducing these type of faults, it is of interest to observe the impact of these type of tests on the grid-side of the testing setup. Observe that the oscillatory active power P_{wt}, shown in Fig. 7.13(b), can be a great disturbance for the DC voltage control-loop of

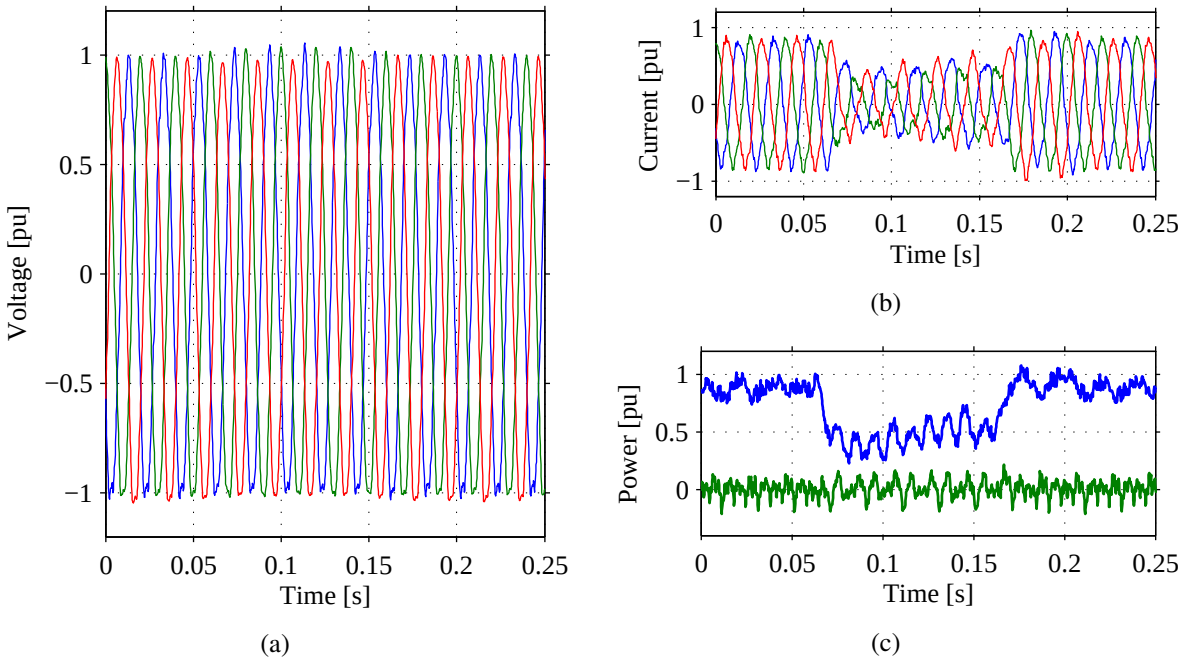

Fig. 7.14 Single-phase voltage dip in laboratory setup. Plot (a): Three-phase grid voltage $\underline{e}_{\mathrm{g}}$; Plot (b): Three-phase grid current $\underline{i}_{\mathrm{g}}$; Plot (c): active power P_{grid} (blue) and reactive power (green) Q_{grid} output towards AC grid.

the testing equipment. For this reason, the performance of the testing device in maintaining a reliable grid-operation during the test must be addressed. The focus will be on the three-phase grid voltage $\underline{e}_{\mathrm{g}}$, the grid current $\underline{i}_{\mathrm{g}}$ and on the active and reactive power output P_{grid} and Q_{grid}, respectively, of the grid-side of the testing system.

Figure 7.14(a) shows the three-phase grid voltage $\underline{e}_{\mathrm{g}}$. Observe that for the major part of the time the voltage is balanced. However, a small unbalanced voltage can be seen between 0.06 s to 0.15 s. This unbalance is mainly due to the fact that the grid voltage at the measurement point is decoupled from the grid by the inductor L_1 and can be easily affected by the negative sequence component that is present in the unbalanced current shown in Fig. 7.14(b). Moreover, the active power oscillation experienced between the wind turbine and the testing equipment (P_{wt} in Fig. 7.1) also affects the output power P_{grid} injected by the testing system into the interconnecting grid, as depicted in blue traces in Fig. 7.14(c). Specialized positive and negative sequence controllers such as the one described in [70] can be of use on both the grid-side of the testing equipment and also on the wind turbine system controllers, if an evident mitigation of the oscillatory response is needed.

7.5.2 Consecutive two-phase voltage dips

In the following experiment, the wind turbine system is tested against two consecutive two-phase voltage dips. Here, only the resulting wind turbine voltage $\underline{e}_{\mathrm{w}}$ and output current $\underline{i}_{\mathrm{w},2}$ active P_{wt} and reactive Q_{wt} power are plotted. The results are given in Fig. 7.15. As for the previous study,

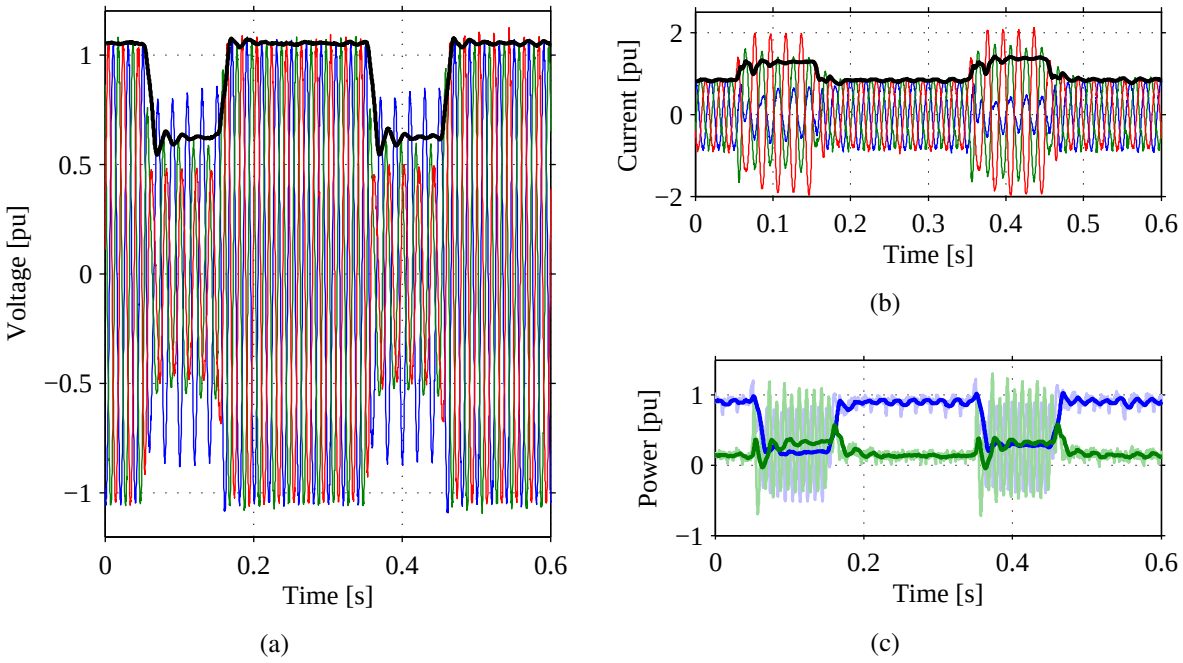

Fig. 7.15 Two-phase voltage dip in laboratory setup. Three-phase voltage $\underline{e}_{\mathrm{w}}$ and its magnitude (black); Plot (b): Active power P_{wt} (blue) and reactive power Q_{wt} (green) output of the wind turbine model and their mean values. Plot (c): Three-phase current $\underline{i}_{\mathrm{w}}$ and its magnitude (black); Plot (d): Active current $\hat{i}_{\mathrm{w_d}}$ (blue) and reactive current $\hat{i}_{\mathrm{w_q}}$ (green) with their mean values.

the wind turbine controller is affected by the negative sequence component measured in both the voltage and the current.

The unbalance condition is here achieved by varying phase a and phase b from 1 pu to 0.2 for 100 ms. The resulting wind turbine voltage $\underline{e}_{\mathrm{w}}^{(\mathrm{abc})}$ and its magnitude are shown in Fig. 7.15. Observe that the resulting minimum voltage on the faulted phases is 0.5 pu approximately, while the magnitude of the complete voltage vector is 0.65 pu. The resulting voltage is, however, sufficiently low to lead to a reduction of the active power production down to 0.15 pu, while the reactive power is increased to 0.3 pu, as shown in Fig. 7.15(c). The resulting wind turbine current is depicted Fig. 7.15(b) including its magnitude. Although the instantaneous value of $\underline{i}_{\mathrm{w}}$ reaches 0.2 pu for one of the phases, the magnitude value is controlled in proximity 1 pu during the voltage dip.

The second voltage dip occurs at 0.35 s and lasts for another 100 ms. The system under test respond in a similar way with respect to the first voltage dip. The magnitude of the current is controlled at 1 pu, as seen from the black curve in Fig. 7.15(b). The LVRT algorithm reacts against the voltage dip by reducing the actual active power production in order to increase the reactive power injection into the imposed grid. The injected reactive power and the reduced active power of the wind turbine are both coincidentally set to 0.2 pu during the dip. Note that the set-point of the wind turbine during LVRT is dependent on the pre-set priority of the q-current over the d-current together with the level of the retained voltage.

Observe, however, that the active power is quickly brought to its pre-fault value, as seen in

Fig. 7.15(c), as soon as the voltage is restored, meaning that the 500 ms waiting time, required by some of the selected Grid Codes, is ignored by the wind turbine controller. The performance observed on the response of the LVRT control is mainly due to the negative sequence component in both current and voltage when these quantities are transferred into the dq-coordinates.

The reactive power set-point and therefore the resulting limitation on the active power controller during the fault is strictly related to the time instance during the fundamental period in which the voltage dip is executed, especially if an unbalance dip is reproduced and therefore an oscillatory component is present in the measured voltage $\underline{e}_{\mathrm{w}}^{(\mathrm{dq})}$. The latter voltage is the input signal of the LVRT control algorithm, as shown in Fig. 4.15 where the control diagram of the modelled wind turbine system is depicted. For this reason, the resulting wind turbine set-point slightly differs from each-other. Nevertheless, the overall response of the wind turbine system can be improved if a positive and negative sequence current controllers are implemented.

7.6 Grid emulator algorithm in open-loop

In this test, the testing equipment is used to emulate the effect of a weak grid at the terminals of the tested wind turbine. The current $\underline{i}_{\mathrm{w},2}^{(\mathrm{dq})}$ is measured by the testing equipment and the reference voltage of the turbine-side VSC of the testing device is varied according to (6.6).

Similar to what has been discussed in Section 6.4.3, curves for the resulting voltage and wind turbine operating point for different levels of stiffness are combined and shown in Fig. 7.16. Starting with a stiff regulation in open-loop, the resulting voltage and wind turbine active and reactive power output are depicted in black traces in Fig. 7.16(a), Fig. 7.16(b) and Fig. 7.16(c), respectively.

Observe in Fig. 7.1 that the passive components between the testing equipment and the modelled wind turbine system will affect the resulting current that is used when calculating the voltage drop over the virtual impedance. For the following grid emulated scenarios, the output voltage reference of the turbine-side VSC of the testing equipment has been slightly modified so that the pre-fault wind turbine voltage is always 1 pu (300 V). The pre-fault reactive power is 0.15 pu, as seen in Fig. 7.16(c) at 0 s.

Although the reference voltage (shown in black dashed traces in Fig. 7.16(a)) is set to 0.3 pu for 500 ms, the resulting magnitude of the wind turbine voltage $|\underline{e}_{\mathrm{w}}|$ reaches 0.41 pu, as shown in black traces, together with 0 pu of active power and 0.45 pu of reactive power. The wind turbine start to increase the active power output 500 ms after the voltage is restored. Full active power production is restored at 1.7 s.

In the following, a short-circuit power of 10 pu is emulated and the same voltage dip to 0.3 pu for 500 ms is applied. The resulting waveforms are plotted in Fig. 7.16 in blue traces. Observe that the voltage is now boosted above 0.55 pu due to the 0.5 pu of reactive power injected. The increased voltage allows for the active power set-point to be 0.25 pu, meaning that the LVRT control algorithm does not reduce the active current $i_{\mathrm{w_d}}$ completely to zero, as compared to the previous case. The wind turbine model maintains the active current set-point for 500 ms after the voltage is restored to 1 pu. Afterwards, the power is ramped to 0.9 pu.

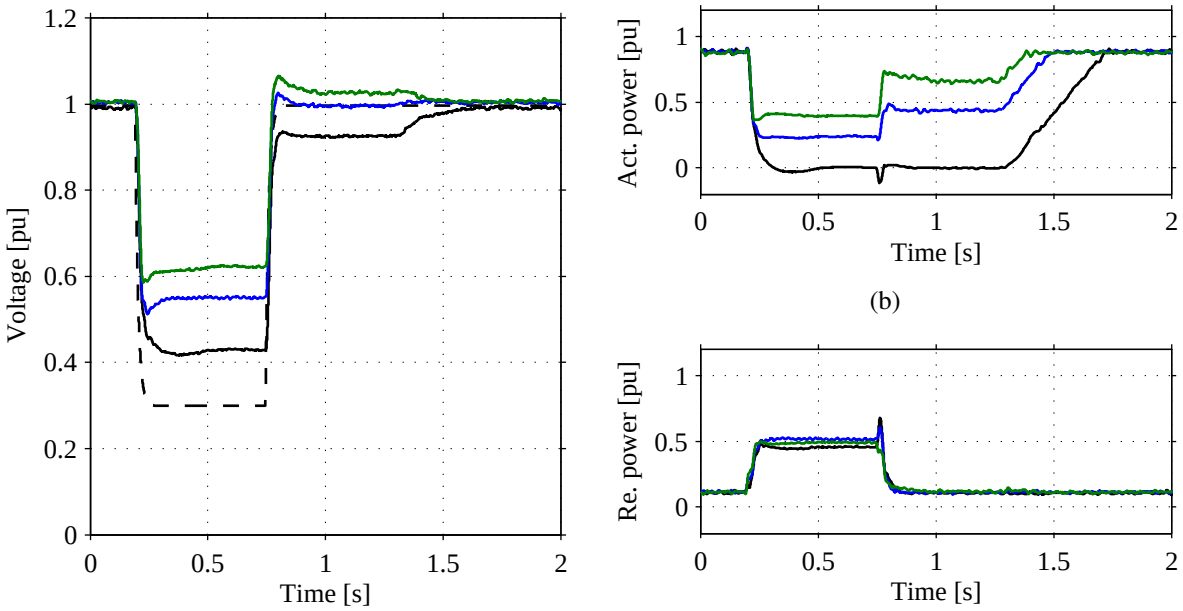

Fig. 7.16 Voltage dip test with impedance emulation by test equipment. Plot (a): voltage magnitude $|\underline{e}_{\mathrm{w}}|$; Plot (b): active power output, and Plot (c): reactive power output of wind turbine model. In plots: dashed-black: voltage reference in test equipment; black-solid: results when using open-loop control without grid emulation; blue: emulated grid of 10 pu; green; emulated grid of 2 pu.

The wind turbine LVRT control waits between 10 to 20 ms after acknowledging the fault in order to freeze the active current $i_{\mathrm{w_d}}$. The different active and reactive power curves seen between 0.25 s and 0.5 s are mainly due to the interaction of the capacitive and inductive elements of the actual circuit together with the virtual impedance emulation control in the test equipment.

Finally, the third scenario corresponds to the weakest emulation of a short-circuit power of 2 pu. The results are plot in Fig. 7.16 with green traces. An increased value for the virtual impedance results in a greater impact of the reactive current on the PCC voltage. In this case study, the voltage peaks at 0.62 pu during the dip. The reactive power is always in proximity to 0.5 pu, meaning that the reactive current $i_{\mathrm{w_q}}$ is reduced as the voltage reaches higher levels, depending on the emulated short-circuit power. The current $i_{\mathrm{w_d}}$ is maintained for 500 ms after the dip. The active power is restored to 0.9 pu at 1.5 s. Note that the initial retained voltage of 0.3 pu in conjunction to the different emulated short-circuit power allow for a partial reduction of the active power set-point. Moreover, the simulation results given in Section 6.4.3 lead to a complete reduction of the active power in all simulated grid-scenarios, while the reactive power was varied in function of the retained voltage.

7.7 Test for phase-angle variation

In this test, the testing equipment is used to vary the angle of the applied voltage. The wind turbine model is here operated in steady-state and a 20 degrees phase shift is applied at the

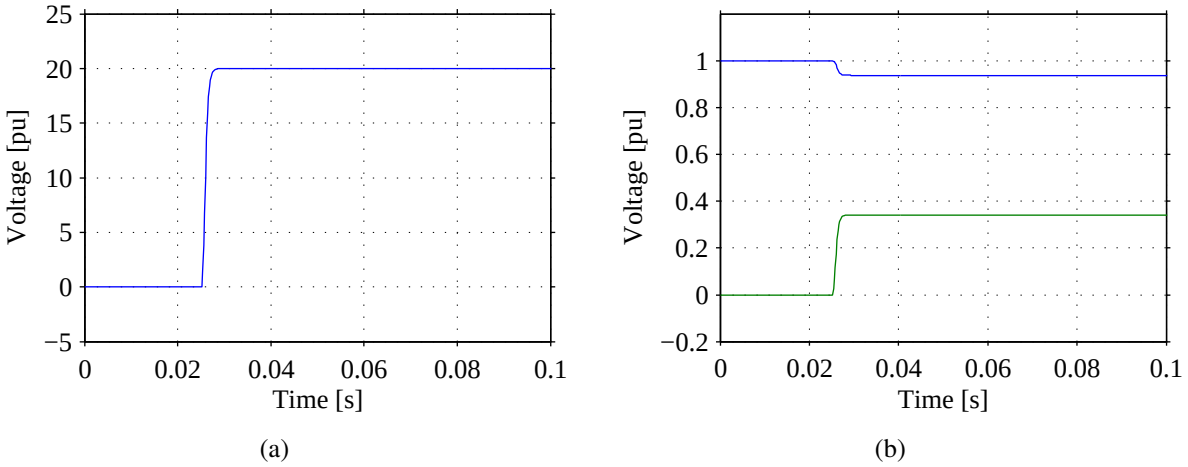

Fig. 7.17 Phase-angle variation test in the laboratory. Plot(a): Phase-angle jump in testing equipment controller; Plot(b): d (blue) and q (red) components of the terminal voltage $\underline{u}$ in test equipment.

reference voltage $\underline{u}^{(dq)^*}$. The step applied in the angle is shown in Fig. 7.17(a) and the resulting d and q components of the reference voltage are shown in Fig. 7.17(b) in blue and green traces, respectively. The step function has been filtered with a LPF which delays the signal 3 ms approximately, in order to represent a typical phase-angle variation [79]. The effect of the filter can be seen in both the angle and on the varied voltage components.

The wind turbine model is operated at 0.9 pu and its reactive power output is kept at 0 pu. The results of the experiment is shown in Fig. 7.18. In the figure, the blue curves correspond of the response of the system when $\alpha_{\mathrm{p,w}}$ is set at $0.2\omega_{\mathrm{s}}$, while the black curves correspond to the results when $\alpha_{\mathrm{p,w}}$ is set at $0.05\omega_{\mathrm{s}}$. For both scenarios, plots for PLL measured frequency and power output are given in Fig. 7.18.

Adding a phase-shift on the angle of the applied voltage is a perturbation to the PLL. The effect of the applied angle variation can be seen on the estimated angular frequency $\hat{\omega}_{\mathrm{s}}$ shown in Fig. 7.18(a). When increasing the PLL bandwidth, the phase-angle variation seems to disrupt the estimated frequency in a harsh way. In addition, the wind turbine PLL integrates the estimated frequency $\hat{\omega}_{\mathrm{s}}$ in order to obtain the angle needed when transforming the measured voltage and current from $\alpha\beta$ to dq-coordinates. Reducing the PLL bandwidth gives a smooth response against phase-angle variations, thus, the transformation angle and therefore the whole dq frame is less perturbed. Using a reduced bandwidth on the PLL implemented of the generating unit helps the system to be less oscillatory against these type of perturbations.

The selection of the PLL bandwidth affects the transients in both the active power and reactive power output, as shown in Fig. 7.18(b) and Fig. 7.18(c), respectively. Observe that large transients can be experienced on the wind turbine operating point, especially if a greater PLL bandwidth is used, as depicted in blue traces. Again, a decreased bandwidth helps to reduce the effect of the perturbation on the power output of the generating unit, as seen in the amplitude of the oscillation depicted with black traces.

Observe the effect of the phase-angle shift in the current output of the wind turbine system $\underline{i}_{\mathrm{w},2}^{(abc)}$.

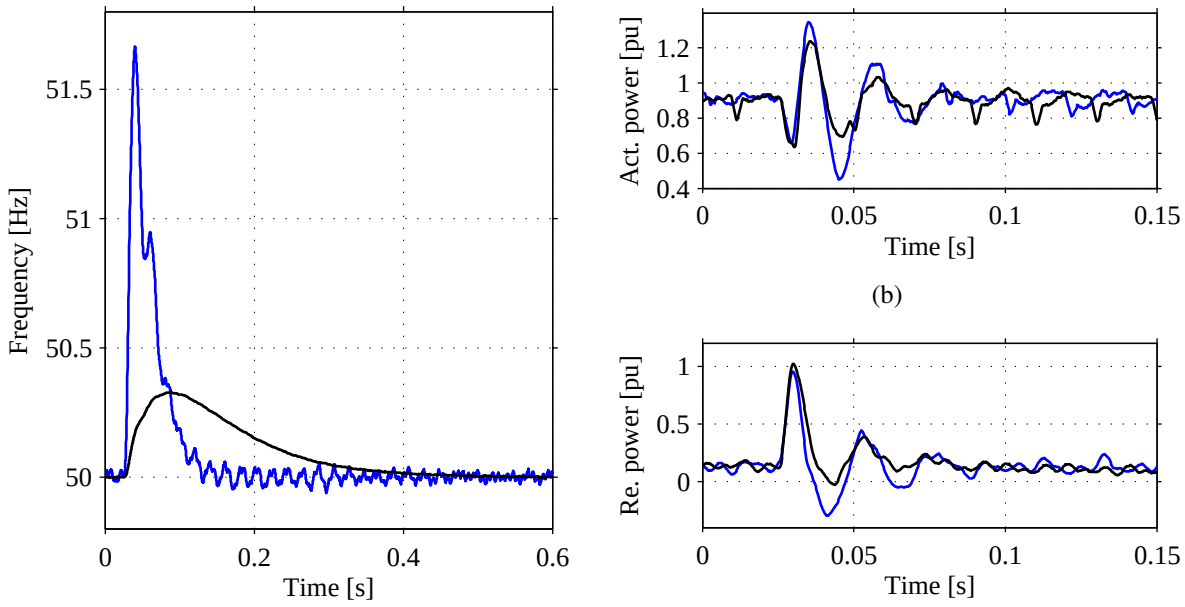

Fig. 7.18 Phase-angle variation test in the laboratory. Plot (a): measured angular frequency $\hat{\omega}_{\mathrm{s}}$ by wind turbine PLL. Plot (b): active power output. Plot (c): reactive power output of the modelled wind system. In plots: system response when $\alpha_{\mathrm{p,w}}$ is set at $0.2\omega_{\mathrm{s}}$ (blue) and $0.05\omega_{\mathrm{s}}$ (black).

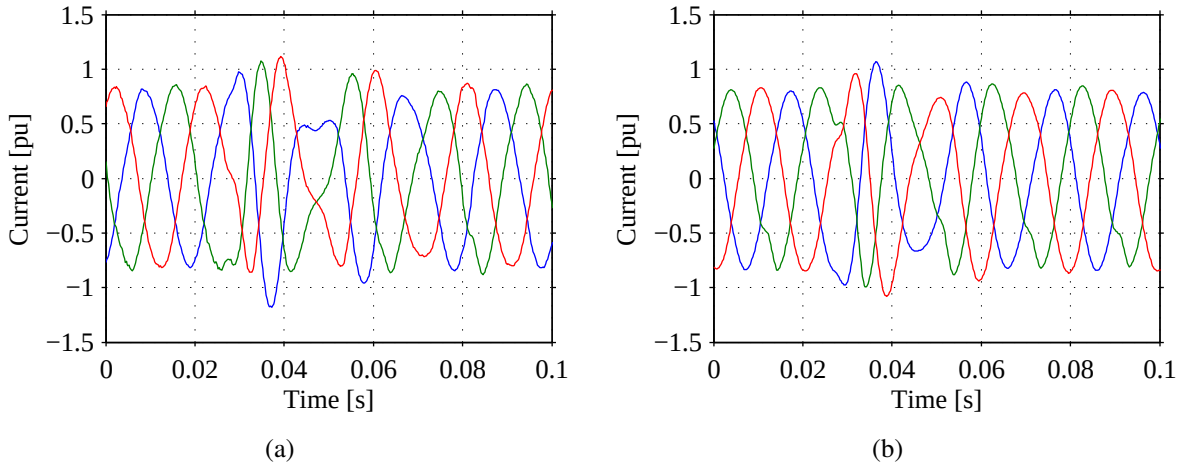

Fig. 7.19 Current output $i_{\mathrm{w},2}^{(abc)}$ of the wind turbine model. Plot (a): $\alpha_{\mathrm{p,w}}$ is set at $0.2\omega_{\mathrm{s}}$; Plot (b): when $\alpha_{\mathrm{p,w}}$ is set at $0.05\omega_{\mathrm{s}}$

A greater current disturbance is seen when $\alpha_{\mathrm{p,w}}$ is increased, while the opposite effect is seen when $\alpha_{\mathrm{p,w}}$ is reduced. It is important to note that in the first case the current peaks above ± 1 pu, while in the second case the current transients are somewhat limited. This is of importance because the selection of $\alpha_{\mathrm{p,w}}$ can negatively impact the integrity of both the filters as well as the power electronic devices implemented on the wind turbine system, especially if large transient current is experienced.

7.8 Test for frequency deviation

Many modern wind turbines are able to provide active power support in case of frequency disturbances [80]. Although in an FPC wind turbine system the generator is decoupled from the grid, specialized controllers, such as the one presented in [81], allows for the extraction of kinetic energy from the wind turbine rotation mass. On the other hand, the flexibility of the VSC-based testing equipment allows for the full control of the system frequency. In this regard, it is of interest to explore the ability of the testing equipment in reproducing a grid frequency deviation at the terminals of the wind turbine terminals.

In this section, the ability of the wind turbine system in providing active power support is evaluated. The active power output of the wind system model has been varied in relation with the frequency/power profile given in Fig. 7.20, which is similar to the ones given in some of the selected Grid Codes. The turbine is operated at 0.9 pu with unity power factor. Here, the interest is on the frequency deviation profile controlled by the testing equipment and on the variations of the active power output of the modelled wind turbine.

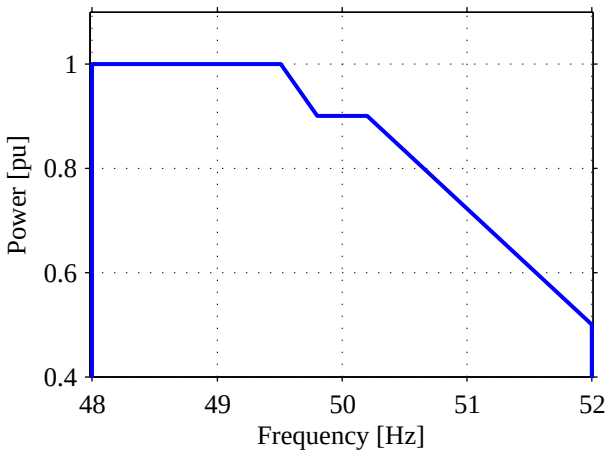

Fig. 7.20 Frequency droop profile implemented in wind turbine model in the laboratory.

A simple power/frequency droop control [81] has been implemented. Observe in Fig. 7.20 that the dead-band is a narrow segment between 49.8 to 50.2 Hz, instead of a common range of 50 Hz $\pm$0.5 Hz. Moreover, power production of 1 pu must be achieved if the frequency drops below 49.5 Hz. On the other hand, the power output must be decreased linearly if the frequency is between 50.2 Hz and 52 Hz. After 52 Hz the modelled generating unit is set to block the pulses, emulating a sudden disconnection from the grid.

The applied frequency has been varied according to the frequency dip and swell shown in Fig. 7.21(a) in blue and green traces, respectively. These variations are based on grid events previously recorded by PMU measuring systems placed in the Nordic grid [82].

As expected, the turbine reacts by varying its active power production as shown in Fig. 7.21(b). An increase active power set-point is seen when a frequency drop is detected (blue trace). The minimum frequency is 49.45 Hz at 20 s. This value is still within the range where the wind turbine model is operated with droop control. For this reason, the maximum active power output

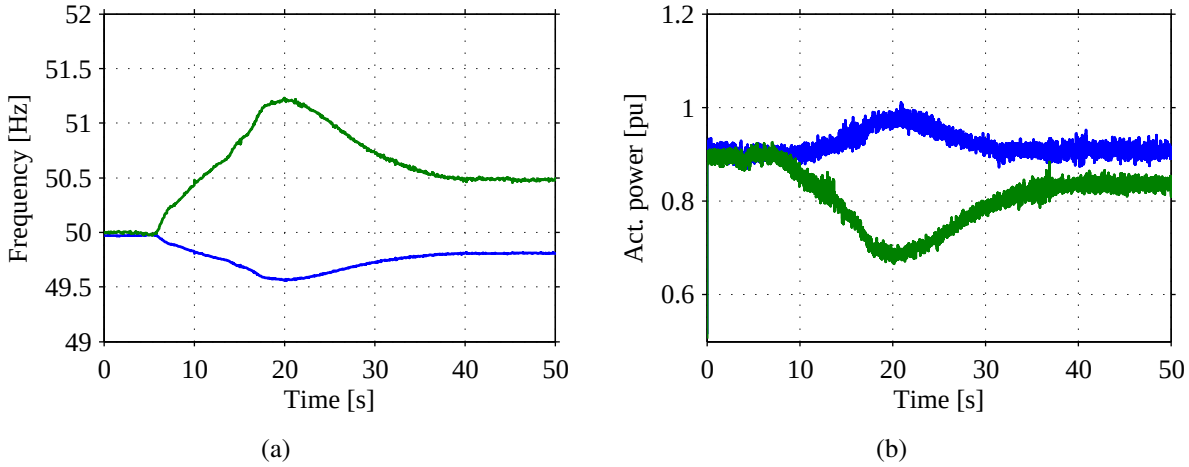

Fig. 7.21 Frequency variations tested in the laboratory: Plot (a): Frequency signal sent into testing equipment controller. Plot (b): active power response from wind turbine model. In plots: frequency drop (blue) and frequency swell (green).

is 0.98 pu. Moreover, the frequency reaches a steady-state value within the dead-band of 49.8 Hz, meaning that the wind turbine power is set back to 0.9 pu.

A second scenario is simulated in the laboratory in which the applied frequency is increased to a maximum value of 51.22 Hz and brought back to a steady-state value of 50.5 Hz. The frequency variation is plotted with green traces in Fig. 7.21(a). The response of the turbine is also plotted with green traces, in 7.21(b). The minimum active power set-point is 0.7 pu at 20 s and it is set according to the droop control for frequencies above the dead-band. From the figure it is also possible to observe that the steady-state active power production is 0.82 pu which corresponds to the production level for a frequency of 50.5 Hz, meaning that the pre-event production level of 0.9 pu is not achieved.

The droop control is found to be relativity slow in varying the active power output of the wind turbine system. Moreover, it only acts according to the actual value of the system frequency without taking into consideration other equally important aspects such as the derivative of the frequency or the actual time that the frequency stays in a particular range [82]. Other type of power controllers include the use of proportional-derivative (PD) control which allows for a better performance by taking a control action according to the rate of change of the varying frequency [81]. However, this simple but illustrative example demonstrate that active power curtailment and frequency support capabilities can be tested on a wind turbine system by using the investigated testing device. The full control over the system frequency allows for the emulation of realistic frequency disturbances, which can be easily implemented in the in the controller of the testing equipment.

7.9 Frequency scan and estimation of the input admittance

In this final experiment, the testing equipment is used to perform a frequency sweep on the small-scale wind turbine model. The frequency scan has been carried out in the abc-reference frame. The excitation voltage signal is set to 0.025 pu and the harmonic content is retrieved by FFT analysis from the measured voltage $\underline{e}_{\mathrm{w}}^{(abc)}$ and current $\underline{i}_{\mathrm{w},2}^{(abc)}$ shown in Fig. 7.1. Observe that the current is here considered to flow in the opposite direction, meaning that the frequency scan is performed by measuring upstream into the wind turbine system . The system is run according to the control parameters listed in Table 7.1 and the admittance $Y_{\mathrm{w}}(j\omega)$ is calculated as described in Section 6.5.

7.9.1 Wind turbine model with nominal parameters

Here, the wind turbine model has been scanned while running at four different operating condition. The value of the real part of the admittance $Y_{\mathrm{w}}(j\omega)$ is plotted in Fig. 7.22(a) for the scanned sub-synchronous frequencies. The black dots correspond to the evaluation of $Re\{Y_{\mathrm{w}}(j\omega)\}$ at a production level of 0.9 pu while the blue dots correspond to a power output of 0.15 pu, both at unity power factor ($i_{\mathrm{wq}}^{*} = 0$ pu).

Observe in Fig. 7.22(a) that the real part of $Y_{\mathrm{w}}(j\omega)$ is reduced together with the reduction of the active power output, confirming the findings obtained in the previous chapters (see Section 5.2 and Section 6.5). The passivity of the modelled wind turbine varies according to the active power operating point, while the turbine seems to show a capacitive behavior throughout the sub-synchronous range, as shown in Fig. 7.22(b). Moreover, when only the reactive power set-point is varied (maintaining 0.9 pu of active power) the imaginary part of $Y_{\mathrm{w}}(j\omega)$ remains

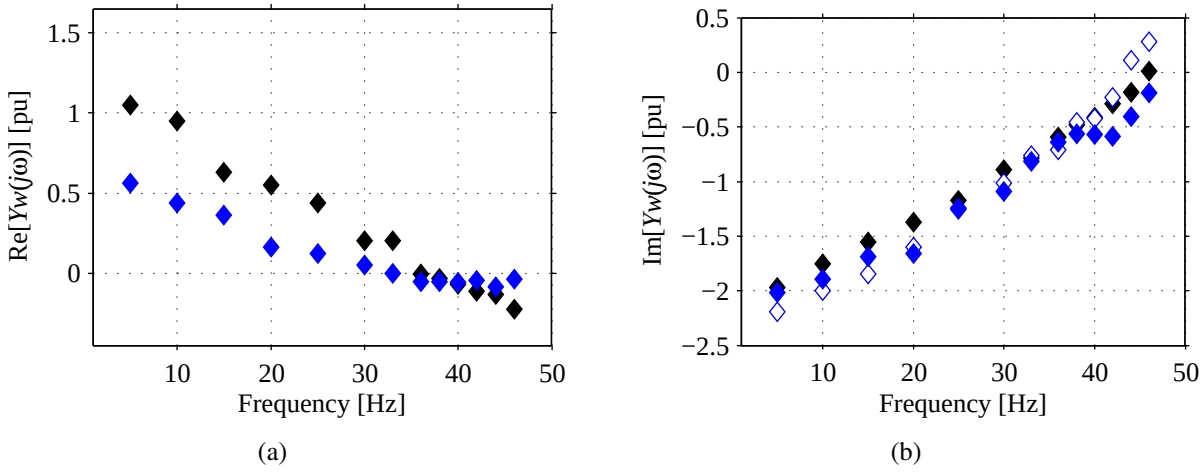

Fig. 7.22 Evaluation of $Y_{\mathrm{w}}(j\omega)$ of the small-scale wind turbine model operated at 0.9 pu with unity power factor (black). Plot(a): variation of the $Re\{Y_{\mathrm{w}}(j\omega)\}$ when reducing the active power production to 0.15 pu. Plot(b): variation of $Im\{Y_{\mathrm{w}}(j\omega)\}$ when injecting reactive power (blue) and absorbing reactive power (white) of 0.3 pu.

almost unvaried for the majority of scanned frequency range. Only a small variation can bee seen in proximity to 50 Hz, which can be explained by the direction of the reactive power flow at these frequencies, controlled by the wind turbine VSC.

7.9.2 Wind turbine model with control parameters varied

In this final laboratory experiment, the impact of the control settings on the wind turbine admittance is investigated. Here, the control parameters are varied and the wind turbine model is scanned in the sub-synchronous range. The evaluation of $Re\{Y_{\mathrm{w}}(j\omega)\}$ is shown in Fig. 7.23.

Figure 7.23(a) shows the impact of the selection of the PLL bandwidth $\alpha_{\mathrm{p,w}}$ in the real part of the wind turbine admittance $Y_{\mathrm{w}}(j\omega)$, when it is varied to $0.2\omega_{\mathrm{s}}$ (blue dots) and at $0.05\omega_{\mathrm{s}}$ (white dots). As previously discussed in other sections of this thesis, an increased value of the PLL bandwidth reduces the real value of the admittance of the controlled VSC-based wind turbine system. On the other hand, decreasing $\alpha_{\mathrm{p,w}}$ has the opposite effect By comparing the resulting admittances with the evaluation of $Re\{Y_{\mathrm{w}}(j\omega)\}$ at nominal parameters (black), the trend on the different curves in 7.23(a) verify what has been found with simulations.

The effect of the selection of the wind turbine current control bandwidth $\alpha_{\mathrm{c,w}}$ on $Re\{Y_{\mathrm{w}}(j\omega)\}$ is shown in Fig. 7.23(b). Here, $\alpha_{\mathrm{c,w}}$ is varied to $1.5\omega_{\mathrm{s}}$ (blue dots) and to $2.5\omega_{\mathrm{s}}$ (white dots). Similarly, black dots correspond to response of $Re\{Y_{\mathrm{w}}(j\omega)\}$ at nominal system parameters.

Observe that, contrasting to what has been found previously from the evaluation of the mathematical model and from the frequency response of the time-domain simulation model, the current control bandwidth $\alpha_{\mathrm{c,w}}$ does affect the admittance of the scanned system. The results Fig. 7.23(b) show that the higher the bandwidth $\alpha_{\mathrm{c,w}}$, the more damped the system becomes in the low frequency range, while lowering the bandwidth brings the system slightly less damped.

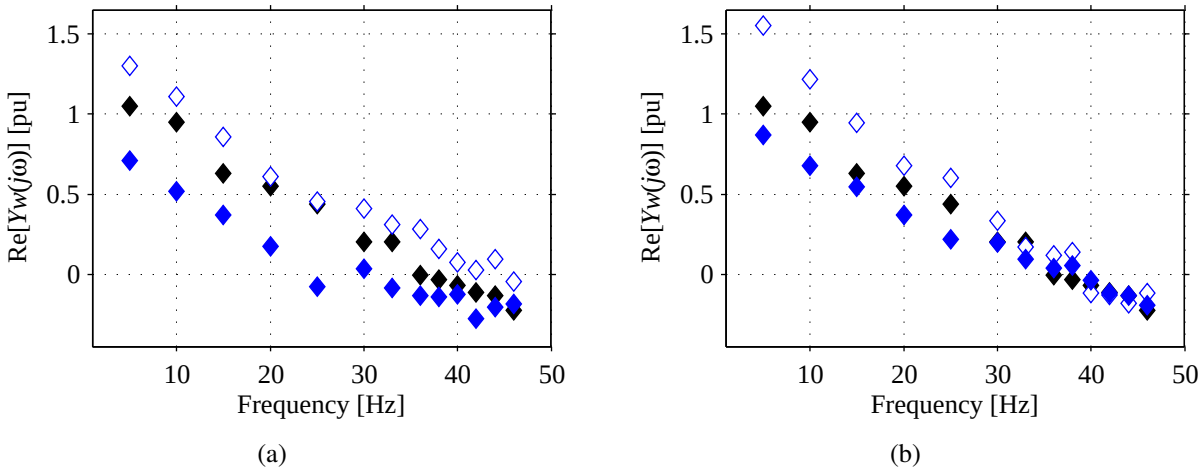

Fig. 7.23 Evaluation of $Re\{Y_{\mathrm{w}}(j\omega)\}$ of the small-scale wind turbine model operated at 0.9 pu, with nominal parameters (black). Plot(a): variation of the admittance when $\alpha_{\mathrm{p,w}}$ is set at $0.2\omega_{\mathrm{s}}$ (blue) and at $0.05\omega_{\mathrm{s}}$ (white). Plot(b): variation of the admittance when $\alpha_{\mathrm{c,w}}$ is set at $1.5\omega_{\mathrm{s}}$ (blue) and $2.5\omega_{\mathrm{s}}$ (white).

It is of convenience to recall that a discrete LPF has been placed on the feed-forward of the grid voltage in the current control of the small-scale wind turbine model, in order to deal with the harmonic content present in the system (see Fig. 7.5). The cut-off frequency of this filter changes together with the close-loop bandwidth of the current controller. As discussed in [51] and [58], the bandwidth of the LPF applied on the wind turbine grid voltage $\hat{\underline{e}}_{\mathrm{w}}^{(\mathrm{dq})}$ in the current control impacts input admittance of a VSC. On the other hand, in order to keep the derived models fairly simple, the LPF in the grid voltage has not been included in the analytical model neither in the time-domain simulation model. Therefore, it is cautious to conclude only that a faster current control allows for the PI controller to counteract quicker any grid disturbance that exist on the imposed grid voltage $\underline{e}_{\mathrm{w}}$.

7.10 Conclusions

In this chapter, the investigated testing methodology has been verify extensively by the use of small-scale prototype in a laboratory environment. First, the integration of all the subsystems that constitute the laboratory setup has been described. With focus on both the control algorithm and the system hardware, a reduced FPC wind turbine model and back-to-back VSC-based testing equipment have been interconnected. Experiments have been carried by the use of the investigated testing device, which allows for a full characterization of the electrical behavior of the modelled wind turbine system. With focus on the dynamic behavior of the wind energy system, different control aspect of the generating unit have been tested, for example: operation during grid faults and grid frequency deviations, as well as the evaluation of the implemented synchronization method against phase-angle variations, among other test.The open-loop controller implemented on the test equipment is found to be robust in controlling the voltage across the AC-link. If special attention is paid to the selection of ramp-rates when testing for voltage dip, the PCC voltage can be controlled smoothly without undesired transients.

Another aspect that has been here discussed is the impact of different control settings and operating points on the wind turbine input admittance. The admittance has been evaluated thanks to the use of a frequency scan control feature included in the testing equipment controller. The information obtained through the frequency scans is of importance, especially if stability studies regarding grid integration of this type of energy systems are conducted.

For further validation of the investigated methodology, field test results of a 4 MW wind turbine scanned by an 8 MW VSC-HVDC system in back-to-back are presented.

Chapter 8

Validation of the methodology by field test

8.1 Description of the testing facility

Finally, field test results of a 4 MW FPC offshore wind turbine are presented in this chapter. The testing equipment is an 8 MW back-to-back HVDC station placed in the harbour of Gothenburg, Sweden. A picture of the actual wind turbine is given in Fig. 8.1(a). The wind turbine is located at the edge of the land in proximity to the sea. During the majority of the time, the wind turbine receives offshore wind from the northern part of Denmark.

In this installation, only the three-phase voltages an three-phase currents at the PCC are sampled by a computer located in the control room of the HVDC station. The instantaneous active and reactive power are calculated off-line. Technical data of the testing setup are given in Table 8.1 and the schematic of the interconnection of the wind turbine with the test equipment is shown in Fig. 3.11. A series of field tests were carried out during several days between January 2015 and April 2016; for this reason, different operating conditions of the wind turbine are shown throughout the results. The PCC voltage is controlled in open-loop, meaning that the voltage reference is sent directly at the terminals of the turbine-side VSC of the fully-rated testing equipment.

TABLE 8.1. PARAMETERS OF THE FIELD TESTING SETUP.

Base values	10 kV, 4.2 MVA
Wind turbine rating	1 pu
Testing equipment rating	2.0 pu
Type of AC filter in TE	LCL
Type of AC filter in WT	LCL
Impedance of coupling transformer in TE	0.08 pu
Impedance of step-up transformer in WT	0.06 pu
Interconnection between TE and WT	300 mts. underground cable

(a)

(b)

(c)

Fig. 8.1 Testing facility in Gothenburg. Plot(a): 4.2 MW FPC “Big Glenn” wind turbine; Plot(b): turbine-side VSC house of the back-to-back HVDC station, and Plot(c): coupling inductor (back) and AC filters (front) inside the house.

8.2 Test for voltage dip at full power production

One of the first tests carried out on the testing facility corresponds to a voltage dip at full power production. The following tests were conducted on the 13th of January 2015. The first attempt was to select a relatively small voltage variation, with a smooth transition between normal operation level and retained level. In order to safely conduct the experiment while learning the dynamics of the system, the voltage is reduced from 1 pu to 0.9 pu for 100 ms. The results are shown in Fig. 8.2.

The three-phase PCC voltage is shown in Fig. 8.2(a). At 0.05 s the voltage is reduced from 1 pu to 0.9 pu. At 0.15 s the voltage is brought back to 1 pu with a ramp function. In order for the wind turbine to maintain constant power production during the voltage reduction, the generating unit increases the magnitude of the current, as depicted in Fig. 8.2(b). The injected active and reactive power are given in Fig. 8.2(c). During the voltage variation, the wind turbine maintains its active power set-point, injecting a steady 0.9 pu of active power into the imposed grid. From the figure, it is possible to observe that the wind turbine does not engage its LVRT control. Thus, the reactive power is reduced only due to the reduction of the voltage across the AC-link between the wind turbine and the testing equipment. Note the resemblance between this case study and the one given in Section 7.3.3 where a wind turbine with constant power output is simulated in the laboratory.

A second test has been carried out the same day. Here, the voltage is varied from 1 pu to 0.65 pu for 100 ms while the wind turbine is producing nominal active power. The results are depicted Fig. 8.3. The three-phase PCC voltage is dropped at $t = 0.05$ s, as shown Fig. 8.3(a). In this

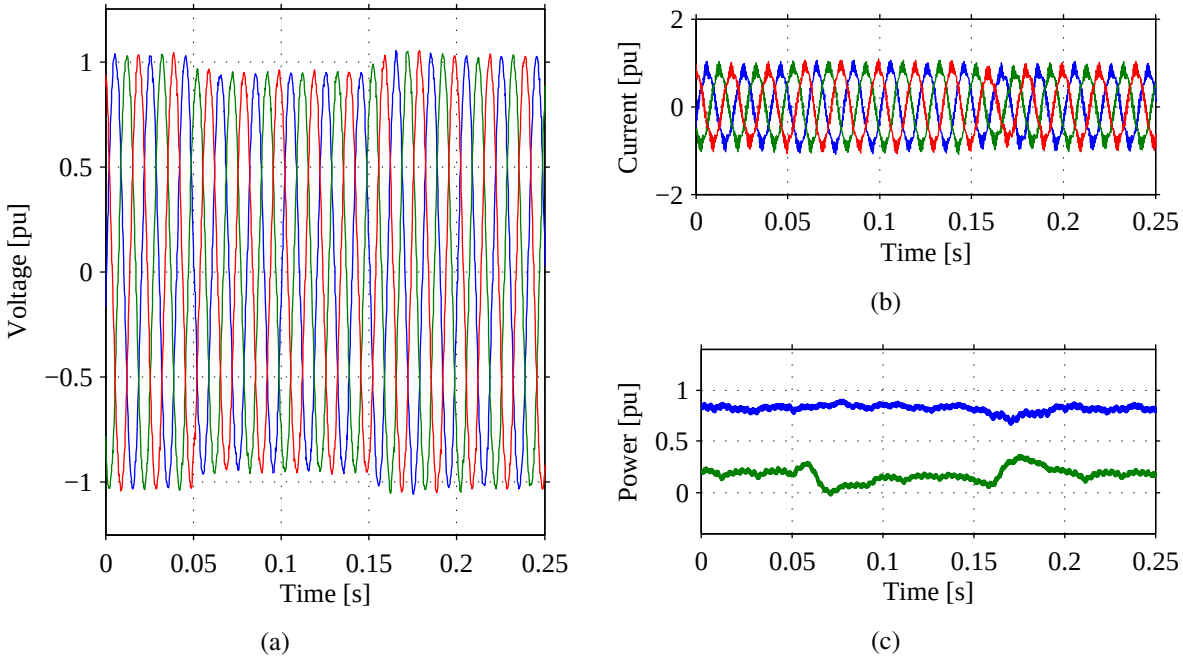

Fig. 8.2 Wind turbine tested for voltage dip at full power. Plot (a): three-phase voltage; Plot (b): three-phase current; Plot (c): active (blue) and reactive (green) power.

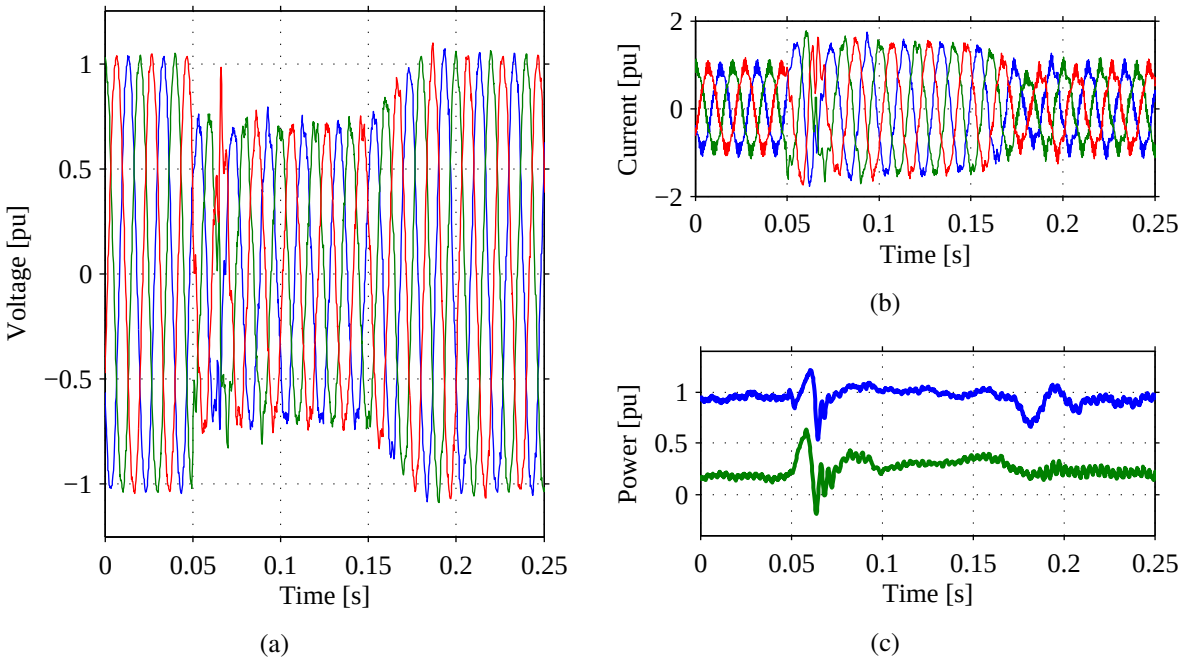

Fig. 8.3 Wind turbine tested for LVRT. Plot (a): three-phase voltage; Plot (b): three-phase current; Plot (c): active (blue) and reactive (green) power.

scenario, a stiff ramp rate of 0.2 pu/ms has been selected for the voltage dip while a ramp of 0.0125 pu/s has been set for the recovery.

At 0.075 s it is possible to observe a transient in both the current, shown in Fig. 8.3(b) and the voltage. The transient lasts for 7 ms and the wind turbine manages to control its current output during the voltage dip. The wind turbine active power set-point is maintained at 0.95 pu, as depicted in Fig. 8.3(c), while the reactive power is boosted reaching a mean value of 0.4 pu during the voltage dip. Finally, in Fig. 8.3(c) it is possible to observe that the pre-fault reactive power exchange at the measurement point is 0.2 pu. The wind turbine injects an additional 0.2 pu of reactive power when detecting the voltage dip at its terminals. Therefore, a total of 0.4 pu is maintained until the voltage is increased back to 1 pu.

The voltage starts to recover at 0.15 s with a ramp function. Observe that the current is also reduced at the same time that the reactive power is brought back to 0.2 pu. The active power oscillates at 0.18 s while the voltage has reached a steady-state level of 1 pu. Observe that the current is above 1 pu during the voltage dip, meaning that the wind turbine have over-current capabilities and it is capable to momentarily increase the output current beyond nominal values during the voltage dip.

8.3 Reactive power control during balanced voltage dip

A similar test has been carried out on the 17th of May of 2016. Unfortunately, the wind turbine was operating at low wind speed. However, the lack of produced active power made the variations

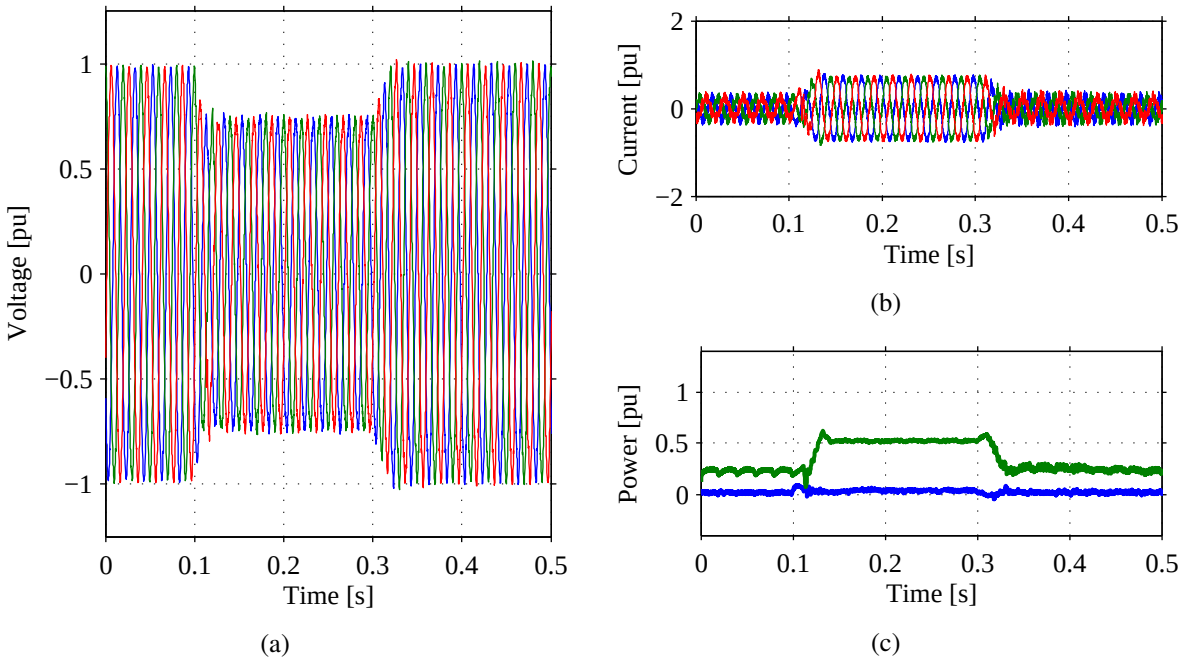

Fig. 8.4 Wind turbine under voltage dip test at low power production. Plot (a): three-phase voltage; Plot (b): three-phase current; Plot (c): active (blue) and reactive (green) power.

in the reactive power more prominent, as later see in this section. This experiment consists in a voltage variation from 1 pu to 0.75 for about 200 ms. In order to avoid an oscillatory response similar to the ones experienced in the previous experiment, the down-slope ramp of the controlled VSC voltage is set at 0.02 pu/ms and the recovery ramp is set at 0.01 pu/ms. From the voltage waveform given in Fig. 8.4(a), it is possible to observe that the voltage is controlled in an effective and smooth way.

The active power was set to 0 pu during this test. Moreover, the reactive power seen in Fig. 8.4(c) is mainly due to the capacitor bank of the local LCL filter placed at the terminals of the turbine-side VSC of the testing equipment, while the variation observed during the voltage dip is due to the control action of the wind turbine.

When the voltage dip is detected at 0.12 s, the wind turbine injects reactive current. As shown in Fig. 8.4(b), the current reaches 0.85 pu, meaning that the turbine is operated in proximity to the rated current. In order to quickly boost the voltage, the reactive power shown in Fig. 8.4(c) is increased with a ramp function. There is a small overshoot in the current that is reflected on the reactive power at 0.14 s, mainly due to the fact that the voltage has reached steady-state during the dip while the current continues to increase. This can be attributed to the voltage monitoring system and the reactive power controller of the wind turbine during dynamic condition of the grid.

The reactive power injection is maintained for the complete duration of the voltage dip. The (mainly reactive) three-phase current is later reduced when the voltage is restored to 1 pu. At 0.31 s, a small overshoot in the reactive power is experienced. Note that the current is maintained during a short period of time at 0.85 pu, while the voltage has already started to increase towards

1 pu. The system reaches a post-fault steady-state at 0.34 s. It can be observed that there is a slightly increase of the reactive power set-point after the voltage dip, when compared to its pre-fault set-point. This can be attributed to the wind turbine control action when calculating a reactive current reference based to the instantaneous measured voltage. At 0.42 s, thus 80 ms after the voltage is fully restored, the wind turbine resumes normal operation, reducing the current (and therefore the reactive power output) to its pre-fault operating point.

8.4 Reactive power control during unbalanced voltage dip

In this section the response of the wind turbine under unbalanced voltage dip is studied. This test was carried out again on the 17$^{\text{th}}$ of May of 2016, at low wind conditions. The turbine-side VSC of the actual testing equipment is controlled in open-loop and the voltage in phase a and b are dropped from 1 pu to 0.7 pu for 200 ms. The voltage in phase c is maintained at 1 pu during all the duration of the test. The resulting PCC voltage is given in Fig. 8.5(a) .

Observe in Fig. 8.5(b) that, as compared with the laboratory experiment given in Section 7.5, the current here is maintained well below 1 pu during the unbalanced voltage dip. Moreover, the reactive power shown in green traces in Fig. 8.5(c) is increased from 0.25 pu to 0.35 pu approximately, while a small oscillation at 100 Hz in both active and reactive power is seen.

These last two examples show in a clear way the response of the wind turbine, particularly the reactive power controller during an a balanced and unbalanced voltage dip. Note that this results differs from the one given in Section 7.5, where a similar tests have been carried out on the

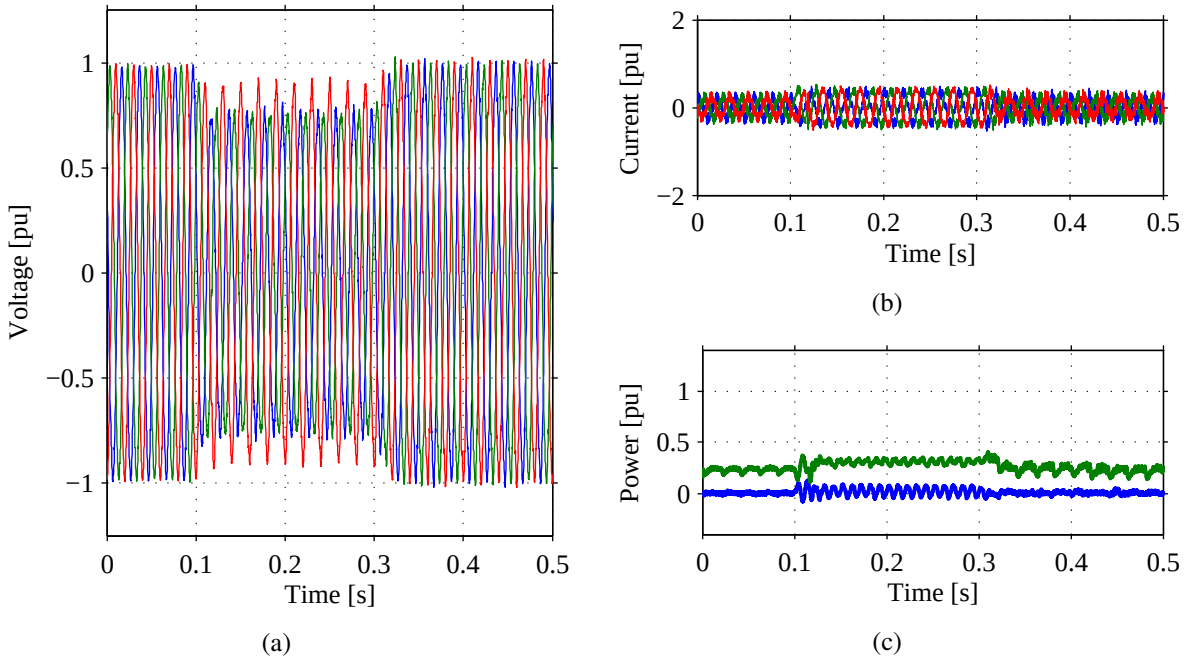

Fig. 8.5 Wind turbine under unbalanced dip test at low power production. Plot (a): three-phase voltage; Plot (b): three-phase current; Plot (c): active (blue) and reactive (green) power.

small-scale laboratory model. Considering that the control system of the tested wind turbine is unknown, these results suggest that the controller implemented on the wind turbine accounts also for the negative sequence, while still experiencing small oscillations in its output power.

8.5 Test for frequency deviation

In this case study, the voltage applied to the 4 MW wind turbine is controlled at 1 pu and only the frequency is varied. The obtained results are given in Fig. 8.6. In order to measure for a long period of time, the voltage and the current are here measured by a portable measurement unit located upstream of the LCL filter. In particular, at the converter-side of the coupling transformer placed at the turbine-side VSC-HVDC station shown in Fig. 8.1(c). For this reason, the reactive power depicted in green curves in Fig. 8.6(a) has a different value with respect to the other case studies shown throughout this chapter.

Here, only the measured frequency and the active and reactive power output are shown. The first scenario corresponds to a frequency drop of 0.5 Hz for 15 seconds. From Fig. 8.6(a) it can be noticed that the frequency is varied with a ramp of 0.2 Hz/s, or 5 seconds per varied Hz, for both the drop and the recovery of the frequency. According to the Swedish Grid Code [32], the wind turbine should maintain its active power production at any given frequency within the normal frequency range (49.5 Hz to 50.5 Hz). The lower plot in Fig. 8.6(a) shows that the active power is kept constant at 0.7 pu for the majority of the test. At 30 s the active power is slightly reduced, mainly due to the variations in the wind speed at the moment of the test.

The second scenario corresponds to two consecutive frequency swells of 1 Hz. The frequency is initially controlled at 50 Hz and varied upwards with a ramp of 0.05 Hz/s, or 20 seconds per varied Hz. A frequency of 51 Hz is maintained for 25 seconds approximately. Afterwards, the

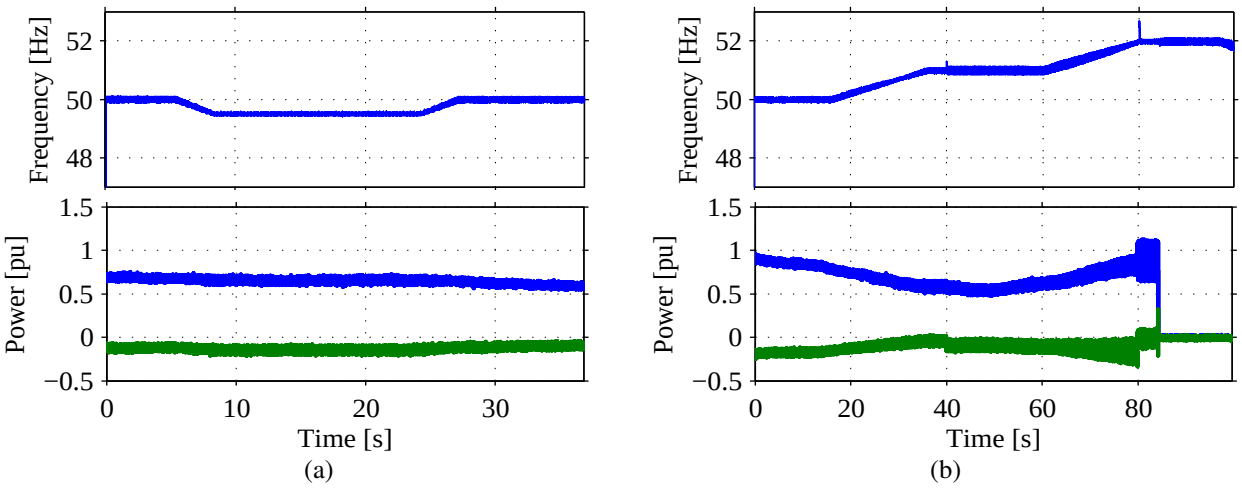

Fig. 8.6 Frequency variation test. Plot (a): Frequency drop of 0.5 Hz and active (blue) and reactive (red) power out of the wind turbine. Plot (b): Two consecutive frequency swells of 1 Hz and active (blue) and reactive (red) power out of the wind turbine.

frequency is increased to 52 Hz. The results are shown in Fig. 8.6(b). Observe in the lower plot that the upwards and downwards tendency of the output power suggest that the wind turbine is varying its operating point according to the wind speed and not in demand of the applied frequency. In addition, the active power is slightly increased 10 seconds after the frequency reaches 51 Hz, at 40 s, while continues to increase with the increasing of the system frequency at 60 s. Finally, a critical point is encountered at 80 s when the frequency reaches 52 Hz. The wind turbine enters into an operation mode that affects the active power output while experiencing an oscillation at 104 Hz. The wind turbine shuts down by an over-frequency protection relay, 5 seconds after the frequency reaches 52 Hz, at t =85 s. The different power production levels experienced when performing the test are also somewhat reflected on the reactive power output of the wind turbine, as seen in green traces in Fig. 8.6(b).

8.6 Frequency scan on actual wind turbine

This section shows first the frequency scan test carried out on the 20$^{\text{th}}$ of June, 2016, when the wind turbine was operating at 0.6 pu power of production. Afterwards, the result from the frequency scan test, carried out on the 17$^{\text{th}}$ of May, 2016, at low power production, is given. The current and voltage are measured at the HVDC station, where the voltage applied to the wind turbine is controlled. The frequency scan is performed by adding a voltage component of magnitude 0.015 pu modulated at the interested frequency, on top of the fundamental reference voltage of 1 pu.

Note that this section is only illustrative and cannot be considered as a field verification test of the modelled turbine. While classical control algorithms have been implemented in the simulation models, the information about the actual wind turbine control strategy is not available for the author. For this reason, it is only possible to identify and compare the trend of the measured wind turbine input admittance on the frequency range of interest.

The wind turbine is changing its operating conditions during each tested frequency and these are shown in Fig. 8.7(a). The average output power of the wind turbine is of 2.9 MW. However, a wide variation between 2.6 MW and 3.5 MW has been encountered during the test. The wind turbine impedance $Z_{\text{w}}(j\omega)$ is obtained as an average of the phase impedances. The measured phase voltage and line current are evaluated at the frequency of interest by using the methodology given in Section 6.5.2.

The admittance $Y_{\text{w}}(j\omega)$ can be calculated by the inverse of (6.8). The real and imaginary part together with the magnitude of the measured phase admittance $Y_{\text{w}}(j\omega)$ are shown in Fig. 8.7(b) with blue and green dots respectively. The magnitude of the admittance is plotted in white dots.

The resulting measured points for $Re\{Y_{\text{w}}(j\omega)\}$ in Fig. 8.7(b) suggest that the wind turbine presents a positive real part for frequencies below 22 Hz, with a maximum measured value of 2.8 pu at 10 Hz. On the other hand, a relatively high non-passivity behavior is exhibit for frequencies above 30 Hz, meaning that the wind turbine could resonate if these frequencies are encountered in the network. The minimum value for $Re\{Y_{\text{w}}(j\omega)\}$ is -1.5 pu and can be observed at the last scanned frequency of 34 Hz.

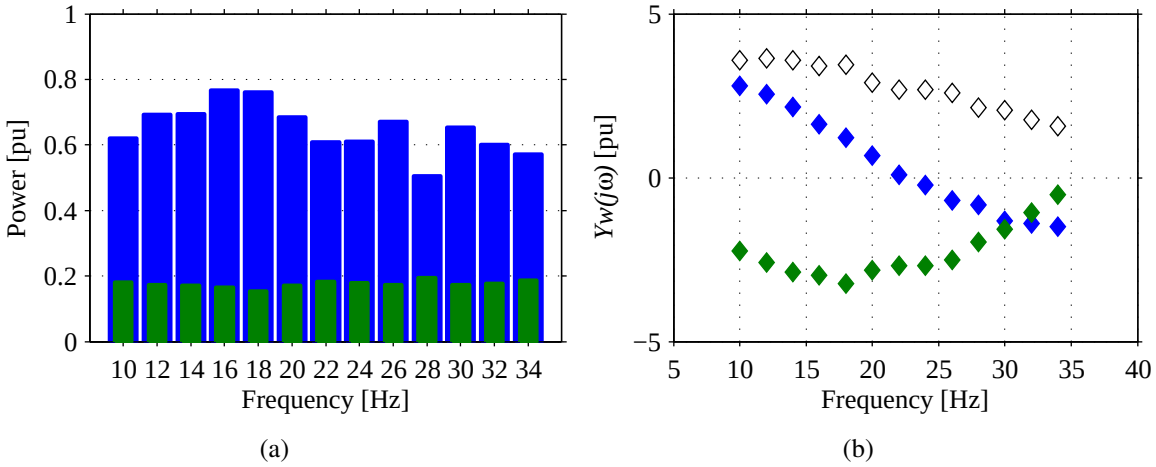

Fig. 8.7 Frequency scan results of an actual FPC wind turbine at 65% of power production. Plot (a): Active power (blue) and reactive power (green) operating points of the actual wind turbine prior frequency scan. Plot (b): Admittance component $Re\{Y_{\mathrm{w}}(j\omega)\}$, $Im\{Y_{\mathrm{w}}(j\omega)\}$ and $|Y_{\mathrm{w}}(j\omega)|$ plotted in blue, green and white dots respectively.

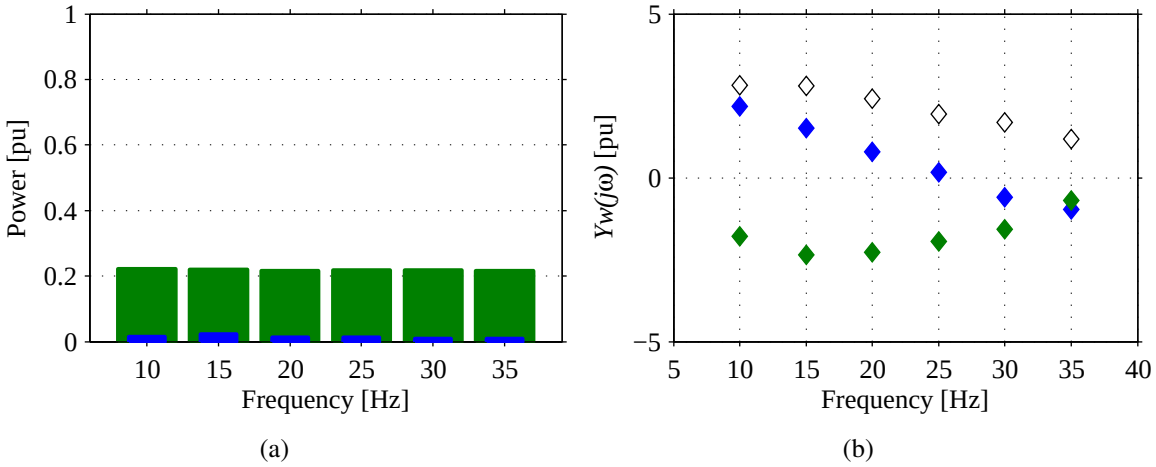

Fig. 8.8 Frequency scan results of an actual FPC wind turbine at low power production. Plot (a): Active power (blue) and reactive power (green) operating points of the actual wind turbine prior frequency scan. Plot (b): Admittance component $Re\{Y_{\mathrm{w}}(j\omega)\}$, $Im\{Y_{\mathrm{w}}(j\omega)\}$ and $|Y_{\mathrm{w}}(j\omega)|$ plotted in blue, green and white dots respectively.

The scanned imaginary part of the admittance $Im\{Y_{\mathrm{w}}(j\omega)\}$ is also shown in Fig. 8.7(b) in green dots. The turbine seems to present a capacitive behavior for most of the studied frequency range. The reactive power set-point at the measurement point is dependent on both the configuration of the filtering stage at the terminals of the VSC-HVDC and on the wind turbine reactive power controller. The minimum value of $Im\{Y_{\mathrm{w}}(j\omega)\}$ is found to be -2.4 pu at 18 Hz. For frequencies above 20 Hz, $Im\{Y_{\mathrm{w}}(j\omega)\}$ increases up to a maximum of -0.4 pu measured at 34 Hz. Observe, however, that reactive power set-point shown in Fig. 8.7(a) is kept relatively constant at 0.2 pu (0.9 MVAr) during all the test.

The absolute value of the measured wind turbine admittance $|Y_{\mathrm{w}}(j\omega)|$ is also shown in Fig. 8.7(b) in white dots. The operating point of the wind turbine at the moment of each test impacts both the amplitude and also the vector components of its input admittance. For this reason, the uneven trend of $|Y_{\mathrm{w}}(j\omega)|$ somewhat matches the variation on the output power of the wind turbine at each scanned frequency. Observe that this aspect has not been highlighted in the previous chapters due to the fact that the power set-point of the simulation and small-scale models is kept constant during the frequency scan.

Finally, one last case scenario is given in Fig. 8.8. The test was carried out in a very low windy day; therefore, the wind turbine is operated at low power production. Figure 8.8(a) shows the active and reactive power set-points at the moment of each test. From the figure, it is possible to note that the power flow is mainly dominated by reactive power coming from the filter banks between the wind turbine and the testing equipment. The measured reactive power is 0.023 pu for all the test. The calculated admittance components are shown in Fig. 8.8(b).

The real part of the admittance $Re\{Y_{\mathrm{w}}(j\omega)\}$, show in blue dots in Fig. 8.8(a), is slightly reduced to 2.2 pu, as compared to 2.8 pu given for the previous case. The main difference is the zero-crossing of the real part, which in this case occurs at 26 Hz, instead of 23 Hz at mid-power operation. From the plots where the reactive power is given, this second scenario shows a small increase in the reactive power measured at the HVDC station. Thus, the imaginary part of the measured admittance can be affected by the operating point of the wind turbine, making the green trace in Fig. 8.8(b) slightly closer to 0 pu, as compared with Fig. 8.7(b). Finally, the total magnitude $|Y_{\mathrm{w}}(j\omega)|$ of the admittance is decreased from 4 pu from the first scenario, to 2.7 pu when operated at no power, as shown in white dots in Fig. 8.8(b).

8.7 Conclusions

Field test results of a 4 MW wind turbine and 8 MW testing equipment have been included in this thesis. Here, the open-loop control has been implemented and the dynamic performance of an actual wind turbine has been described. The tests carried out on the actual wind turbine system include balance and unbalanced voltage dips, defined by different retained voltage and different ramp-rates, as well as frequency variation tests and frequency scan. The results shows that a LVRT control strategy is implemented on the tested system injecting reactive power when a voltage dip is detected. Moreover, it has been shown that the generating unit maintains a smooth control of the reactive power output during unbalanced voltage dips, at least for low power set-points. These results demonstrate that a VSC-based testing device can be use to evaluate how well a wind turbine system can withstand the technical requirements given in the Grid Codes.

The multi megawatt FPC wind turbine system has also been swept by means of the converter based testing equipment. The frequency scanning technique has been demonstrated by field test and the input admittance of the generating unit has been evaluated for two operating conditions. The frequency trend of the scanned turbine is found to be similar to the developed models, exhibiting a non-passive behavior at higher frequencies within the sub-synchronous range while also exhibiting capacitive behavior throughout the whole scanned range.

Chapter 9

Conclusions and future work

9.1 Conclusions

With the increasing use of wind energy, the reliability of the electricity grid is becoming more dependent not only on how well wind turbines are prepared to withstand grid disturbances but also on their grid support capabilities. In this regard, this thesis has dealt with the implementation and control of a fully-rated VSC-based testing equipment to characterize the dynamic and steady-state electrical behavior of a wind turbine system. The main focus has been on the study of the dynamic response of the overall system, particularly on the use of the investigated testing device in emulating different abnormal grid scenarios that can be experienced at the terminals of a wind turbine. This include, for example, voltage dips (both balanced and unbalanced), frequency variations and phase-angle shift. Furthermore, the use of the testing equipment for the emulation of the short-circuit impedance of the interconnecting grid, as well as a tool to estimate the characteristic impedance of the wind turbine at different frequencies have been described. The testing setup has been implemented analytically and through time-domain simulation model in order to assess the stability of the system and its transient performance. The obtained results have been verified through laboratory experiments and the investigated testing methodology has been validated by field tests.

General conclusions

To the best interest of the author, the main concluding points have been summarized as follows

- In this thesis it has been demonstrated that the full characterization of the wind turbine system can be carried out by the use of a flexible VSC-based test equipment. The full controllability of the testing device allows for testing of multiple grid scenarios, making it possible to determine the behavior of the generating unit against common grid contingencies.
- The wind turbine testing methodology investigated in this thesis can be used not only to test for compliance of the technical requirements given in the Grid Codes, but also to

evaluate the performance of the generating unit in further improving the overall reliability of the grid. This includes, for example, the evaluation the operating modes that are of interest for the stability of the interconnected power system.

- The controllers implemented on the testing equipment that allows for the testing of the wind turbine system have been developed and discussed throughout this thesis. This includes: the grid-emulation algorithm, the phase-angle variation and frequency variation control algorithms, as well as the necessary controllers for carrying out the frequency scan on the tested generating unit.

- The laboratory experiments and the unique field tests presented in this thesis have provided an experimental validation of the proposed wind turbine testing methodology, particularly on the wind turbine impedance characterization and on the evaluation of its dynamic performance against grid disturbances.

Specific remarks

In the following, the specific conclusion of the thesis regarding practical implementation issues as well as remarks on the stability of the system are presented in the following

- With focus on the topology of the PCC voltage control implemented on the testing equipment, the stability analysis given in Chapter 5 shows that both the open-loop controller and the PI-based close-loop controller maintain the low-frequency system poles well damped. However, high-frequency poles are always present in the system and their location is almost independent of the selection of the control topology of the testing equipment. The analysis concludes that the stability of the system is maintained when implementing both control strategies on the testing device, even if external parameters such as control bandwidth of the tested wind turbine or its interface impedance are varied. For this reason, the simplicity of the open-loop control is an advantage.

- Simulation results shows that when performing a voltage dip, the use of an open-loop control might lead to an oscillatory response. However, if careful selection of the applied ramp-rates on the reference VSC voltage is given, these oscillations can be significantly reduced, improving the overall performance of the system. In addition, the PI-based controller allows the system to respond without any larger transients.

- Open-loop control allows for an easier implementation in the controller of the testing device, enabling independent control of each phase of the output voltage applied to the wind turbine unit. This approach has been successfully used when carrying out tests in simulation, laboratory and field test environment.

- As demonstrated in this thesis, the impact of the testing is constrained mainly between the tested object and the turbine-side VSC. However, laboratory experiment have demonstrated that the voltage at the connection point of the testing setup is affected when an unbalanced voltage dip test is carried out on the wind turbine model.

- The frequency characteristic of the wind turbine has been evaluated by aim of frequency scan. Simulation and laboratory results have been used to verify the derived analytical model. It has been found that the non-passive behavior of the input admittance of the generating unit is mostly dependent on the selection of the bandwidth of the PLL, while the impact of the inner current controller and DC voltage controller is marginal. While the laboratory experiments confirm the former claim, they also show that the admittance can vary at low frequencies when the current control bandwidth is varied. Special attention must be given particularly in the use of LPF implemented in the current control structure, in order to properly highlight the impact of the current control bandwidth of the wind turbine system.

- Experimental verification of the investigated testing methodology has been carried out on an actual 4 MW FPC wind turbine using a 8 MW two-level back-to-back VSC system. In addition to the voltage dip test and frequency variation test presented in this thesis, the wind turbine has also been scanned for the entire sub-synchronous range and the input admittance has been evaluated. This demonstrates that a wide variety of test can be carried out by the use of the investigated testing device, allowing for the full characterization of the wind turbine system.

9.2 Future work

In this thesis, the dynamic characterization of an FPC wind turbine system by the use of the converter-based testing device has been investigated. For the best interest of the reader, in the following, a few ideas are presented that can lead to a better and more accurate characterization of a wind turbine system:

- The simplifications adopted on the time-domain simulation model as well as on the laboratory setup have been to exclude the dynamics of the mechanical system focusing only on the modelling of the electrical system. The introduction of these sub-systems can lead to a different result during the simulated tests, which can relate more closely to the results obtained from the field tests. In addition, this modification will allow, for example, to asses the limits of the synthetic inertia provided by an FPC wind turbine. Similarly, pitch control system and wind measurement data can be also included in this analysis.

- In order to have a better representation of the wind turbine system, positive and negative sequence controllers can be implemented on the generating unit. In this regard, the results from the unbalance voltage dip test can be more realistic, closing the gap between the results obtained from simulation and laboratory environment with the ones obtained by field test. Similarly, the impact of the test at the grid connection point of the testing device can be re-evaluated.

- Power oscillation damping capabilities of the wind turbine system can be evaluated by developing specifics control strategies for the testing equipment. For example, the testing device can be controlled in such way that it can emulate the dynamical behavior of a synchronous generator together with its mechanical system.
- Finally, the derived grid emulation control for the testing equipment can be improved, for example, by emulating the connection point of a multi-machine power system at the terminals of the wind turbine. This modification will allow not only to evaluate voltage support capabilities of the wind turbine during voltage dips, but also to test ancillary services, such as voltage regulation and frequency support, if such control features are implemented on the tested generating unit.

References

[1] F. Blaabjerg and K. Ma, "Future on power electronics for wind turbine systems," *Emerging and Selected Topics in Power Electronics, IEEE Journal of*, vol. 1, no. 3, pp. 139–152, Sept 2013.

[2] M. Tsiliand and S. Papathanassiou, "A review of grid code technical requirements for wind farms," in *IET Renewable Power Generation*, vol. 3, no. 3, Sept. 2009, pp. 308 – 332.

[3] Göteborg Energi AB. Göteborg wind lab. [Online]. Available: http://www.goteborgwindlab.se

[4] Z. Ma, A. Pesaran, V. Gevorgian, D. Gwinner, and W. Kramer, "Energy storage, renewable power generation, and the grid: Nrel capabilities help to develop and test energy-storage technologies," *IEEE Electrification Magazine*, vol. 3, no. 3, pp. 30–40, Sept 2015.

[5] N. R. E. Laboratory. Nrel. [Online]. Available: https:/http://www.nrel.gov/

[6] C. Saniter and J. Janning, "Test bench for grid code simulations for multi-mw wind turbines, design and control," *IEEE Transactions on Power Electronics*, vol. 23, no. 4, pp. 1707–1715, July 2008.

[7] R. Lohde and F. Fuchs, "Laboratory type pwm grid emulator for generating disturbed voltages for testing grid connected devices," in *Power Electronics and Applications, 2009. EPE '09. 13th European Conference on*, Sept 2009, pp. 1–9.

[8] R. Pollanen, L. Kankainen, M. Paakkonen, J. Ollila, and S. Strandberg, "Full-power converter based test bench for low voltage ride-through testing of wind turbine converters," in *Power Electronics and Applications (EPE 2011), Proceedings of the 2011-14th European Conference on*, Aug 2011, pp. 1–10.

[9] K. Daychosawang and Y. Kumsuwan, "Balanced and unbalanced three-phase voltage sag generator for testing electrical equipment," in *Electrical Engineering/Electronics, Computer, Telecommunications and Information Technology (ECTI-CON), 2014 11th International Conference on*, May 2014, pp. 1–6.

[10] R. Zeng, H. Nian, and P. Zhou, "A three-phase programmable voltage sag generator for low voltage ride-through capability test of wind turbines," in *Energy Conversion Congress and Exposition (ECCE), 2010 IEEE*, Sept 2010, pp. 305–311.

[11] Global Wind Energy Council (GWEC), *Global Wind Energy Report Annual Market Update Update 20153*. Global Wind Energy Council (GWEC), Apr. 2016. [Online]. Available: http://www.gwec.net/

[12] EWEA, *Wind in Power, 2015 European statistics*. The European Wind Energy Association, Feb. 2016. [Online]. Available: http://www.ewea.org/

[13] EWEA, *The European offshore wind industry, key trends and statistics 2015*. The European Wind Energy Association, Jan. 2016. [Online]. Available: http://www.ewea.org/

[14] Joachim Härsjö, *Modeling of PMSM Full Power Converter Wind Turbine with Turn-to-Turn Fault*. Gothenburg, Sweden: Chalmers University of Technoology, 2014. [Online]. Available: http://www.chalmers.se/

[15] Gastón O. Suvire, *Wind Farm - Technical Regulations, Potential Estimation and Siting Assessment*. InTech, 2011.

[16] Abram Perdana, *Dynamic Models of Wind Turbines*. Gothenburg, Sweden: Chalmers University of Technoology, 2014. [Online]. Available: http://www.chalmers.se/

[17] N. Espinoza, M. Bongiorno, and O. Carlson, "Grid code testing of full power converter based wind turbine using back-to-back voltage source converter system," in *EWEA 2013 Annual Event Conference Proceedings*, Feb. 2013. [Online]. Available: http://www.ewea.org/

[18] M. Mohseni and S. M. Islam, "Review of international grid codes for wind power integration: Diversity, technology and a case for global standard," in *Renewable and Sustainable Energy Reviews*, vol. 16, no. 6, 2012, pp. 3876–3890. [Online]. Available: http://www.sciencedirect.com

[19] Andreas Petersson, *Analysis, Modeling and Control of Doubly-Fed Induction Generators for Wind Turbines*. Gothenburg, Sweden: Chalmers University of Technoology, 2005. [Online]. Available: http://www.chalmers.se/

[20] M. Bongiorno and T. Thiringer, "A generic dfig model for voltage dip ride-through analysis," *Energy Conversion, IEEE Transactions on*, vol. 28, no. 1, pp. 76–85, Mar. 2013.

[21] E. H. Camm, M. R. Behnke, O. Bolado, M. Bollen, M. Bradt, C. Brooks, W. Dilling, M. Edds, W. J. Hejdak, D. Houseman, S. Klein, F. Li, J. Li, P. Maibach, T. Nicolai, J. Patino, S. V. Pasupulati, N. Samaan, S. Saylors, T. Siebert, T. Smith, M. Starke, and R. Walling, "Characteristics of wind turbine generators for wind power plants," in *2009 IEEE Power Energy Society General Meeting*, July 2009, pp. 1–5.

[22] J. F. Conroy and R. Watson, "Low-voltage ride-through of a full converter wind turbine with permanent magnet generator," *IET Renewable Power Generation*, vol. 1, no. 3, pp. 182–189, September 2007.

[23] A. Beeckmann, V. Diedrichs, and S. Wachtel, "Evaluation of wind energy converter behavior during network faults - limitations of low voltage ride through test and interpretation of the test results," in *9th International Workshop on Large-Scale Integration of Wind Power into Power Systems as well as on Transmission Networks for Offshore Wind Power Plants*, Oct. 2010.

[24] C. N. Kendeck and A. K. Raji, "Control of permanent magnet synchronous generator based wind turbine and fault ride-through improvement during faulty grid conditions," in *2016 International Conference on the Industrial and Commercial Use of Energy (ICUE)*, Aug 2016, pp. 298–304.

[25] IEC 61400-21 ed2.0, *Wind turbines - Part 21: Measurement and assessment of power quality characteristics of grid connected wind turbines*. Germany: International Electrotechnical Commission, 2008.

[26] E.ON, *Grid Code - High and Extra High Voltage*. Bayreuth, Germany: E.ON Nets GmbH, April. 2006.

[27] ——, *Requirements for Off-Shore Grid Connection in the E.On Nets Network*. Bayreuth, Germany: E.ON Nets GmbH, April. 2008.

[28] National Grid, *The Grid Code, Issue 5, Revision 19, 30th September 2016*. National Grid Electricity Transmission plc, September 2016.

[29] Red Electrica de España, *Resolution-P.O.12.3-Requisitos de respuesta frente a huevos de tensión de las instalaciones de producción de régimen especial*. REE, March 2006.

[30] EirGrid, *EirGrid Grid Code Version 6.0*. EirGrid, July 20105.

[31] ENERGINETDK, *Technical regulation 3.2.5 for wind power plants with a power output greater than 11 kW*. Energinet.dk, September 2010.

[32] Svenska Kraftnät, *The Business Agency Svenska kraftnats regulations and general advice concerning the reliable design of production plants*. Svenska Kraftnat, July 2005.

[33] Nordel, *Nordic Grid Code 2007, Nordic Collection of Rules*. Nordic Grid, Januray 2007.

[34] ENTSO-E. (2016, April) Entso-e network code for requirements for grid connection applicable to all generators. [Online]. Available: https://www.entsoe.eu

[35] M. Altın, O. Göksu, R. Teodorescu, P. Rodriguez, B. B. Jensen, and L. Helle, "Overview of recent grid codes for wind power integration," in *Optimization of Electrical and Electronic Equipment (OPTIM), 2010 12th International Conference on*, Sept. 2010, pp. 1152–1160.

[36] I. Erlich and U. Bachmann, "Grid code requirements concerning connection and operation of wind turbines in germany," in *Power Engineering Society General Meeting, 2005. IEEE*, vol. 2, June 2005, pp. 1253–1257.

[37] M. Molina, J. A. Suul, and T. Undeland, "A simple method for analytical evaluation of lvrt in wind energy for induction generators with statcom or svc," in *Power Electronics and Applications, 2007 European Conference on*, Sept. 2007, pp. 1–10.

[38] I. Martinez and D. Navarro, "Gamesa dac converter: the way for ree grid code certification," in *Power Electronics and Motion Control Conference, 2008. EPE-PEMC 2008. 13the*, Sept. 2008, pp. 437–443.

[39] W. asbl/vzw. (2016) Windeurope. [Online]. Available: https://windeurope.org

[40] ENSTO-E, *ANNUAL REPORT 2015, Electricity without borders*. ENSTO-E European Network of Transmission System Operators for Electricity, 2015.

[41] Y. Yang, F. Blaabjerg, and Z. Zou, "Benchmarking of voltage sag generators," in *IECON 2012 - 38th Annual Conference on IEEE Industrial Electronics Society*, Oct 2012, pp. 943–948.

[42] C. Wessels, R. Lohde, and F. Fuchs, "Transformer based voltage sag generator to perform lvrt and hvrt tests in the laboratory," in *Power Electronics and Motion Control Conference (EPE/PEMC), 2010 14th International*, Sept 2010, pp. T11–8–T11–13.

[43] J. C. Ausin, D. N. Gevers, and B. Andresen, "Fault ride-through capability test unit for wind turbines," *Wind Energy*, vol. 11, no. 1, pp. 3–12, 2008. [Online]. Available: http://dx.doi.org/10.1002/we.255

[44] S. Hu, J. Li, and H. Xu, "Comparison of voltage sag generators for wind power system," in *Power and Energy Engineering Conference, 2009. APPEEC 2009. Asia-Pacific*, March 2009, pp. 1–4.

[45] I. J. Gabe, H. Grundling, and H. Pinheiro, "Design of a voltage sag generator based on impedance switching," in *IECON 2011 - 37th Annual Conference on IEEE Industrial Electronics Society*, Nov 2011, pp. 3140–3145.

[46] W. Jian, H. Zhihao, X. Dianguo, and H. Ke, "An experimental research on comparison of two kinds of voltage sag generators," in *Power Electronics and Motion Control Conference (IPEMC), 2012 7th International*, vol. 4, June 2012, pp. 2784–2788.

[47] M. Diaz and R. Cardenas, "Matrix converter based voltage sag generator to test lvrt capability in renewable energy systems," in *Ecological Vehicles and Renewable Energies (EVER), 2013 8th International Conference and Exhibition on*, March 2013, pp. 1–7.

[48] J. He and Y. W. Li, "Generalized closed-loop control schemes with embedded virtual impedances for voltage source converters with lc or lcl filters," *Power Electronics, IEEE Transactions on*, vol. 27, no. 4, pp. 1850–1861, Apr. 2012.

[49] Y. Liu and Z. Li, Chen, "A flexible power control method of vsc-hvdc link for the enhancement of effective short-circuit ratio in a hybrid multi-infeed hvdc system," *Power Systems, IEEE Transactions on*, vol. 28, no. 2, pp. 1568–1581, May 2013.

[50] M. Bongiorno and J. Svensson, "Voltage dip mitigation using shunt-connected voltage source converter," *Power Electronics, IEEE Transactions on*, vol. 22, no. 5, pp. 1867–1874, Sep. 2007.

[51] L. Harnefors, M. Bongiorno, and S. Lundberg, "Input-admittance calculation and shaping for controlled voltage-source converters," *Industrial Electronics, IEEE Transactions on*, vol. 54, no. 6, pp. 3323–3334, Dec 2007.

[52] R. Ottersen, "On control of back-to-back converters and sensorless induction machine drivs," Ph.D. dissertation, Chalmers University of Technology, Gothenburg, Sweden, June 2003.

[53] M. R. Centre. Pscad/emtdc v4.2. [Online]. Available: https://hvdc.ca/pscad/

[54] F. Blaabjerg, M. Liserre, and K. Ma, "Power electronics converters for wind turbine systems," in *2011 IEEE Energy Conversion Congress and Exposition*, Sept 2011, pp. 281–290.

[55] F. D. Freijedo, A. Vidal, A. G. Yepes, J. M. Guerrero, O. Lopez, J. Malvar, and J. Doval-Gandoy, "Tuning of synchronous-frame pi current controllers in grid-connected converters operating at a low sampling rate by mimo root locus," *IEEE Transactions on Industrial Electronics*, vol. 62, no. 8, pp. 5006–5017, Aug 2015.

[56] L. Harnefors, X. Wang, A. G. Yepes, and F. Blaabjerg, "Passivity-based stability assessment of grid-connected vscs," *IEEE Journal of Emerging and Selected Topics in Power Electronics*, vol. 4, no. 1, pp. 116–125, March 2016.

[57] K.R. Padiyar, *Analysis of Subsynchronous Resonance in Power Systems*. Springer US, 1999. [Online]. Available: http://www.gwec.net/

[58] L. Harnefors, "Analysis of subsynchronous torsional interaction with power electronic converters," *IEEE Transactions on Power Systems*, vol. 22, no. 1, pp. 305–313, Feb 2007.

[59] S. Chernet and M. Bongiorno, "Input impedance based nyquist stability criterion for subsynchronous resonance analysis in dfig based wind farms," in *Energy Conversion Congress and Exposition (ECCE), 2015 IEEE*, Sept 2015, pp. 6285–6292.

[60] B. Wen, D. Boroyevich, R. Burgos, P. Mattavelli, and Z. Shen, "Analysis of d-q small-signal impedance of grid-tied inverters," *IEEE Transactions on Power Electronics*, vol. 31, no. 1, pp. 675–687, Jan 2016.

[61] B. Wen, D. Dong, D. Boroyevich, R. Burgos, P. Mattavelli, and Z. Shen, "Impedance-based analysis of grid-synchronization stability for three-phase paralleled converters," *IEEE Transactions on Power Electronics*, vol. 31, no. 1, pp. 26–38, Jan 2016.

[62] M. Cespedes and J. Sun, "Three-phase impedance measurement for system stability analysis," in *Control and Modeling for Power Electronics (COMPEL), 2013 IEEE 14th Workshop on*, June 2013, pp. 1–6.

[63] I. The MathWorks. Matlab r2011a/r2013b. [Online]. Available: http://se.mathworks.com/

[64] Wolfram. Wolfram mathematica 8. [Online]. Available: https://www.wolfram.com/

[65] H. Liu and J. Sun, "Voltage stability and control of offshore wind farms with ac collection and hvdc transmission," *Emerging and Selected Topics in Power Electronics, IEEE Journal of*, vol. 2, no. 4, pp. 1181–1189, Dec 2014.

[66] B. Wen, D. Boroyevich, P. Mattavelli, R. Burgos, and Z. Shen, "Modeling the output impedance negative incremental resistance behavior of grid-tied inverters," in *Applied Power Electronics Conference and Exposition (APEC), 2014 Twenty-Ninth Annual IEEE*, March 2014, pp. 1799–1806.

[67] A. Uphues, K. Notzold, R. Wegener, S. Soter, and R. Griessel, "Inverter based voltage sag generator with pr-controller," in *IECON 2012 - 38th Annual Conference on IEEE Industrial Electronics Society*, Oct 2012, pp. 1037–1042.

[68] S. Seman, J. Niiranen, R. Virtanen, and J.-P. Matsinen, "Low voltage ride-through analysis of 2 mw dfig wind turbine - grid code compliance validations," in *Power and Energy Society General Meeting - Conversion and Delivery of Electrical Energy in the 21st Century, 2008 IEEE*, July 2008, pp. 1–6.

[69] J. He and Y. W. Li, "Analysis, design, and implementation of virtual impedance for power electronics interfaced distributed generation," *Industry Applications, IEEE Transactions on*, vol. 47, no. 6, pp. 2525–2538, Nov./Dec. 2011.

[70] M. Bongiorno and J. Svensson, "Voltage dip mitigation using shunt-connected voltage source converter," in *Power Electronics Specialists Conference, 2006. PESC '06. 37th IEEE*, June 2006, pp. 1–7.

[71] T. Wijnhoven, G. Deconinck, T. Neumann, and I. Erlich, "Control aspects of the dynamic negative sequence current injection of type 4 wind turbines," in *2014 IEEE PES General Meeting — Conference Exposition*, July 2014, pp. 1–5.

[72] S. K. Chaudhary, R. Teodorescu, P. Rodriguez, P. C. Kjaer, and A. M. Gole, "Negative sequence current control in wind power plants with vsc-hvdc connection," *IEEE Transactions on Sustainable Energy*, vol. 3, no. 3, pp. 535–544, July 2012.

[73] C. Liu, D. Xu, N. Zhu, F. Blaabjerg, and M. Chen, "Dc-voltage fluctuation elimination through a dc-capacitor current control for dfig converters under unbalanced grid voltage conditions," *Power Electronics, IEEE Transactions on*, vol. 28, no. 7, pp. 3206–3218, July 2013.

[74] Nicolás Espinoza, *Grid Code Testing of Wind Turbines by Voltage Source Converter Based Test Equipment*. Gothenburg, Sweden: Chalmers University of Technoology, 2015. [Online]. Available: http://www.chalmers.se/

[75] G. Francis, R. Burgos, D. Boroyevich, F. Wang, and K. Karimi, "An algorithm and implementation system for measuring impedance in the d-q domain," in *Energy Conversion Congress and Exposition (ECCE), 2011 IEEE*, Sept 2011, pp. 3221–3228.

[76] dSPACE GmbH. dspace system. [Online]. Available: http://www.dspace.com

[77] M. Beza and M. Bongiorno, "Improved discrete current controller for grid-connected voltage source converters in distorted grids," in *Energy Conversion Congress and Exposition (ECCE), 2012 IEEE*, Sept 2012, pp. 77–84.

[78] M. Beza, "Power system stability enhancement using shunt-connected power electronic devices with active power injection capability," Ph.D. dissertation, Chalmers University of Technology, Gothenburg, Sweden, Januaey 2015.

[79] D. D. Patel, N. G. Chothani, and K. D. Mistry, "Sequence component of currents based differential protection of power transformer," in *2015 Annual IEEE India Conference (INDICON)*, Dec 2015, pp. 1–6.

[80] F. Gonzalez-Longatt, A. Bonfiglio, R. Procopio, and D. Bogdanov, "Practical limit of synthetic inertia in full converter wind turbine generators: Simulation approach," in *2016 19th International Symposium on Electrical Apparatus and Technologies (SIELA)*, May 2016, pp. 1–5.

[81] J. F. Conroy and R. Watson, "Frequency response capability of full converter wind turbine generators in comparison to conventional generation," *IEEE Transactions on Power Systems*, vol. 23, no. 2, pp. 649–656, May 2008.

[82] Mattias Persson, *Frequency Response by Wind Farms in Islanded Power Systems with High Wind Power Penetration*. Gothenburg, Sweden: Chalmers University of Technoology, 2015. [Online]. Available: http://www.chalmers.se/

Appendix A

Transformations for Three-phase Systems

This appendix reports necessary transformations to calculate voltage vectors from three-phase quantities and vice versa. Expressions of the voltage vector both in the fixed and rotating reference frames are given in the general case of unsymmetrical three-phase quantities.

A.1 Transformation of three-phase quantities into vectors

A three-phase positive system constituted by the three quantities $v_1(t)$, $v_2(t)$ and $v_3(t)$ can be transformed into a vector in a complex reference frame, usually called $\alpha\beta$-frame, by applying the transformation defined by

$$\underline{v}(t) = v_\alpha + \mathrm{j}v_\beta = K\left[v_1(t) + v_2 e^{\mathrm{j}\frac{2}{3}\pi}(t) + v_3 e^{\mathrm{j}\frac{4}{3}\pi}(t)\right] \tag{A.1}$$

where the factor K is equal to $\sqrt{3/2}$ or $3/2$ to ensure power invariance or voltage invariance, respectively, between the two systems. Equation (A.1) can be expressed as a matrix equation as follows

$$\begin{bmatrix} v_\alpha(t) \\ v_\beta(t) \end{bmatrix} = \mathbf{C}_{23} \begin{bmatrix} v_1(t) \\ v_2(t) \\ v_3(t) \end{bmatrix} \tag{A.2}$$

where, using power-invariant transformation, the matrix $\mathbf{C}_{23}$ is equal to

$$\mathbf{C}_{23} = \begin{bmatrix} \sqrt{\frac{2}{3}} & \frac{-1}{\sqrt{6}} & \frac{-1}{\sqrt{6}} \\ 0 & \frac{1}{\sqrt{2}} & \frac{-1}{\sqrt{2}} \end{bmatrix} \tag{A.3}$$

The inverse transformation, assuming no zero-sequence, is given by

$$\begin{bmatrix} v_1(t) \\ v_2(t) \\ v_3(t) \end{bmatrix} = \mathbf{C}_{32} \begin{bmatrix} v_\alpha(t) \\ v_\beta(t) \end{bmatrix} \tag{A.4}$$

where

$$\mathbf{C}_{32} = \begin{bmatrix} \sqrt{\frac{2}{3}} & 0 \\ \frac{-1}{\sqrt{6}} & \frac{1}{\sqrt{2}} \\ \frac{-1}{\sqrt{6}} & \frac{-1}{\sqrt{2}} \end{bmatrix} \tag{A.5}$$

A.2 Transformation between fixed and rotating coordinate systems

Let the vectors $\underline{v}(t)$ and $\underline{u}(t)$ rotate in the $\alpha\beta$-frame with the angular frequency $\omega(t)$ in the positive (counter-clockwise) direction. If the vector $\underline{u}(t)$ is taken as the d-axis of a dq-frame that rotates in the same direction with the same angular frequency $\omega(t)$, both vectors will appear as fixed vectors in that frame. The components of $\underline{v}(t)$ in the dq-frame are thus given by the projections of the vector on the direction of $\underline{u}(t)$ and on the orthogonal direction, as illustrated in Fig.A.1.

The transformation can be written in vector form as

$$\underline{v}^{(dq)}(t) = \underline{v}^{(\alpha\beta)}(t)e^{-\mathrm{j}\theta(t)} \tag{A.6}$$

with the angle $\theta(t)$ in Fig.A.1 given by

$$\theta(t) = \theta_0 + \int_0^t \omega(\tau)d\tau \tag{A.7}$$

The inverse transformation, from the rotating dq-frame to the fixed $\alpha\beta$-frame is defined by

$$\underline{v}^{(\alpha\beta)}(t) = \underline{v}^{(dq)}(t)e^{\mathrm{j}\theta(t)} \tag{A.8}$$

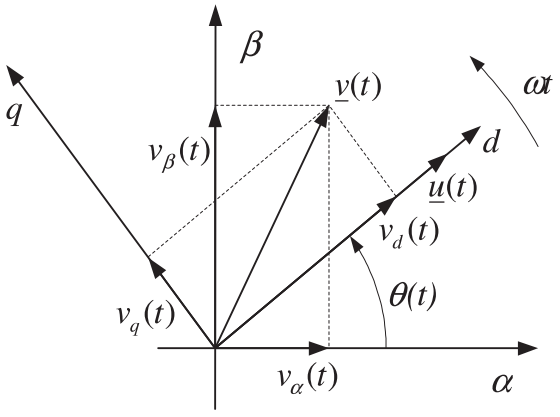

Fig. A.1 Relation between $\alpha\beta$-frame and dq-frame.

The components in the dq-frame can be determined from Fig.A.1. In matrix form, the transformation from the fixed $\alpha\beta$-frame to the dq-frame can be written as

$$\begin{bmatrix} v_d(t) \\ v_q(t) \end{bmatrix} = \mathbf{R}(-\theta(t)) \begin{bmatrix} v_\alpha(t) \\ v_\beta(t) \end{bmatrix} \tag{A.9}$$

while the inverse is given by

$$\begin{bmatrix} v_\alpha(t) \\ v_\beta(t) \end{bmatrix} = \mathbf{R}(\theta(t)) \begin{bmatrix} v_d(t) \\ v_q(t) \end{bmatrix} \tag{A.10}$$

where the projection matrix is

$$\mathbf{R}(\theta(t)) = \begin{bmatrix} \cos(\theta(t)) & -\sin(\theta(t)) \\ \sin(\theta(t)) & \cos(\theta(t)) \end{bmatrix} \tag{A.11}$$

A.3 Voltage vectors for unsymmetrical three-phase systems

The phase voltages for a three-phase system can be written as

$$\begin{array}{ll} e_{\mathrm{a}}(t) & = \widehat{e}_{\mathrm{a}}(t)\cos\left[\omega(t) - \varphi_{\mathrm{a}}\right] \\ e_{\mathrm{b}}(t) & = \widehat{e}_{\mathrm{b}}(t)\cos\left[\omega(t) - \frac{2}{3}\pi - \varphi_{\mathrm{b}}\right] \\ e_{\mathrm{c}}(t) & = \widehat{e}_{\mathrm{c}}(t)\cos\left[\omega(t) - \frac{4}{3}\pi - \varphi_{\mathrm{c}}\right] \end{array} \tag{A.12}$$

where $\widehat{e}_{\mathrm{a}}(t)$ and φ_{a} are the amplitude and the phase angle of the phase voltage $e_{\mathrm{a}}(t)$, while ω is the angular frequency of the system.

If the voltage amplitude of the three phases are unequal, the resulting voltage vector $\underline{u}^{(\alpha\beta)}(t)$ in the fixed $\alpha\beta$-coordinate system can be expressed as the sum of two vectors rotating in opposite directions and interpreted as positive- and negative-sequence component vectors

$$\underline{u}^{(\alpha\beta)}(t) = E_{\mathrm{p}} e^{\mathrm{j}(\omega t + \varphi_{\mathrm{p}})} + E_{\mathrm{n}} e^{-\mathrm{j}(\omega t + \varphi_{\mathrm{n}})} \tag{A.13}$$

where E_{p} and E_{n} are the amplitudes of the positive and negative voltage vectors, respectively, and the corresponding phase angles are denoted by φ_{p} and φ_{n}.

When transforming the voltage vector $\underline{u}^{(\alpha\beta)}$ from the fixed $\alpha\beta$-plane to the rotating dq-coordinate system, two rotating frames can be used, accordingly. These two frames are called positive and negative synchronous reference frames (SRFs) and are denoted as dqp- and dqn-plane: the positive SRF rotates counterclockwise with the angular frequency, while the negative SRF rotates clockwise with the same frequency. These two frames can be defined by the following transformations

$$\begin{array}{ll} \underline{u}^{(dqp)}(t) & = e^{-\mathrm{j}\theta(t)} \underline{u}^{(\alpha\beta)}(t) \\ \underline{u}^{(dqn)}(t) & = e^{\mathrm{j}\theta(t)} \underline{u}^{(\alpha\beta)}(t) \end{array} \tag{A.14}$$

From the latter, it is straightforward to understand that a positive-sequence component corresponds to a DC-component (zero frequency) in the positive SRF, while a negative-sequence component corresponds to a vector that rotates with 100 Hz clockwise in the positive SRF

$$\underline{u}_{\mathrm{n}}^{(dqp)}(t) \quad = e^{-\mathrm{j}\theta(t)} e^{-\mathrm{j}\theta(t)} \underline{u}^{(dqn)}(t) = e^{\mathrm{j}2\theta(t)} \underline{u}^{(dqn)}(t) \tag{A.15}$$

An analogous relation can be derived for a positive-sequence component in the negative SRF.